

EDGE

Accelerate Design Innovation



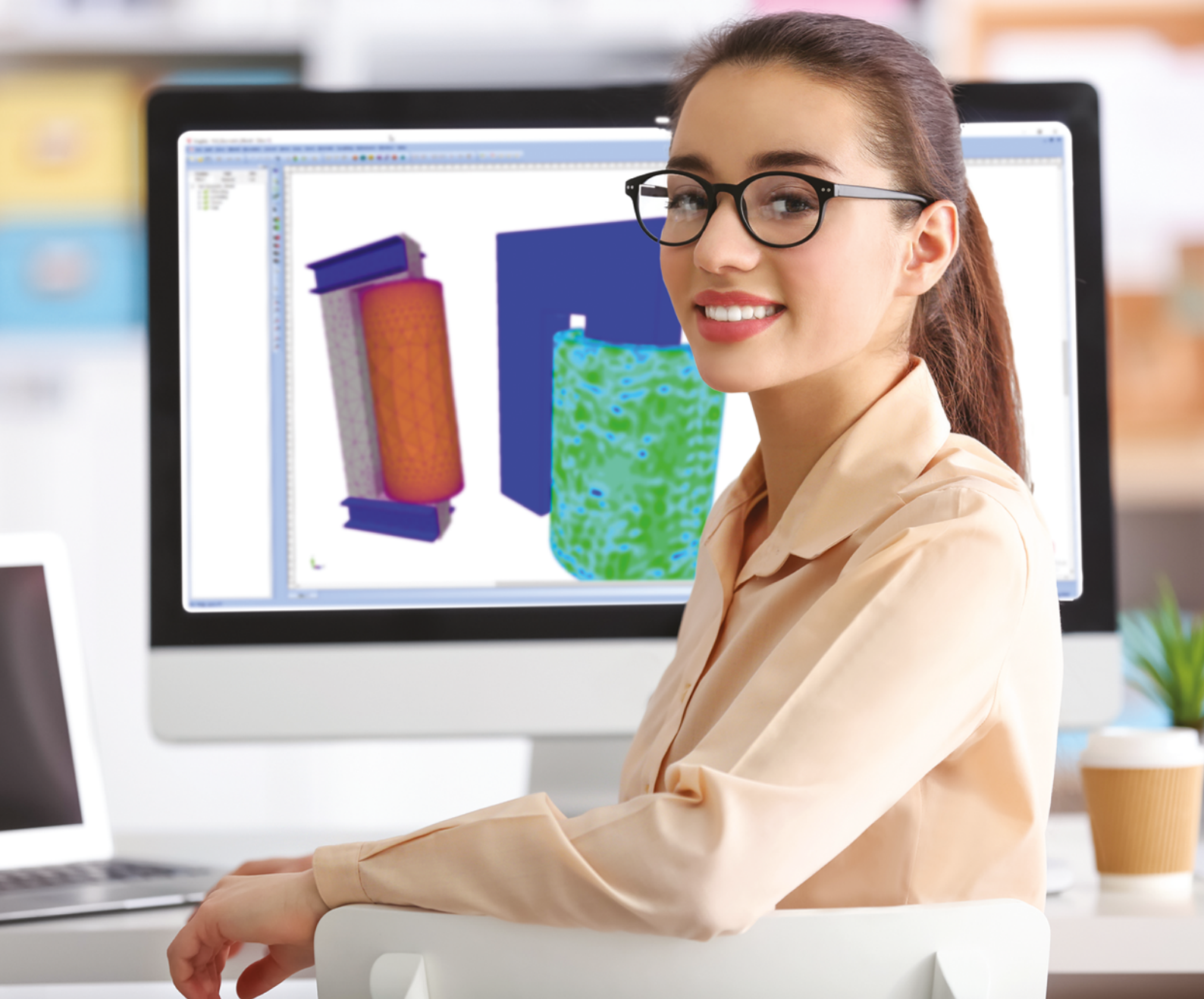
Syn Trac Engineers Create A Perfect Working Machine

Page 14

Hitachi Chemical Develop
New Materials For Power
Semiconductors
Page 24

Series Car Brake Cooling
By Continental
Page 62

Save time. Design more.



Virtual prototyping software to help you save time and money

Building physical prototypes is costly and time consuming. Our Electromagnetic and Thermal analysis software can accurately predict performance before testing and measuring, which reduces cost and speeds up the design process.





Vol. 07, Issue. 01

Greetings! Welcome to our new Infolytica readers who may be experiencing Engineering Edge for the first time. Last year we were very pleased to include Infolytica Corporation, with its world class MagNet and MotorSolve solutions, into our family of designer focused CAE products. Infolytica very much pioneered the low frequency electromagnetic FEA simulation market 40 years ago. Prof. David Lowther, their former CEO and now our Electromagnetics Technical Director shares some of his thoughts with us on digital twins and virtual reality as applied to the design of electrical machines on page 28.

It hardly seems like yesterday that we released FloMASTER V8 and now we have put V9 out with an exciting, and we believe world-leading, CAD2FM pipe network abstraction capability. It takes complex 3D geometries of pipework in MCAD formats and converts them to 1D components in a system network suitable for FloMASTER to use, all at the push of a button.

We do get excited when we see customers using combinations of our products and solutions to improve workflows and product development processes. Hence, seeing FloTHERM and T3Ster stories from Hitachi Chemical (page 24) and Denso Corporation (page 56) in Japan as well as Philips Lighting (page 92) in Europe in this edition confirms that this approach is adding value to our customers. Under the umbrella of Siemens Simcenter, we are seeing stories related to FloMASTER and Amesim in the aerospace industry from UEST, China (page 33) for a space vehicle launcher, and Parker Hannifin for MagNet and Amesim applied to aircraft hydraulic valve design (page 96) as proof of the synergies Mentor MAD brings to Siemens PLM users.

In connection with the Internet of Things (IoT) you can read of efforts from Dell (page 19) and Iceotope (page 67) who are using our tools to address this emerging market

need. FloEFD, our market leading multi-CAD embedded CFD tool is put to the test in terms of its accuracy with several stories in this edition across a breathtaking range of industries and applications including tractors (our cover story from SYN TRAC), turbochargers, the Space Shuttle, UAVs, eyes, heat exchangers, brake cooling, engine rooms, and thermo-electric coolers to name a few.

Lastly, this year we will be focusing on the Siemens Simcenter Conferences in Michigan on the 15-17th of October along with Prague on the 4-5th of December where all our products will be showcased. I would encourage you to participate in these unique customer presentation led events and I look forward to meeting a number of you at them.

**Roland Feldhinkel, General Manager,
Mechanical Analysis Division,
Mentor – A Siemens Company**

Mentor, a Siemens Business

Pury Hill Business Park,
The Maltings,
Towcester, NN12 7TB,
United Kingdom
Tel: +44 (0)1327 306000
email: ee@mentor.com

Editor:

Keith Hanna

Managing Editor:

Natasha Antunes

Copy Editor:

Jane Wade

Contributors:

Andrey Ivanov, Barbara Hazard, Doug Kolak, Jane Wade, Jean Paul Prevot, John Parry, John Wilson, Keith Hanna, Leonid Gurov, Maxim Popov, Mike Croegear, Mike Gruetzmacher, Nazita Saye, Prasad Tota, Prof. David Lowther, Puneet Sinha, Robin Bornoff, Svetlana Shtilkind and Vladimir Kirichenko

With special thanks to:

Apex Group, Borusan R&D, Ciena Corporation, Continental, Dell, Denso Corporation, EFD Corporation, Esteq Group, Hitachi Chemical Co., Ltd, Iceotope, Middle East Technical University, Ngee Ann Polytechnic, NXP Semiconductors, Parker Hannifin Corporation, Philips Lighting,

Rocky Mountain Technologies, termoflow.com and University of La Coruña

©2018 Mentor, a Siemens Business, all rights reserved. This document contains information that is proprietary to Mentor, a Siemens Business and may be duplicated in whole or in part by the original recipient for internal business purposes only, provided that this entire notice appears in all copies. In accepting this document, the recipient agrees to make every reasonable effort to prevent unauthorized use of this information.

All trademarks mentioned in this publication are the trademarks of their respective owners.

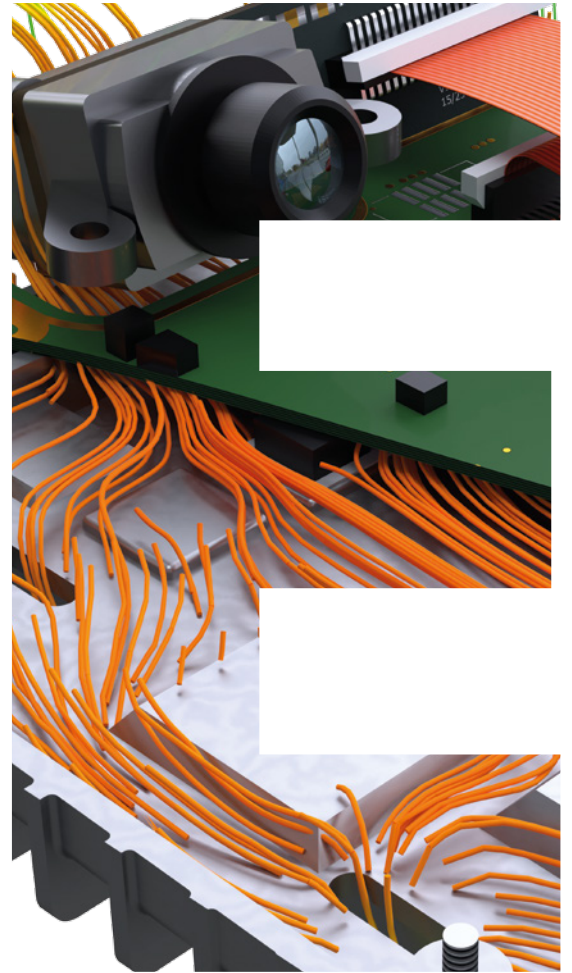


News

- 6** New Release: FloMASTER 9.0
- 7** New Release: FloTHERM 12.1
- 7** Free FloEFD Student Edition
- 8** FloEFD Award Announcement
- 9** FloTHERM Award Announcement
- 10** Vehicle Autonomy Design Challenges and Opportunities

Engineering Edge

- 14** Thermal Simulation of a SYN TRAC Powerpack
- 18** Edge Devices are Hot for IoT
- 21** Distributed Chilled Water Pumping AC System
- 24** Reliability Evaluation of Sintered Copper Die Bonding Materials
- 28** Virtual Reality and Modeling Tools
- 33** Simulation of Hydraulic Servo Gimbal Control of a Space Launch Vehicle
- 40** A Study of Aerothermal Loads
- 46** Development of a Turbocharger with FloEFD
- 50** Risk Prevention & Energy Saving in Ships
- 56** Three Thermal Simulation & Test Innovations for Electronics Equipment Design
- 62** Series Car Brake Cooling
- 67** Liquid Cooling Turned on its Side
- 70** Thermal Analysis of an ADAS Camera



- 75** Thermal Design Leading the Charge
- 78** Understanding Die Attach Thermal Performance
- 82** Rapid Beverage Cooling Analysis
- 84** Bitcoin Mining: A Thermal Perspective
- 88** Designing High Efficiency, Low-Cost Synchronous Reluctance Motors
- 90** From Measurements to Standardized Multi-Domain Compact Models of LEDs
- 94** A Cool Emulator
- 96** Achieving Precision in 1D Dynamic Models of Hydraulic Servo Valves
- 102** Using FloEFD as an Engineering Tool
- 106** Comparison between Experimental & Computational Results
- 112** Design of a High Speed Decoy UAV
- 114** Thermal Interface for Pluggable Optics Modules

Regular Features

- 32** Ask the GSS Expert
- 36** How to... Convert CAD Geometry into a FloMASTER Sub-System
- 54** Interview: Takuya Shinoda, Denso Corporation
- 118** Geek Hub: What do Engineers see in Coffee Grounds?
- 122** Brownian Motion

New Release: FloMASTER 9.0

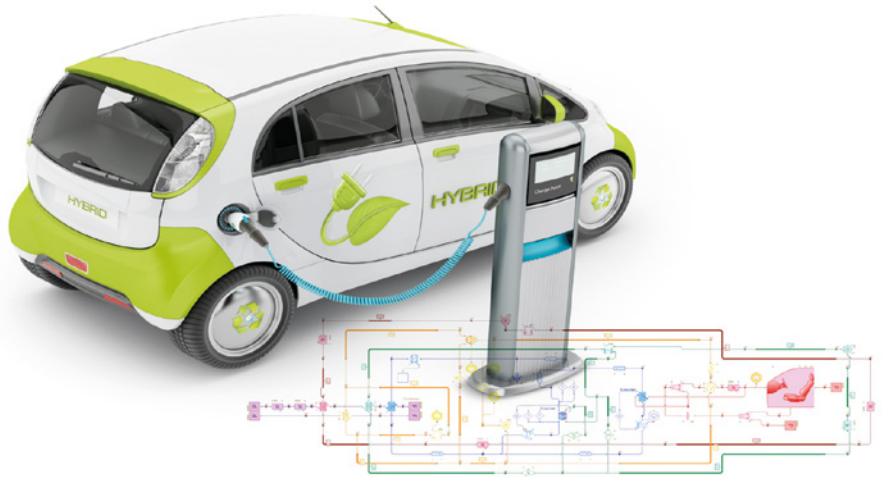
The latest release of the FloMASTER® 1D thermo-fluid system modeling software was announced in March. Combining integration with 3D mechanical computer-aided design (MCAD) with new physics and an improved user experience, the latest release of the FloMASTER tool is the result of extensive years of research and development. It's accuracy validated by running more than 13 million unit test runs.

The new FloMASTER release offers significant advancements in productivity through automated connectivity to 3D CAD design tools. The new "CAD-to-FloMASTER" (CAD2FM) functionality enables design engineers to rapidly create representations of their 3D systems. CAD2FM automatically abstracts the 3D descriptions of piping networks into a collection of connected FloMASTER components, reducing manual, labor-intensive and error-prone measure and re-enter methods.

"With the new CAD2FM capability in the FloMASTER release, we managed to massively speed up the conversion process of our piping systems from a 3D MCAD model to a system model," stated Stefano Morlacchi, CFD solution specialist, CADLOG. "We achieved this while still maintaining the accuracy of a fully-detailed FloMASTER network with all pipes, bend and junctions defined."

The highly automated workflow allows users to control the fidelity level of the abstracted models and the number of FloMASTER components created to represent the piping geometry for efficient thermo-fluid simulation. This new one-touch workflow is available in a standalone version, as well as integrated within PTC Creo, Dassault CATIA V5, and Siemens NX™ software and Solid Edge® software CAD tools.

In addition, the FloMASTER release includes new functionality for air conditioning (AC) systems. Enhancements have been made to the FloMASTER Enthalpy Solver and 14 new components added to the vapor Cycle (VC) component library. These enhancements enable AC systems to be modeled and simulated for a wide range of use cases, from traditional automotive and building systems, to complex, multi-component and multi-loop



systems for aerospace and advanced electrical vehicle (EV) cooling applications. By leveraging both the new AC developments and the existing VC components, several advanced thermodynamic cycles can be investigated including (but not limited to) Trilateral Flash Cycles, Trans-critical Rankine Cycles, and advanced multi-stage cycles. Using these powerful engineering components, designs can be quickly and easily created at the earliest stage possible, enabling accurate and quick system level design exploration.

The FloMASTER release also enhances the user experience through a number of new and improved features that offer improved result processing while facilitating common operations. In this framework, a new results dashboard is available as a quick reference tool to monitor critical results for transient simulations. A new gas turbine cavity result viewer provides the user with all results of a cavity in a single location. In addition, output parameters have been enhanced to allow the user to quickly view the result at the end of

the simulation, while the addition of schematic annotation allows users to highlight areas of interest and improve system understanding.

"Our new FloMASTER release provides feature-rich capabilities that deliver the accuracy, flexibility, and speed that address many key areas important to our customers, including those in today's highly competitive automotive systems market," stated Roland Feldhinkel, general manager of Mentor Graphics' Mechanical Analysis Division, now part of Siemens PLM Software's simulation and test division. "Leveraging our extensive knowledge and expertise in 1D and 3D mechanical analysis, our new 1D/3D CAD import tool represents a step change in automation that will significantly benefit our customers."

New Release: FloTHERM® 12.1

with New Command Center for Productivity and Performance

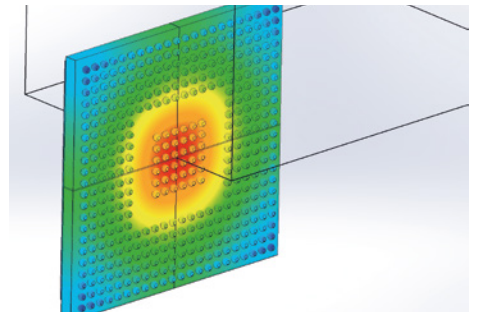
April sees the release of FloTHERM V12.1 with a selection of new features to improve accuracy and increase speed to useable results. With the new release it is now possible to import multiple measurements from T3Ster and for each measurement set the corresponding FloTHERM model temperature to calibrate. This option vastly improves confidence that calibration produces the right answer for the right reason.

Electrical noise at the start of a T3Ster measurement is now replaced with simulation data and then merged with the rest of the experimental data. This gives a common initial transient response between measured and simulation for every scenario.

Further enhancements to Command Center make it easier for users to identify the main effects of the design input, identify thermal domains in the product and helps to improve

design decisions. In this release a correlation matrix can be generated identifying where simulation time is best spent.

In addition FloTHERM V12.1 has improved scalability at higher core counts, enhancements to FloSCRIPT and version support where parts of the supply chain are not using the latest version.



Free FloEFD

for Solid Edge Student Edition

Mentor, a Siemens Business, is proud to announce the availability of FloEFD for Solid Edge Student Edition. FloEFD is a general purpose Computational Fluid Dynamics (CFD) software that is fully embedded in Solid Edge – one fully integrated interface for both design and CFD analysis. It offers fast and accurate results to keep pace with the design flow.

Taking advantage of synchronous technology, FloEFD takes design with Solid Edge to the next level. And now FloEFD for Solid Edge is available FREE to students using the educational version of Solid Edge.

Most importantly, it offers all the functionality of its commercial counterpart so engineering students can conduct realistic tests on their designs and be fully prepared to enter the workforce.

Fast. Accurate. Intuitive to use. Students: download and work with FloEFD for Solid Edge Student Edition now: <http://go.mentor.com/4XKnn>



FloEFD

Award Winners

2017 FloEFD Frontloading Computational Fluid Dynamics (CFD) Award Winners

This award recognizes individuals who have successfully implemented the practice of moving CFD simulation early into their design process using the Mentor® award-winning FloEFD™ technology. This methodology reduces the overall simulation time by as much as 65-75% and offers x2 to x40 user productivity enhancement relative to traditional CFD approaches.

A panel of judges selected the finalists based on submission criteria. Entrants were required to demonstrate the application of frontloading CFD with quantifiable results through published or publicly presented documentation. This included published technical and conference papers, PowerPoint presentations, articles, videos and/or website content that is accessible to the public. All winners were presented with their awards at the 2017 FloEFD Simulation Conference held in Berlin, Germany.

The First Place Award winner is Paul-Henri Matha from Renault in France for his presentation, Why Is Thermal Management Important for Automotive Lighting Systems, which was delivered at the 2016 FloEFD Simulation Conference in Frankfurt, Germany. Mr. Matha received a trophy and a \$1,000 Amazon gift card.

Two runners-up were also selected. Koen Beyers, Voxdale, received his award for an article published in Engineering Edge titled, Bike Valley Builds a Wind Tunnel Using FloEFD. The article was based on his presentation at the 2016 FloEFD Simulation Conference as well. The other runner-up was Enrico Lorenz from Dr. Schneider Unternehmensgruppe GmbH for his article FloEFD Helps Dr. Schneider's Mission: To Make the Car the Best Place in the World published in Engineering Edge.

"Mentor's FloEFD award-winning frontloading CFD solution provides our customers with the ability to conduct simulation early in the design process for optimum design success," stated



Roland Feldhinkel, general manager of the Mentor Mechanical Analysis Division. "We congratulate our 2017 award recipients who have demonstrated the value of FloEFD by optimizing the performance of their products while saving critical design time."

FLOTHERM Award Winners

2017 FloTHERM Award winners for Electronics Thermal Design Excellence

We are pleased to announce the winners of the inaugural annual FloTHERM® ΔTJ Award for Excellence in Electronics Thermal Design. For over 30 years, the FloTHERM solution has been the de facto computational fluid dynamics (CFD) solution for electronics cooling. The FloTHERM product provides tight connectivity with electronic design automation (EDA) and mechanical design automation (MDA) development process flows, and is used to predict airflow, temperature, and heat transfer in components, boards, and complete systems.

FloTHERM ΔTJ Award winners were required to demonstrate an application using the FloTHERM technology (including FloTHERM XT, FloTHERM PCB or FloTHERM IC) to successfully address a design problem. This included a return on investment (ROI) improvement due to quantifiable use of CFD technology.

The first place award winner is the team from the Institute of Microelectronics (IME), Agency of Science, Technology and Research in Singapore. The team comprising: Gong Yue Tang, Yong Han, Boon Long Lau, Xiaowu Zhang, and Daniel Min Woo Rhee, received a trophy for their paper, Development of a Compact and Efficient Liquid Cooling System with Silicon Micro-cooler for High-Power Microelectronic Devices. The team also received a \$1,000 Amazon gift card, which they have donated to the Singapore Children's Society.

"Microchannel based liquid cooling and thermal management technology has been used to develop the compact and efficient cooling system for high power electronics systems," stated Gong Yue Tang. "Through the thermal modeling and simulations, FloTHERM has been demonstrated as a fast and cost-effective thermal design tool to evaluate and optimize the thermal performance of the liquid cooling system proposed in this study."

Two runners-up were also selected. Hugo Ljunggren Falk, KTH School of Industrial Engineering and Management in Sweden received a \$500 Amazon gift card for

his paper, Thermal Management in an IR-Camera. And Gabriel Ciobanu from Continental Corporation in Romania also received the same for his paper, co-written with Boris Marovic from Mentor, entitled The Fundamentals of Improving PCB Thermal Design.

"Used by thousands of engineers across the globe, FloTHERM is the award-winning CFD electronics cooling solution used by the world's leading companies," said Roland Feldhinkel, general manager of the Mentor Mechanical Analysis Division. "This is our inaugural FloTHERM Award competition and we are honored by the broad range of successful applications we received. Congratulations to our 2017 winners, and we look forward to next year's competition."



Figure 1. Gong Yue Tang, Yong Han, Boon Long Lau, Xiaowu Zhang, and Daniel Min Woo Rhee, First Place Winners of the 2017 Mentor FloTHERM® ΔTJ Award



Figure 2. Hugo Ljunggren Falk, Runner-up for Mentor's 2017 FloTHERM® ΔTJ Award.



Figure 3. Gabriel Ciobanu, Runner-up for Mentor's 2017 FloTHERM® ΔTJ Award.

Design Challenges & Opportunities

for Electric Powertrain with Vehicle Autonomy

By Puneet Sinha, Automotive Manager & Doug Kolak, Technical Marketing Engineer, Mentor, a Siemens Business

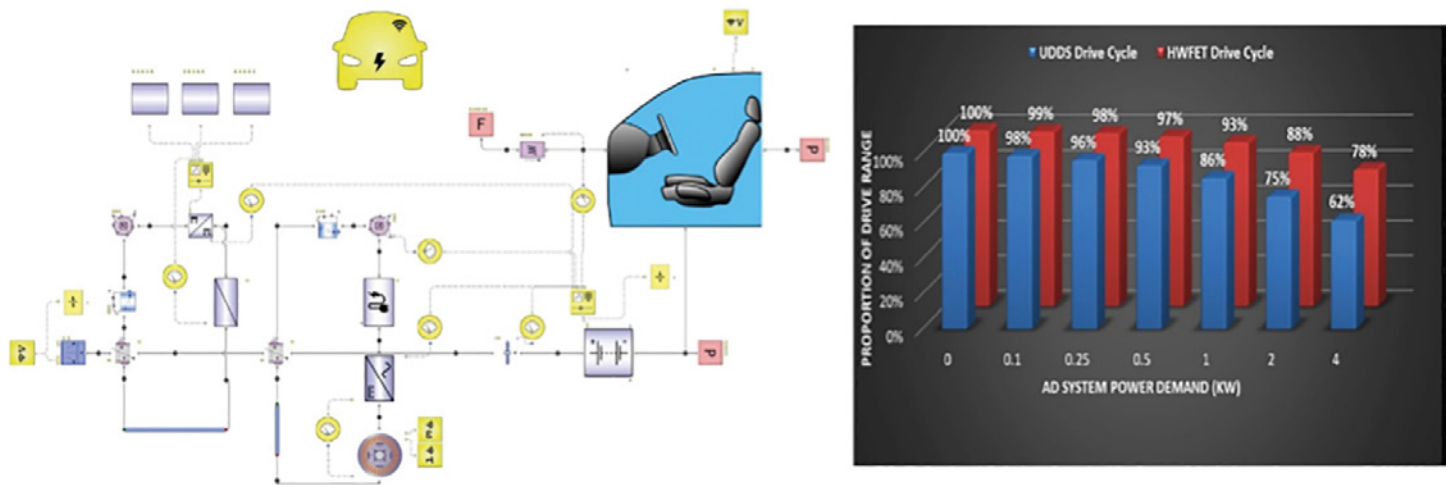


Figure 1. FloMASTER AV system model with drive range results for varying drive cycles and AD system power demand

By 2030, nearly 25% of all miles driven in the United States could be in shared autonomous electric vehicles, as per a recent study by the Boston Consulting Group [1]. The majority of autonomous vehicles announced by automakers or that are in fleet testing have electric powertrains (if not full electric, then hybridized). An electric powertrain is indispensable for autonomous vehicles because of higher fuel efficiency and reduced CO₂ emissions. It is an easier platform to support drive-by-wire systems needed for vehicle autonomy; and, as battery prices keep dropping sharply, electric is an attractive proposition because of lower cost of ownership and maintenance, especially for fleet owners in a ride-sharing ecosystem.

However, the integration of vehicle autonomy with electrification is not a matter of simple plug-and-play manufacturing. It has its challenges, and these issues need to be taken into account from the earliest design/conceptualization phase for an autonomous electric vehicle. For starters, auxiliary power demand from the significant increase in vehicle electronics can reduce electric drive range. In this article, we will highlight some of the key new challenges and unique cost reduction and optimization opportunities that come with using electric powertrains in autonomous vehicles. For the sake of simplicity, we will focus on level 4/5 autonomous electric cars.

Impact of Vehicle Autonomy on Electric Drive Range

Fully autonomous cars (level 5) will have many more electronics (sensors, sensor fusion box, ECUs for drive-by-wire systems), than standard drive vehicles. With a fully electric powertrain, these electronics that enable autonomous functionality will need to be powered by the high-voltage battery, through a DC-DC converter for the 12-V line. This increased burden will reduce electric drive range and thus pose a critical challenge for developers of autonomous electric vehicles. On the other hand, machine

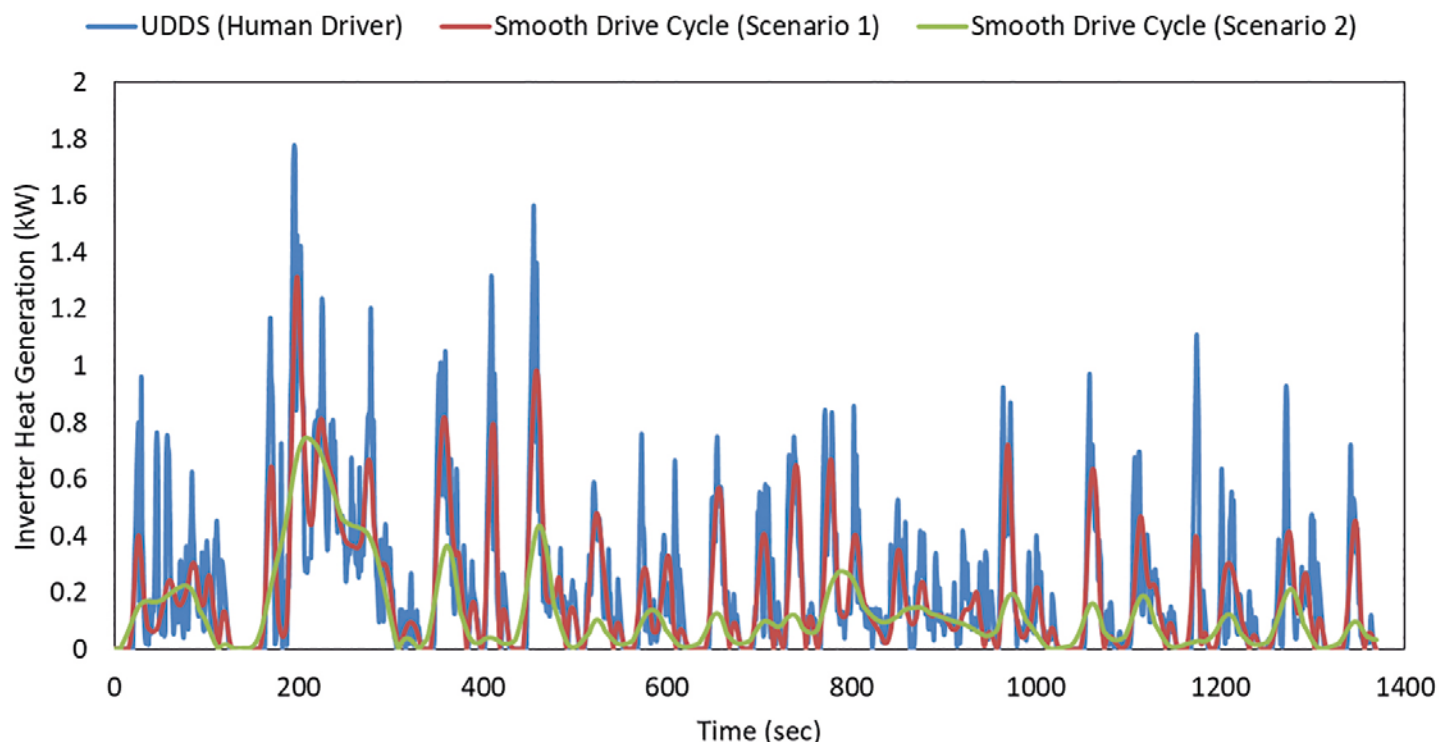


Figure 2. Energy and thermal management simulation, using FloMASTER™, for level 4/5 autonomous electric compact sedan accounting for increase in vehicle electronics and potential drive cycle smoothing that will come with machine driving. Simulations are for city drive cycle at 25oC ambient conditions. Drive cycle smoothing scenarios are provided by Dr. Kara Kockelman of UT Austin.

driving is expected to deliver a smoother drive pattern compared to human driving behavior. Smoother drive cycles allow more efficient use of battery energy, delivering a higher electric drive range. These trade-offs become a lot more interesting if we quantify the end effect!

The first part of the design we can look at is how the overall power requirements of the significant number of sensors and the sensor fusion box effect the total power consumption and in turn the overall drive range. To quantify the potential effects of different levels of autonomy as well as the potential for future improvements to the different components, it makes sense to look at several levels of total power requirements for the autonomous functionality enabling electronics systems. Figure 1 shows the reduction in drive range with different levels of power (and associated thermal) consumption from the autonomous systems as calculated with the model analyzed in FloMASTER. For this example, we are considering a compact sedan with a pure electric powertrain.

The challenge associated with minimizing power consumption becomes clear when looking at the reduction for power levels of 2-4kW which is the range of many of the current test vehicles on the roads today. This analysis further shows the advantage

of using a low power-consuming centralized sensor fusion architecture, such as Mentor's DRS360™ that promises to limit sensor fusion box power consumption to 100W.

However, autonomous driving can also have a potential benefit to drive range. Let us consider the example of a level-5 autonomous, electric, compact sedan with 30 sensors (lidars, radars, and cameras), and one sensor fusion box. The total load for this example is 1kW. How the drive profile will change for a connected autonomous vehicle is unknown and is an area of active research. Auto OEMs with autonomous vehicle test fleet on the road may have information about drive cycle smoothing for their vehicles. Alternatively, as auto OEMs are increasingly relying on virtual traffic scenarios and vehicle driving simulations for autonomous vehicle testing, simulation tools such as PreScan from Siemens, can be used to determine what level of drive profile smoothing to expect from machine driving.

For this example, we will use two scenarios from the simulated drive-cycle smoothing scenarios discussed in the research [2] conducted by Dr. Kockelman's group at the University of Texas in Austin. Scenario 1 (Figure 2) represents moderate smoothing

L4/5 autonomous vehicle EE architecture

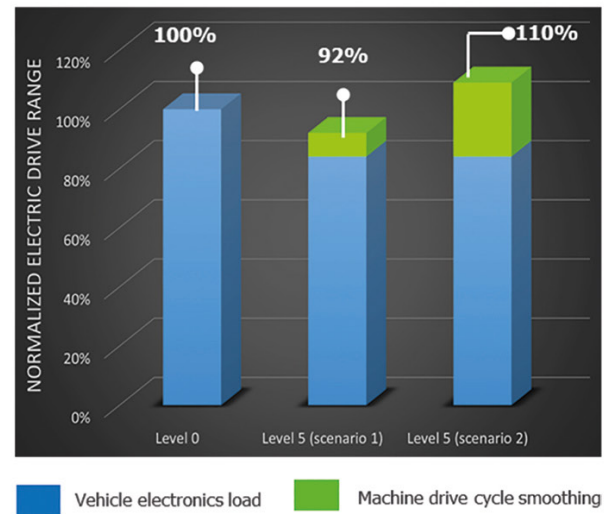
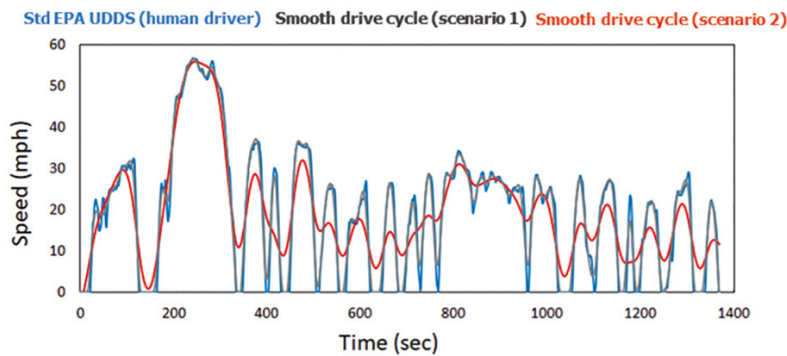
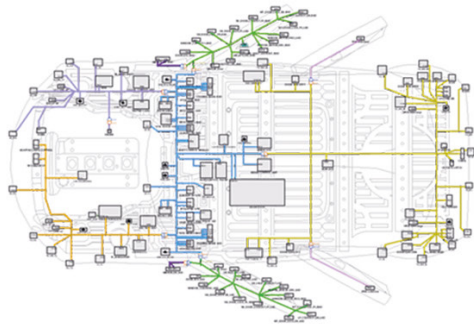


Figure 3. Comparison of heat generated by the inverter for different levels of machine driving profiles

of the drive profile throughout the cycle but especially at the points of complete stop and acceleration. Scenario 2 represents significantly more smoothing to a point where the connected autonomous vehicle can anticipate upcoming stops during city drive and slow down/accelerate accordingly without coming to a complete stop. For both these scenarios, the overall commute time has no change.

For city driving at 25°C ambient conditions and for this specific vehicle study, our analysis showed that the added electronics power demand on the main battery resulted in a nearly 16% reduced drive range. Reduction in drive range will be far higher if a higher power consuming, sensor-fusion box is used. Scenario 1 offers an 8% increase in electric drive range by better allocating battery energy to the wheels but still results in 92% electric drive range for a level 4/5 autonomous EV compared to a level 0 car. The significant increase in smoothing in scenario 2 delivers 110% electric range for a level 4/5 autonomous vehicle compared to a level 0 electric vehicle!

This analysis shows that the overall electronics load, especially power (and thermal load) of the sensor fusion box (which likely is the biggest power draw component from an autonomous driving system), needs to be minimized. More

importantly, depending on the change in the driving profile and what manufacturers are able to achieve through their machine-learning algorithms, the overall electric powertrain energy efficiency (for example, the battery design) needs to be improved or the battery pack size resized—either can help reduce cost. These numbers will differ depending on the characteristics of the powertrain (battery and motor design), vehicle size, electronics integration, and EE configuration of the vehicle, among other factors. But the underlying opportunity for e-powertrain optimization, outlined here, remains valid.

Other factors, such as platooning, especially for trucks/commercial fleet highway driving, can further enhance drive range, as shown in the work from NREL [3] showing the effect on fuel consumption of platooning a class-8 vehicle. This can open up additional opportunities for resizing the battery and other powertrain components.

Electric Powertrain Life and Reliability Implications

One major application for level 4/5 autonomous electric cars is the ride-sharing fleet, and it is expected that these vehicles may log 80,000 miles or more per year. For reference, New York taxis log approximately 70,000 miles per year. This

is a sharp contrast to today's predominant driving pattern where cars are parked more than 80% of the time. For batteries in electric vehicles today, shelf life (a measure of battery aging when it is resting at a certain state of charge and temperature), plays a significant role, in addition to their cycle life (a measure of battery aging when it is charged and discharged continuously) in determining overall battery life. For ride-sharing, autonomous electric vehicles, emphasis will be significantly more on cycle life while designing and characterizing batteries. Similarly, a smoother driving profile with machine driving can significantly reduce overall thermal load for the inverter and motor, which will provide opportunities to innovate new thermal management schemes for e-powertrain components. For instance, Figure 3 shows the change in instantaneous heat generation for an inverter, which is the 2nd largest cost component of e-powertrain after the battery, that may come with drive cycle smoothing with machine driving. Since temperature is the leading indicator of an inverter's reliability, the reduction in thermal load results in lower stringent thermal management requirements to ensure field reliability. Mentor's integrated testing and simulation workflow for inverter thermal management and lifetime characterization [4] can allow engineers to evaluate new architectures and accurately estimate inverter life for autonomous electric vehicles. These factors can allow OEMs to further reduce e-powertrain cost.

In summary, adding level 4/5 autonomous functionality to the electric powertrain introduces new challenges and opportunities that warrant resizing/ optimization of the battery, motor, and inverter, as well as their interactions in a powertrain. The example analysis shown here is helpful for manufacturers to not only account for powertrain design needs, but also to set power consumption targets for sensor fusion and other electronics vendors as well as develop target drive-cycle smoothing that needs to be achieved via machine learning and vehicle control strategies. Our combined Mentor-Siemens portfolio is unique in that it allows auto OEMs to frontload these considerations from earliest design stages, and create an accurate digital twin of an autonomous electric vehicle and a digital twin of autonomous vehicle driving behavior.

So the bottom line: Adding electric powertrain and autonomous vehicle makes perfect sense but like any other partnership, this one also needs work!

References:

- [1] By 2030, 25% Of Miles Driven in Us Could Be in Shared Self-driving Electric Cars
<https://www.bcg.com/d/press/10april2017-future-autonomous-electric-vehicles-151076>
- [2] "Anticipating the Emissions Impacts of Autonomous Vehicles Using the MOVES Model", J. Liu, K.M. Kockelman and A. Nichols, 96th Annual Meeting of the Transportation Research Board (2017)
- [3] "Effect of Platooning on Fuel Consumption of Class 8 Vehicles Over a Range of Speeds, Following Distances, and Mass", M.P. Lammert, A. Duran, J. Diez and K. Burton, SAE 2014 Commercial Vehicle Engineering Congress (2014)
- [4] "Field Lifetime Estimation of Effect of Power Modules Using Active Power Cycling", a Mentor White Paper.



Powerpack Thermal Simulation & Cooling air Requirements

By Kolio Kojouharov, General Manager, termoflow.com



The SYN TRAC is a completely new vehicle for different application areas, developed by SYN TRAC GmbH in Austria. The SYN TRAC is a more advanced and flexible vehicle than the market has been offered before. Its innovative coupling method allows for an automatic connection for hydraulics, pneumatics, electronics/CAN-bus, ground speed power take-off (PTO) and general operating concepts without leaving the vehicle.

The combination of the vehicle and the attachments form optimal synergies. The SYN TRAC engineers created a perfect working machine. They realized a wide range of possible configurations and flexible applications, for agriculture, transport infrastructure, municipal services, forestry, and special applications such as disaster control. Due to the automation of the coupling process, the operator does not have to enter the 'danger zone', they can remain in the vehicle cab, and so simultaneously save considerable time.

Being a completely new product, there were high expectations in terms of reliability, robustness for agricultural demands, costs and series-production readiness, being comparable to series automotive demands. This required enormous efforts from all participating disciplines. For this reason, the SYN TRAC engineers had to employ significant amount of digital prototyping and simulation from the very beginning. One major issue is the thermal management of the powerpack/powertrain and the heat balance of the engine compartment. Cooling airflow, fan performance and an appropriate cooler integration are strongly influenced by complex geometries and decreased available design space. The consideration of all these factors is crucial for the correct determination of the volume flow dependent pressure drop in the engine

With FloEFD, we were able to fulfill the challenge of short schedule and supported the high degree of digital prototyping."

**Kolio Kojouharov, General Manager,
termoflow.com**

compartment (system impedance) and thus for the selection of a suitable fan. In this respect the team of SYN TRAC worked with Kolio Kojouharov from Termoflow.com, an experienced consultancy in powerpack/ powertrain thermal management and state of the art CAE computational methods. Termoflow.com introduced CFD into the design process and worked on a simulation program in tight accordance with the SYN TRAC design team. In the course of this, a heat balance study and simulation of the cooling air of the engine bay for the two operating conditions at 0 km/h and 10 km/h ambient velocity were conducted to identify improvements.

The vehicle standstill condition (0 km/h) is always one of the most critical for thermal management because no ambient air for cooling is moved. Vehicle standstill and low speeds, with simultaneous full thermal load, are crucial for these areas of application (agricultural activities on fields, working at trees, municipal services on roads). In addition, due to the dusty air in the application areas, overpressure should be present in important engine regions and short circuits in the air flow distribution should be avoided wherever possible.

The following factors were identified:

- Velocity distribution of the cooling air in the machine;
- Pressure distribution of the cooling air in the machine;
- Temperature distribution of the cooling air in the machine;
- Pressure losses. Cooling air pressure drop vs. volume flow rate
- Cooling air inlet temperature; and
- Velocity distribution at cooler outlet.

Being aware of the challenge of dealing with a highly complex geometry within a short schedule, Termoflow.com used FloEFD™ with its efficient mesh generation capabilities and broad range of physical models, alongside their valuable experience with the tool in other projects.

One of the key benefits was the prediction of the system impedance, which helped find the optimal design point of the cooling system (Figure 1). Because of the dusty operating environment, the engine bay has to be capsuled as much as possible, though it needs to provide the required airflow for appropriate cooling across the entire engine operating range.

The CFD simulation was conducted for an ambient temperature of 45°C, the

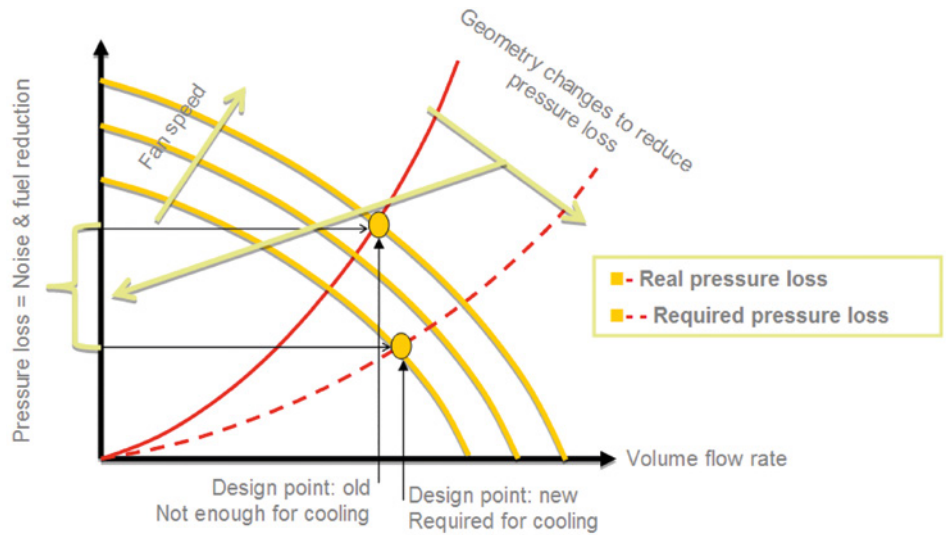


Figure 1. Cooling air vs. pressure loss

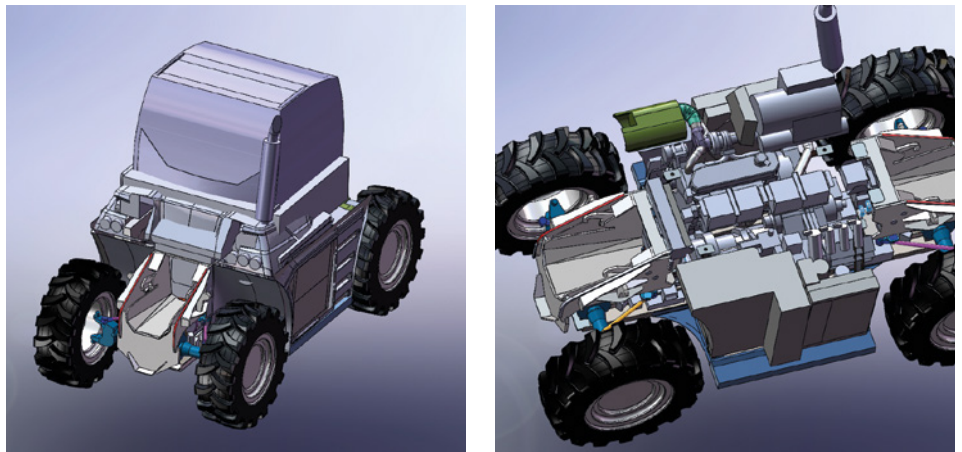


Figure 2a, b. CAD model of the SYN TRAC

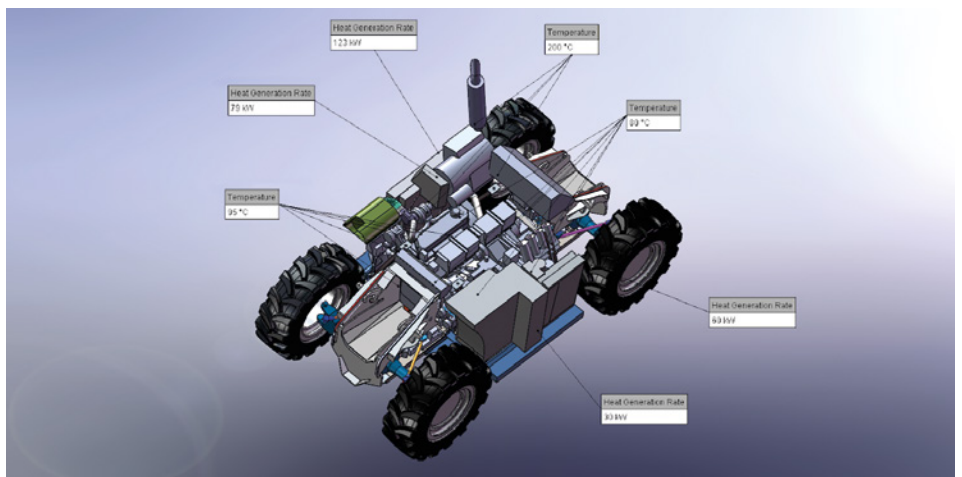


Figure 2. Boundary conditions

temperatures of the motor etc. were defined as boundary conditions.

One of the main tasks was the design of the coolers for charge air, cooling water and oil with a cooling capacity between 30 and 120 kW.

The air intake and exhaust should be as free as possible. For reliable operation, it is very important to avoid an intake of air that is much hotter than the ambient air.

The engineers compared a large number of result output images and investigated the flow distributions and temperature fields, based on the two operating stages simulated in FloEFD.

In Figure 3, the flow field at the back view is shown for the ambient velocity of 10 km/h. When the vehicle comes to a standstill, the air is only moved by the fans. The different flow profile to the moving vehicle is clearly visible in the image.

With these findings, the pressure resistance curves (cooling air pressure drop depending on volume flow rate) for several operating conditions were generated. Based on this, the design specifications for the fans could be determined also taking into account the installation conditions and space requirements. Another aspect that the engineers considered at an early stage, was the drive power for the fans, which also influences the overall vehicle efficiency.

The SYN TRAC engineers in collaboration with Termoflow.com gained a deep understanding of the flow distribution and the temperature fields, even for areas that are not visible without simulations, and realized the unique SYN TRAC.

References

- [1] <https://www.syn-trac.at/>
- [2] <https://www.termoflow.com/>
- [3] <https://www.youtube.com/watch?v=NdxjbVBHcWU>
- [4] <https://www.youtube.com/watch?v=YHtlb-X37dQ>

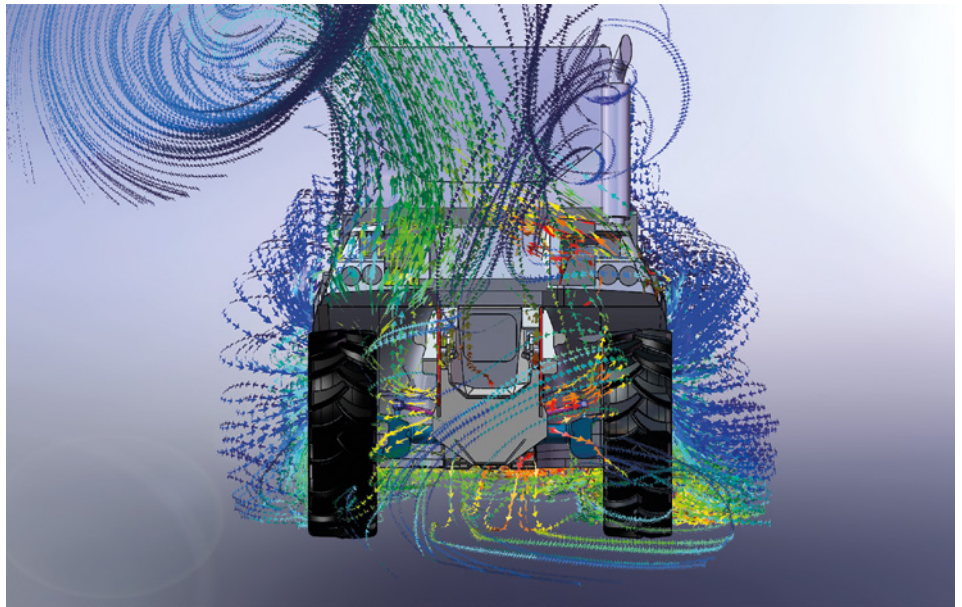


Figure 3. Flow field at the back view

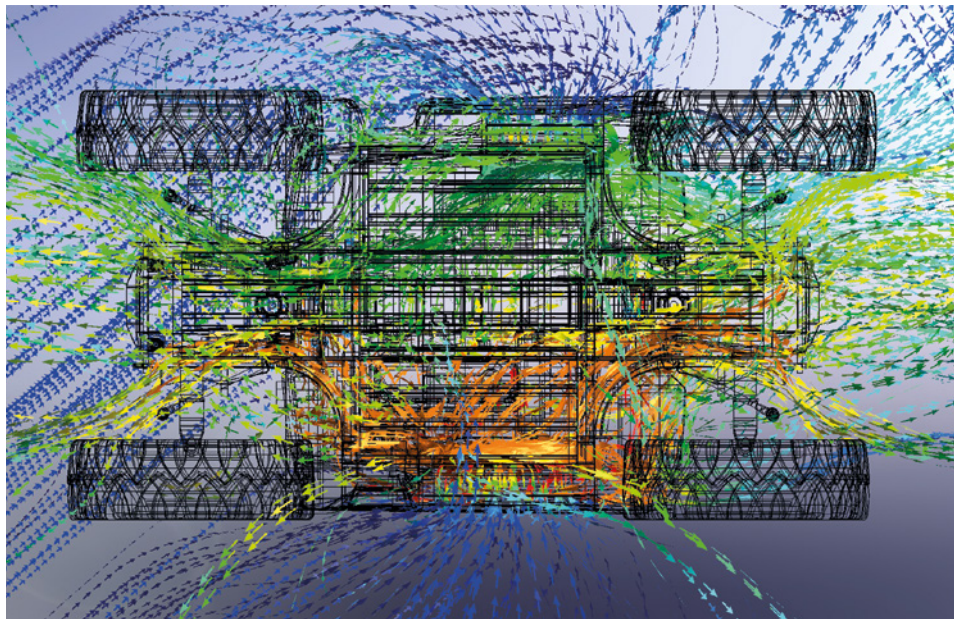


Figure 4. Cooling airflows into the undercarriage

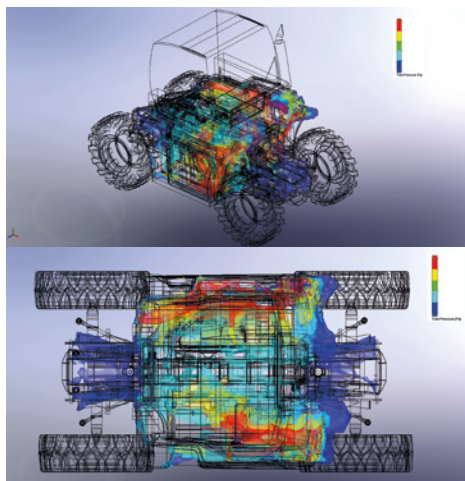


Figure 5 a, b. Analysis of the overpressure areas

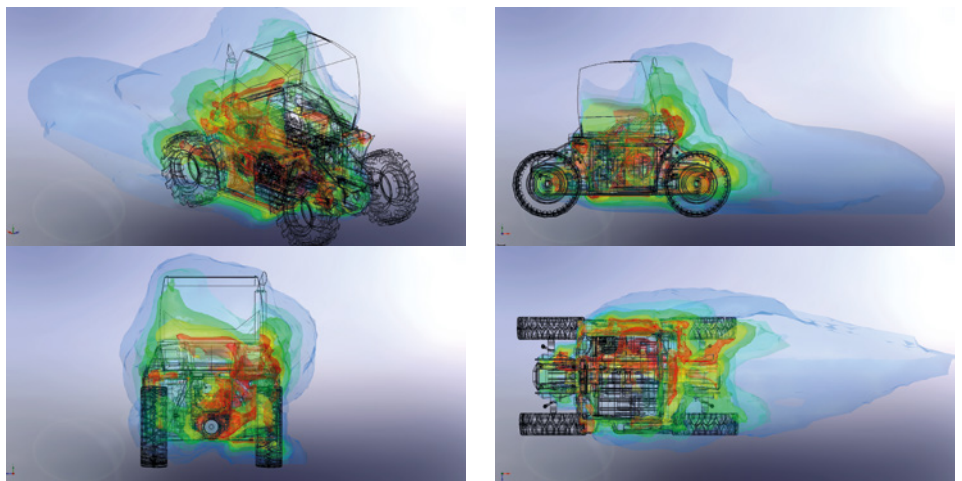


Figure 6 a - d. Analysis of the temperature distribution



Edge Devices are **Hot for IoT**



By Chris Helberg, Systems Architect, Thermal, Dell and Prasad Tota, Application Engineer, Mentor, a Siemens Business

Dell has been working on improving their IoT device (Internet of Things), Edge Gateway Model which helps with integration of IT and operation technology. The latest model 5100 from Dell is focused on creating an intelligent gateway that can operate reliably in extreme temperatures and help connect endpoints even in the most challenging industrial or enterprise environments.

Thermal Challenge

The latest model is expected to operate in an industrial environment and cannot employ a fan for cooling to ensure reliability. The Edge Gateway product could be wall mounted or DIN-rail mounted and be able to sustain a wide range of environment temperature from -30°C to 70°C. The IoT device should also be able to operate in a rugged enclosure which is IP65-rated, lockable and hardened to protect the Edge Gateway when wall mounted in unsecure indoor locations, inside factories and in outdoor applications where the device is exposed to the elements.

Dell used FloTHERM to optimize the rugged enclosure for heat dissipation for the new Model 5100 without requiring a fan, which would reduce reliability.

Our customer Chris Helberg had this to say about his experience, "FloTHERM allows the user to quickly create a 3D representation of the geometry when the detailed CAD is not available. We have taken full advantage of the parametric objects in FloTHERM to very quickly create a detailed thermal model and further study various design trade-offs. This helps avoid expensive late design changes. I would also like to add that the customer service and guidance we receive from the Mentor team in using the tool has been excellent."

The IoT device consists of a PCB (190x185 mm) with a CPU (BGA component) dissipating 5W and other components like



Dell Edge Gateway 5100

DDR, LAN and WAN adding up to another 10.7W. The maximum allowed junction temperature of CPU is 100°C.

This device is wall mounted and hence the thermal design needed to conduct the heat from powered components into walls of the metal cover or enclosure to spread it.



Rugged Enclosure

A heatsink is mounted on the top of front cover (Aluminum) to further spread the heat over a larger surface area. The overall design restricted the maximum size of heatsink base to 180x 140 mm but other heatsink parameters like fin height, number of fins and pitch could be modified. It was impractical to build prototypes to study all the possible design scenarios and hence Mentor's thermal analysis tool FloTHERM was used.

FloTHERM is Computational Fluid Dynamics (CFD) software focused on thermal management and analysis of electronics systems. In this case our customers at Dell took advantage of heatsink smart part in FloTHERM; where one can quickly vary heatsink design, by varying parametric dimensions in a property sheet. This parametric nature of parts is further taken advantage by Command Center (CC) module in FloTHERM where a user can define input parameters that can vary in a design space and have the software create a Design of Experiments (DoE) to analyze these multiple scenarios formed by various combinations of the variable parameters. CC can then be used to study the sensitivity of thermal design to different parameters using Response Surface Optimization (RSO) algorithm. Dell was able to very quickly design a heatsink with optimum number of fins and spacing using CC.

The next challenge was to design the vents in the cover for cool air to enter the device and the heated air to exit. The powerful visualization tools in FloTHERM helped our Dell customer to visualize the airflow distribution and identify dead zones, in other words regions with recirculation which can trap heat. The particles visualization in FloTHERM (Figure 1) is analogous to a smoke test where the source of smoke can be placed either outside the cover (left) or inside the cover (right) to visualize both the airflow and air temperature distribution. The airflow visualizations aided in sizing and designing the cover and vents. Such insight is very difficult to obtain using traditional testing methods which are time consuming and expensive.

After the optimum heatsink and vents were obtained the component temperatures can be visualized using surface temperature distribution on the top and bottom sides of the MB (Figure 2). The numerical values of temperatures or flow rates can also be obtained in the post processing window, Visual Editor (VE).

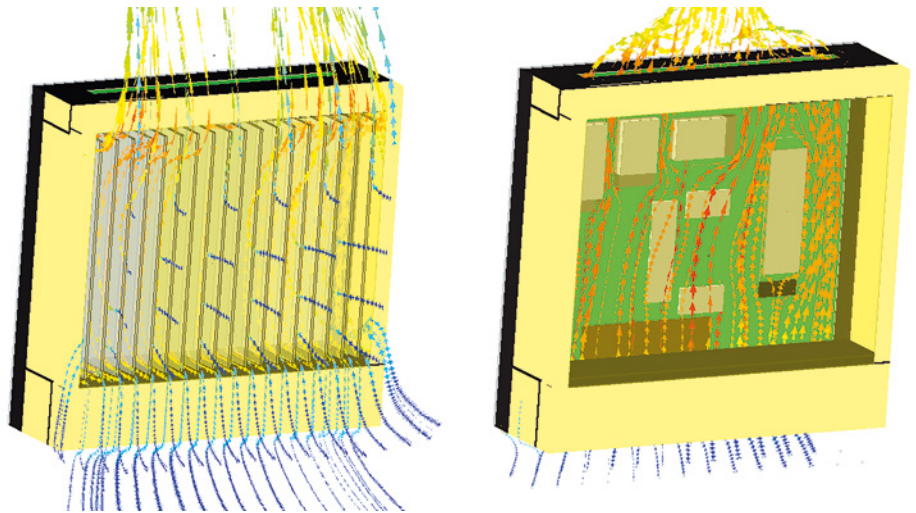


Figure 1. Airflow cooling heatsink (left) and cooling motherboard, MB (Right)

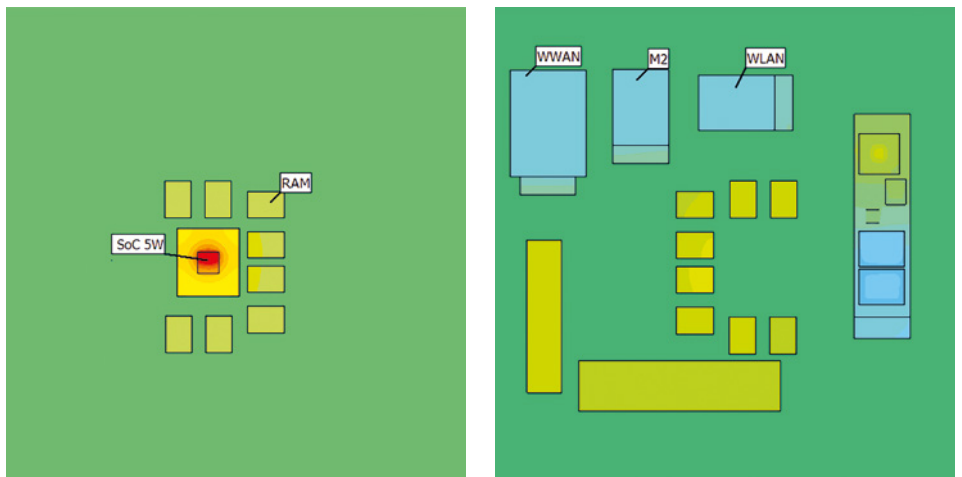


Figure 2. Surface temperature of components on top side (Left) and bottom side (Right) on MB

In addition to surface temperatures the user can inspect the temperature and heat flux distribution at a plane or section cutting through the geometry. In Figure 3, the plot on left shows the temperature distribution at a plane cutting through the SoC component highlighting the hot spot. A gap pad and a heat spreader move the heat from CPU into the metal cover and this heat spreading effect can be visualized in a cut plot colored by magnitude of heat flux (Fig. 3 right). Heat flux plots are a great way to visualize the preferred heat transfer paths and identify the bottle necks that result in higher component temperatures. The user is encouraged further reading on how to plot and analyze non-dimensional parameters Bottle neck number (Bn) and Shortcut number (Sc) in VE.

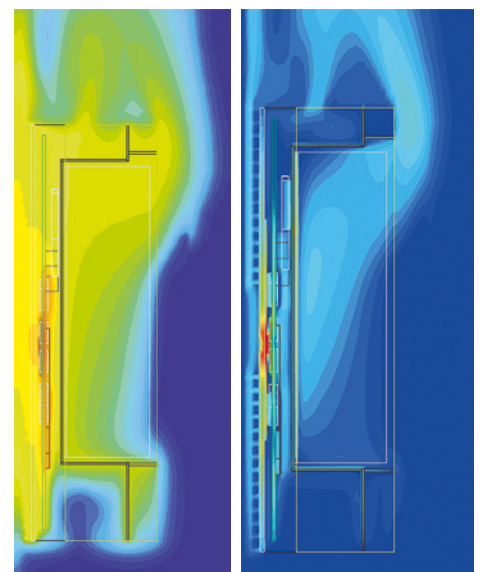


Figure 3. Cut plot colored by temperature (Left) and magnitude of heat flux (Right)

Implementing **New Distributed** Chilled Water Pumping System

for Air-Conditioning Systems

By Sam Lam K. H., Senior Specialist, Ngee Ann Polytechnic

When designing or upgrading a building, there are several areas that require significant engineering to ensure they can operate in as green a manner as possible. One of these areas is the chilled water system for air conditioning. In these systems, whether they are primary, primary-secondary, or primary-secondary-tertiary, the pumping energy can account for up to 10% of the total power required to run the system. This usage of energy means newer system designs are required to meet or exceed pumping power limitations set out by government and industry to improve the efficiency of air conditioning systems. These requirements (along with improvements in the efficiency of low flow, high head variable speed pumps), have led to an investigation of other pumping strategies. As part of the work carried out for the building design, an investigation into a Primary-Coil Secondary pumping system was carried out using 1D Computational Fluid Dynamic software tool, FloMASTER.

Chilled Water System Designs

For the building being investigated, there were two main areas: the office area will receive conditioned air from air handling units (AHU) that are cooled by the chilled water system; the other area, is a factory floor which does not have air conditioning, except for a test area. It is important to note that the process equipment on the factory floor is cooled by the same chilled water system as the office area.

Primary-Only (P-Only) Design

The building's existing chilled water system can be seen in Figure 1 and is configured as a primary only pumping system. Two pumps equipped with Variable Frequency Drives (VSD) distribute the chilled water through the system with one of the pumps used as a standby. The speed of the primary pump is controlled so that the correct differential pressure is maintained in the loop as measured at the main chilled water header. From the pumps, the water is reduced to 10°C by two screw chillers before distributing to different AHUs in the building. In the factory and office building, the AHUs

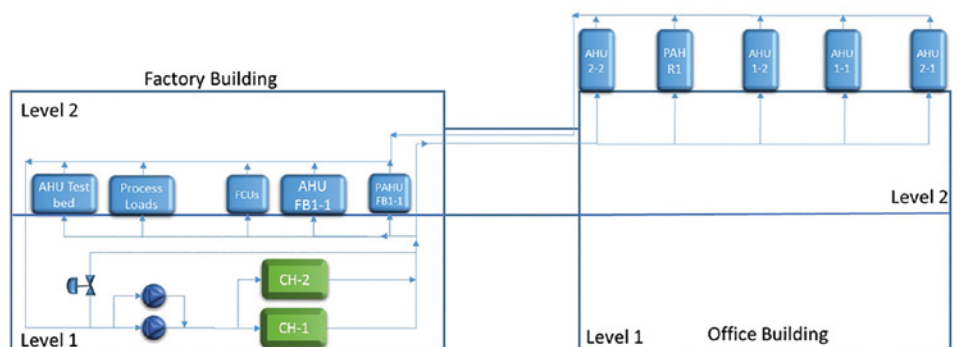


Figure 1. P-Only chilled water pumping system

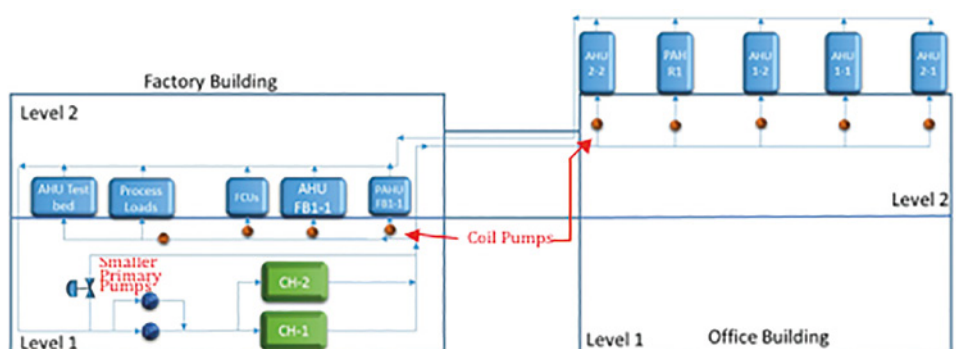


Figure 2. P-CS chilled water pumping system

are controlled by two-way valves set up to maintain the supply air temperature at the given set point. The process equipment is cooled using plate and frame heat exchangers with modulating control valves determining the flow rate. Several of the smaller spaces such as offices and meeting rooms use Fan Coil Units (FCU) that also use modulating control valves to control the flow.

Primary-Coil Secondary (P-CS) System

To explore improvements to the current system a primary-coil secondary system was investigated similar to what is shown in Figure 2. This type of system still contains the primary pump and chillers to provide chilled water through the system, but it also has coil pumps at each consumer limit. In this design the primary pumps are used to ensure a minimum flow rate can be maintained without fluctuation throughout the system. The coil pumps replace the modulating and balancing valves and instead control the water flow rate by varying valve opening, they directly adjust rotational speed based on the AHU and FCU temperature requirements. It is also possible to use a single coil pump to supply multiple loads in a single branch by maintaining the pressure in the loop. By replacing the modulating valves and balancing valves, this can help reduce the pressure drop in the system as well as offset the cost for additional pumps.

Computer Simulation

It is important to understand that maintaining temperatures inside of a building is a dynamic process. The cooling capacity required can change significantly based on factors such as outside air temperature, humidity, solar load and number of people in the building. Since these factors are always changing, so too must the pressures and flow rates throughout the building. Because of this, FloMASTER was used to perform system level thermo-fluid simulation to get a solid understanding of the system behavior so that appropriate controls could be introduced. The piping model was constructed from the air-conditioning and mechanical ventilation drawings for the building. Two models were created, the first replicating the existing P-Only configuration (Figure 3a) and the second a P-CS configuration with coil pumps at each demand and the balancing valves removed (Figure 3b).

To accurately model the system in FloMASTER, it was necessary to provide

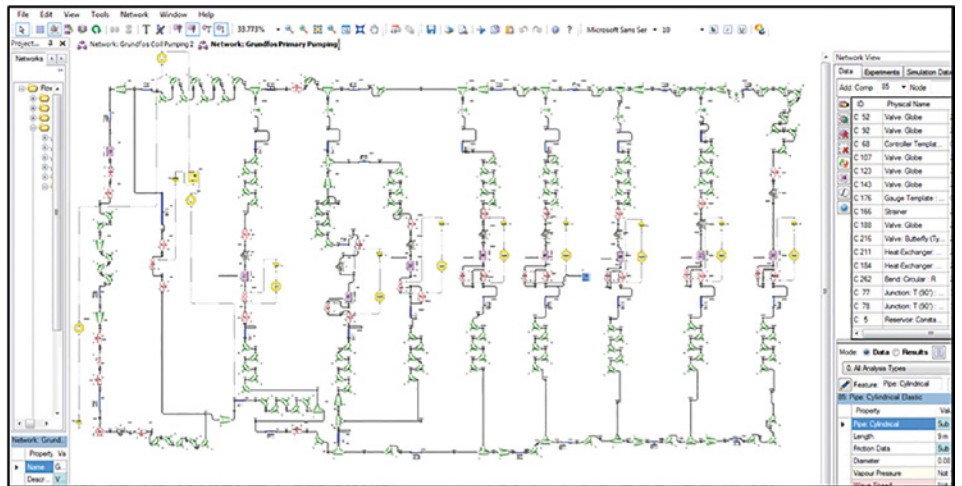


Figure 3a. FloMASTER model of P-Only chilled water pumping system

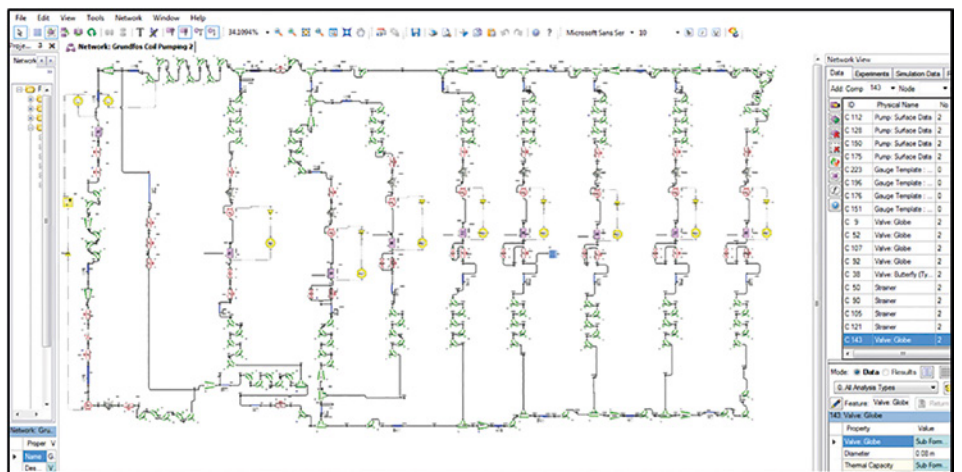


Figure 3b. FloMASTER model of P-CS chilled water pumping system

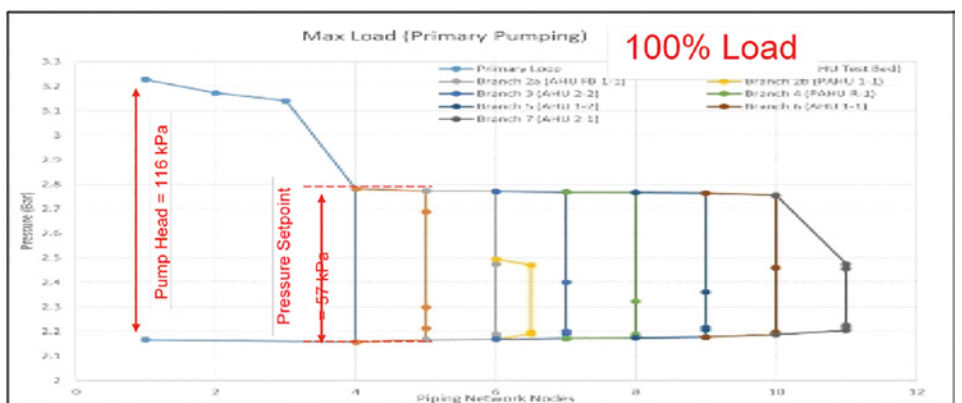


Figure 4. Pressure profile of P-Only system at 100% Load

a pressure drop versus flow curve for the chiller which was provided by the manufacturer as was the pump performance data. This same information was required for the cooling coil which was calculated from actual flow and pressure drop measurements. For all of the other piping components such as the valves, pipes, bends, and T-junctions FloMASTER

provides loss data based on Internal Flow System by D.S. Miller. To control the system, the built-in Proportional-Integral (PI) controller was used which modulated the opening position of each of the control valves to ensure the specified flow rates were achieved. It is important to note that since power consumption was one of the key areas of interest in the study, data for pump efficiency versus flow rate and speed was calculated and used to ensure accurate calculation of pump power.

Results and Discussions

Two sets of simulations were run including one for variable P-Only pumping using a fixed pressure set point and one of P-CS pumping. For P-Only system, control engineers often control the primary pump speed using the bypass pressure. For the simulations a bypass differential pressure set point of 58kPa was used based on the simulation of the maximum AHU load conditions. Figure 4 shows pressure along the piping system for full load conditions. Because the pressure drop in each branch is determined by the pressure set point at the bypass there is not a significant drop based on the load. This means there is minimal ability to reduce pump head or pump power to become more efficient. The P-CS pumping system is not based on a pressure set point. Instead the control will adjust the primary pump speed to ensure the demand for flow of the supply water is being achieved. Figure 5 shows the same pressure profile for the P-CS system. Since the pressure difference at the decoupler is equal to zero, it has no flow through it, meaning the chilled water is supplied by only the amount needed each of the demands. As an added benefit, the line pressure in the P-CS system is lower all along the system.

It is also important to look at power consumption. Table 1 shows the power consumed by both pumping systems. Overall, the savings of the P-CS system over the P-only system vary significantly. When running at 100% demand, the P-CS system could save about 7.4% of power. However when looking at lower flow rates such as 50%, the savings could be up to 34%. It is also important to note that the P-Only values assume a fixed constant pressure set point optimization, which in the real world is unlikely to be implemented. The potential power savings are expected to be higher than shown here.

As part of the process, the original P-Only system was measured to have an average specific pumping power of 0.059 kW/

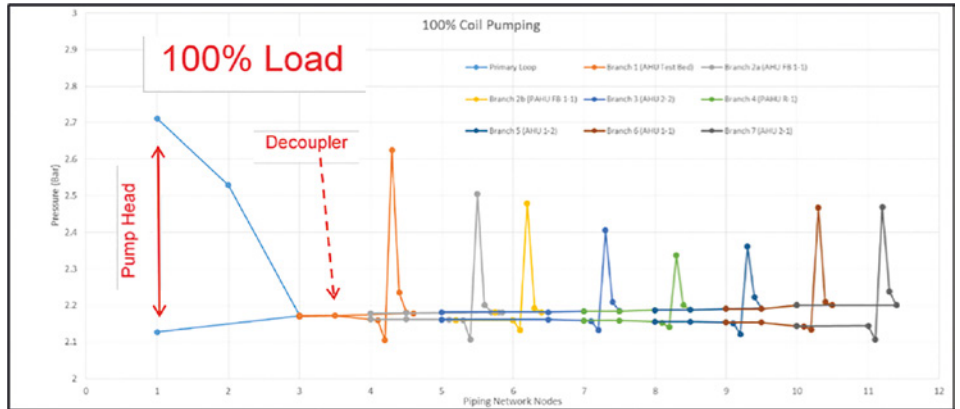


Figure 5. Pressure profile of P-CS system at 100% load

Flow Rate	Total Pumping Power (kW)		Savings
	P-Only (Fixed Pressure Set Point @58 kPa)	P-CS	
100%	5.08	4.70	7.4%
75%	2.71	2.22	18.3%
50%	1.40	0.92	34.1%

Table 1. Simulation results - pumping powers

System	Pumping Energy	Specific Power
	kWh	kW/RT
P-Only System	1.727	0.059
P-CS System	773	0.032
Savings	55%	46%

Table 2. Measured energy consumptions after implementation

RT. After implementing the described P-CS system, the new pump power was measured at 0.032 kW/RT. Table 2 shows the energy consumption of both systems, with the P-CS system saving over 55% during a full four week study.

Conclusion

When looking to design a new building or implement an upgraded system to an existing structure, it is important to look at different options for the system design. One of the fastest and most cost effective methods for looking at these designs is the use of 1D computational fluid dynamics tools such as FloMASTER. In this example, simulating the introduction of efficient low flow, high head chilled water pumps meant that using a Primary-Coil Secondary pump system greatly improved the overall efficiency even for a smaller chilled water system.

Reliability Evaluation of Sintered Copper Die Bonding Materials

for Pressureless Bonding using the MicReD Power Tester and FloTHERM

By Chie Sugama, Hitachi Chemical Co., Ltd, Japan

Hitachi Chemical
Working On Wonders

Hitachi Chemical is one of the group of companies of Hitachi Ltd and we have about 19,000 employees with annual revenues of ~\$5Bn/yr. About 50% of our business is in materials manufacture and 50% is in the application of these materials to a wide range of devices and systems, including applications in the automotive, life sciences, environmental and energy sectors. Materials products we make include epoxy moldings for semiconductors, die bonding materials, polishing materials for semiconductor circuits, varnish for electrical insulation, and carbon anodes for Lithium Ion batteries plus other carbon products.

I work in the R&D Group at Hitachi Chemical developing new materials for power semiconductors. In 2014 we established an 'open laboratory' where customers could bring their electronics components to us for free so as to be mounted and evaluated using our bonding materials with the aim of delivering shorter customer development cycles and to propose and develop new mounting processes.

Recently we developed innovative copper-based sintered die bonding materials (see Figure 1) as adhesives for automotive Electric Vehicle / Hybrid Electric Vehicle (EV/HEV) Power Modules with excellent thermal and adhesive properties. Metallic sintered bonding materials offer tremendous benefits for power devices and various binding products made from silver and copper are available in the market today because they support high heat dissipation rates and high heat resistance (see Table 1). Copper is roughly one-third the price of silver, and because we found that when placed in a solvent with ~90% wt% copper, a useful cost-effective paste with good microstructure properties could be created. Crucially, the copper paste can be bonded without pressure with all the manufacturing benefits that brings, i.e. a significant reduction in chip cracking and damage. We

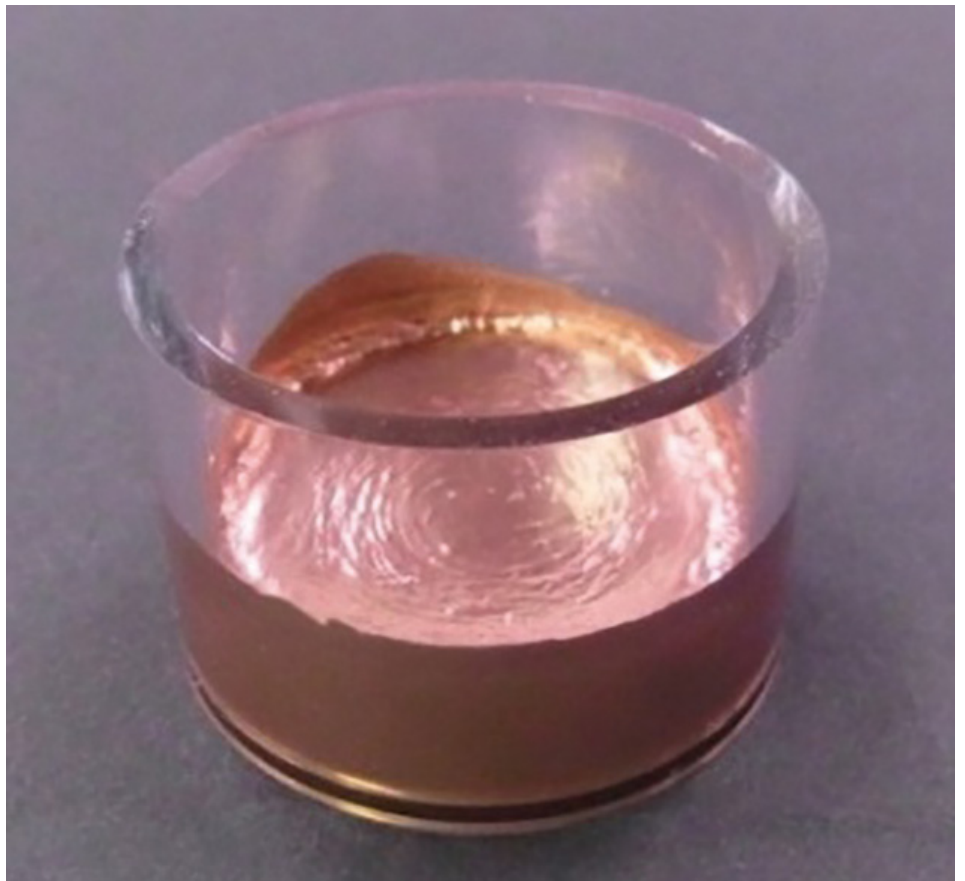


Figure 1. Copper Sinter Paste



← Power Tester (T3Ster)

FloTHERM →

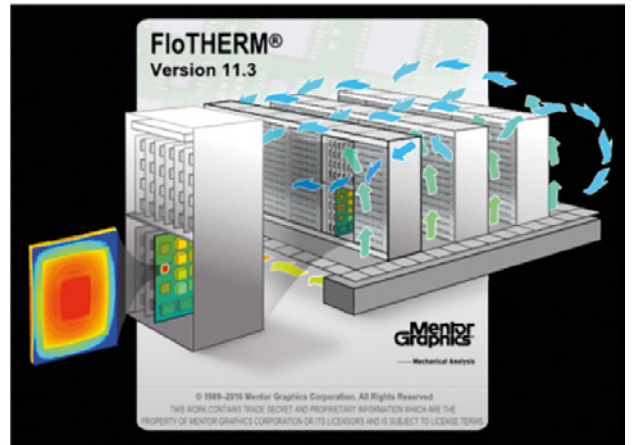


Figure 2. Mentor Graphics 1500A Power Tester (left) and FloTHERM (right) electronics thermal tools

therefore wanted to evaluate our product’s thermal lifetime performance and so we chose Mentor’s MicReD Power Tester and FloTHERM CFD software (Figure 2) to test it. We chose Mentor’s 1500A Power Tester because it allowed us to test our copper paste over various power cycling scenarios to destruction. The Power Tester is based on Mentor’s T3Ster technology and has ‘structure functions’ that allow for transient heat path measurements through devices under test thus revealing non-destructive constituent part performance. Ultimately we wanted to demonstrate the long-term reliability (power cycle life and destruction mechanisms) of sintered copper applied as a die bonding material for a SiC power device. These copper pastes can withstand relatively high temperatures of 200°C with good mechanical properties such as elasticity, flexural strength, flexural strain, and 0.2% proof stress. They also have good resistance to shearing forces.

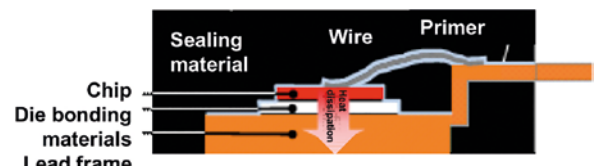
We devised a test whereby we selected a SiC Schottky barrier diode T0-247 (Figure 3) package (with aluminum wire) and used both sintered copper and conventional lead solder bonds (Figure 4). We poured the copper paste into our own mold for the SBD under test. Junction temperatures in the Power Tester for the devices under test, $T_{j\max}$, were calculated from the result of temperature characteristic investigations on the sample made in advance (using JESD 51-1). The measured current was 10 mA, and measurement temperature range was 20-120°C. We applied a power cycle test on the samples over 40,000 3 s on and 7 s off power cycles. In the case of the sintered copper bond, a power of 6 to 9 W higher than for the lead solder was applied because the rise in the junction temperature was suppressed more and we found it performed well up to 175°C (Figure 5). Our test was similar to that of Lutz et al. [1] where voltage

Item		Sintered Cu	Sintered Ag	High-lead solder	Lead-free solder
Bonding conditions	Environment	H ₂	Atmosphere	H ₂ / formic acid	N ₂ / formic acid
	Pressure	Pressureless	Pressurized (20 MPa)	Pressureless	Pressureless
	Temperature	225 – 300 °C	250 – 350 °C	350 °C	260 °C
Bond strength (MPa) (Sputter coating)	Cu, Ni	> 40	15	25	> 40
	Ag	> 40	> 40	25	> 40
	Au	> 30	> 40	25	> 40
	Pd	> 40	-	-	-
Characteristics	Thermal conductivity (W/m ² K)	180 (Compactness: 80 %)	280 (Compactness: 90 %)	24	55
	Usable temperature (°C)	≤ 200	≤ 200	≤ 150	≤ 130
Substances of environmental concern		Not contained	Not contained	Pb	Not contained

Table 1. Comparison of physical properties of various die bonding materials



Evaluation sample (SiC Schottky barrier diode)



Internal cross-section and heat dissipation path

Figure 3. SiC SBD device in TO-247 packaging (with aluminum wire)

increases due to wire lift-off in the power cycle. Their test was conducted at constant electric power to suppress the load on the wire during voltage increase. In the tests on sintered copper at 150 W and lead solder at 96 W the voltage during energization rises leading to us adjusting to a constant power. We concluded that sintered copper had a superior power cycle life when compared to lead solder even when greater power was applied to it (Figure 5).

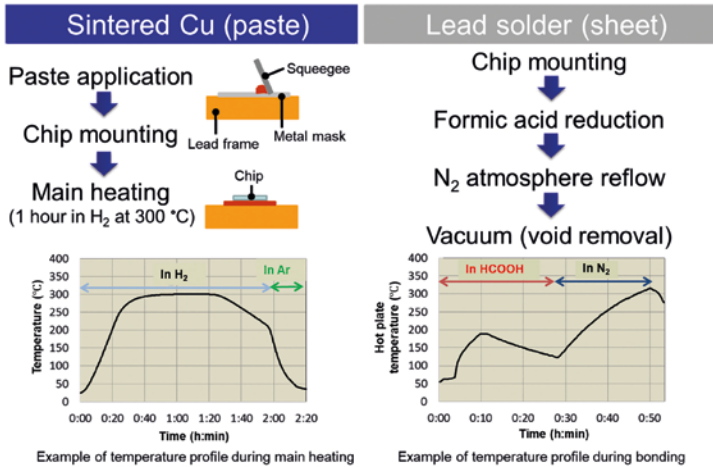


Figure 4. Method of bonding chips in the test by die-bonding material

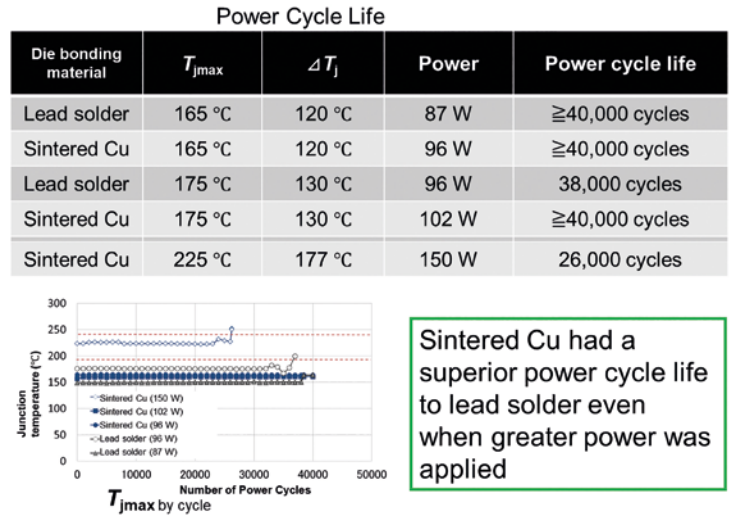


Figure 5. Measured T_j max for Power Cycles on Copper and Lead bonded samples

We also carried out some Temperature Cycling Tests (Figure 6) to check for the peeling off of mold resin from the lead frame. To compare with two other commercially available products that we also used lead bonding material. Hence, the bonding material is the same but the adhesive is different. Maintenance of adhesion was confirmed for both sintered Cu and lead solder in power cycle test as shown in lower part of Figure 6.

We know from the published literature [2] that one of the big advantages with the Power Tester is its structure function diagnostics that allow us to evaluate the structure of our devices under test non-destructively to see where thermal problems are originating and the extent of the damage caused. In particular, for our tests we used 'differential structure functions' to evaluate the change in thermal conductivity of the device under test and then used that as an input to our FloTHERM CFD simulations. Elleffendi et al. [3] recently empirically demonstrated that there is a correlation between the "K" value of a differential structure function from the Power Tester and the bonding layer interface area of each chip. Hence, we decided to take the T3Ster data from our tests and connect it to a FloTHERM CFD model we had created of the device under test (Figure 7). In our test the heating current was 20 A for 30 s and the heat generation area of chip was $3.8 \times 3.8 \times 0.004 \text{ mm}^3$. We wanted to use FloTHERM to identify the interface between the chip and the bonding layer better. Figure 8 shows the FloTHERM simulations in this model under test where it was judged that the thermal resistance was around 0.03 K/W at the interface between the chip and the bonding layer (the orange arrow). This graph is also a comparison of thermal conductivity of the

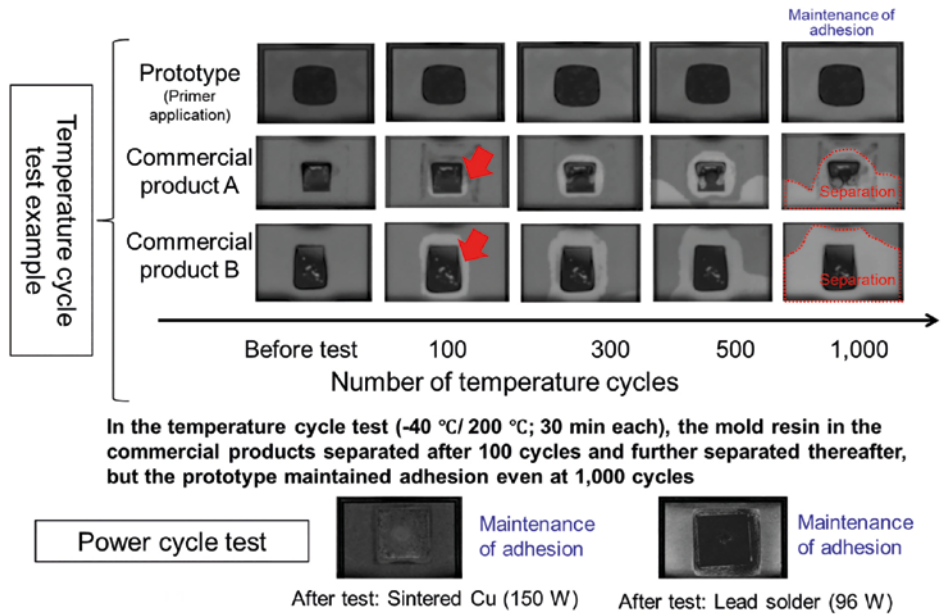


Figure 6. Measured adhesion of mold resin in each temperature cycle test and power cycle test

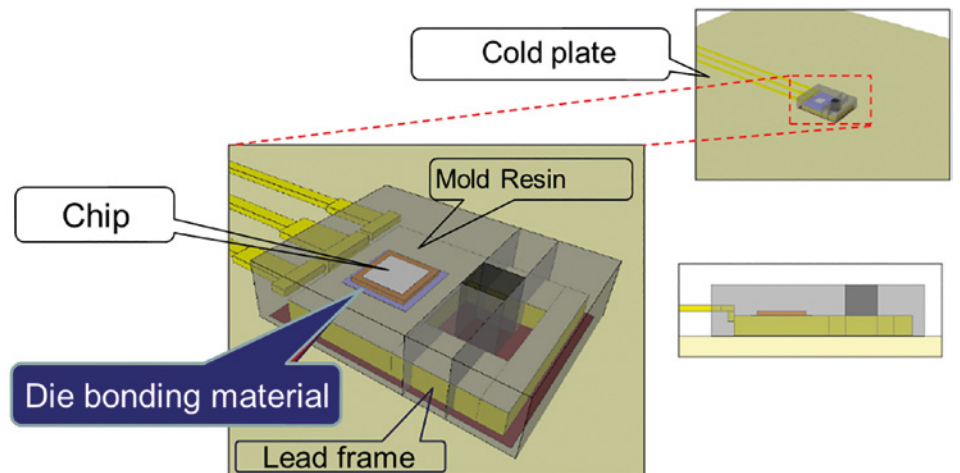


Figure 7. FloTHERM model of the SBD device under test

bonding material from a small value to a large value. So from this comparison we can understand from where the bonding material starts in the structure function.

For the two bonding samples we examined, the sinter copper and the lead solder, we used detailed SAM and SEM measurements before and after the tests (Figures 9 and 10) and deduced from the combined T3Ster structure function and FloTHERM simulation approach that the bonding area of the chip shrank in the copper sinter case whereas the lead solder experienced significant damage to the bonding layer.

Conclusions

Hitachi Chemical has developed a pressureless sintered copper die-bonding paste with a strength of 30 MPa and evaluated its long-term reliability when applied to power electronic devices for EV/HEVs. We have shown that sintered copper demonstrates superior power cycle life to lead solder even when greater power was applied. Our use of the MicReD Power Tester and the FloTHERM CFD software now gives us better insights into our electronics bonding pastes with high degrees of accuracy. In particular, we can see why they fail, such as bonding layer damage or change in junction area of the chip, and thus seek ways to improve their performance. This is a competitive advantage for us in that we can test competitor products as well as our own. This validation methodology should allow us to develop new materials with low baking temperatures going forward. The MicReD Power Tester allows us to power cycle 12 samples in parallel and is thus a powerful R&D tool.

References:

- [1] Lutz, J., Schlangenotto, H., Scheuermann, U., De Doncker, R.: Semiconductor Power Devices (Springer, 2011) p.392
- [2] Székely, V.: Microelectronics Journal 28 (1997) 277-292
- [3] Eleffendi, M.A., Yang, L., Agyakwa, P., and Johnson, C.M.: Microelectronics Reliability 59 (2016) 73-83

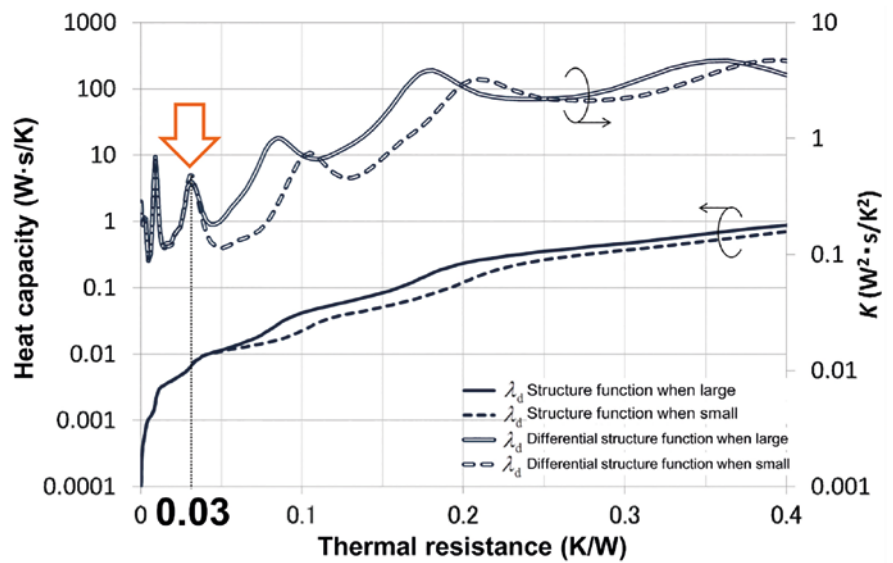


Figure 8. Structure functions given by thermal-fluid analysis in FloTHERM

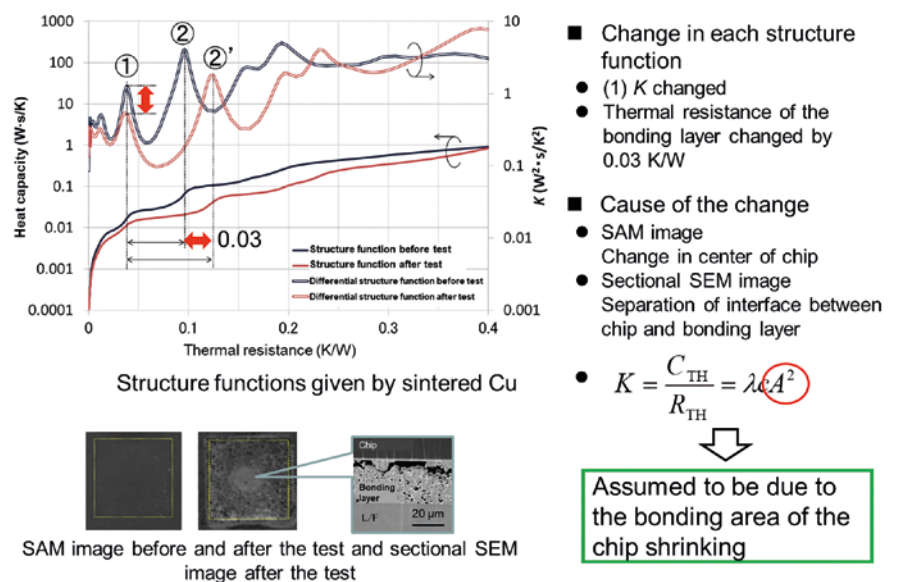


Figure 9. Change in each structure function with sintered Cu (150 W) and the cause thereof

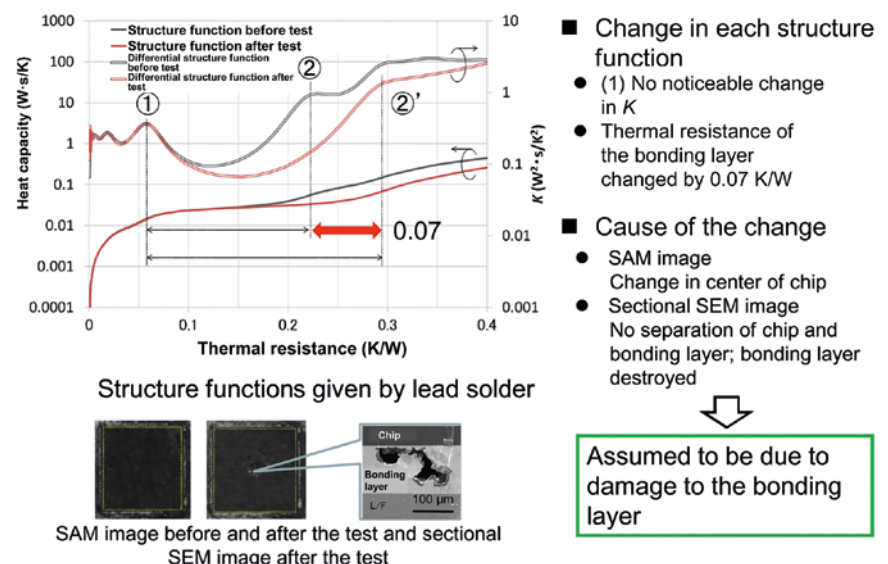


Figure 10. Change in each structure function with lead solder (96 W) and the cause thereof

Virtual Reality and Modeling Tools

for the Design of Electromagnetic Devices

By Prof David Lowther, McGill University, Canada; and Mentor, a Siemens Business



In the 200 years since the links between electricity and magnetism were discovered and formulated by Oersted, Ampère and Faraday (Refs 1, 2 and 3.), society has become dependent on electromagnetic systems to deliver electrical energy to end-users. The majority of the electrical energy produced - about 25,000 Terawatt hours in 2016 (Ref 4.) – is created by transforming mechanical to electrical energy through turbo- and hydro-generators and wind turbines. Every Watt hour of energy generated also passes through several transformers (electromagnetic systems) on its way to the end-user.

At the end of the transmission system, the majority of the electrical energy is converted back to mechanical energy through the use of electrical machines and actuators, Figure 1. These devices convert energy at efficiencies of 90% to 95%. This represents over 1,000 Terawatt hours of energy loss per year and is equivalent to about 50 power stations each rated at about 2 Gigawatts. Reducing this loss presents the designers of electro-magneto-mechanical devices with significant challenges. Meeting these requires advanced computer based simulation tools. The impact of design tools based on these virtual simulations is clear in advanced industrial societies where the electrical energy demands have actually fallen by over 3% over the last decade as a result of efficiency gains in the conversion processes.



Figure 1. Large electrical machine from Siemens

The goal of this article is to review the various representations of electrical machines available to a designer and discuss their use in the design process, given the demands being made to increase efficiency, reduce costs, increase power per unit volume, etc..

Virtual Reality and Surrogate Models of Electrical Machines

The lack of computer power to simulate electrical machines did not deter the designers of the nineteenth and twentieth century. Society needed the capabilities provided by the flexible use of electrical energy and the impact of electrical machines has changed the lives of everyone on the planet. Who can survive now without hairdryers, vacuum cleaners, dishwashers, clothes washers,

kitchen machines, electric drills? The list is endless and growing daily. What industry can operate without the use of electrical energy to run manufacturing machines, implement transportation systems or inspect finished products?

To design machines, models were needed and while Maxwell developed the physics equations which would ultimately, in the late twentieth century, lead to virtual reality models of devices (refs 5, 6, 7), he also provided conceptual models based on the “flow” of a magnetic field which allowed simplistic representations to be created. These models, based on concepts of magnetic resistance (reluctance), and energy storage and loss in various parts of the machine topology gave

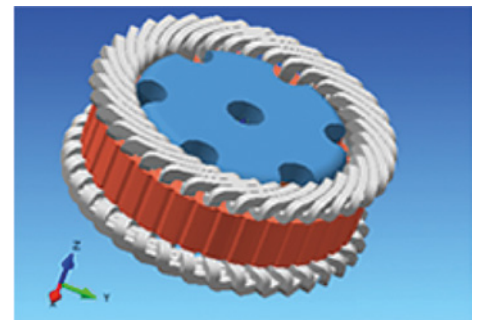


Figure 2. MagNet model of an automotive claw-pole alternator.

rise to simple equivalent circuit models. These models could then be tuned by adjusting various parameters based on experimental measurements. As long as new designs stayed “near” to existing designs, then the circuit approach could, and still can, produce fast predictions of machine performance. Until the late twentieth century, equivalent circuits, together with simple analytical solutions for small parts of the machine, formed the basis of most machine design. However, the demands placed on modern designs began to show the inadequacies of the approach.

The development of digital computers provided an approach for solving the full field equations. As computing equipment has become more powerful, it has been possible to solve the underlying equations to high levels of accuracy. However, solving the equations alone does not imply the generation of an accurate simulation of reality. To create a virtual reality model which behaves like its physical counterpart, four components are needed. The first is an ability to model complex three-dimensional geometric structures both for the magnetic (the iron) components and for the electric parts (the windings) in a way which can be discretized to match the solution methodologies for the physics equations. The second is to represent the excitation structures in both time and space correctly. The third component requires that the material behavior is simulated accurately (non-linearity, saturation and hysteresis). The magnetic properties of materials are fundamental to the designed operation of an electromagnetic device.

The fourth is to stably and efficiently solve the equations systems which result from embedding the first three components in the physics equations. This is now possible and virtual reality models which accurately predict the performance of the real device can be constructed (Figures 2 and 3). However, the computational cost of doing this is high and can take from minutes to days for an accurate prediction. This is not an effective design tool. However, it does provide access to information on device performance which cannot be achieved any other way. In a real device, it is difficult to measure the magnetic flux in the center of the core; hotspots cannot easily be located; areas where material is not being used effectively cannot be identified, etc. (Figure 4) Thus the virtual model complements the physical device – it is a true digital twin.

However, simpler models are needed if the design process is to be “interactive”. Generating such models often means losing detailed information. Figure 5 shows the levels of approximation from full virtual reality to

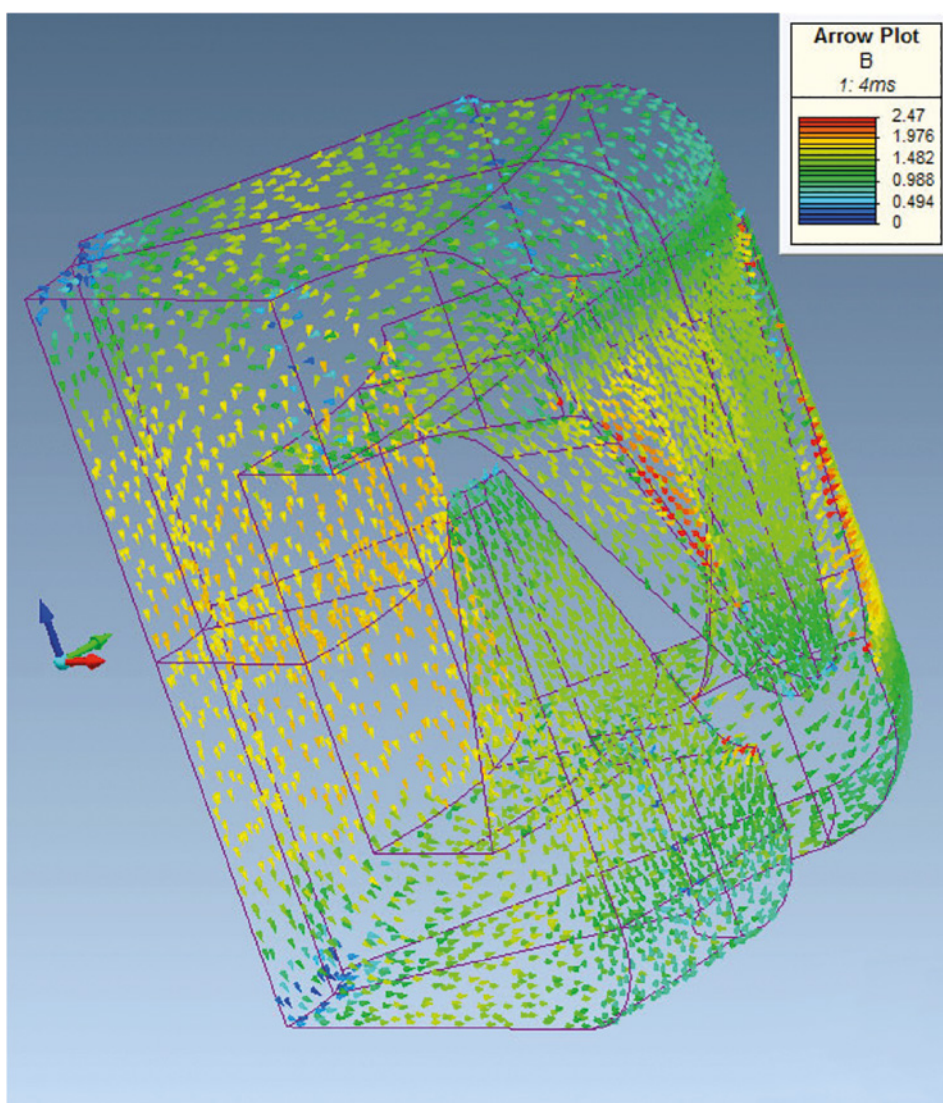


Figure 3. Magnetic flux distribution in the claw pole alternator at 1.4 milliseconds into a transient.

simple equivalent circuits – as the response time of the models decreases, the information available also decreases. It is possible to consider the full numerical model as no more than an extremely detailed magnetic equivalent circuit. As in any circuit model, the coefficient (in this case, reluctance) matrix can be “condensed”, i.e. intermediate points in the circuit removed and parts of the circuit collapsed into macro-elements. This loses the detailed local information but maintains the global features of the problem. Each level of condensation generates a new surrogate, or virtual model. This, however, is expensive to do. As a first stage, other approximations can be made – a two-dimensional representation can be considered (most electrical machines are, essentially, two-dimensional); material hysteresis can be ignored; the geometry can be simplified to ignore features such as fillets in the slots, bolt holes, tooth tip shapes, etc. All these reduce the information, add in errors to the model but do allow simpler surrogates to be developed. In the extreme, if magnetic

non-linearity is ignored and the resulting matrix is condensed to a few entries, then the conventional equivalent circuit developed from Maxwell's conceptual model can be created. However, the errors in global performance are likely to be large and almost all the detailed information has been removed. At this point, to regain some accuracy, the resulting model needs to be calibrated by setting a series of parameters to match the performance of the full virtual model (just as in the experimental approach of the nineteenth century!).

Alternately, at any point in the approximation process from the full virtual reality model, a response surface of the device can be produced – this would, in effect, provide global performance parameters but underlying the surface could be a non-approximated virtual model. The response surface can be expressed in the form of a polynomial or a neural network. Either of these can respond with a performance prediction as quickly as an equivalent circuit but with considerably more accuracy and with no need for calibration.

Design Tools for Electrical Machines

Designers need tools which can allow them to explore a design space quickly and with models which have a level of accuracy appropriate to the stage of the design. The major issue here is “wall clock time”, i.e. the length of time it takes to explore the space and find a solution which might satisfy the requirements. A model with limited accuracy which might run fast (such as an uncalibrated equivalent circuit model) may be of little use in even the early stages of design. However, if that model could be calibrated by a suitable virtual model (e.g. a two-dimensional finite element model), then it could provide a tool for the designer in the early stages of design (ref 8). This is the approach taken by the SPEED system from CCM (the former CD-adapco). However, given the gains in computational speed, and the fact that the designer is working with trade-offs between wall-clock time, model accuracy and an ability to explore generalized topological structures, the question is whether a reduced accuracy two-dimensional numerical model of the field in the device can provide more information to the designer in a time similar to that of an equivalent circuit? This is the rationale behind the MotorSolve system from Mentor. MotorSolve can generate equivalent circuit models when needed for some classes of device, it can also generate accurate real-time surrogate models of devices for use in hardware-in-the-loop testing, and everything inbetween. The accuracy of the numerical models can gradually be increased as the

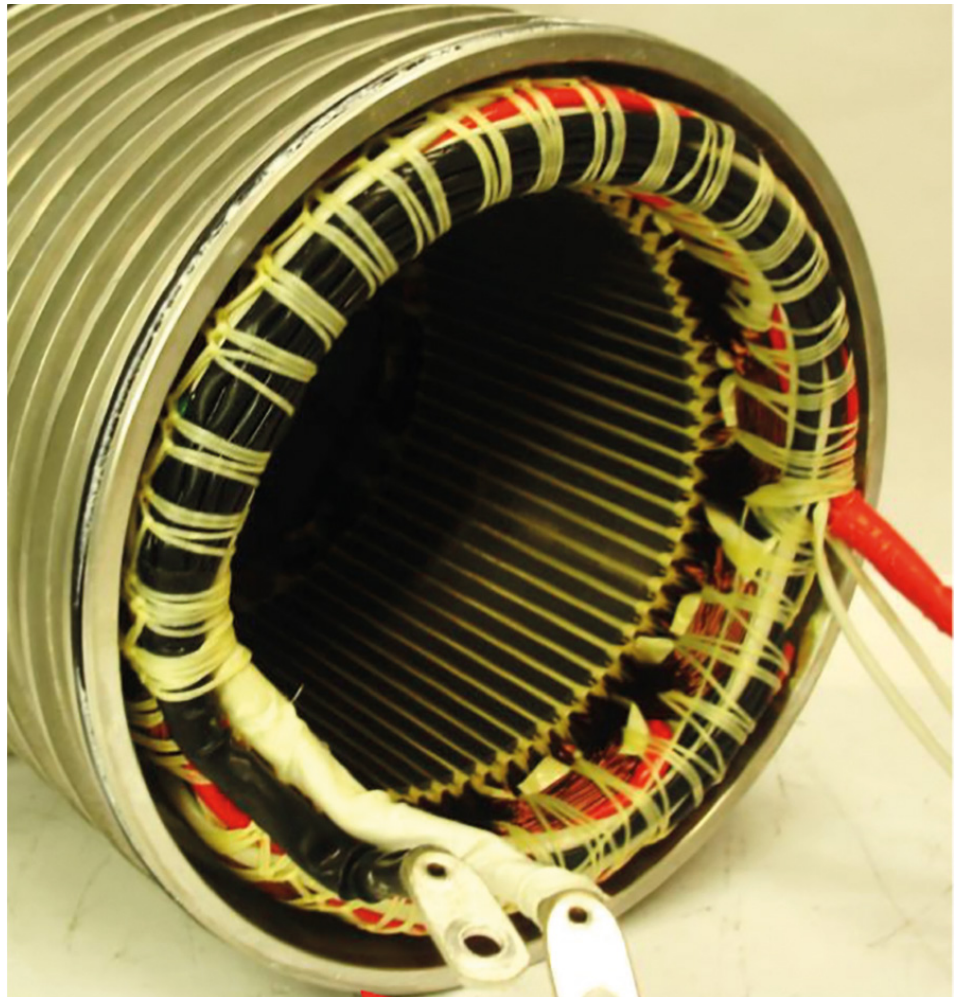


Figure 4. Stator of the BMW i3 Traction Drive – inserting a thermal or field probe in the core is nearly impossible.

designer locates the area in the design space for a possible solution and wants to explore the solutions in that area in more depth. In addition, MotorSolve models can be exported for use in system simulators through VHDL-AMS exports and can connect to full three-dimensional electromagnetics modeling through an export to the MagNet suite of tools. It provides flexibility in modeling to match the needs of the designer.

Multi-physics Modeling of Electromagnetic Devices

All electromagnetic systems give rise to multi-physics problems. An electromagnetic field exerts forces on electric charges and magnetic poles. These forces result in effects which may or may not be wanted. The movement of charges in a conductor can result in energy losses which will appear as heat in the system; alternately, the energy can appear as mechanical work, i.e. the forces and torques which are the goal of an electric machine, and also as stresses and strains in the components of a device which can lead to vibrations, acoustic noise and, possibly,

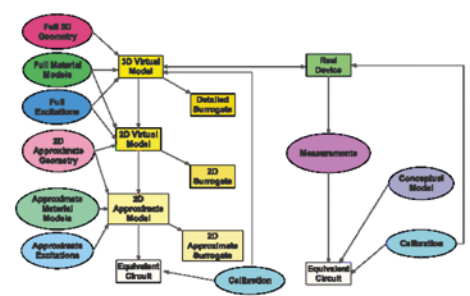


Figure 5. Levels of approximation in simulation and measurement.

structural failures. Thus creating a complete virtual reality simulation of any device requires connections to multi-physics, and material models which include the information on thermal and structural behavior as well as magnetics. MotorSolve provides a coupled three-dimensional thermal analysis to predict the operating temperature of a machine and through MagNet, can connect to structural and acoustics analysis using the Siemens Simcenter 3D tools.

While a complete virtual reality simulation needs detailed multi-physics analysis, there are other applications which only need global information. One such is the development of a cooling system for an electric vehicle that includes a motor and other heat generation components. To enable this form of multi-physics, MotorSolve provide a link to FloMASTER for high level cooling system design, Figure 8.

Conclusion

The design of low frequency electromagnetic devices is a complex process and the goal of a design system (such as MagNet/MotorSolve from Mentor) is to provide the designer in particular with a tool which can operate rapidly at multiple levels with a single underlying physical geometry. It can move from low to high accuracy; from 2D to 3D models; and from single physics to multi-physics through systems such as those available in Siemens Simcenter 3D. The system can also produce reduced order, or 1D, models which can be used in other simulation systems to include the impact of the motor performance on the rest of the system and real time models for hardware-in-the-loop testing. The impact of these tools is to enable the production of more efficient devices more cheaply for everything from dentists' drills and electric cars to turbo-generators and industrial drives. The reduction in overall energy demands as a result of the gains in efficiency, and the reduction in costs through the optimization of material usage, will minimize the impact on the future of the planet while continuing to provide all the benefits of electrical energy to society.

References

- [1] H.C. Oersted, "Experimenta circa effectum conflictus electrici in acum magneticum," Copenhagen, July 21, 1820. (English translation in *Annals of Philosophy*, Vol. 16, 1820)
- [2] A.-M. Ampere, Paper read 26 December 1820 reported in *Journal de Physique, de Chimie*, January 1821
- [3] M. Faraday, Paper read to the Royal Society, London, November 1831

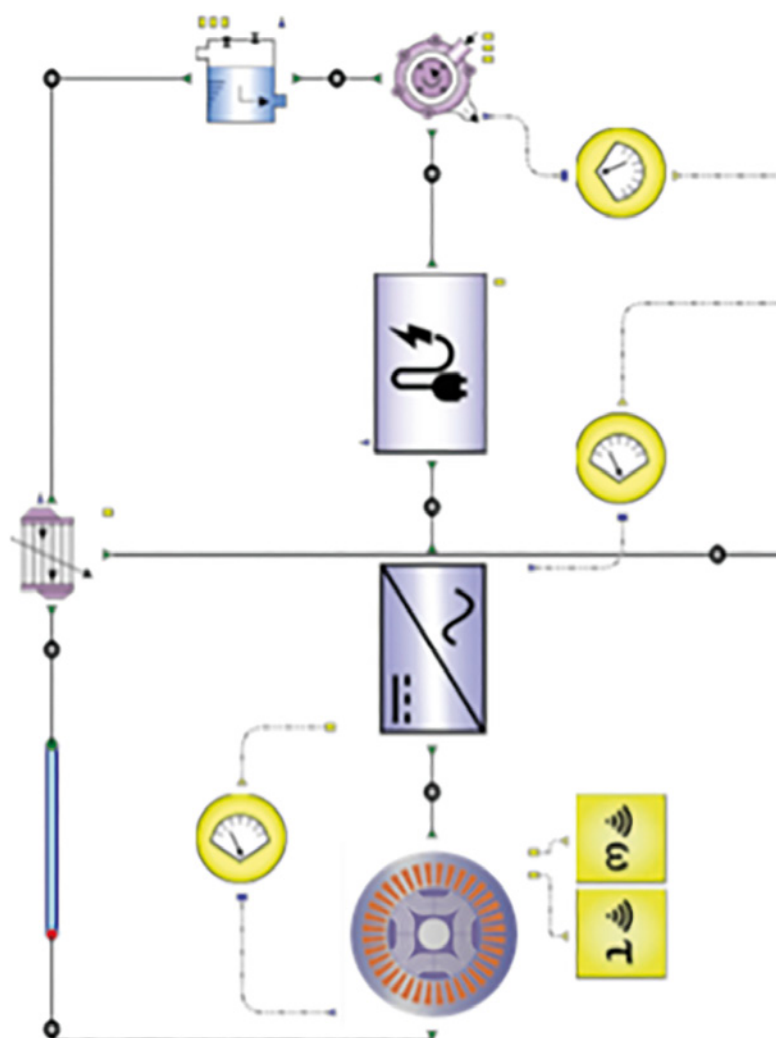


Figure 6. The FloMASTER model of the high temperature cooling loop in an electric vehicle with the charger, power inverter and motor represented with a MotorSolve 1D loss surface.

- [4] Global Energy Statistical Yearbook 2017, <https://yearbook.enerdata.net/electricity/electricity-domestic-consumption-data.html>, accessed 26 March 2018.
- [5] J.C. Maxwell, "A Treatise on Electricity and Magnetism," The Clarendon Press, Oxford, 1873.
- [6] D.A. Lowther, E.M. Freeman, "The Application of the Research Work of James Clerk Maxwell in Electromagnetics to Industrial Frequency Problems," *Phil. Trans. Roy. Soc., Part A*, Vol. 366, 1871, May 2008, pp. 1807-1820.
- [7] D.A. Lowther, P.P. Silvester, "Computer-Aided Design in Magnetics", Springer-Verlag, New York, 1985.
- [8] J.R. Hendershot, T.J.E. Miller, "Design of Brushless Permanent-Magnet Machines", Motor Design Books LLC, Venice, Florida, 2014.

Ask The GSS Expert

FloTHERM Advanced Training from GSS

The FloTHERM Advanced Training course is designed to follow the introductory class. Some of the topics, such as advanced gridding and troubleshooting, advanced component level modeling, handling advanced applications in the command center, and import/export options are extensions of material discussed in the introductory class. Other topics, such as transient analysis and joule heating, are presented for the first time in the advanced session.

The transient analysis section begins with a discussion of the reasons for choosing a time dependent simulation as opposed to steady state. Then the modeling options available in FloTHERM are presented along with the steps required for set up. The hands on lab session provides an opportunity to work through a transient analysis from set up to post processing during the class.

The joule heating session is designed similarly to the transient analysis one in that the lecture discusses the theory, and then continues through the set up to post processing in FloTHERM. There is a hands on tutorial for this subject as well.

The advanced gridding and troubleshooting presentation begins with a quick review of topics from the introductory class and then moves on to advanced techniques. There is typically much discussion and demonstration throughout this portion of the class.

Advanced component level modeling also begins with a quick review of the topics covered in the introductory class. This is followed by a more in depth discussion about resistor networks as compared with resistor capacitor networks, how to acquire them and when to use them.

The session covering advanced applications using the Command Center offers a more applied look at the automated parametric analysis and optimization capabilities available

The course very well showcased V12.0. As well, the various small tips and best practices mentioned by both the instructor and other users in the class is certainly invaluable information.

Jeffrey Auclair, Hardware Engineer, Dell EMC

in this module. This session includes demonstration as well as a hands on lab session.

Finally, the lecture on import and export options available in FloTHERM begins with a quick review of mechanical CAD and EDA import capabilities and then progresses to the import of power maps, scripting options as well as bridges to other analysis tools.

Contact Barbara Hazard at barbara_hazard@mentor.com with any questions regarding registration or the topics covered.



Simulate the Hydraulic Servo Gimbal Controls of a Space Launch Vehicle

University of Electronic Science & Technology of China utilize co-simulation of AMESim and FloMASTER to accurately Simulate the Hydraulic Servo Gimbal Controls of a Space Launch Vehicle.

Edited by Mike Croegaert, Aerospace Industry Manager, Mentor, a Siemens Business

University of Electronic Science & Technology of China utilize co-simulation of AMESim and FloMASTER to accurately Simulate the Hydraulic Servo Gimbal Controls of a Space Launch Vehicle.

Gimbaled thrust systems are the common method for providing stability and control for space launch vehicles. They allow the exhaust nozzle of the rocket engine to be swiveled from side to side. This allows the direction of the thrust to change with respect to the center of gravity.

A sophisticated guidance system that uses computers and sensors to determine the orientation, location and speed of the vehicle is utilized to maintain the stability and desired trajectory. The guidance system compares current values for the direction and speed to the desired values and will send signals to hydraulic servo controls which will activate hydraulic actuators attached to the rocket engine which in turn change the gimbal angle of the engine and therefore the direction of the thrust.

This process occurs continually during the flight of the vehicle. The control strategy that is used by the guidance system is extremely complex and there is great interest in simulating the control to verify that it will function as is desired. The software tools such as Simulink allow the control system programming to be simulated to ensure proper outputs for a specific set of inputs but what

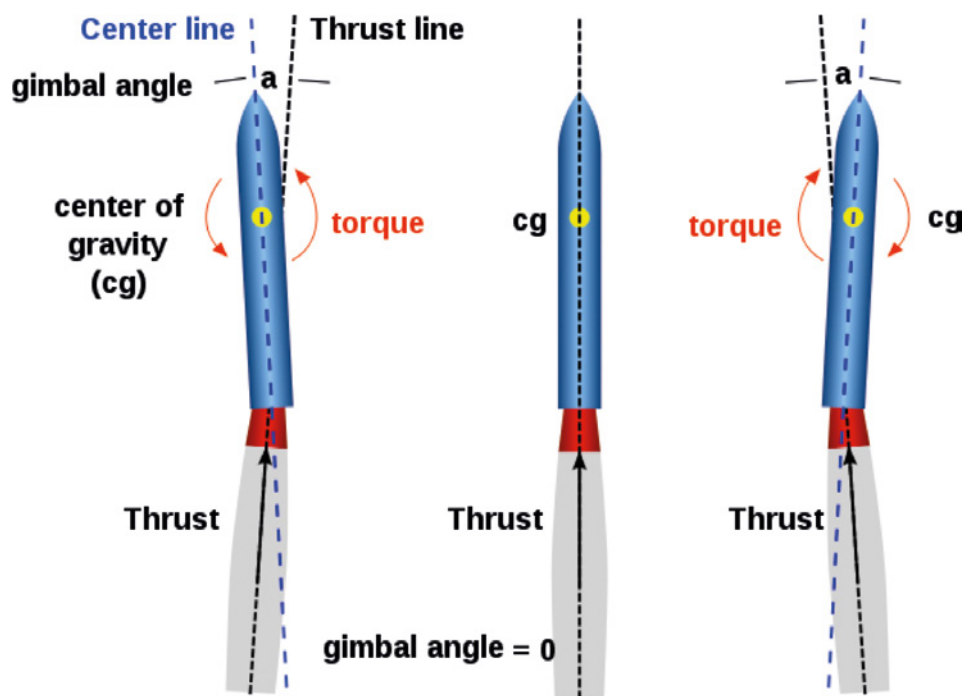


Figure 1. Gimbal rocket control

these tools cannot do easily is simulate the interaction of the fluid / mechanical systems with the control system programming.

University of Electronic Science & Technology of China has overcome this shortcoming by utilizing AMESim and FloMASTER to simulate the fluid and mechanical systems of the launch vehicle. Through a co-simulation approach, that marries all three systems together, to take the first steps in developing a digital twin of the vehicle's propulsion and control systems.

Simulink is used to simulate the guidance system logic which takes input from onboard sensors to determine the current position, speed and trajectory of the launch vehicle and evaluates this against predetermined parameters or land based commands. It then determines the appropriate adjustments to the thrust and gimbal angle (ie engine position) required to achieve the desired changes in flight. These commands are sent to the fuel flow control valves and the hydraulic servo control system. At this point the simulation tasks are taken over by AMESim and FloMASTER.

Launch Vehicle hydraulic servo control system is shown in Figure 3. The electro-hydraulic servo valve is the core component of the rocket hydraulic servo control system. The system is composed of the hydraulic power source, the load mechanism and the detection feedback device. The feedback device sends the displacement signal back to the PID control to compare the deviation of the actual displacement to the desired displacement. The signal PID control module output is adjusted and sent to the servo valve as an input, servo valve then changes the valve fluid flow and system pressure, thereby adjusting the rocket nozzle load.

Figure 4 shows the servo system as constructed in AMESim which consists of a pump, pressure relief valve, directional control valve (servo), cylinder and Interface components for communicating with Simulink and FloMASTER. Similarly, Figure 5 is a load system created in FloMASTER that includes an earth (anchor component), spring, and cylinder. It also has gauges and controllers that are used to communicate with Simulink and AMESim.

With this configuration, Simulink will send a control signal to the servo system in AMESim which will perform the operation which consists of a displacement of the directional control valve. This displacement is then sent to FloMASTER where the spring component is compressed or expanded and the resultant load is returned as feedback.

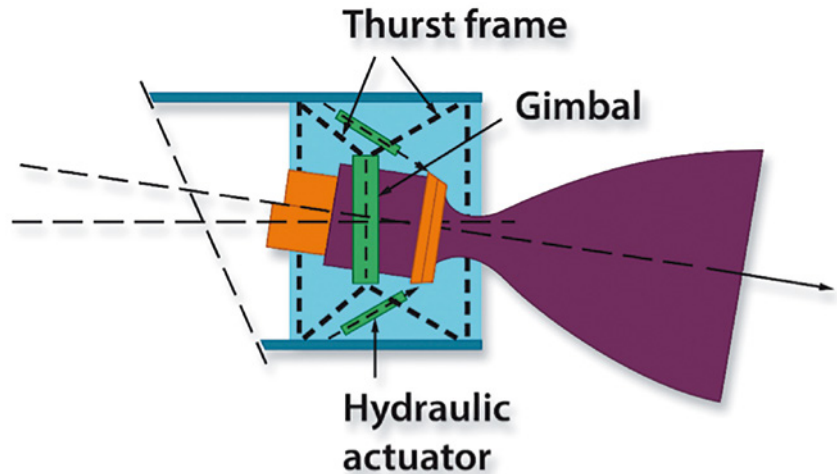


Figure 2. Gimbal mounted rocket engine

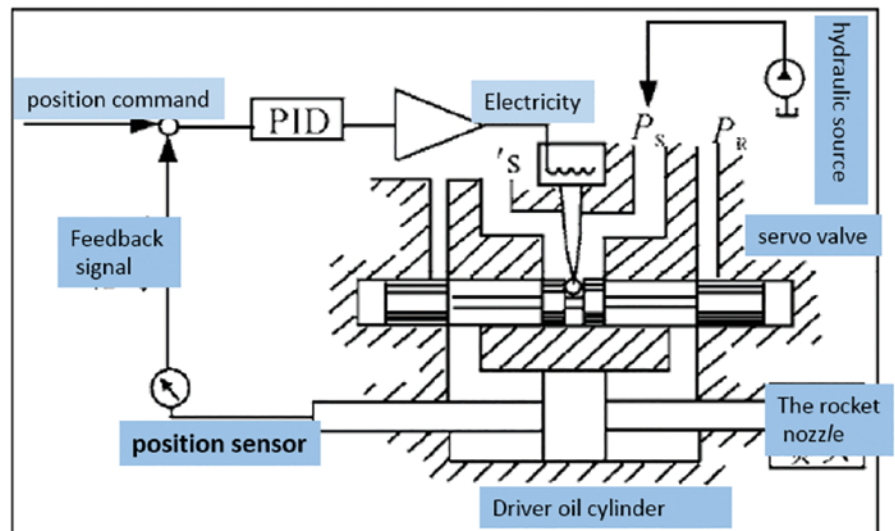


Figure 3. Launch Vehicle hydraulic servo control system

For this study, two different control algorithms were created in Simulink and tested. The first is a traditional PID control strategy that is shown in Figure 6.

Figure 7 shows a Fuzzy Logic algorithm that uses a more sophisticated approach. Either approach can be sent to the servo system controller in AMESim to determine which approach is best suited for this application.

Figure 8 (a), shows the launch vehicle displacement curve when the simulation is run with the PID control and Figure 8 (b) is for the same simulation but utilizing the fuzzy control algorithm. It can be seen from the figure that with fuzzy control, the rocket nozzle displacement has less noise (ie, is more stable) when reaching a stable position, but settling time is slightly longer than PID control, 0.2 sec vs 0.07 sec.

This is an example of one servo control sub-system on a typical space launch vehicle.

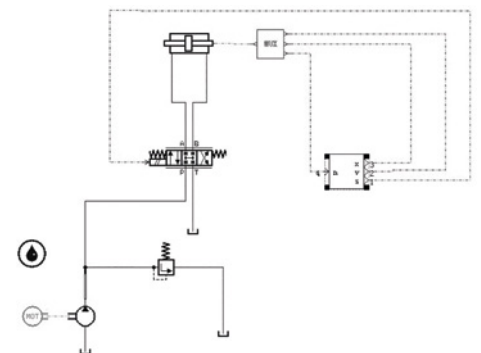


Figure 4. Servo Module (AMESim)

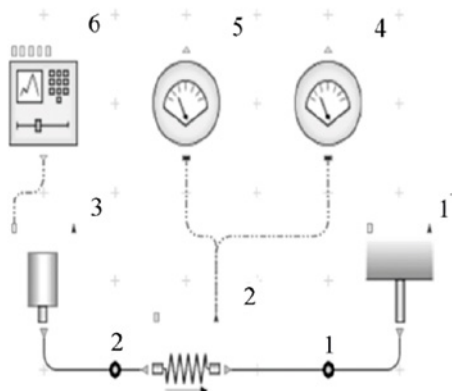


Figure 5. Spring Load Module (FloMASTER)

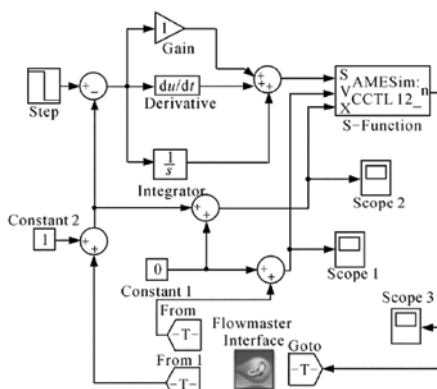


Figure 6. PID Control Algorithm

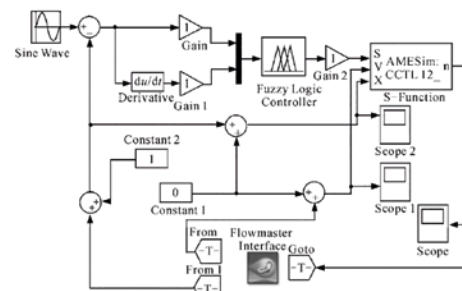


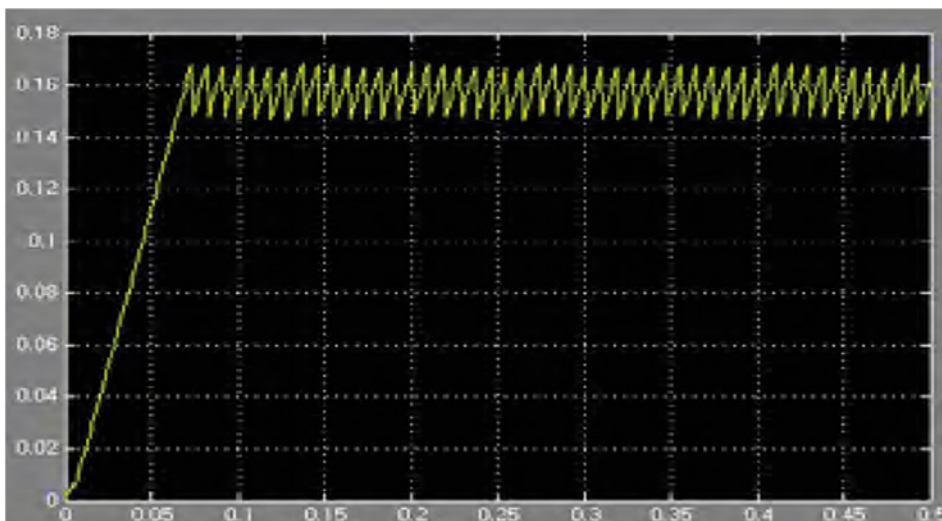
Figure 7. Fuzzy Control Algorithm

There are multiples of these sub-systems on each vehicle and with each one comes a degree of uncertainty. When all of these sub-systems are combined to create the system of systems the level of uncertainty that is facing the rocket guidance engineers is enormous. By including the fluid mechanical system simulations in the guidance control simulations it allows the engineers to manage the uncertainty and recognize possible system shortcomings.

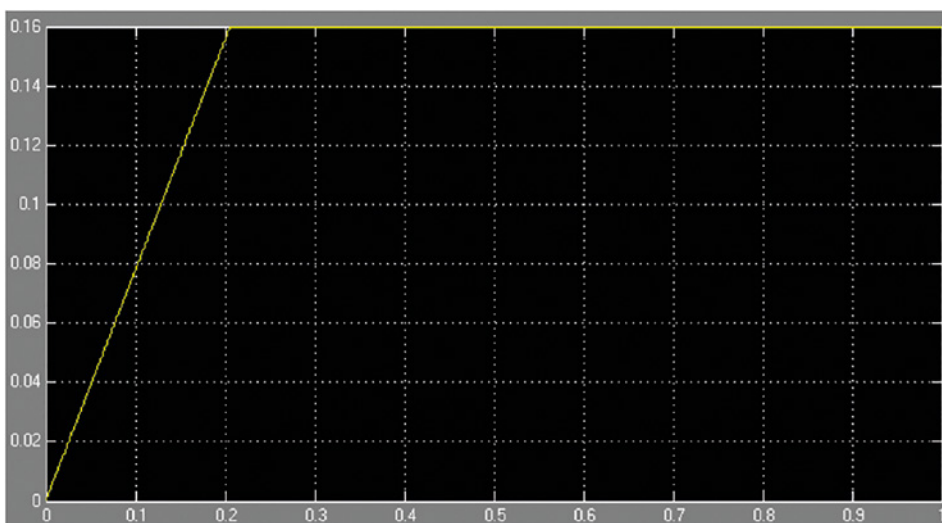
Utilizing the core strengths of both FloMASTER and AMESim in a co-simulation environment with the guidance system software provides the control system engineers with realistic fluid mechanical feedback allowing them to adjust the control strategy without requiring an in-depth knowledge of the physical attributes of the gimbal thrust system. This can greatly reduce the level of uncertainty and significantly reduce the workload of the programmers who can concentrate on the guidance system simulation and not the physical systems. It also provides them a platform for doing rapid what-if scenarios using different servo sub-system controls to determine which approach best fits the design and performance requirements of the overall space launch vehicle.

References

- [1] Co-Simulation System of AMESim / FloMASTER on Simulink Main Platform. Zhang Xinbin, Xian Yaping, Zhou Wenzhang & Chen Yong. September, 2016 http://en.cnki.com.cn/Article_en/CJFDTotal-BGZD201609011.htm
- [2] Shanghai Institute of Spaceflight Control Technology, Shanghai 201109, China;
- [3] Shanghai Servo System Engineering & Technological R&D Center, Shanghai 201109, China;
- [4] School of Energy Science & Engineering, University of Electronic Science & Technology of China, Chengdu 611731, China;
- [5] Institute of Electric Vehicle Driving System & Safety Technology, University of Electronic Science & Technology of China, Chengdu 611731, China)



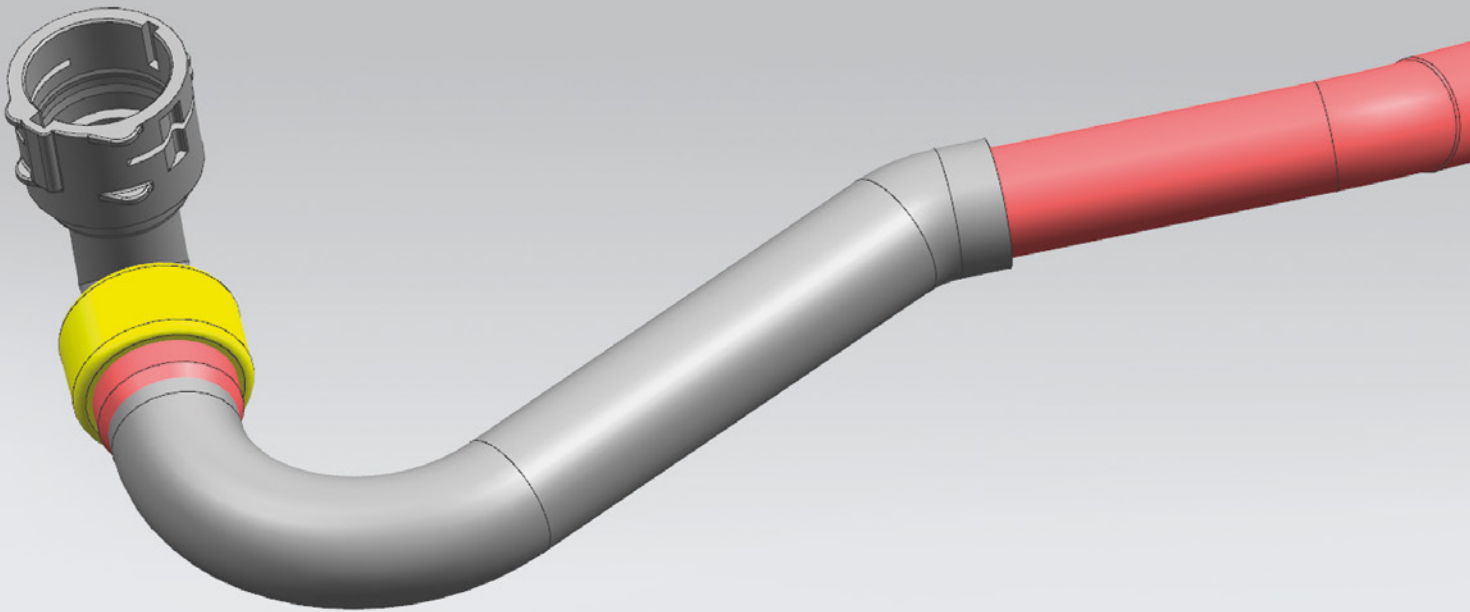
a. PID algorithm displacement curve



b. Displacement curve of the fuzzy control algorithm

Figure 8. Sample simulation results

Figure 1. Radiator to Surge Tank Piping Assembly in Siemens NX



How to....

Convert CAD geometry into a FloMASTER Sub-System

Systems simulation using FloMASTER enables rapid simulation, sizing and optimization of components in a piping network. New with FloMASTER V9 is a fully automated function to convert MCAD piping geometry into an equivalent FloMASTER sub-system, bypassing data re-entry errors and compressing the time required for such a conversion from hours to minutes.

Traditionally a network can be manually specified in FloMASTER, using an extensive catalogue of pre-characterized pipe, bend and junction components. These components need just to be parametrically specified in terms of their length, diameter, bend radius and any other pertinent dimensions. They are then connected together, flow or pressure boundary conditions specified and a steady state or transient simulation conducted. The unique numerical approach to solving the hydrodynamic and thermal governing equations on such a network enables a solution to be provided extremely quickly. Compared to alternative full 3D CFD approaches, a systems simulation approach enables highly complex applications to be addressed on industrial time scales.

If it is the case that an existing 3D MCAD representation of the application exists in a tool such as Siemens NX, Solid Edge etc. then the required component geometric parameters can be extracted using a manually intensive 'measure and re-enter' approach. This entails creating a component in FloMASTER, using the MCAD tool's measure function to extract the parameters and typing those parameters into the FloMASTER component property sheet. This being done for each section of the MCAD geometry that is related to the corresponding manually created FloMASTER component. Such a model building approach can be prone to data re-entry errors and often takes much longer to perform than the resulting FloMASTER analysis itself.

The new automated approach for the conversion of CAD geometry to a FloMASTER sub-system is achieved in a few simple steps:

1. Load 3D geometry

The 'CAD to FloMASTER' (CAD2FM) workflow starts with a loaded assembly in the MCAD tool, in this example an automotive radiator to surge tank piping assembly in Siemens NX (Figure 1).

2. Extraction of Fluid Volume

The automated 'abstraction' of this geometry into an equivalent collection of FloMASTER components first requires that the fluid volume within the pipe be identified. This requires the inlet and outlet of the pipe to be 'lidded' so as to isolate the internal fluid volume. This is done via a lidding function, requiring selection of two planar pipe end faces (Figure 2).

The CAD2FM function is then accessed, the fluid volume identified and displayed rendered on top of the geometry (Figure 3).

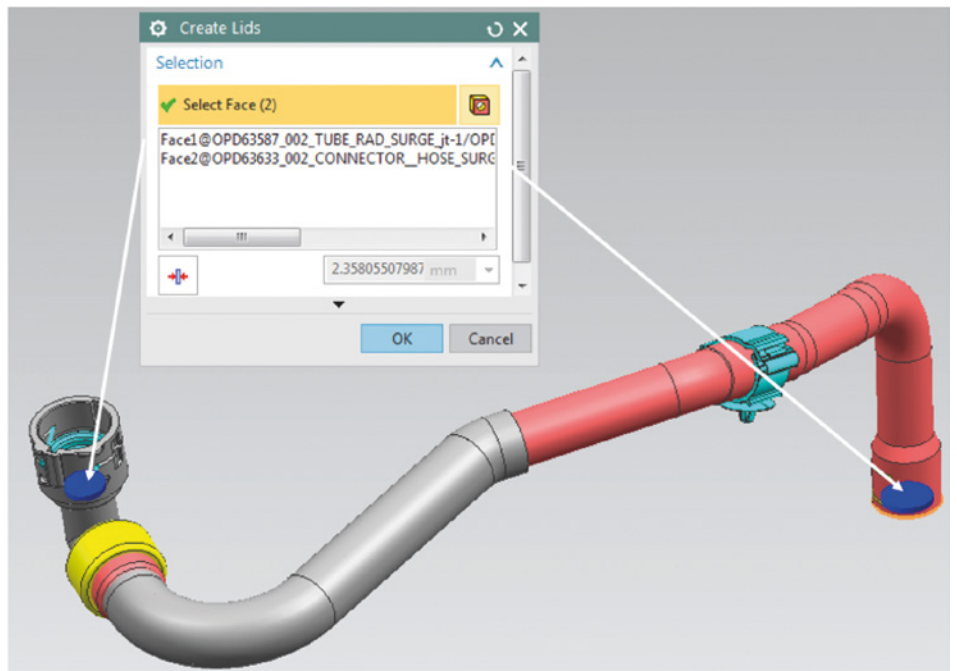


Figure 2. Lidded inlet and outlet faces

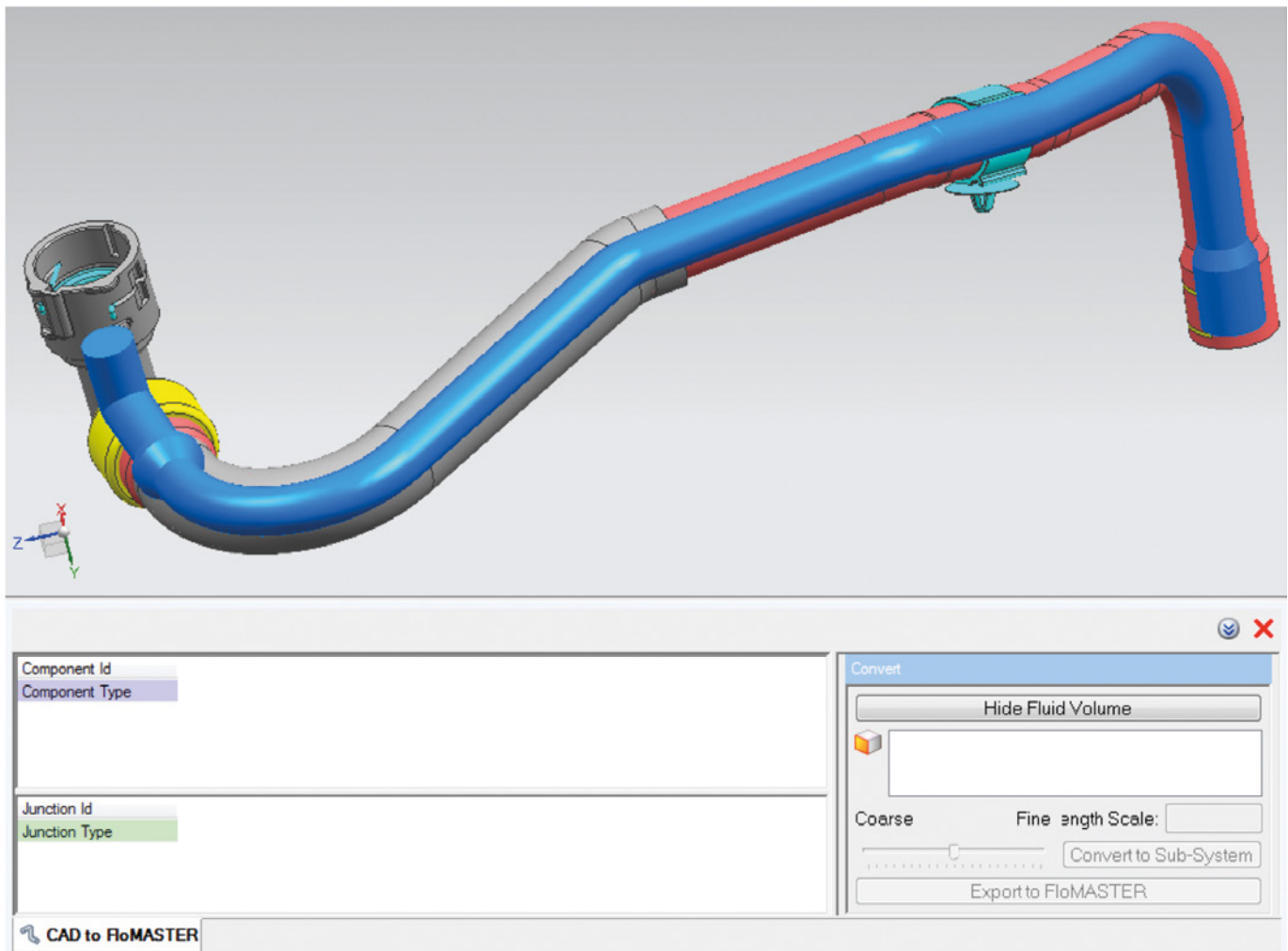


Figure 3. Fluid volume identified

3. Convert to Sub-System

Next, the face that represents the inlet to the pipe is selected and the 'Convert to Sub-System' button pressed. The conversion process involves the automatic extraction of the fluid volume centerline, analysis of its curvature and change in cross section along it, automatic 'splitting' of the centerline into segments whose curvature and cross section relate most directly to equivalent FloMASTER components, then a graphical and tabular display of those components is provided (Figure 4).

4. Refine

A 'coarse to fine' slider bar can be used to control the level of refinement of the abstraction. At the far left 'coarse' slider bar location, a single pipe would be created whose length is preserved and whose diameter is determined from a conservation of fluid volume. At the far right, a maximum number of components is created. Differing slide bar locations and reconversion to a sub-system collection of components can be investigated rapidly until such time as an acceptable representation is achieved.

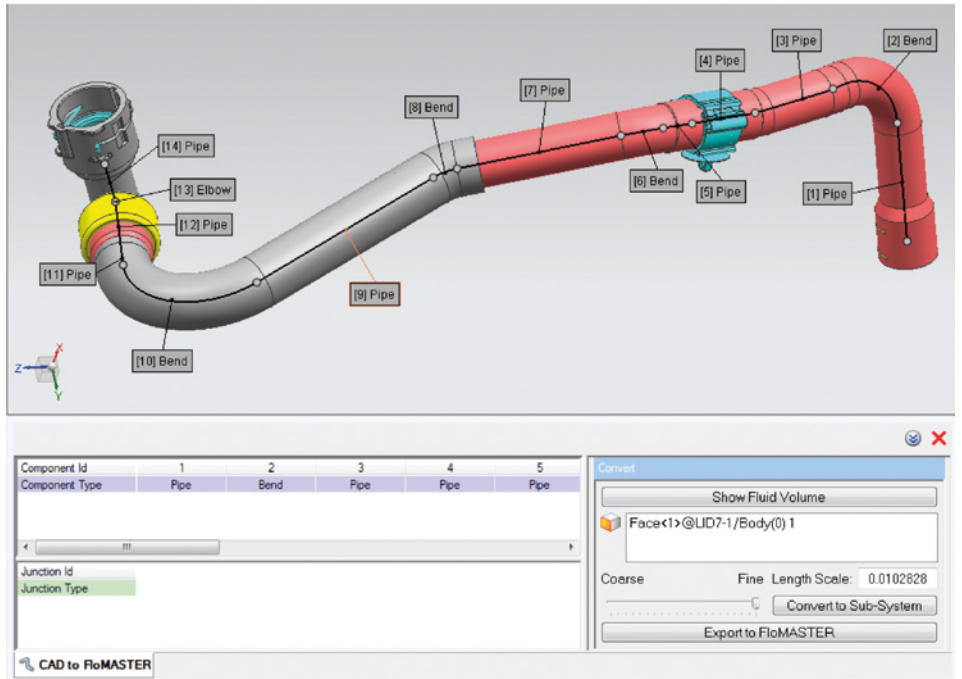


Figure 4. Resulting automatically identified components

5. Export

At that stage the Export to FloMASTER button is used to export a '.cad2fm' file that is then imported into FloMASTER (Figure 5).

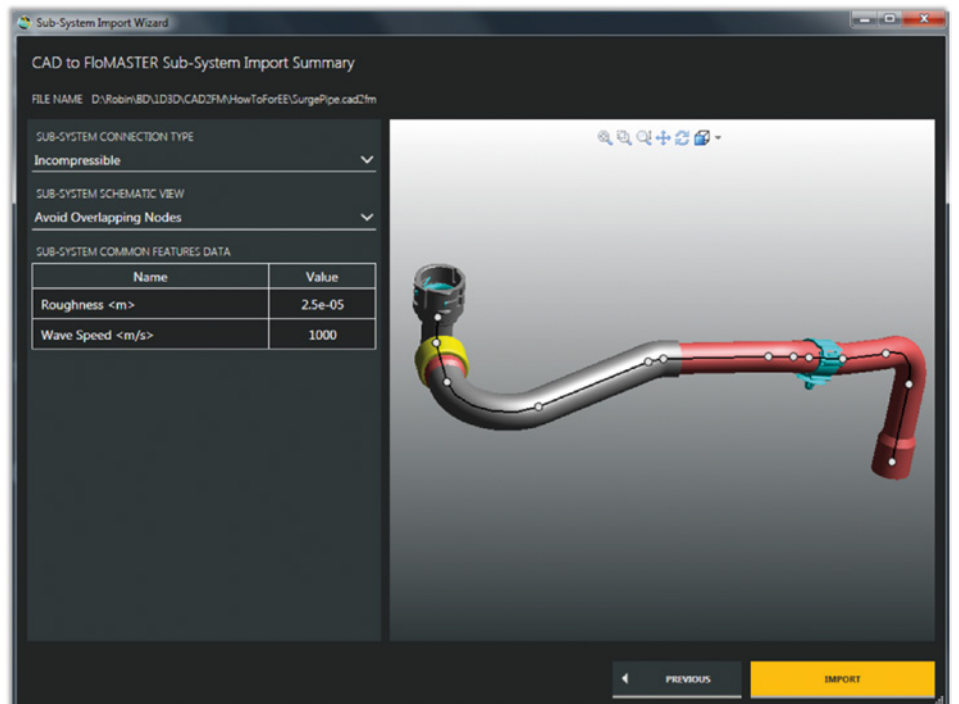


Figure 5. CAD2FM import wizard

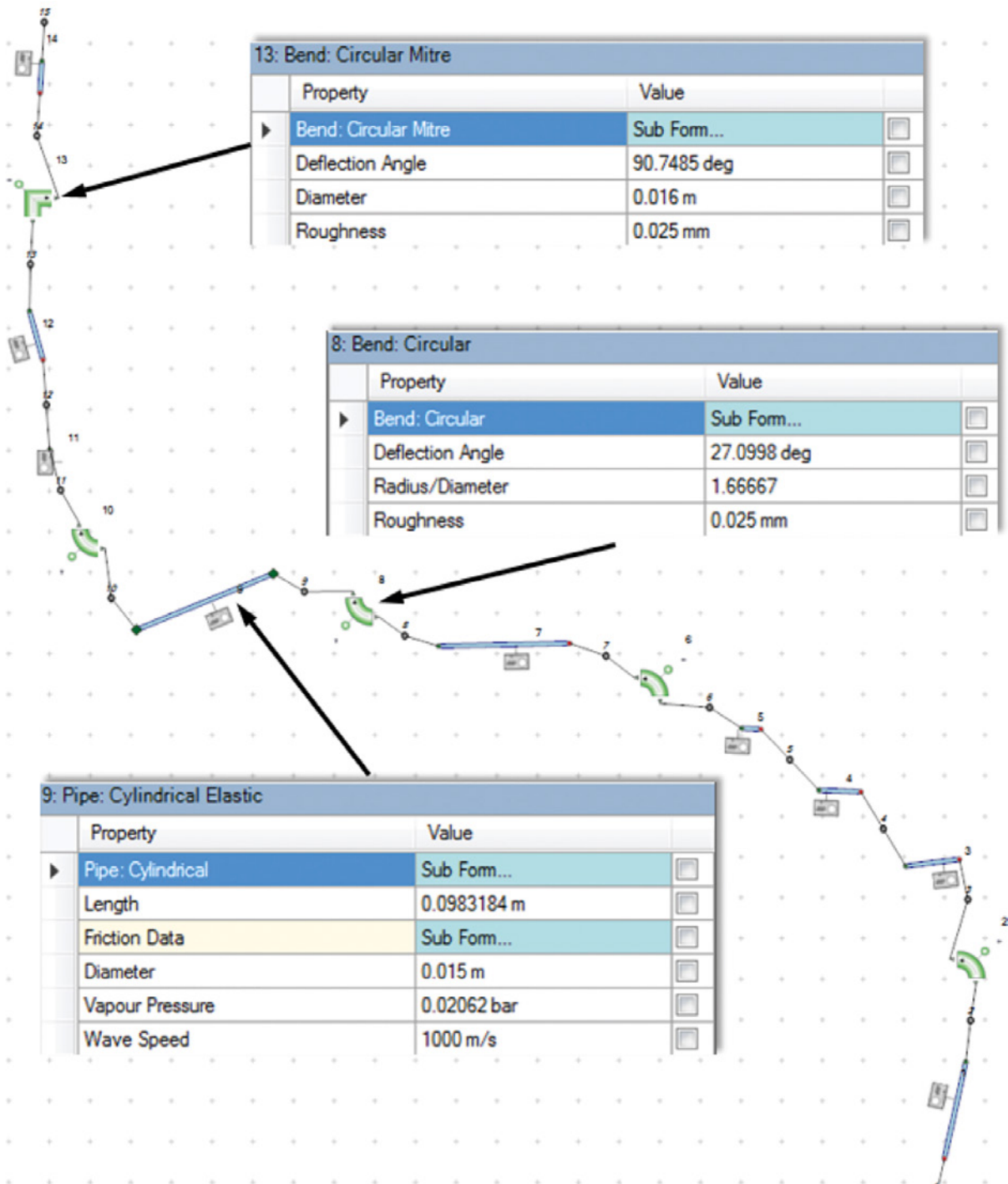


Figure 6. Resulting sub-system definition

6. Import

During import, the original CAD geometry is displayed together with the segmented centerline. Additional information, not extractable from the CAD tool, such as pipe roughness and wave speed (for incompressible transient simulations), can be set. How the sub-system is to be displayed in FloMASTER can also be controlled. Either preserving the exact orientation and component layout as viewed in the import wizard, or to 'explode' the graphical layout

of components to ensure all interconnecting hydraulic nodes are visible (Figure 6).

The resulting sub-system can be optionally manually modified prior to saving it to the sub-system catalogue for reuse in other FloMASTER network simulations.

In this example pipes, bends and miter bends were identified. In addition to these component types, Y and T Junction component identification is also supported.

Generally, compared to manual 'measure and re-enter' approaches, a 90% reduction in time can be expected when using CAD2FM to convert 3D MCAD piping geometry into an equivalent FloMASTER sub-system. The CAD2FM export function is incorporated in FloEFD and supported on Siemens NX, SolidEdge, Creo, CATIA V5 and Standalone platforms.

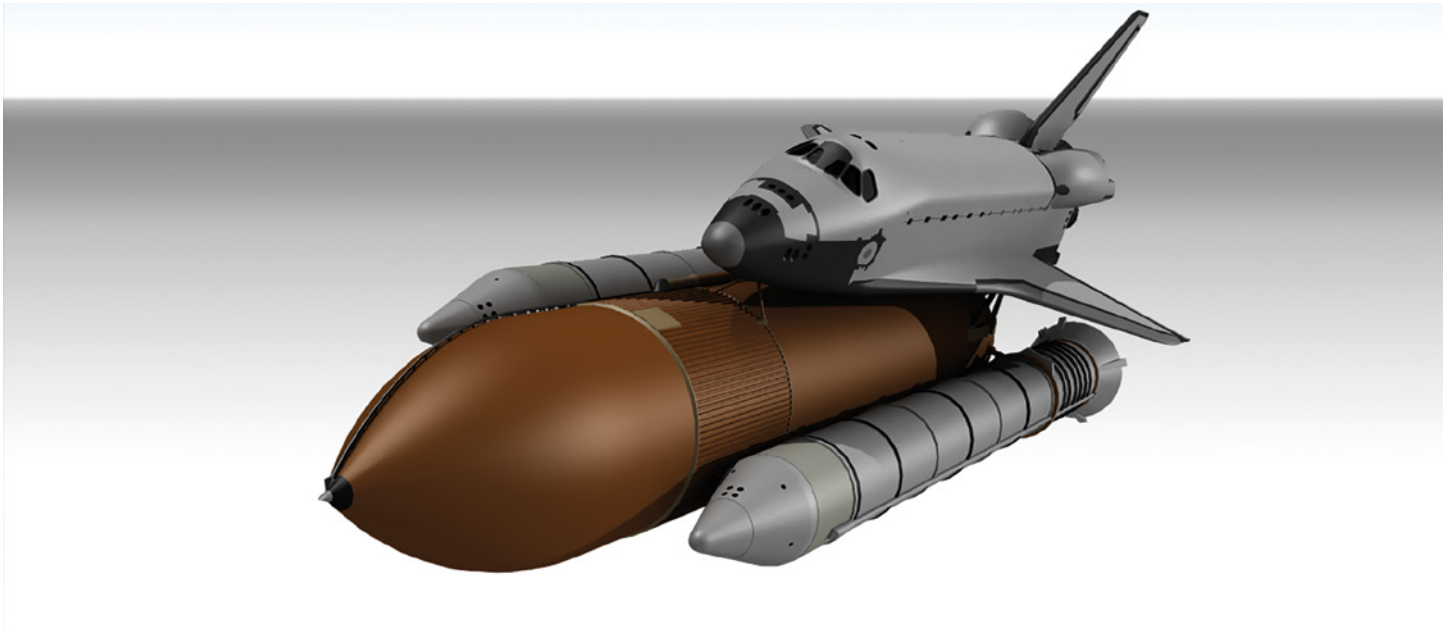
A Study of Aerothermal Loads

in the Presence of Edney Type IV Interaction

By Dr. Leonid Gurov, Dr. Andrey Ivanov, Mentor, a Siemens Business

The simulation of supersonic flow over aircraft is usually focused on shockwave drag and aerothermal loads estimation. For hypersonic vehicles, where aerodynamic heating becomes more prominent, the accurate prediction of the latter is essential in order to design an efficient Thermal Protection System (TPS). If the analyzed geometry represents real prototype of the vehicle (rather than some simplified model) one can expect a highly complex flow structure that includes multiple shockwaves, expansion fans and contact discontinuities. Under these conditions the interaction between the shocks and boundary layer flow may lead to localized heat fluxes that are several times higher than the ones at the stagnation point. This article gives an account of the FloEFD simulations, where such effects are known to occur.





The investigation of shock/shock interaction in a 2D supersonic flow around a cylinder with an impinging shock generated by a wedge gives a good understanding of the processes affecting the surface heat transfer. Depending on the relative coordinates of the point where the wedge shock crosses the cylinder bow shock, six types of interaction [1] are possible (Figure 1). Two cases that draw most attention are known as “Type III” and “Type IV” interactions, where the oblique shock crosses the normal shock. Such interactions should be avoided as they lead to the most significant increase of heat flux. A mixing layer impinges on the body surface in the first case, while the second case is notable for the formation of a small-scale supersonic jet that penetrates a region of low subsonic flow. The remaining four “types” have a minor effect.

To demonstrate how the peak values of pressure and heat flux vary with the change of shock interaction type and freestream conditions, a set of experimental measurements is available. Some of these experiments [2] were initiated after testing early layout of the Space Shuttle system (for its main elements, see Figure 2), where extremely high heat fluxes were detected on the Orbiter nose. Obviously, External Tank played the part of the wedge here and resulted in Type III/IV interaction near the nose. Ever since the 2D shock/shock interaction problem has become a well-known benchmark test case. Such a test is considered in the first part of this article.

The second part is focused on the study of Type IV interaction near the nose of the actual Space Shuttle Orbiter. It should be noted that the “Final” layout of this system minimizes the

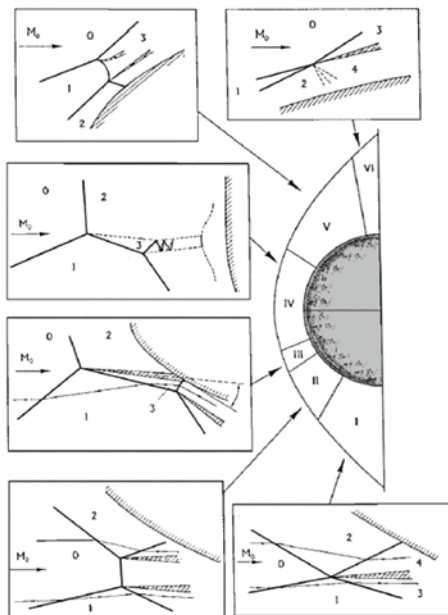


Figure 1. Six types of shock/shock interaction as classified by Edney [1]

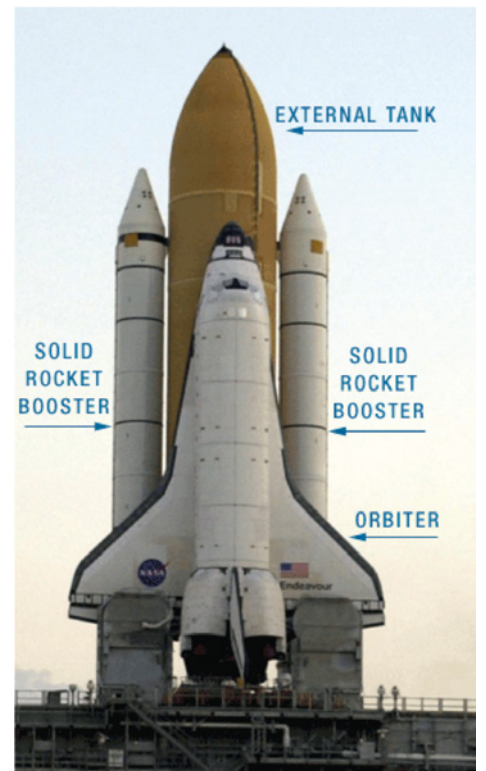


Figure 2. Space Shuttle system with its main elements

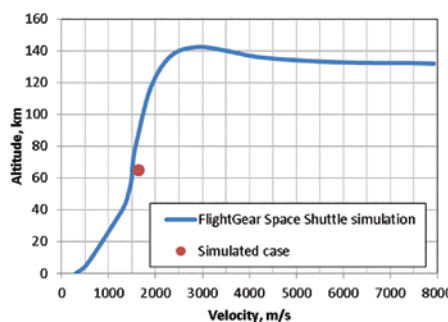


Figure 3. Dependencies of Space Shuttle flight altitude on velocity

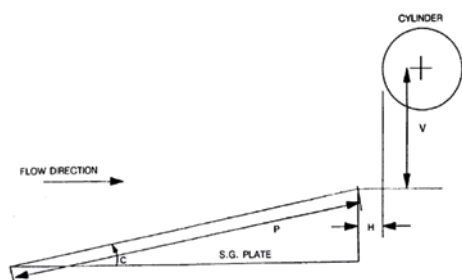


Figure 4. Schematic diagram of the shock/shock interaction model [2]

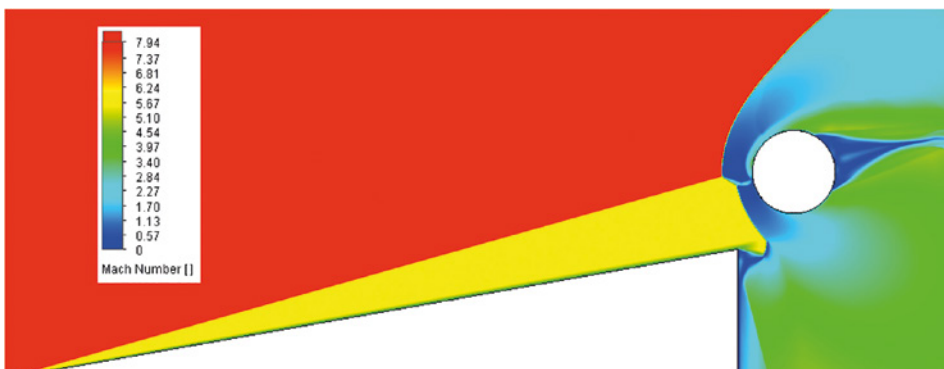


Figure 5. Mach number contours

probability of such an incident. To be more specific, when the velocity of vehicle is about Mach 5 to 10 and the pitch angle is close to zero, the oblique shock does not cross the normal shock near the Orbiter nose, so one can expect a Type V/VI interaction at most. Further acceleration (up to $M=25$) occurs at the altitude of approximately 100km (Figure 3), where the mean free path of a particle is of the same scale (≈ 1 m) as the actual vehicle size, obviously such cases cannot be handled by Navier-Stokes equations. Moreover, the External Tank is discarded at the altitude of 113 km. As a compromise a special case is considered, where the pitch angle is assumed to be well below zero and the flight conditions correspond to the altitude of 65km (solid boosters are discarded at the altitude of 45km).

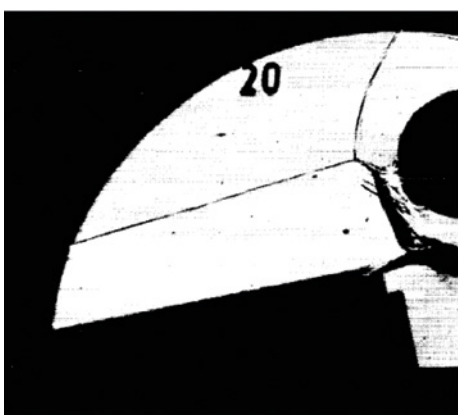


Figure 6a

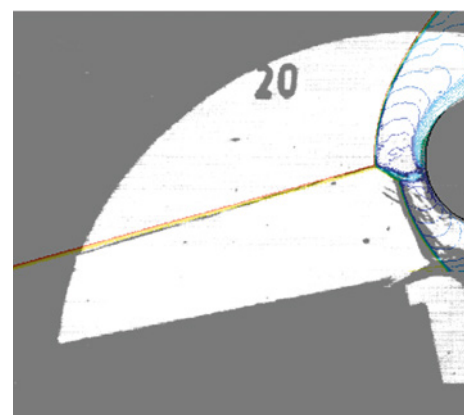


Figure 6b

Figure 6. Schlieren photography as taken from [2] (a) and merged with Mach number isolines (b)

Case 1 - Shock/shock interaction in a 2D flow around circular cylinder

This validation case demonstrates FloEFD capabilities to predict surface heat flux in the presence of shock/shock interaction. The input data for the calculation was taken from [2] and corresponded to the experimental run #20. Figure 4 shows the original experimental layout, where a 3-inch-diameter cylinder was used. In the considered case, $V=2.78$ in, $H=0.5$ in, $P=26.5$ in and $C=10^\circ$.

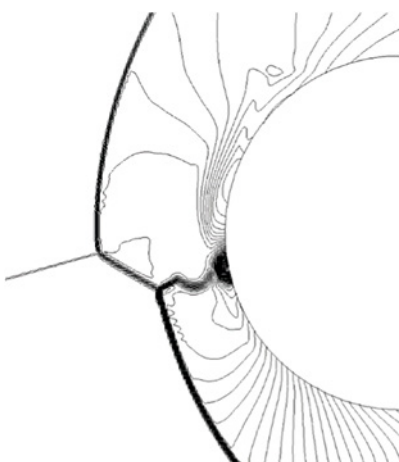


Figure 7a

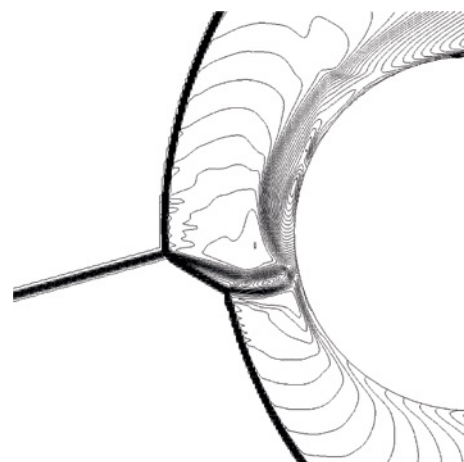


Figure 7b

Figure 7. Isolines of pressure (a) and Mach number (b) near cylinder

The freestream conditions were as follows: $p_\infty=0.06607$ psia, $T_\infty=126.8$ K; $M_\infty=7.944$. Wall temperature was fixed to 294.4K.

A uniform square mesh was used to discretize computational domain with the characteristic cell size being 1/150 of cylinder diameter. To attain stable shock structure, "time-dependent" option was enabled.

Figure 5 shows the Mach number contours over the whole computational domain. A Mach 2 jet near cylinder is prominent and indicates the Type IV interaction. The comparison with the available Schlieren

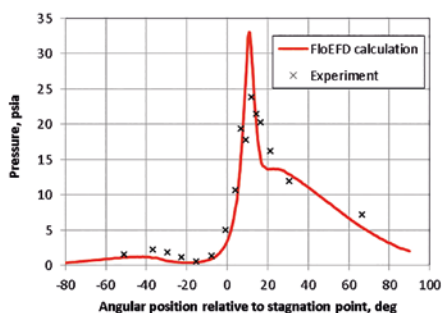


Figure 8. Pressure distribution over cylinder surface

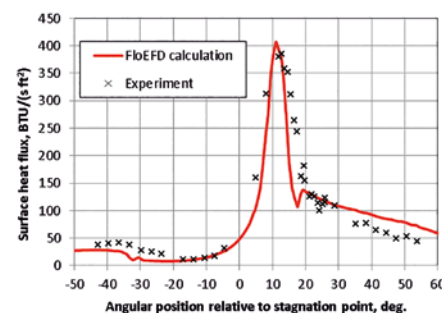


Figure 9. Heat flux distribution over cylinder surface

photography shows good agreement with the experiment in terms of flow structure (Figure 6).

Let us study the flow near the cylinder in more detail by plotting pressure and Mach number isolines (Figure 7). According to these plots, the size of the produced jet in a transverse direction is about 1/20 of cylinder diameter. From the top and bottom sides it is 'bounded' by a contact discontinuity. Before reaching the cylinder jet passes through a series of oblique shocks and a terminal normal shock. The resulting flow splits into two halves; the one in the upper direction accelerates and becomes supersonic, while the flow in the lower direction remains subsonic.

Figure 8 shows the comparison between the calculated and measured pressure distributions around the cylinder. One can see a good agreement with experiment in terms of peak pressure relative coordinate, although the actual value is a bit over-predicted.

The corresponding distribution of heat flux (Figure 9) shows good agreement with experiment in terms of both, peak value and its relative coordinate. As a matter of fact, the obtained peak value (400 BTU/ft²-s) is almost 13 times larger comparing to the estimated value at the stagnation point (30 BTU/ft²-s) in case of the symmetry flow around cylinder (no shock interaction).

The increase of heat flux at the angular position of -30° is due to laminar-turbulent transition in the boundary layer. Although minor, this effect was captured in the calculation. Similar transition is observed at the angular position of 25°. One can notice that the predicted laminar-turbulent transition is shifted 5° towards the stagnation point. Such error can be considered insignificant.

Case 2 - Flow over space shuttle orbiter with external tank

While the preceding case was mainly focused on the quantitative flow analysis keeping the CAD model as simple as possible, this case is notable for the complex geometry analyzed. To perform the simulation it was convenient to use a CAD model of the Space Shuttle available online [3]. In order to attain the angle of the oblique shock generated by the External Tank so that it could cross the normal shock near the Orbiter nose and, thus, result in type IV interaction the external flow Mach number was set to 5.6, while the pitch angle was adjusted to -23°. The freestream conditions corresponded to the altitude of 65 km ($p_\infty=9.922$ Pa; $T_\infty=231.45$ K).

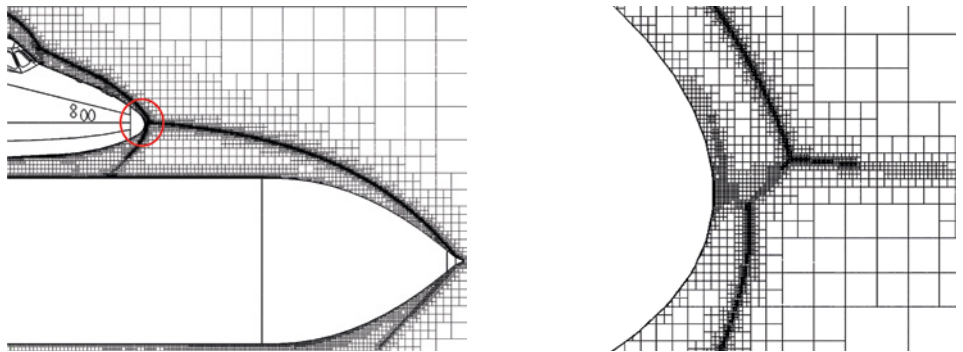


Figure 10. Computational mesh generated after Solution-Adaptive Refinement

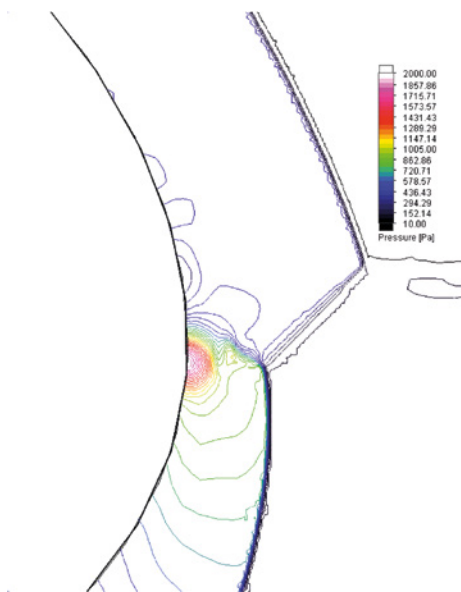


Figure 11a

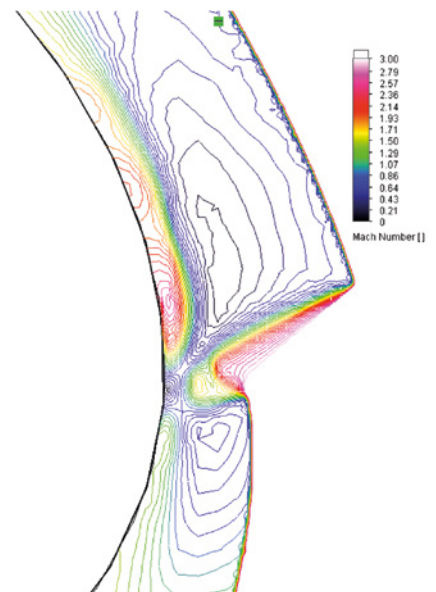


Figure 11b

Figure 11. Isolines of pressure (a) and Mach number (b) near the Orbiter nose

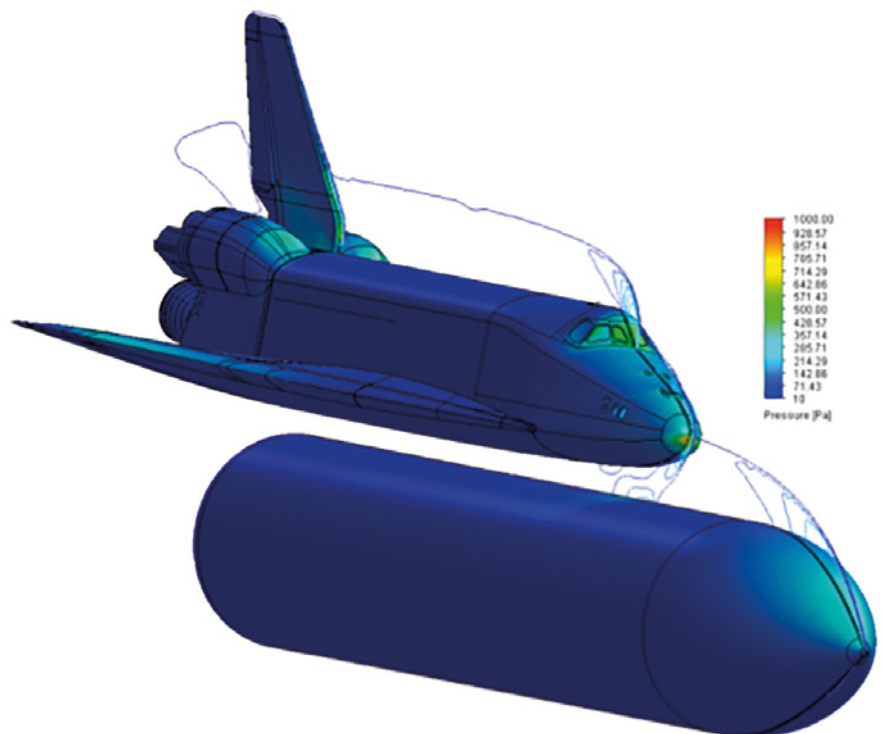


Figure 12. Surface pressure and pressure isolines in the symmetry plane

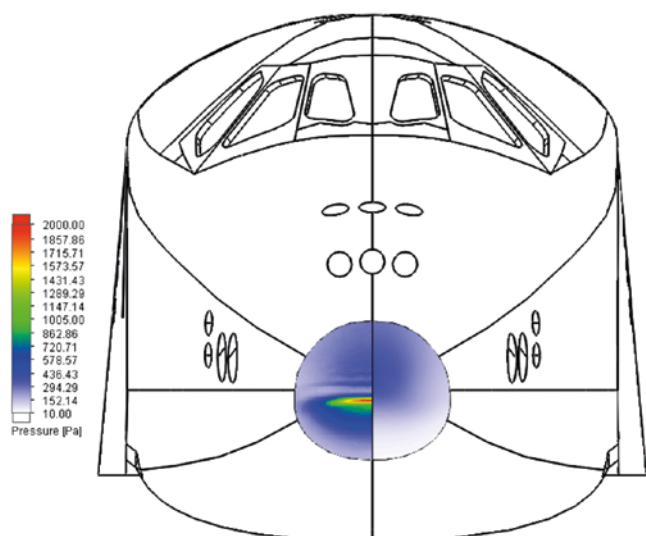


Figure 13. Pressure distribution along the Orbiter nose in the presence of Type IV shock/shock interaction (left) and in case of single Orbiter flow (right)

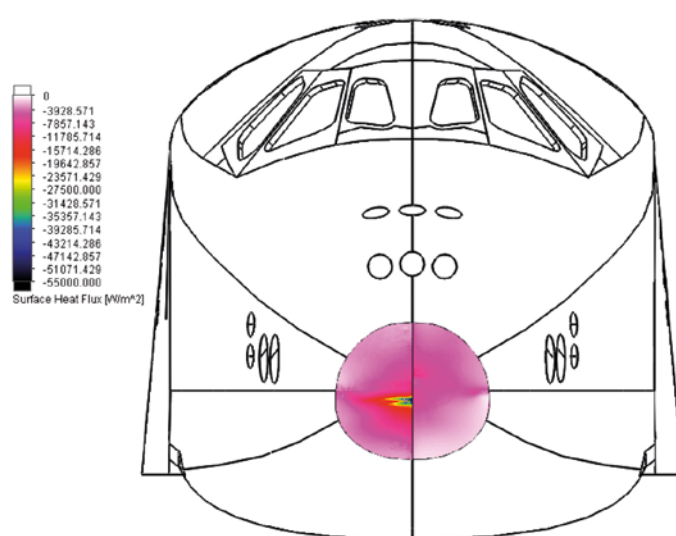


Figure 14. Heat flux distribution along the Orbiter nose in the presence of Type IV shock/shock interaction (left) and in case of single Orbiter flow (right)

While preparing the geometry, specifying mesh settings and boundary conditions several assumptions were made that helped to reduce the overall CPU time for analysis. These had only minor effect on the accuracy of the solution in the regions of interest.

A uniform half-symmetry mesh was used, where the characteristic cells size in the basic mesh was about 1/5 of the External Tank diameter. To refine mesh in the regions of interest (impinging shock, Orbiter bow shock, etc.), Solution-Adaptive Refinement (SAR) was used. The resulting mesh obtained after running SAR seven times comprised of about five million cells (Figure 10). The calculation was stopped after obtaining the converged values of the following surface goals specified on the Orbiter nose – min/max pressure, average surface heat flux.

Figure 11 shows the pressure and Mach number isolines near the Orbiter nose. Comparing to the preceding case, the supersonic jet turned out to be shorter in length; still, the 'bounding' contact discontinuities and a terminating normal shock can be easily distinguished.

The pressure contours plotted over the whole Orbiter surface (Figure 12) give a good idea of the size of the region, where pressure increase caused by Type IV shock/shock interaction is prominent. Comparing to the results obtained in the flow analysis around the single Orbiter (Figure 13-14), the presence of Type IV interaction leads to the increase of peak pressure and heat flux values by 5.5 times (Figure 15). A larger quantitative difference was observed in the preceding case. That was partly due to the larger Mach number of the external flow.

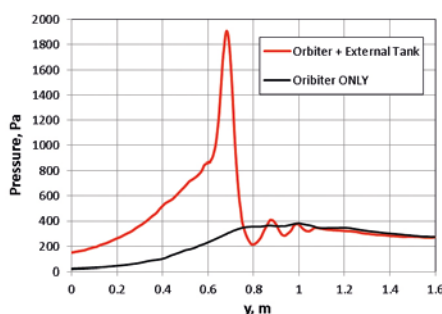


Figure 15a

Figure 15. Distributions of pressure (a) and heat flux (b) along the nose in the symmetry plane

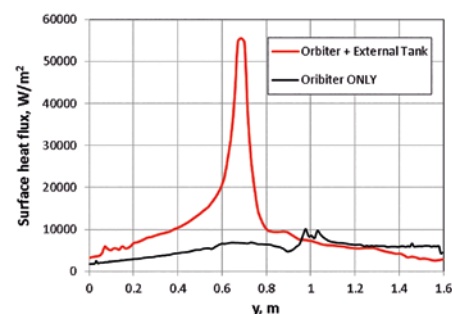


Figure 15b

Summary

The effect of heat transfer rate increase caused by Edney type IV shock/shock interaction has been investigated with FloEFD. A well-known benchmark case was used for the initial test that showed good agreement with experimental data in terms of flow structure, surface pressure and heat flux distributions. The results obtained in the FloEFD analysis of Space Shuttle revealed a small-scale region on the Orbiter nose with a moderate increase of surface heat transfer rate caused by type IV interaction.

References

- [1] Edney, B., "Anomalous heat transfer and pressure distributions on blunt bodies at hypersonic speeds in the presence of an impinging shock", FFA Report 115, Aero. Res. Institute of Sweden, 1986
- [2] Holden, M. S. et. al., "Studies Of Aerothermal Loads Generated in Regions Of Shock/Shock Interaction In Hypersonic Flow", AIAA paper 88-0477, Jan 1988.
- [3] <http://www.grabcad.com>

A detailed close-up photograph of a turbocharger turbine wheel. The wheel is made of a dark, polished metal and features five curved blades radiating from a central hub. The hub is mounted on a shaft, and the entire assembly is set within a larger, cylindrical housing. The lighting highlights the metallic texture and the precision engineering of the component.

|| We started our new designs and we performed the whole turbocharger simulations, obtained the thermal distributions and found material substitution opportunities. We achieved this with FloEFD

Mert Alpaya, Researcher, Borusan R&D

New Development of a Turbocharger with FloEFD

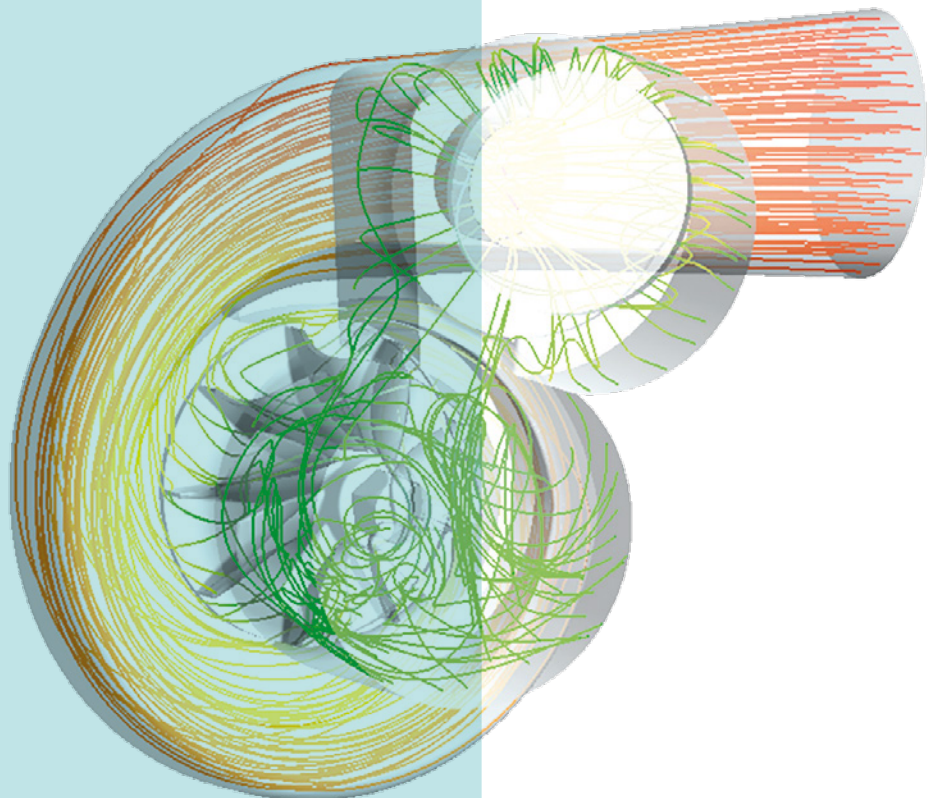
By Mert Alpaya, Borusan R&D



Borusan R&D is responsible for developing R&D strategies and conducting R&D studies for the entire Borusan Group, which comprises the Steel, Logistics, Energy, Automotive and Distributorship divisions. The automotive division, Supsan, produces engine components for the OEM and after sales market. Supsan is the largest manufacturer of engine valves in Turkey and distributes turbochargers, among others. Supsan and Borusan R&D started a collaborative project with the goal of developing and manufacturing completely new turbochargers.

The turbocharger is a small, complex and critical component of the vehicle because it directly determines the engine performance. A turbocharger consists of two different types of turbomachines, a turbine and a compressor, which are combined in one single component. Multiple design studies must be carried out for the design: an analysis of the flow conditions and heat distribution, as well as bearing design and lubrication. The high temperature of the exhaust gases makes the design critical. The exhaust gas from the engine drives the impeller on the exhaust side, and with the common shaft the impeller at the cold air side is driven, which then sucks in and compresses the air on the air intake side. The compressed air increases the combustion efficiency in the engine.

The turbocharger developed in this project is shown in Figure 1. It is designed for 1.5-litre engines in series vehicles. The rotational speed is controlled by a waste gate actuator.



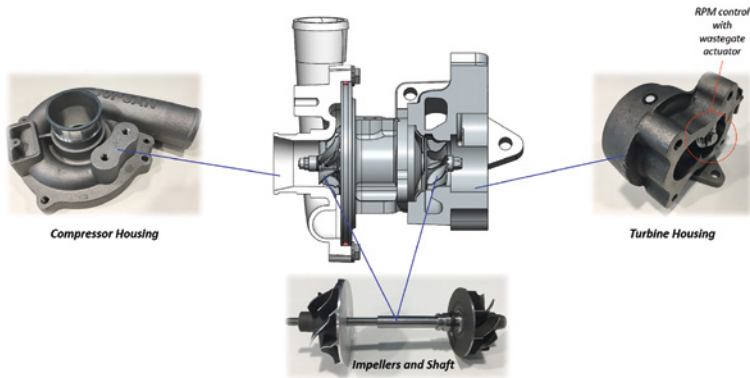


Figure 1. Turbocharger components

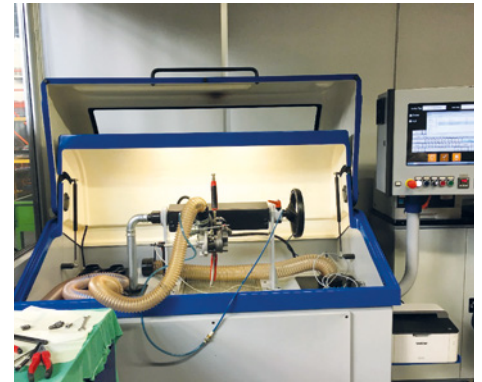


Figure 2. Test rig

The turbocharger was tested on the test rig shown in Figure 2. The turbine inlet pressure has been changed to modify the rotational speed. The flow rate and the pressure were measured. Twelve different test cases were measured on the test rig and later compared with the simulation results.

The CAD model for the compressor side is shown in Figure 3. A fictional body was used to define the rotating area, the boundary conditions were mass flow at the inlet and total pressure at the outlet.

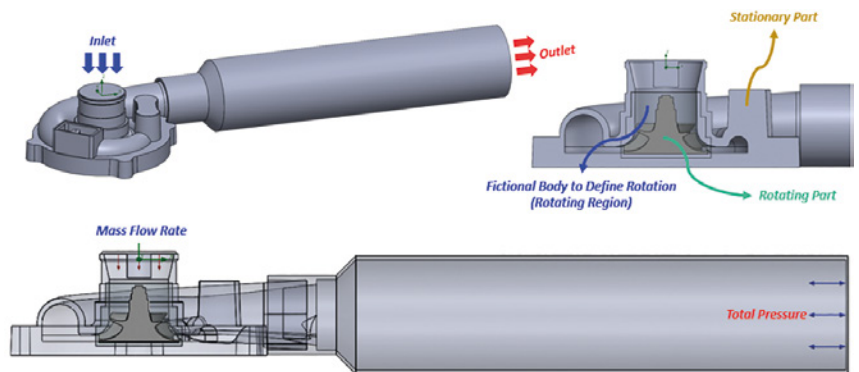


Figure 3. CAD model compressor side

For the turbine side, two different cases were investigated in which the wastegate lid was opened and closed, for different rotational speeds (Figure 4). A total inlet pressure and an environmental pressure for the outlet were applied.

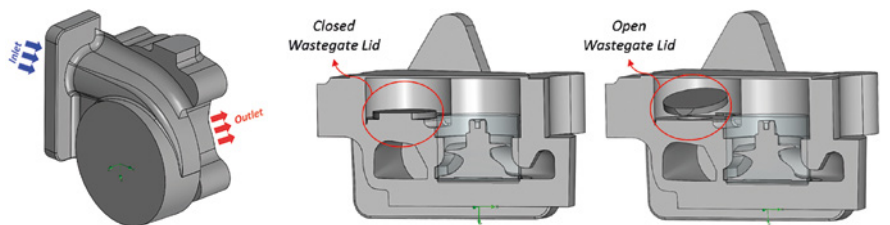


Figure 4. CAD model turbine side

Six loading conditions were investigated for both sides, as shown in Figure 5.

The deviation from the test results is between 2% and 7%, depending on the impeller rotational speed. The results for the six cases are shown in Figure 7.

The results for the waste gas side with closed and opened wastegate are shown in Figure 8. Three different cases were simulated for both positions. The deviation from the test results is a maximum of 9.4 %.

Case	Rotational Speed [rpm]	Inlet Mass Flow Rate [kg/s]	Outlet Total Pressure [Pa]	Case	Rotational Speed [rpm]	Inlet Total Pressure [Pa]	Outlet Pressure [Pa]
1	51.670	0,03222	108.222	1	24.550	111.486	101.325
2	64.753	0,04270	114.138	2	44.360	121.133	101.325
3	86.010	0,06236	122.298	3	57.120	130.652	101.325
4	88.217	0,06704	127.398	1	26.270	111.398	101.325
5	101.050	0,08087	131.682	2	47.370	121.276	101.325
6	104.953	0,08778	136.884	3	63.090	131.656	101.325

Figure 5. Six loading conditions

Following the comparison and the confidence in the simulation based on good agreement, further simulations were quickly conducted with FloEFD. The entire turbocharger, including the hot turbine gases and oil flow, was simulated (Figure 9). The temperature distribution on the entire component and especially for the shaft region was analyzed (Figure 10). Different impeller materials and their effects on the shaft temperature distribution were investigated (Figure 11). After that, the thermal expansions and the clearances for the operating conditions were calculated.

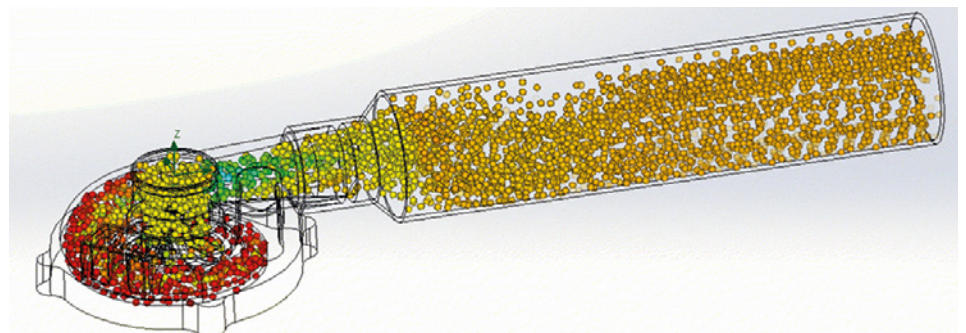


Figure 6. Results post processing

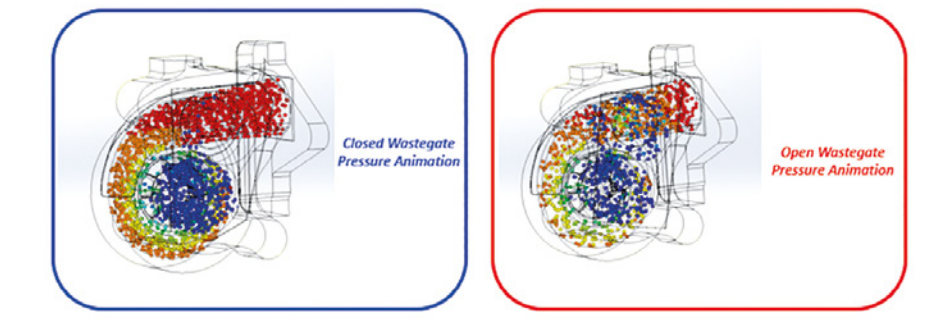
Case	Test Results [m³/s]	FloEFD Results [m³/s]	Deviation [%]	
1	51.670 rpm PR = 1,061	0,02520	0,02550	1,19
2	64.753 rpm PR = 1,119	0,03167	0,03240	2,31
3	86.010 rpm PR = 1,199	0,04316	0,04520	4,73
4	88.217 rpm PR = 1,249	0,04454	0,04680	5,07
5	101.050 rpm PR = 1,291	0,05199	0,05550	6,75
6	104.953 rpm PR = 1,342	0,05428	0,05830	7,41

Figure 7. Results for six cases

A comparison of the initial impeller material and the four alternatives is shown in Figure 12.

The shaft and impeller surface temperatures were exported to MATLAB and the thermal expansions and clearances were calculated. For the alternatives, the differences of the clearances between the bearings, shaft and housing were analyzed. These investigations led to the selection of the appropriate material, which also enabled cost optimizations.

The Borusan R&D engineers developed completely new turbochargers for a series of vehicles. The thermal distributions were determined with the use of FloEFD in the simulation process. The new designs were optimized on the basis of the analyses and the resulting expansions and clearances.



Case	Test Results [kg/s]	FloEFD Results [kg/s]	Deviation [%]	
1	26.270 rpm	0,01839	0,01695	-7,83
2	47.370 rpm	0,02592	0,02460	-5,08
3	63.090 rpm	0,03253	0,02946	-9,44

Case	Test Results [kg/s]	FloEFD Results [kg/s]	Deviation [%]	
1	24.550 rpm	0,03194	0,02950	-7,65
2	44.360 rpm	0,04550	0,04240	-6,81
3	57.120 rpm	0,05642	0,05280	-6,41

Figure 8. Results waste gas side

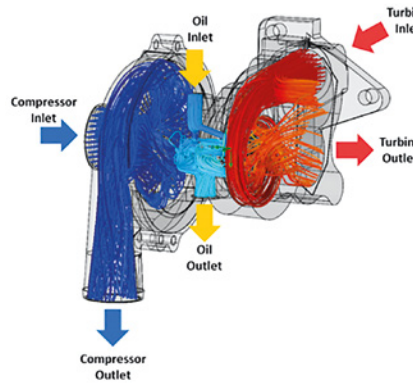


Figure 9. Simulation of the entire turbocharger

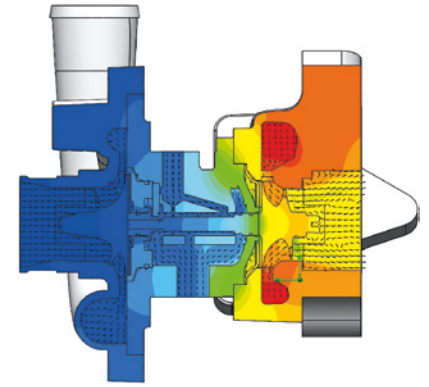


Figure 10. Temperature distribution

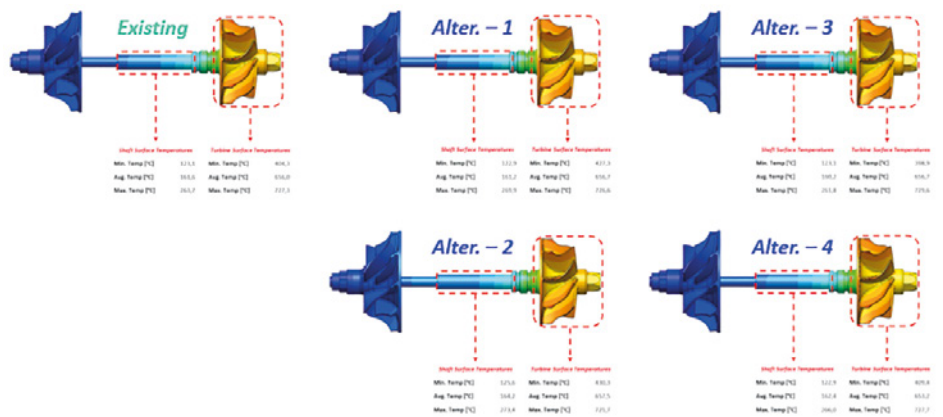


Figure 11. Investigation of different impeller materials

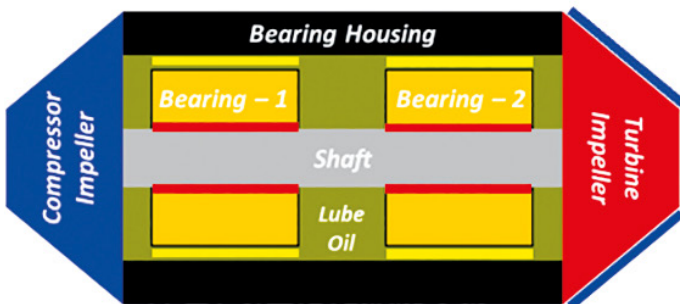
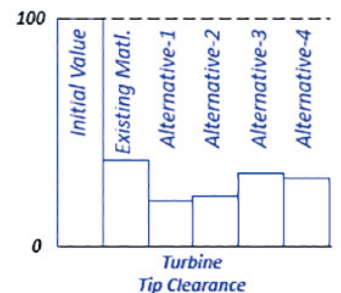


Figure 12. Comparison of thermal expansions and clearances



Risk Prevention & Energy Saving

A new thermal modeling procedure of the ventilation system for work risk prevention and energy saving in ships

By Manuel Pita, Rebeca Bouzón, Ángel M Costa and José A Orosa, University of La Coruña

Today, more than 90% of international commerce is done by maritime transport, their emissions and energy consumption are topics of special interest, with the International Maritime Organization (IMO), being responsible for their regulation and control. The International Convention for the Prevention of Pollution from Ships (MARPOL) adopted in 1973, was the first international attempt to reduce pollution by ships, both from operational and accidental causes. By 2050, the emissions from maritime transport will triple compared to the current scenario. As a result, in 2011, IMO developed some compulsory additions to the MARPOL Annex VI, to improve energy efficiency and reduce greenhouse gas emissions from ships. This is the first legally binding climate change treaty adopted since the Kyoto Protocol.

One of the most interesting recommendations is replacing the traditional single main engine with several low power engines, with an equivalent total power, increasing considerably the time that the engines work at nominal speed and, consequently, their efficiency. Important efforts have also been made in the last few years to improve the most important complementary systems and equipment, to optimize their energy consumption. In this sense, the ventilation system of the engine room must be considered as it can represent about 5% of the installed power.

However, in this case, specific work risk criteria must be applied in addition to energy-saving objectives, considering that the engine room constitutes a typical example of severe working environment, with extreme temperature and relative humidity conditions, as a result of heat released by the main engine.

To date, the standard solution is to cool the engine room with outdoor air throughout the journey at sea, typically with a number of air changes per hour in the ventilation system, without any kind of control or optimization of the energy consumption. In this sense, it must be noted that although several standards

and datasheets have been developed by international standardization organizations, they do not provide clear information about the suitable ambient conditions in the engine room in accordance with the tasks that must be developed.

With the introduction of the Ship Energy Efficiency Management Plan (SEEMP), recommendations and the changes derived from the implementation of new alternative technologies has resulted in new and different heat sources in the engine room, considerably changing the thermal distribution in the engine room, in such a way that previous experience of thermal distribution on board has had limited validity and usefulness. Consequently, advanced technologies such as thermographic analysis and computational fluid dynamics (CFD) are critical to analyze these new indoor extreme ambiances.

In this study, the indoor ambience and working conditions in the engine room of a real ship have been analyzed and simulated, to establish a new procedure to estimate the maximum work time allowed and the corresponding minimum rest time in a controlled environment required to release the cumulated heat. The analyzed ship

shows four main engines with a nominal power of 1250 kW each. Even during normal navigation, only two of the main engines are operating at any one time, the third and fourth engines required only for special positioning maneuvers.

During navigation, all the ventilators are required, while in the port, only a small part of ventilators are used as a consequence of the low heat released by the auxiliary engine, in such a way that the energy consumption of the ventilators in the engine room represents nearly 5% of the installed power, and as consequence, one of the main actuation points to reduce total emissions.

In this distribution, three main areas must be considered: the engine room, the workshop, and the engine control room, as shown in Figure 1.

The engine room has dimensions of approximately 10m x 314m x 35.5 m, and a total volume of 770m³, with 25% of this volume filled by the engines and complementary equipment, whose exact geometry was obtained from the original construction drawings. As shown in Figure 1, this volume is divided into two parts by an ambulation platform, located at a height of 2.8m from the base.

Under normal conditions, the ventilation system removes the air volume of the engine room six times an hour (around 3500m³/h), by nozzles placed over main engine turbochargers, and releases fresh air in significant places, such as over the alternators.

The workshop is a small complementary room of 13.3m² destined to be an independent place to work with machine tools, like milling machines or drills. Its ventilation system is shared with the rest of the engine room, but its temperature is lower as it is situated away from the main engines.

The engine control room is used by marine engineers to monitor the engine's main variables with computers under controlled indoor conditions, about 20 °C and 70% of relative humidity, in such a way that typically marine engineers use this room as a resting point to release the heat accumulated while working in the engine room.

Indoor and outdoor air conditions like dry-bulb temperature, relative humidity, pressure, and air velocity were sampled during navigation on a daily basis, when the ship was in a tropical region, under a temperature



Figure 1. Main engine room distribution.

Sensor	Sensibility	Sampling range
Gemini data loggers (Chichester, UK)	±0.1 °C, 1% RH, 1Pa	-40 to 125
Anemometer Testo 425	0.01 m/s	0 to 20 m/s
Thermographic camera TESTO 885-2	lower than 30 mK	0 to 1200 °C

Table 1. Sensors and its technical characteristics

of 29°C and a relative humidity of 90%, with calibrated data loggers and anemometers, which technical specifications are shown in Table 1.

Under these conditions, the main engine room's average indoor temperature was nearly 35.3°C, the relative humidity 69.5%, and the pressure about 1 bar. At the same time, the surface temperature in the engines was about 77.5 °C and 47.8 °C in the alternators. Figure 2 provides a representative thermal image of the engine room, showing engine number three in service, considering an emissivity of 85%.

A complete 3D model of the engine room was created from the original construction drawings using Solid Edge ST7, while the thermodynamic simulation and analysis was done with Mentor's FloEFD. FloEFD is an advanced simulation tool specially designed to simulate and study turbulent flows, considering critical indoor ambience variables such as relative humidity and moist air phase change, the parameters not usually analysed by classical CFD software.

The simulations reproduce the real navigation conditions in tropical regions (an average outdoor temperature of 29°C and a relative humidity of 90%), with two main engines working (numbers one and three), to predict indoor air velocity, temperature, relative humidity, and operative temperature among others variables.

The simulation mesh was especially designed to define the indoor conditions with great accuracy in two specific areas: near the

turbochargers (the hottest place) and in the workshop. As the engine room showed a platform over which marine engineers walk, it was considered appropriate to analyze these variables at 1.5m over this platform, which corresponds approximately to the height of the center of mass of an individual over the platform. Under these conditions, about 350 iterations and a simulation time of 5½ hours are required in an Intel i5 – 4200U computer to obtain an adequate accuracy.

To validate the CFD simulations of the indoor air thermodynamic parameters, the simulation results were compared with the values sampled during real navigation, these being the values obtained with six air changes per hour in clear agreement with the measured data. In this sense, the main engine and alternator surface temperatures estimated were totally in agreement with the values obtained by the thermographic camera, about 77.1°C and 48.1°C, respectively, as shown in Figure 2.

At the same time, estimated average indoor air temperature was nearly 35°C, relative humidity about 69%, and pressure about 1 bar, in accordance with the values sampled during navigation, as shown in Figures 3 and 4.

As can be inferred from these curves, due to the asymmetrical distribution of air nozzles in the engine room, the most adverse working conditions (the critical point) occur in the area of turbocharger number three. Once the CFD model was validated, similar simulations were done at three and twelve air changes per hour, as shown in Table 2. The most relevant parameters in the critical point, are both in the engine room, and in the workshop.

As previously mentioned, the hottest zones in the engine room were analyzed in order to define the critical tasks and the maximum time that a worker can stay under a higher Met value, being the most critical, removing injectors from the main engine, where crew members must do an intense work (with a high metabolic rate), in the hottest place of the engine room, near the turbocharger.

Under these extreme conditions, the maximum time allowed to do the job and the minimum time required to release the accumulated heat in the control engine room is reflected in Figures 5 and 6 as a function of the globe temperature.

To define Figure 6, it was necessary to establish the relationship between indoor conditions in the control engine room and the time needed to restore the thermal

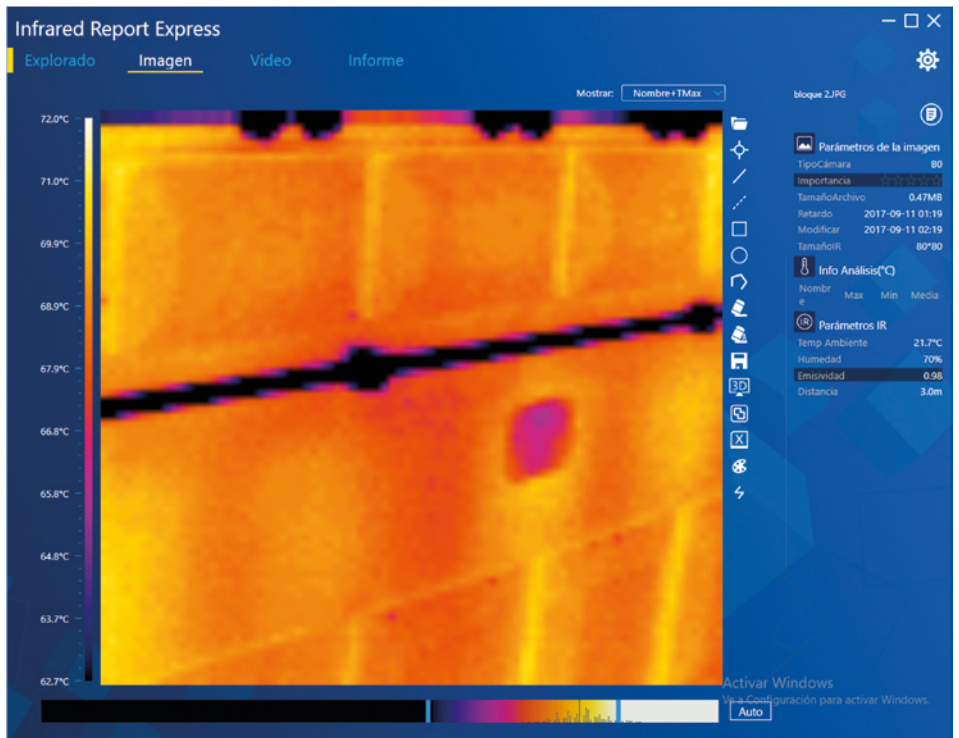


Figure 2. Main engine thermographic photo.

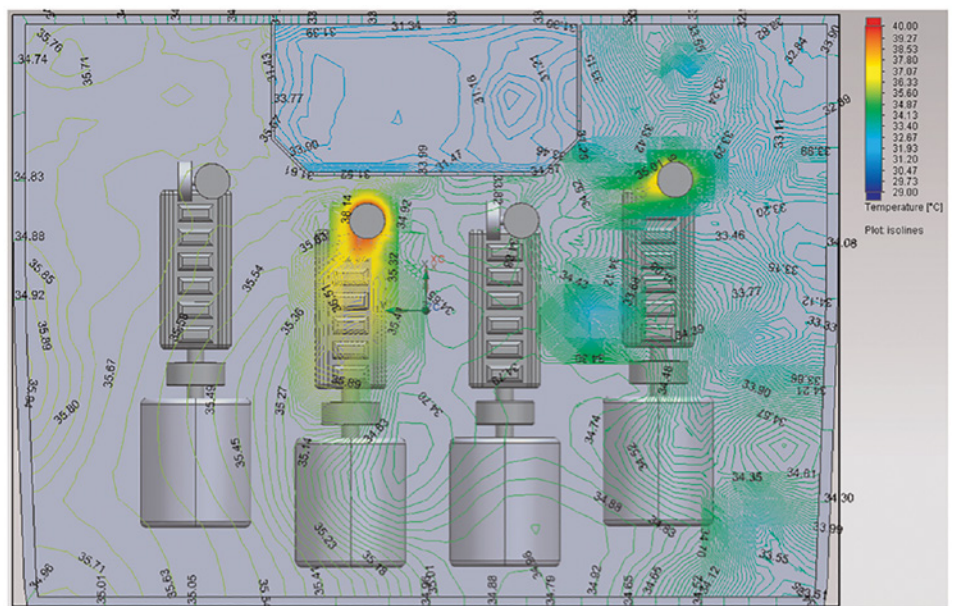


Figure 3. Dry-bulb temperature in the engine room (6 ACH).

equilibrium, considering that the control engine room shows a low air velocity of about 0.1 m/s, a dry-bulb temperature of 19.7°C, and a wet-bulb temperature of 17.4°C.

Consequently, even when charts 5 and 6 estimate the time as a function of the global temperature in the sampling place, under air velocities below 0.2 m/s, the difference between operative temperature and global temperature is typically less than 0.6 K, in such a way that it can be used as the operative temperature without any concerns.

Previous investigations showed that increasing the number of air changes is typically the most effective method to cool the engine room, and that in most of the cases, during navigation, all ventilators work at the nominal conditions without considering the kind of task that is being developed on board or the external weather conditions.

Consequently, even when the energy consumption and health risk are not usually considered at the same time, this is clearly an advanced research topic of great interest for designers, in order to fulfill the new energy saving requirements derived from the SEEMP stipulations.

This research establishes a new methodology to analyse and model the engine room ventilation system in order to reduce its energy consumption, respecting the tolerable work risk limits, methodology that can be easily extended to other related severe industrial environments, like cogeneration plants or industrial laundries, among others.

On the basis of a complete 3D CFD simulation of the engine room, the particular zones where heat stress are a clear risk were identified, considering the specific characteristics of the tasks to be developed. Based on this analysis, a 3D model of the maximum working time allowed as a function of indoor conditions in the hottest point and the number of air changes per hour was obtained, allowing to improve indoor conditions before the start of each working task.

As well as this, another 3D model which calculates the minimum time needed to be in the control engine room to release the cumulated heat as a function of the dry-bulb temperature was obtained, in order to optimize the set-point temperature of the engine control room.

Considering its versatility and efficiency, this methodology constitutes an excellent approach to optimize the ventilation system both in existing ships and during the design of new vessels. In this case, a previous 3D CFD simulation of the expected work conditions can be used to optimize both the layout of the engine room and the size and distribution of the ventilation system nozzles, contributing to the reduction of the total energy consumption, but always respecting the permissible limits.

Thanks

The authors wish to express their thanks to Altran Group, CYPE Ingenieros and Energetic Institute of Galicia (INEGA) for their collaboration and sponsor support of this research work.

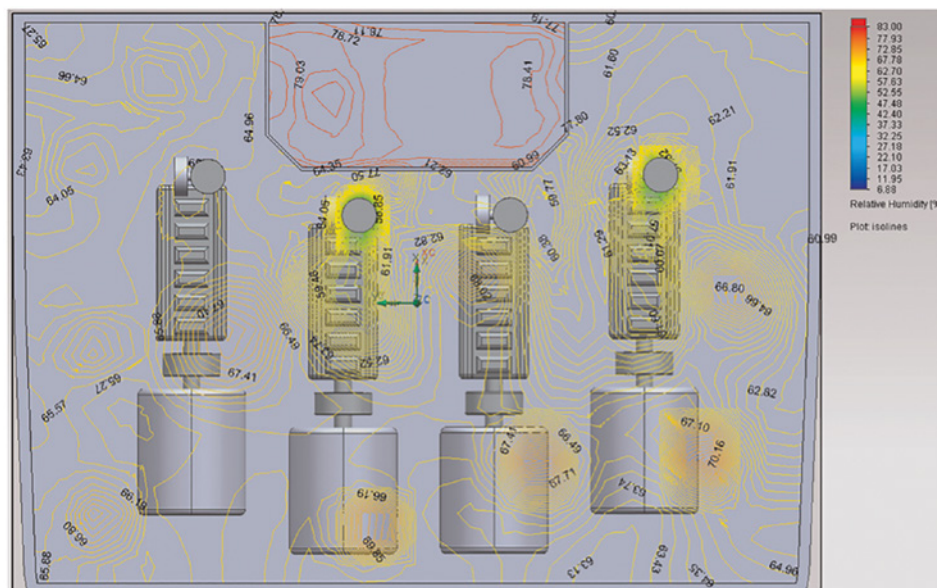


Figure 4. Relative humidity in the engine room (6 ACH)

Place	Air velocity (m/s)	Dry bulb temp. (°C)	Wet bulb temp. (°C)	Operative temp. (°C)	Relative humidity (%)	Maximum time (min)	Air changes (1/h)
Turbocharger	0.133	42.3	31.7	53.7	48.1	41.64	3
	0.137	38.1	33.4	51.7	63.7	46.60	6
	0.253	34.7	30.0	52.1	71.3	47.0	12
Workshop	0.114	35.1	29.0	36.4	64.3	312	3
	0.133	31.1	27.9	32.1	79.6	1367	6
	0.229	29.7	25.7	30.3	73.2	5485	12

Table 2. Maximum time in extreme working conditions during navigation (two engines working) (Weight 70 kg, increment of temp. = 1 °C, Met = 150 kcal/h, Clo = 1).

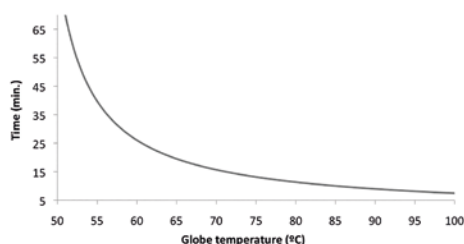


Figure 5. Maximum time near turbocharger (6 ACH).

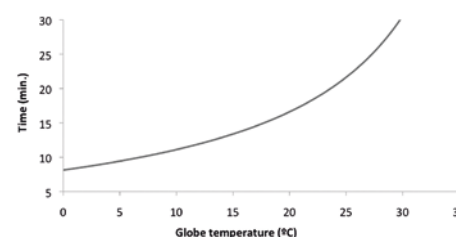


Figure 6. Minimum time in normal environment (control engine room) during navigation (Weight 70 kg, Increment of temp. = 1 °C, Met = 80 kcal/h, Clo = 1) and 6 ACH.

This article is a summary of the original paper: A new modeling procedure of the engine room ventilation system for work risk prevention and energy saving. José A Orosa, Ángel M Costa and José A Pérez. December 2016. Journal of Engineering for the Maritime Environment.

For a full list of references <http://journals.sagepub.com/doi/abs/10.1177/1475090216687148>



INTERVIEW

Takuya Shinoda, Denso, Japan

DENSO
Crafting the Core

Q. Tell our readers about Denso Corporation?

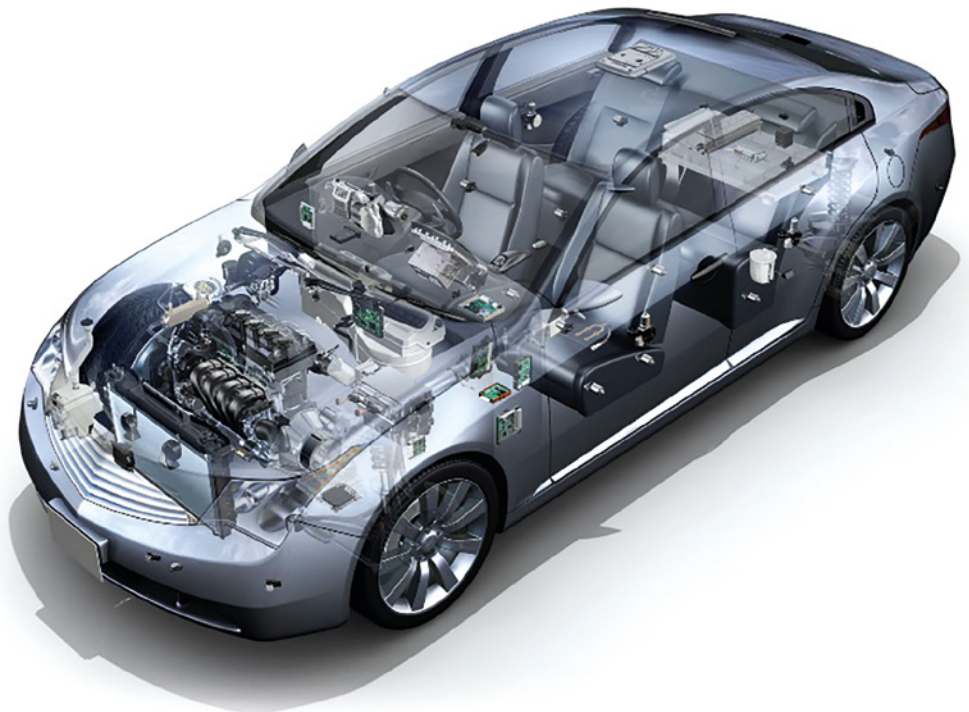
A. Denso is a supplier of advanced automotive technology, systems and components for automakers worldwide. We are headquartered in the city of Kariya, Aichi Prefecture, Japan and last fiscal year we turned over \$40Bn with approximately 150,000 employees globally. I work in R&D in the Substrate Hardware Development Department specializing in thermal analysis technology for next-generation Electronic Control Units (ECUs) development. I am therefore tasked with continuously improving our ECU thermal performance and seeking out size, weight, and cost reductions.

Q. What is your background and your current role as a thermal expert in Denso?

A. This year marks my 31st year inside Denso having joined as an Electronics Engineer in 1987. We use CFD analysis based techniques to improve our products performance - to make our ECUs more reliable, robust, cheap, safe and secure. In 2006 I decided to bring the FloTHERM CFD product from Mentor into our department in order to frontload the thermal design of ECUs. Frontloading CFD with FloTHERM makes our simulations faster and quicker than alternatives. By 2015 we had managed to compress our thermal verification cycles by 62%. Since then, this effort has led to a 78% cost reduction in designing ECUs over a 10 year period.

Q. What are the big trends in automotive ECUs today and in the foreseeable future?

A. We see an inexorable rise in ECUs inside cars now with most having 50-100 on board today. While electrification of vehicles (including EV/HEV) and the emergence of autonomous cars have a big impact on ECU design, we see motors and ECUs associated with those significant emerging



trends. Generally we observe that we need to take into account the wider ECU thermal environment in our design processes. I don't see liquid cooled ECUs as a feasible option as engine ECU in the near future because of reliability and cost issues. Smaller and smaller ECUs are coming and higher density of electronics in each ECU. We therefore need to gain deeper insight into components in these complex environments. On the other hand, there is also a need for combining the functions of multiple individual ECUs into a centralized ECU. However, these will have much more challenging thermal design factors to take into account. And a CPU with its higher clock frequencies than what's currently employed will require protection from electromagnetics for instance.

Q. What is your view of trends in thermal simulation & test for ECU design?

A. Now accurate CFD simulations are mission critical to realize frontloading design practice. At the same time, the actual measurement is becoming more important each year because the actual measurement helps us to reach the required accuracy. We bought our first T3Ster in 2012 so that we can use measured thermal data from the PCBs to improve our FloTHERM simulation results. We now have very high accuracy thermal predictions. Five years ago we were using FloTHERM for steady state thermal analysis. We also had to do transient thermal simulations to accurately measure Tj in car drive cycles (actual driving cycles). Therefore, it has become more important for

us to apply transient thermal measurement into actual measurement. Today, we use transient thermal simulation to analyse ECU thermal performance in accordance with car drive cycles. I view myself as a thermal analysis ‘frontloader’ who does CFD simulation with T3Ster data. T3Ster will be indispensable for creating an accurate FloTHERM analysis.

Q. What are your views on component verification in ECU thermal design?

A. Another challenge I see for assembly makers to frontload their ECU design simulation efforts is a lack of standardized analysis models. We are usually provided models and datasheets from IC makers when they supply us components. There is no standardization of such component models. IC thermal Resistance model (Rth Model) is standardized as DELPHI model based on JEDEC standard. To create a DELPHI model, IC manufacturers need to convert a thermal detail model into a thermal resistance network. However, there is no standard for detailed models. Thus, the accuracy of DELPHI model relies on each IC manufacturer. Also, there is no global standard for Rth-Cth models to be applied to transient thermal analysis.

Today Denso uses T3Ster to characterize IC components coming into Denso so we have accurate values of their thermal resistance and thermal capacitance. I think we should be able to be provided standardized IC thermal datasheets from manufacturers based on T3Ster-FloTHERM models in future.

Q. Tell us about the challenges in getting enough thermal analysis engineers?

A. As the demand for frontloading approach is growing inside Denso, we adopt the tools such as FloTHERM to do CFD simulation. However, a big challenge we and other companies are facing, is a shortage of thermal analysis engineers to use the tools we have. This is partly because thermal analysis of electronics at university is not part of the curriculum. This needs to be addressed collaboratively in future if the annual 20% growth in CFD is going to have enough practitioners of the discipline to satisfy demand from companies who need to use the tools.

By 2015 we had managed to compress our thermal verification cycles by 62%. Since then, this effort has led to a 78% cost reduction in designing ECUs over a 10 year period.

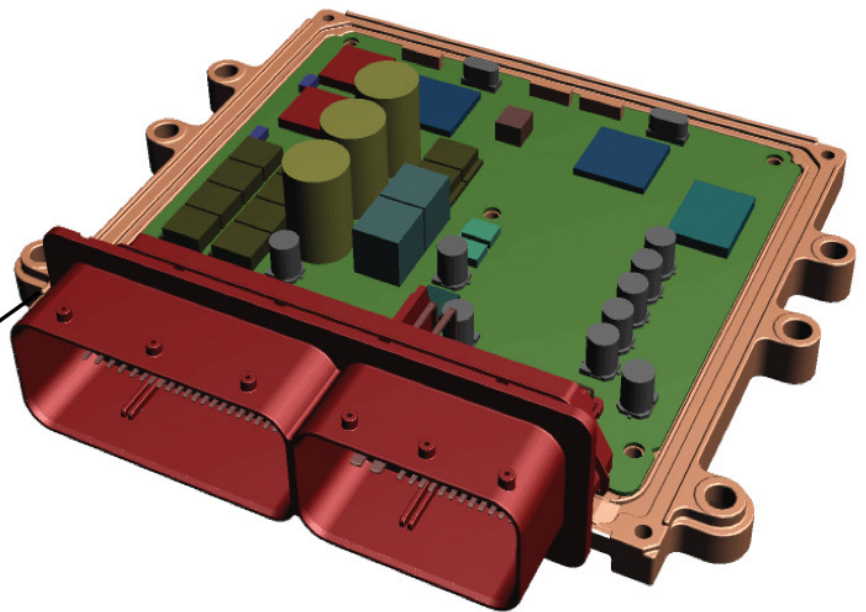
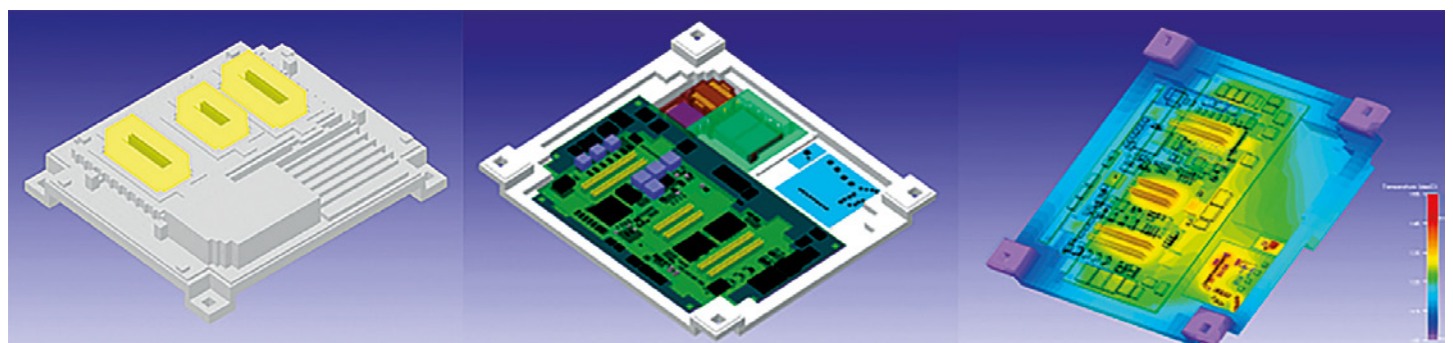


Figure 1. Typical Automotive Engine compartment and Denso ECU geometry



Three Thermal Simulation & Test Innovations for Electronics Equipment Design

By Takuya Shinoda, Denso Corporation, Japan



Over the last 50 years the automotive industry has been going through huge shifts in electrification (Figure 1). And, of course, we are seeing the electric motor starting to replace the mechanical engine with the advent of Electric & Hybrid Vehicles. Not surprisingly, the demand for ever higher density in a confined electronics, leads to a greater and greater need to resolve the resultant thermal issues.

Thermal simulation technology for automotive electronic equipment design is shifting from steady state to transient analysis. Here, I explain detailed Data Network Resistance Capacitance (DNRC) transient models, which are based on Mentor's T3Ster® tester data. In this article, three innovations to methods for creating DNRC models useful in electronics thermal design are outlined:

1. Placement of measurement locations in models so that the gap between actual measurement and analysis can be identified
2. Preliminary verification of component Tj (junction temperature) value by CFD thermal analysis
3. Creation of compact models from manufacturer datasheets and Tj calculations – what we call a DSRC, Datasheet Resistance Capacitance model.

If we consider a typical automotive engine control unit (ECU) in Figure 2; it can be noted that a typical engine underhood compartment in a car hits relatively high temperatures of approx. 105°C and since electronic parts typically have an upper practical operating limit of which threshold must not be surpassed otherwise electronic component quality cannot be guaranteed.

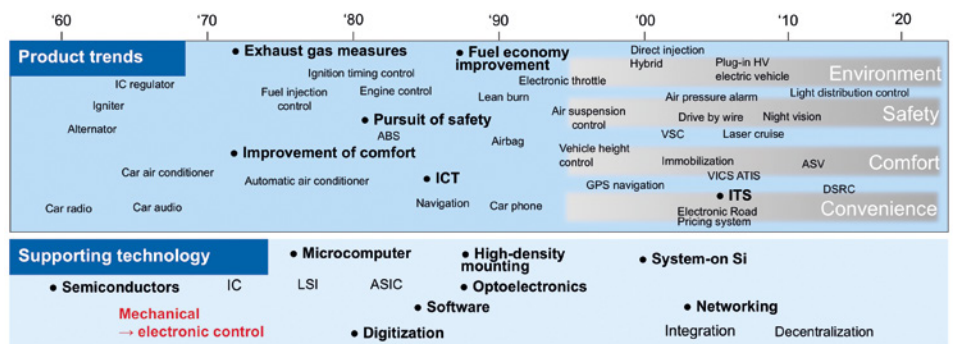


Figure 1. Progression of car electronics product adoption and underlying trend over the last 50 years

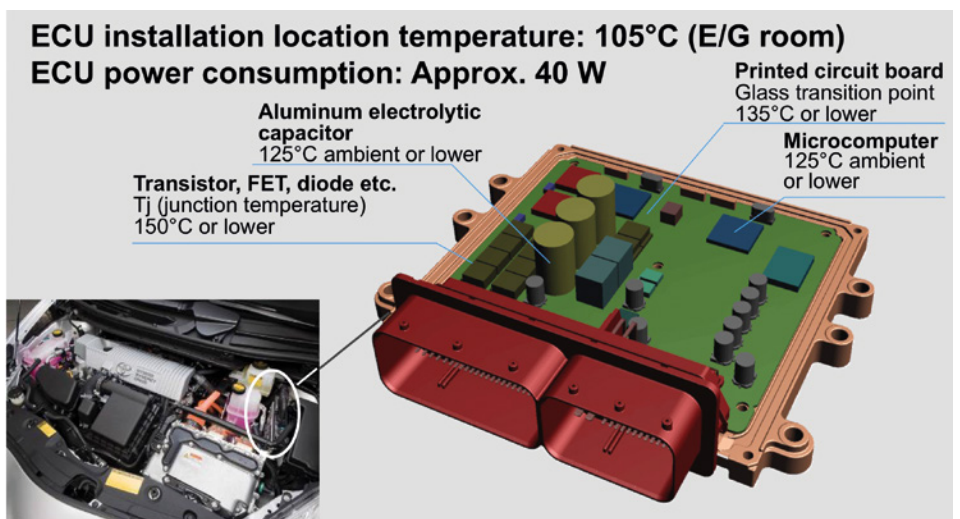


Figure 2. Typical ECU and engine use case and thermal limits

Moreover, we are seeing that with the advent of more vehicle electrification and with autonomous vehicles on the horizon (Figure 3), there is a need to thermally simulate transient heating effects in ECUs more and more, especially while the advent of Advanced Driver-Assistance Systems (ADAS) increases the number of high-frequency ECUs. Hence, it is necessary today to be able to estimate instantaneous heat generation inside ECUs. Transient thermal analysis needs by JEITA in 2013 were identified to be:

- Tj response during LED lighting operation,
- Instant transient analysis of Transistor, FET, IC and other semiconductors; with measurement of junction temperatures,
- Hot spots during SoC (System on Chip) operation,
- Tj response from engine OFF (dead soak), and
- Business need for the verification of accuracy between measurements and thermal analysis.

The target times for transient thermal analyses depends on whether we are dealing with a chip, a package or an assembly (like an ECU) as illustrated by Figure 4.

From the early days of the electronics cooling simulation market there has been some sort of approximation of chips and packages in terms of their thermal performance and the details inside the chip. DELPHI compact thermal models appeared in the 1990s and quickly became the standard way of modeling packages for CFD simulation that also allows for manufacturers to protect their intellectual property. However, the models do only satisfy transient analysis in terms of the accuracy, because the DELPHI compact thermal models are solely represented by thermal resistance values. Figure 5 depicts Denso's way of looking at all types of analysis models that could be employed to solve our thermal simulations. It is the DNRC and DSRC models that we want to investigate in this study because of their inherent high accuracy and ability to be distributed into the semiconductor supply chain. Based on non-destructive electronics thermal transient testing methodology, DNRC is modeled by 'structure functions, featured by Mentor T3Ster tester (Reference 1). While the form of DSRC is the same as that of DNRC, DSRC model is based on the transient response values in IC component datasheet.

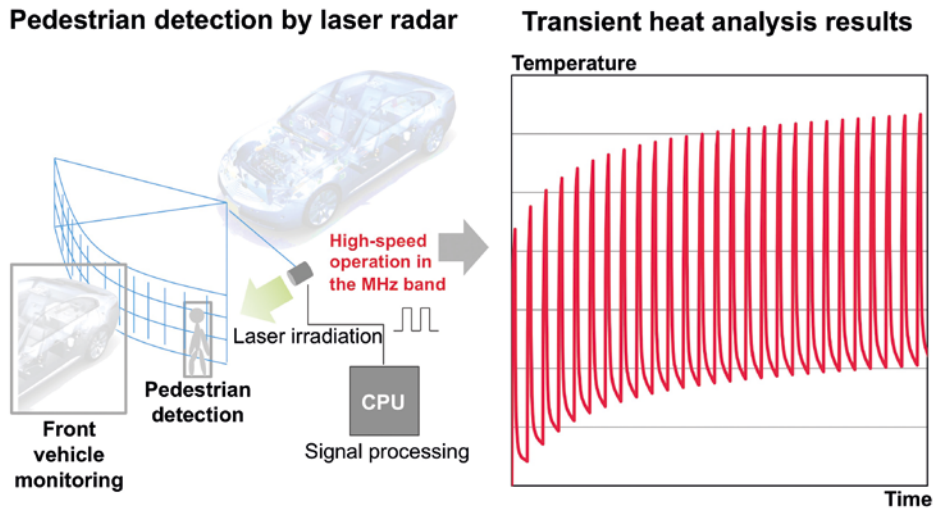


Figure 3. Escalation of transient heat issues with ADAS technology

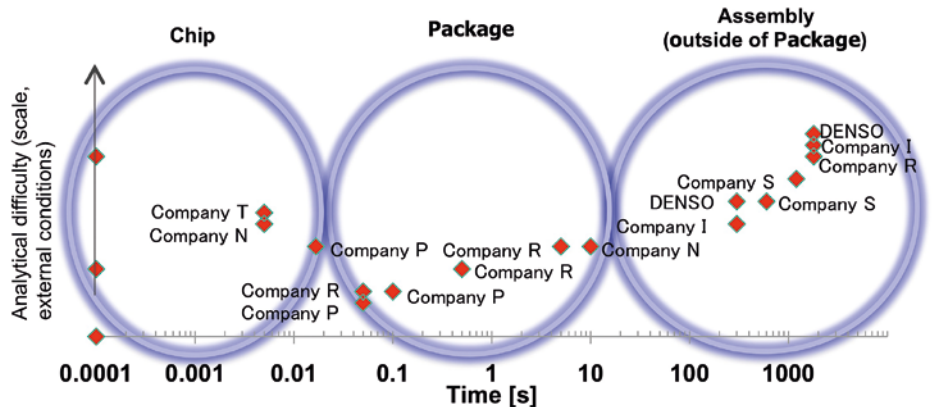


Figure 4. Target time for transient thermal analysis for Chips to Assemblies

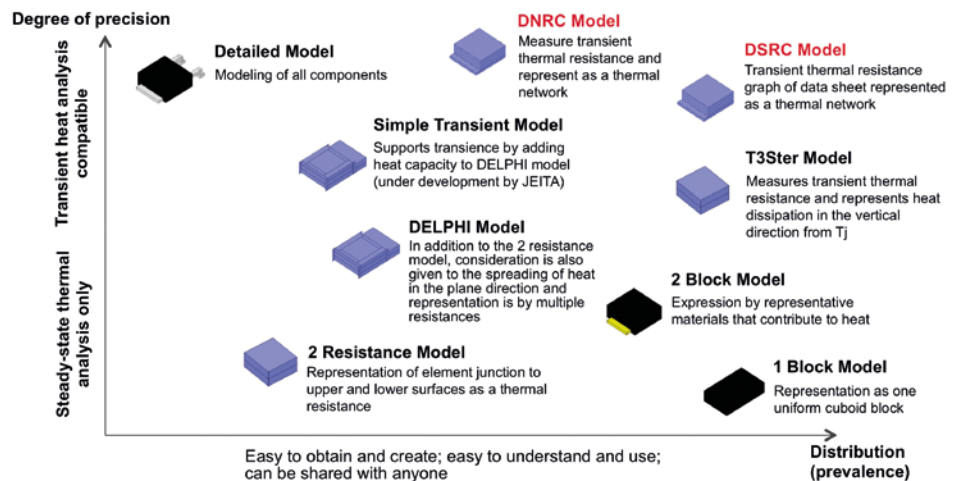


Figure 5. Development of package element models that meet ECU transient thermal analysis needs

This article is not going to go into the details of the T3Ster RC approach for measuring electronic element constituent performance, and how it connects to CFD simulation thermal analysis tools like FloTHERM – see Reference 2 for further details. However, an outline thermal simulation & test workflow is shown in Figure 6 that results in a useful

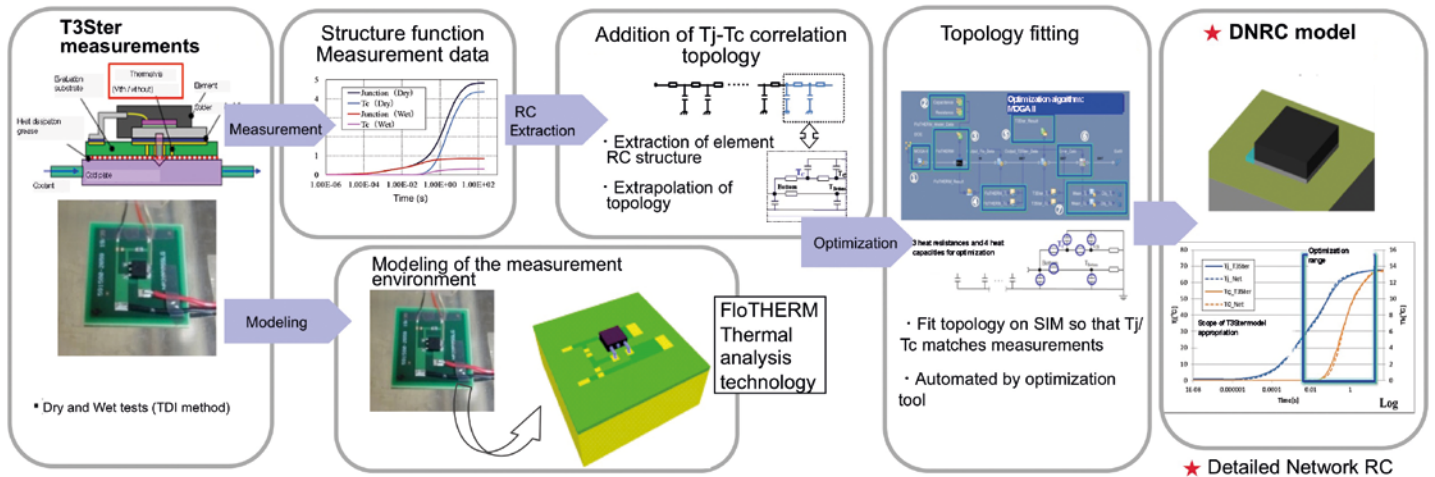


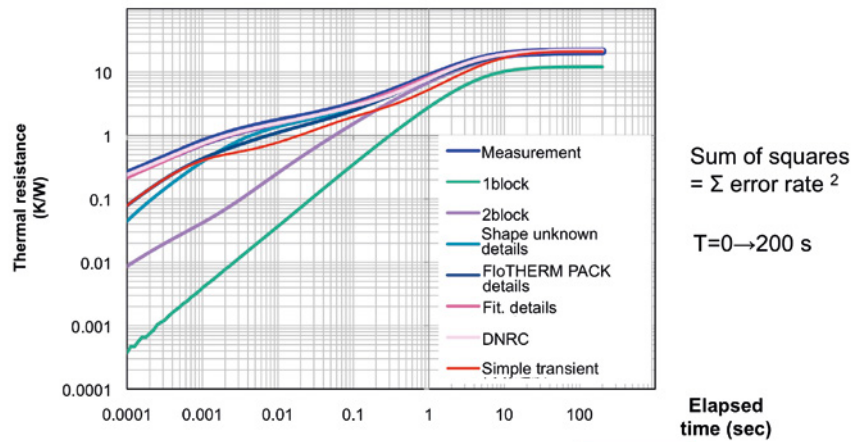
Figure 6. Outline of RC model creation process for a DNRC model by T3Ster measurements & FloTHERM simulations

DNRC model. Here, I emphasize two advantages as below.

- The approach allows for reference point thermal measurement of components in their mounted state on a PCB
- The measured data can be fed into CFD simulation software such as FloTHERM™

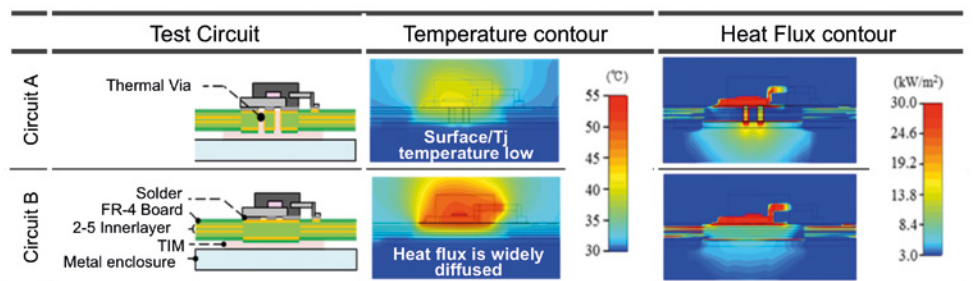
Indeed, the beauty of this approach is that it is possible to create a model even if information such as internal dimensions, specific heat, performance etc. of the component is not readily available. The final DNRC is very high precision, because the model is derived by measuring the thermal resistance and thermal capacitance values. Moreover, because DNRC is a thermal network model and has the Tc node existing for verification by measurement with a thermocouple, the values of the model can be compared with the actual temperature measured at Tc for reconciliation. Crucially, this modeling approach can be used by a component manufacturer who does not know the internals of the elements involved. We have completed a validation study (Figure 7) for a typical electronics component package and heatsink array which calculated the relative accuracy of the different types of models outlined in Figure 5. Using the ‘Sum of Squares’ error estimation method it can be seen that the most accurate approach (the lowest number in the table) is the DNRC approach.

If we now apply this approach to the measurement of transient thermal resistance of a PCB, it is then desirable to measure both the semiconductor component and the PCB simultaneously. We did this with an experiment involving two test circuits with different thermal resistance and



1block	2block	Shape unknown details	FloTHERM PACK details	Fit. details	DNRC	Simple transient
121.0	86.2	49.0	41.5	12.7	0.3	50.3

Figure 7. Results of element model accuracy verification Predictions versus Measurements



The calculation of element Tj depends on the thermal resistance of the substrate
 Necessary to accurately ascertain the substrate and casing thermal resistance
 Changes in thermal resistance due to thickness of substrate copper foil, thermal via and TIM

Implementation environment model required in addition to element model

Figure 8. FloTHERM simulation verification of element temperature and heat flux distribution for a circuit with and without a thermal via

capacitance values – one with a through silicon via and one without (Figure 8). The choice of the through Si via meant that the thermal resistance of the PCB without it is overwhelmingly higher than that of the element as a whole – the element being 3K/W with the substrate at 10-20 K/W. Hence, these simulations prove that an environment model in which the element model is located matters and is required for accurate results. There needs to be measurements with T3Ster of the transient thermal resistance of the element in mounted state on the PCB so as to produce thermal resistances equivalent to those in the actual product. This can be seen in Figure 9 where T3Ster confirms the thermal resistance at each point of the two circuits with and without vias being considered in the study. We even examined slight knicks (cracks) in the two structures and saw that structure functions of inside and outside the semiconductor could be discerned correctly.

If we use T3Ster measurement result to calibrate a detailed thermal model for FloTHERM, we devised a seven step workflow process (Figure 10) to accurately obtain the physical property values of any PCB. It involves using FloTHERM coupled with powerful design space optimization tools in order to search for the optimal solution to curve fit onto the actual T3Ster measurements. This in turn reveals accurate physical property values in terms of the thermal conductivity and specific heat of the actual substrate layers. This data can then be used as shown in Figure 11 to evaluate the two circuits we described earlier. And we were able to simulate 1,000 designs in FloTHERM and fit the results to the structure functions under actual measurement. However, the thermal conductivity in copper foil shows 485W/mk, which is not a realistic value, assuming the thermal conductivity for pure copper is as low as 398w/mk. Finally, we were able to do microscopic cross-section measurements (Figure 12) of the PCB substrate with different layers of copper foil thicknesses as a cross-validation of this T3Ster and FloTHERM approach. It revealed that the copper foil is 1.3 times thicker than the design data. When it is converted to the thermal conductivity, it becomes 1.3 times. We got remarkably good agreement and it shows our approach is valid.

The biggest issue facing manufacturers and assembly makers is in measuring actual Tj values (Figure 13). Device manufacturers usually guarantee their electronic components to less than 150°C but how

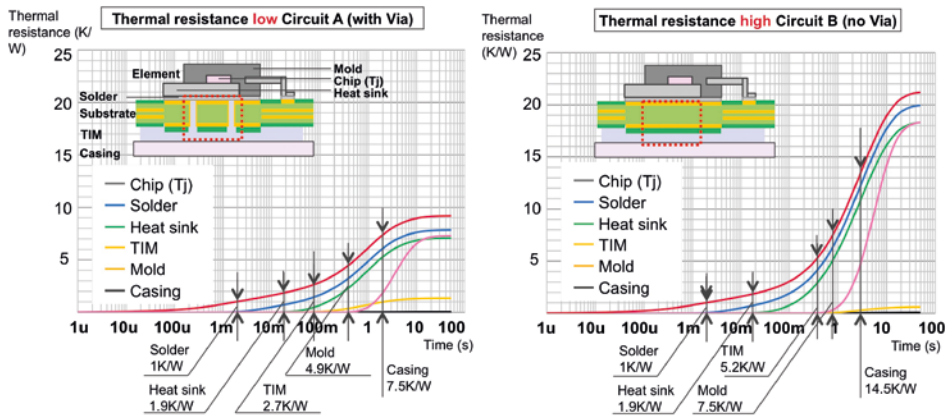
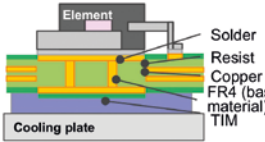
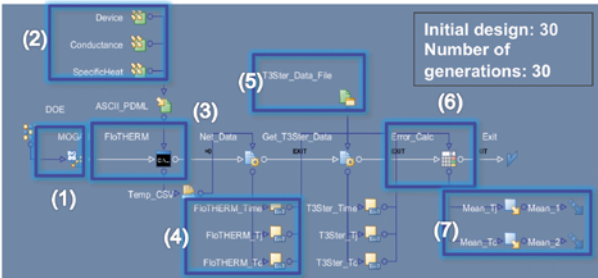


Figure 9. Temperature rise start time and thermal resistance of component for a circuit with and without a thermal via using T3Ster

Optimization process for physical property values

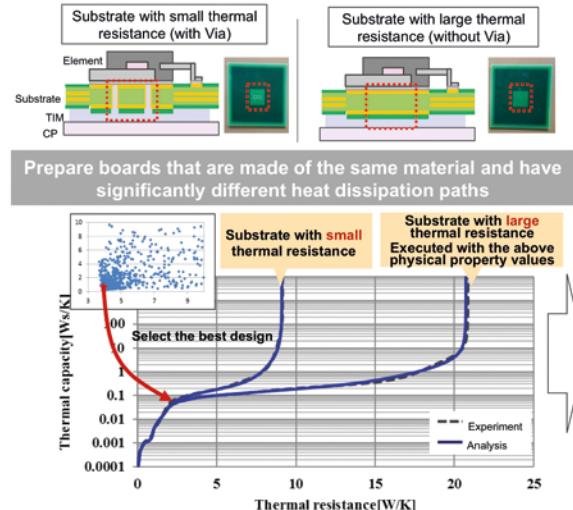
- (1) Set optimization algorithm
Number of designs: 30 Algorithm: MOGA2, 30 generations
- (2) Input variables
Thermophysical property values of substrate member (5 heat conductivity and 5 specific heat for each of 5 members)
- (3) Execute analysis according to input variables
Batch execution of FloTHERM
- (4) Extract analysis results
Output Tj and Tc from analysis results
- (5) Read T3Ster measurement data
Data for comparing results
- (6) Compare results
Calculate absolute error between CFD analysis and T3Ster data
- (7) Objective function
Minimize absolute error of ΔTj and ΔTc ms area: 5%, s area: 1%

Objective: Minimize ΔTj and ΔTc in the entire time range of measurement - SIM



		Min	Max	Theoretical value
Heat capacity Cp Ws/K	B	0.0001	0.1	-
	T _B	0.0001	0.5	0.01
	T _C	0.0001	1	0.01
	T _{CB}	0.0001	1	0.01
Thermal resistance Rth K/W	(Top)	0.001	5	0.05
	B-T _B	0.01	1	0.2
	B-T _C	0.1	100	4
	T _C -T _{CB}	0.1	100	0.5
	(B-Top)	0.1	300	120

Figure 10. Method of determining physical property values of printed circuit boards (PCBs) using FloTHERM and T3Ster



Finally adopted optimal solution

1000 designs

Parameters	Typical	Optimal solution	
Thermal conductivity [W/m·K]	Solder	55	58
	Copper foil	385	485
	Resist	0.2	0.27
	FR4 surface direction		0.36
	FR4 thickness direction	0.63	0.31
Specific heat capacity [J/kg·K]	Solder	255	381
	Copper foil	385	577
	Resist	1100	961
	FR4	900	886
	Gel	700	894

Figure 11. Optimal circuit thermal solution selected from multiple designs

to measure T_j accurately and how to see instantaneous changes in temperature as the device operates? Usually the T_j can be measured by a thermocouple and derived from an electric power waveform analysis and transient thermal graph in datasheet (Figure 13).

If we look at our first proposed innovation, that is, the temperature of the part for coupling with thermal analysis is known. Figure 14 shows this for T_c and T_j values with the various model types outlined in Figure 5. With detailed model and DNRC model, the T_c node enables a comparison with experimental results to ascertain the error of the CFD thermal analysis.

Our second innovation, preliminary verification of the T_j value by FloTHERM thermal analysis is shown in Figure 15. It can be seen that only a detailed DNRC model with a T_c node derived from FloTHERM and T3Ster works well and internal package information is simulated accurately such that a transient T_j and T_c can be estimated in a short period of time.

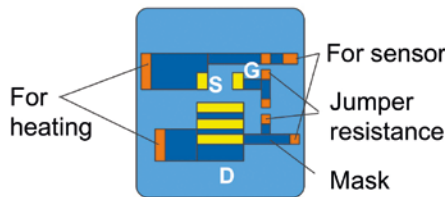
Our third innovation is that it is now possible to create models based on manufacturer's datasheets and calculate actual T_j values. This is shown in Figure 16 where it can be seen that a DNRC model captures the actual transient thermal resistance in the component's mounted state thus leading to an ultra-high precision model that conforms to actual operating conditions. On the other hand, a DSRC model is based on a transient thermal resistance graph. Hence, the value in the datasheet and the DSRC model based on the datasheet are both guaranteed by the manufacturer. Table 1 shows a relative comparison between the recommended usage of DRNC and DSRC models. As noted in the table, a DSRC approach is a great bridge between analysis models and component manufacturer's guaranteed property values in their datasheet. Moreover, as the DSRC matches the manufacturer's datasheet value, it can be guaranteed for product design. If the data applicable in product design can be converted into a model for analysis, both component manufacturer and assembly maker can easily exchange the models, hence both welcome the approach. Another benefit to this approach is relatively lower costs compared with other measurement techniques that have high measurement and labor costs.

Finally, we carried out a validation test in a standard transient thermal analysis JEDEC still air chamber of a component on a PCB

Substrate configuration

6 layer penetration (newFR4 t1.2)
 40*40 Inner layer residual copper ratio 80% solid
 Wiring: 4 terminal method
 Wiring: Short circuit possible between D - G and G - S
 Outer layer pattern 18 + 25 μ m
 Inner layer pattern 35 μ m
 AW shape on the reverse is \square 10 in center of the thermal via

Substrate layout



Optimal solution

Material	Thermal conductivity [W/m·K]		Specific heat capacity [J/kg·K]	
	General value	Optimal solution	General value	Optimal solution
Solder	55	58	255	381
Copper foil	361	485	385	577
Resist		Approx. x 1.3		Approx. x 1.5
FR4	0.63	0.36	900	886
Gel	3.1	4.11	700	894

Microscope cross section measurement

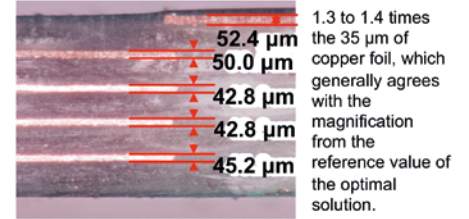


Figure 12. Validation of optimal solution with a structural survey of real substrate samples

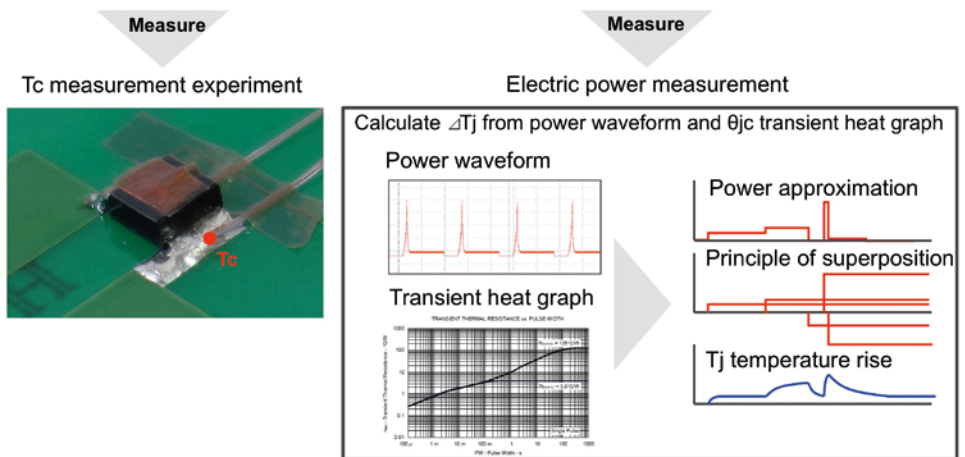


Figure 13. Issues in finding T_j by thermal design for a circuit

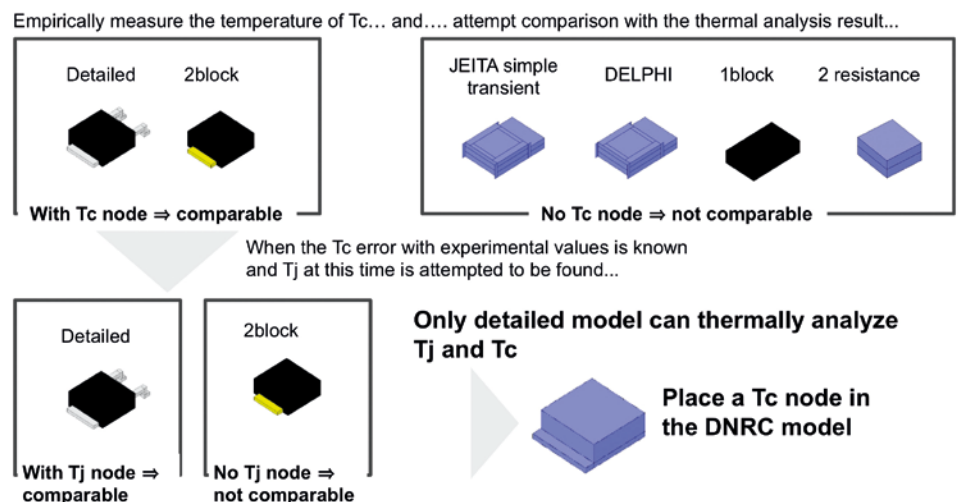


Figure 14. Innovation 1 - Temperature of the part for coupling with CFD analysis is known

	DNRC model	DSRC model
Design phase of model use	Verification of prototype	Concept only
Product status	Actual product assembly	Evaluation environment defined b standards
Transient thermal resistance	Measurement	Manufacturer's guaranteed datasheet value

This is important

Table 1. Comparison of DNRC models and DSRC models for thermal analysis

(see Figure 17) and compared it with the T3Ster and FloTHERM approach outlined above. Error rates were very low and good agreement in the DSRC models to the manufacturer's datasheet values were observed. Hence, DSRC model creation based on manufacturer's datasheet is possible and improved accuracy can be achieved by these in-built substrate models.

Summary

We have shown that by using a coupling of Mentor's T3Ster transient thermal testing hardware and FloTHERM thermal analysis CFD software it is possible to measure thermal resistance of PCBs accurately and to create thermal simulation models of semiconductor component by using DNRC models for unsteady state analysis. The DNRC modeling approach outlined here allows for the calculation of Tj values with a high level of accuracy in the CFD analysis technology. Comparative verification with measurements by Tc nodes are shown to be possible such that the approach is useful for verification experiments. Furthermore, DSRC based on datasheet value can be used for thermal design according to the manufacturer's datasheet values.

References

- [1] Rencz, M. & Székely, V., "Measuring partial thermal resistances in a heatflow path". IEEE TRANSACTIONS ON COMPONENTS AND PACKAGING. 25 (4): 547-553, 2002.
- [2] Bornoff, R. & Vass-Varnai, A., "A detailed IC package numerical model calibration methodology", 29th SEMI-THERM Conference, pp.65-70, 2013.

Transient thermal analysis of Tj by inputting MOS operation waveform into DNRC model

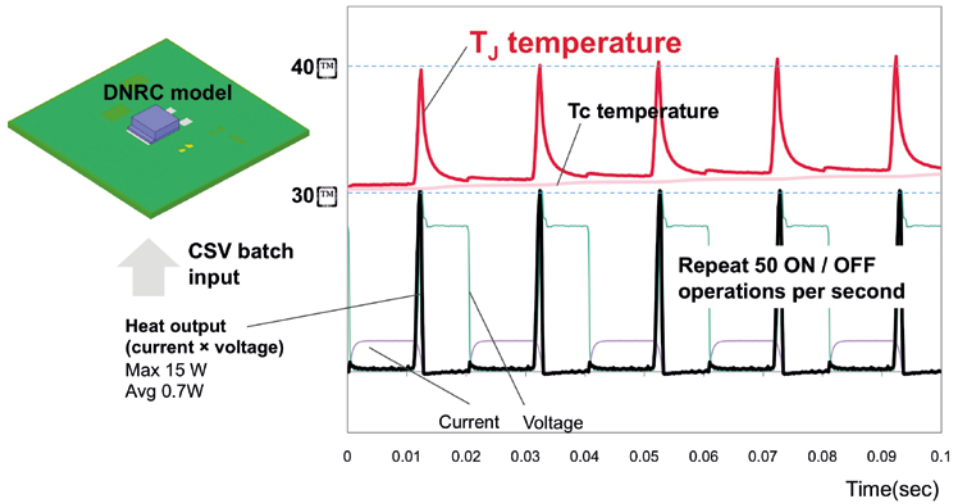


Figure 15. Innovation 2 - Preliminary verification of Tj value possible by FloTHERM thermal analysis

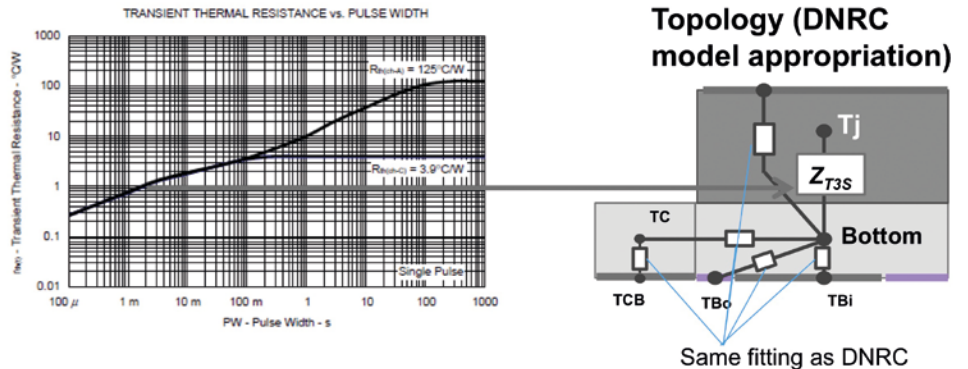


Figure 16. Innovation 3 - Possible creation of models from manufacturer datasheets and calculate Tj

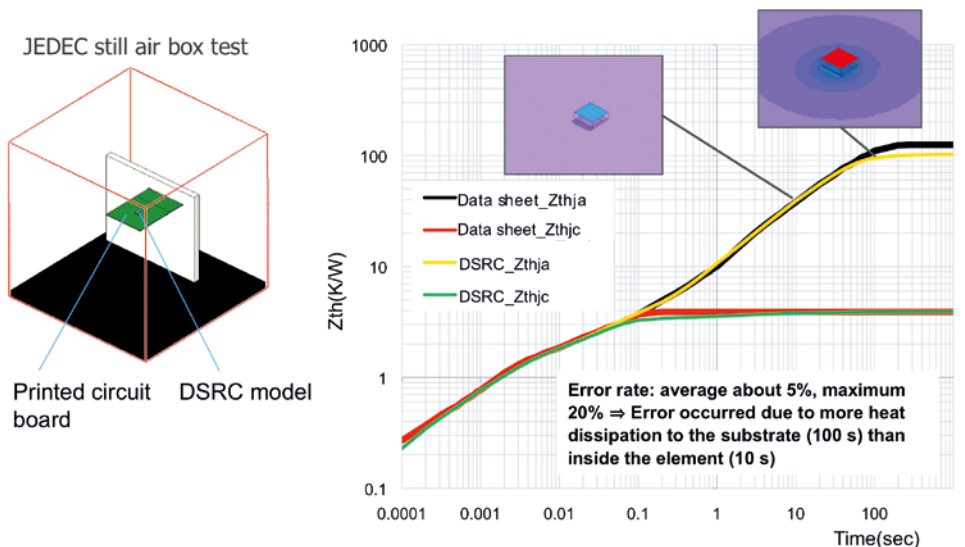


Figure 17. Experimental Validation - Transient thermal analysis in JEDEC environment according to the measurement environment of a component's datasheet value

Series Car Brake Cooling

Test drives and simulating with FloEFD

By Marina Kesjic, Master of Science (M. Sc.), Technische Hochschule Mittelhessen

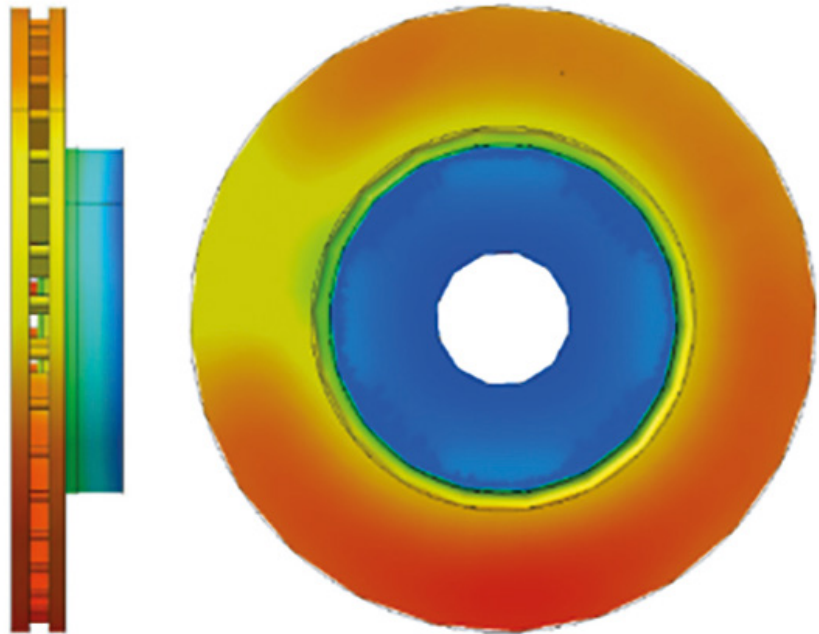
Continental 



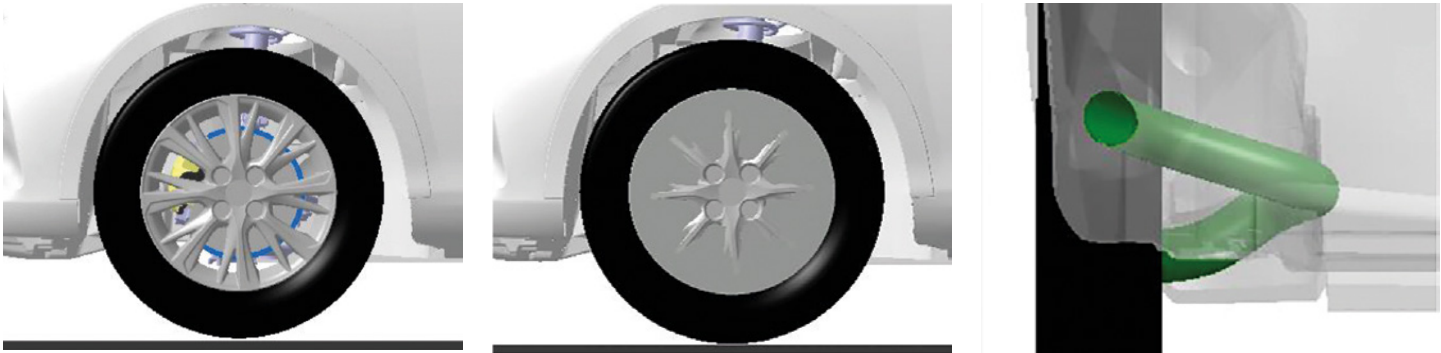
Passenger car brakes are components under high thermal loads. Good ventilation of the brake components and achieving adequate cooling behavior are therefore crucial. The thermal design of the braking system plays a significant role when considering the reliability of braking performance. The directed airflow into the wheelhouse can be in conflict with the aerodynamics of the entire vehicle.

During braking, kinetic energy is converted into heat by means of friction. The brake disc absorbs approximately 90% while the brake linings absorb approximately 10% of this heat. The brake components must be able to resist these high thermal loads in order to ensure consistent reliable performance of the brake. The heat absorbed mainly by the brake disc and brake linings is then dissipated by convection, heat conduction and radiation to the ambient air and the surrounding components such as brake caliper, rim, and wheel carrier.

Driving tests and CFD simulations with FloEFD™ embedded in CatiaV5 were carried out for six design variants, examining the influence on the cooling behavior of the brake disc. The intention of the study was to show the ability of CFD simulation to efficiently evaluate the brake cooling conditions for different configurations based on a phenomenological approach, under consideration that by the use of Computational Fluid Dynamics (CFD) simulations, the sources of possible functional impairments can be identified, evaluated and eliminated early in the vehicle and brake system development. Target for brake system development is that the simulation approach needs to be pragmatic, because of the early stage of car development. One goal was to determine which configurations have the greatest influence on the brake disc cooling capacity and how they affect the flow profile in the wheel housing.

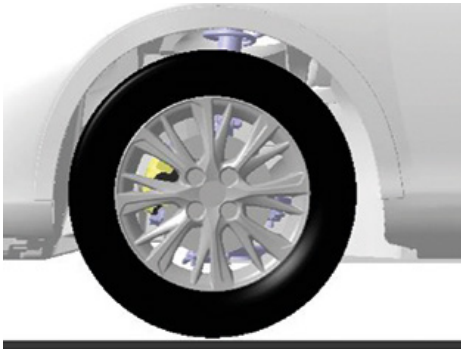
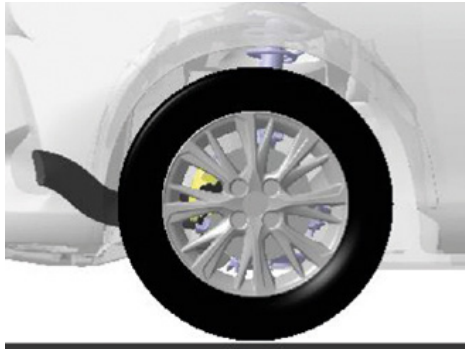


The basic design, variant one, is shown in Figure 1, top left. Variant two was created to clarify the difference between an opened ventilation through the rim and a closed rim. For variant three, an air supply with a tube was installed at the closed rim. For this purpose, an aluminum flex hose with a diameter of 80 mm was installed through the wheel housing directly to the brake disc. For the fourth variant, the open rim was equipped with the hose for an additional air supply. In variant five, the splash shield behind the brake disc (see blue plate in variant one) was completely removed to



examine the cooling process without splash shield. The air supply through the hose was thereby maintained. In the sixth variant, the hose and the splash shield were removed. In comparison to the basic version, the influence of the splash shield on the brake disc cooling performance can be assessed by this configuration.

The test drives were carried out on the Continental test track. The brake disc was heated up to 400°C on the test track with dragging brakes while towing the car. After reaching the target temperature, the temperature level was held by dragging the brakes for another few minutes until the start of the cooling phase to obtain an evenly heated brake disc. The cooling process was started afterwards. For this purpose, the vehicle was driven at a constant speed of 50km/h. The cooling phase was carried out until the brake disc temperature reached 200°C. The temperature of the brake disc was measured at the friction ring. The ambient temperature was in the range of 21 to 26°C.



Variant	Title
V01	Basic Design
V02	Closed Rim
V03	Closed Rim + Hose
V04	Hose
V05	Without Splash Shield + Hose
V06	Without Splash Shield

Figure 1. Six variants

The evaluation of the driving tests showed that variant two produced the worst conditions for the brake disc cooling, which was expected. Variant five showed the best cooling behavior.

In the simulation, the brake cooling was analyzed for a constant speed of 50 km/h, at an ambient temperature of 23°C, with a uniform initial brake disc temperature of 400°C. The physical time period of the simulation was 200 seconds and 300 seconds respectively, depending on the variant.

The basic design model consists of the following parts: Car body, brake disc, caliper, splash shield, wheel bearing, axle, tire, rim, and road. Wheel, rim and wheel housing are particularly important as they have a high influence on the flow field and thus on the cooling behavior of the brake. In the simulation, a quarter of a section

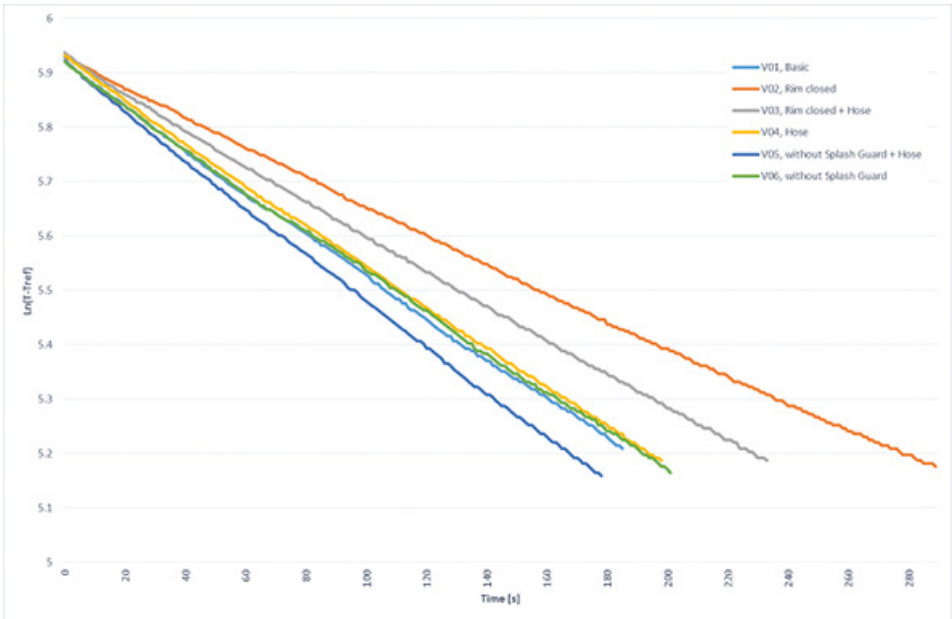


Figure 2. Results test drive

of the vehicle was examined, focusing on the brake disc and the wheel housing. The FloEFD project was defined as an external flow domain, so that the local flow field in the observation area can be well represented.

The “sliding” rotation approach was used for local regions. This multi-zone model of rotation allows for the simulation of cases where the flow field is transient and highly non-uniform around the rotating part. In the local rotating zone the calculation is performed in the local rotating reference frame, whose boundary slides along the static zone’s boundary and the information are exchanged at each time step. The rotating region is shown in Figure 5 and it was defined with an angular speed of 7.12 Hz, which corresponds to a vehicle speed of 50km/h, with a wheel radius of 0.31m. The car body, the road and the tire were defined as thermal insulators, because the thermal influence was considered as negligible in this study. The flow rate for the additional air supply was defined as 0.022m³/s at the beginning of the hose, resulting from a further simulation for an external flow with 50km/h.

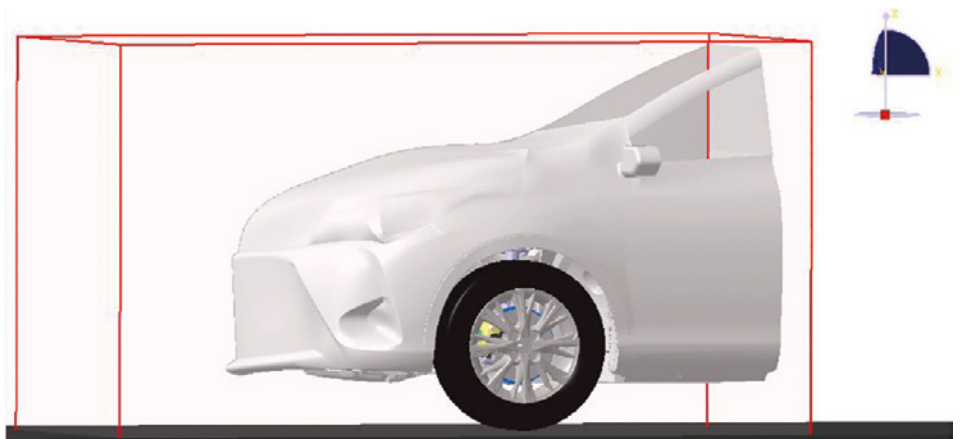


Figure 3. Computational domain for the simulation

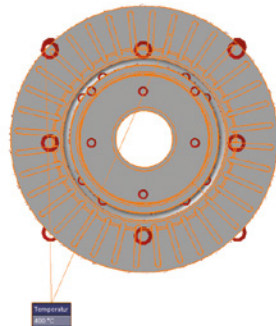


Figure 4. Initial temperature, brake disc

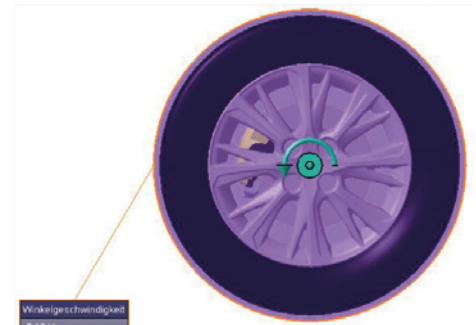


Figure 5. Rotation region

The influence of the radiation was estimated in additional analytical calculations and simulations. These investigations demonstrated consistent results that heat conduction and convection have the biggest influence on the cooling performance for this simulation case with the existing temperatures. Therefore, the radiation was neglected for the simulation and none of the available FloEFD radiation models was applied.



Figure 6 a+b. Additional air supply

The channels in the brake disc, the gap between wheel and car body and the openings in the rim are particularly important. For this reason, a local mesh refinement was defined for these areas, as well as for the area of the additional air supply in the variants three, four, and five.

The automatic simulation time was approximately eight hours, for the transient calculation of 300 physical seconds.

The comparison between the test results and the FloEFD simulations showed a good correlation, for the six investigated variants. Only variant five shows visible deviation, which can be explained by a geometrical deviation of the applied flex hose compared to the simulation model. The outlet of the hose was on a different axial position, caused by the fact that there is no overlapping the rotational domain. In the test

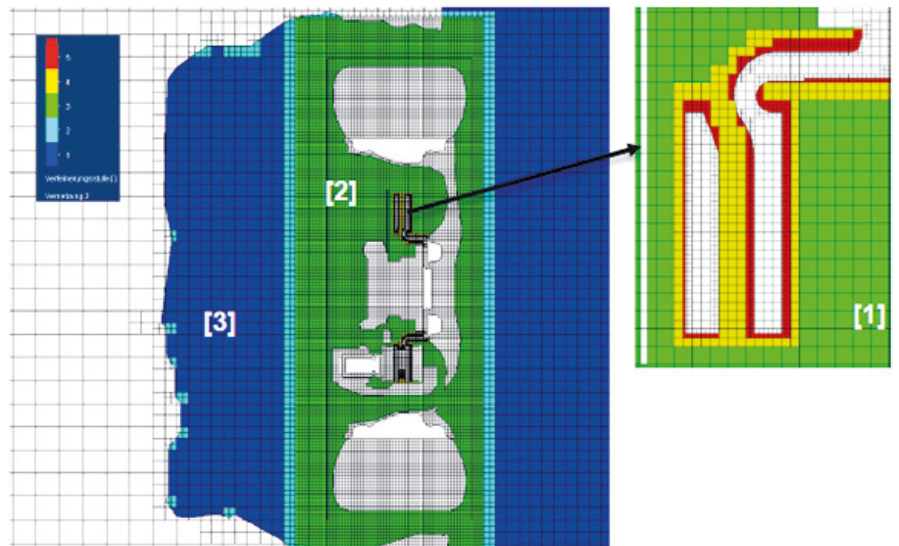


Abbildung 24: Schnittdarstellung – Vernetzung im Radkasten

Figure 7. Cut plots of the mesh in the wheel house

configuration, the outlet was much closer to the disc than in simulation, which explains the better cooling performance. A main advantage of a CAD embedded simulation is that, in addition to providing additional numerical results, it also enables graphical visualization of the interested parameters at any position directly in the CAD model, for velocity or pressure conditions for example.

The comparisons in Figure 12 show variant one (base), variant two (closed rim, worst case) and variant five (splash shield removed, but with hose for additional air supply), after 150 seconds each.

The figures show that in variant one the airflows from the inside outwards, i.e. the flow runs from the wheel house outwards into the rim and gets swirled in front of the brake disc. There are barely any areas without air movement. With variant two, the closed rim avoids air exchange and areas with very low air velocities (approximately 0km/h) can be identified. Variant five generates a very turbulent flow profile with partially higher velocities, but also shows areas with very low air velocities.

For variant one, the velocity in the cooling channels is higher than for variants two and five.

After 150 seconds, the brake disc in variant two had a maximum temperature of 278°C. For variant one, this was 241°C and variant five, with the best cooling conditions, at 233°C.

The closed rim clearly had the strongest influence on the cooling behavior of the brake disc. The test results showed that variant five, the brake disc had the fastest cooling down to the target temperature of 200°C. With this variant, the best conditions for cooling were given. The rim was open, an additional air supply through a hose was provided, and the splash shield was removed. Variant two, on the other hand, took the longest with 296 seconds. Due to the closed rim, this variant did not provide good conditions for the cooling behavior. A closed rim reduces the cooling of the brake disc by approximately 30% compared to the basic version. The removal of the splash shield and the installation of the hose does not improve the cooling behavior individually. The hose position must be selected in such a way that the additionally injected air flow supports or enhances the already existing flow in the wheel arch. In that case, variant four (with hose) would also achieve even better cooling characteristics.

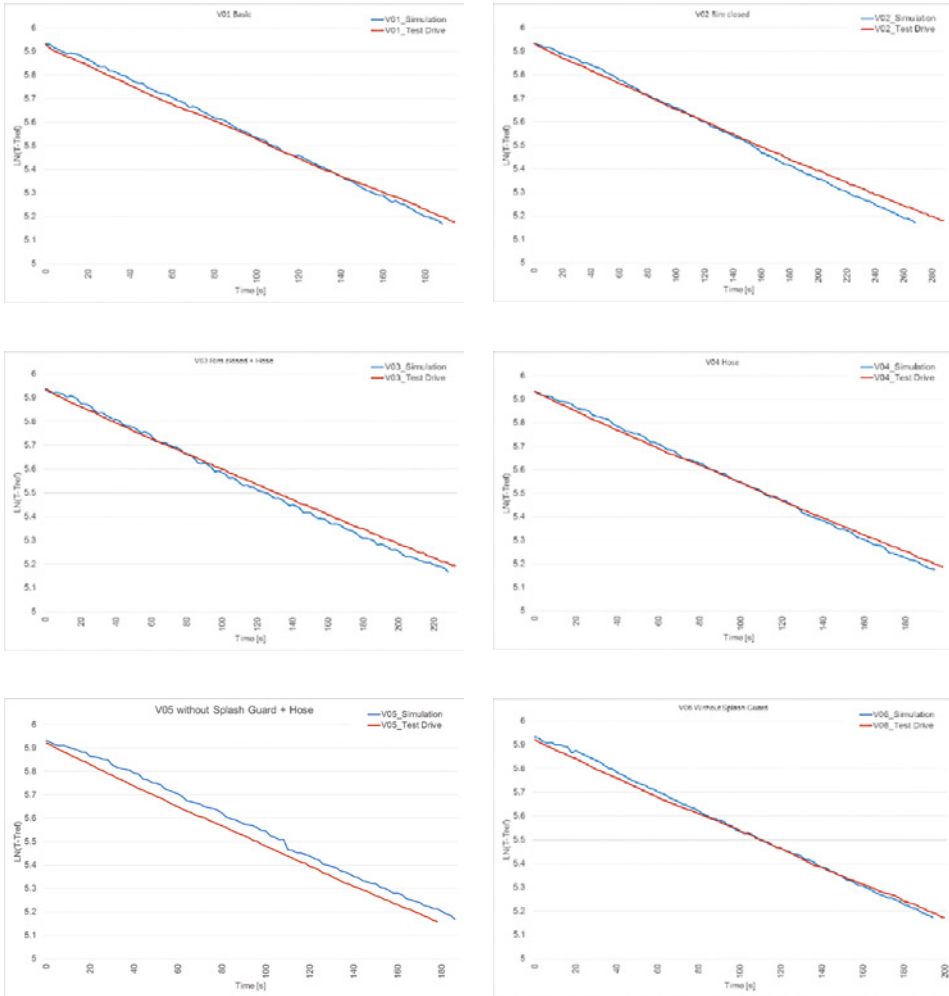


Figure 8. Comparison test drive and FloEFD Simulation

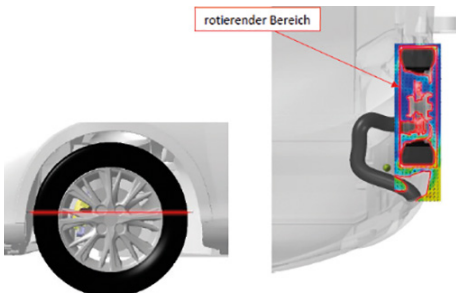


Figure 9. Section XY

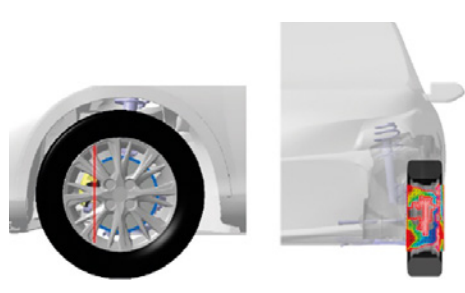


Figure 10. Section YZ

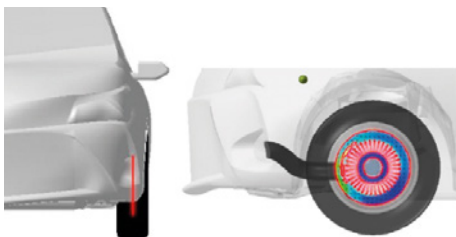


Figure 11. Section XZ

FloEFD provided a quick and easy introduction into flow analysis, due to the easy-to-use and engineering focused user interface. Good results are provided within short calculation times.

Marina Kesjic, Master of Science (M. Sc.), Technische Hochschule Mittelhessen

In variant five, where both (splash shield and hose) were carried out, the cooling performance of the brake disc improved by 10.2%.

The FloEFD simulations illustrated the flow behavior in the wheel house and led to a better understanding of the cooling behavior. The comparison with the test results showed a convincing agreement. The simulation also allows for the evaluation of further concepts and a directed airflow into the entire wheel house, taking into account the overall vehicle aerodynamics. Future optimizations may include, for example, the position of the air supply hose and the design of the splash shield in order to better support the natural airflow in the wheel house.

The investigation with FloEFD showed the ability to identify the drivers of the cooling behavior. To make a final rating the investigation on constant speed needs to be extended from steady state condition to unsteady condition on different speed levels.

References:

- [1] Simulation der Luftströmung im Radkasten eines PKW zur Untersuchung des Abkühlverhaltens von Radbremsenkomponenten“, Marina Kesjic, Masterthesis Master of Science (M. Sc.), Technische Hochschule Mittelhessen, Friedberg 2017-10-30:
- [2] <https://www.continental-automotive.com/en-gl/Passenger-Cars/Chassis-Safety/Brakes/Hydraulic-Brakes/Foundation-Brakes>

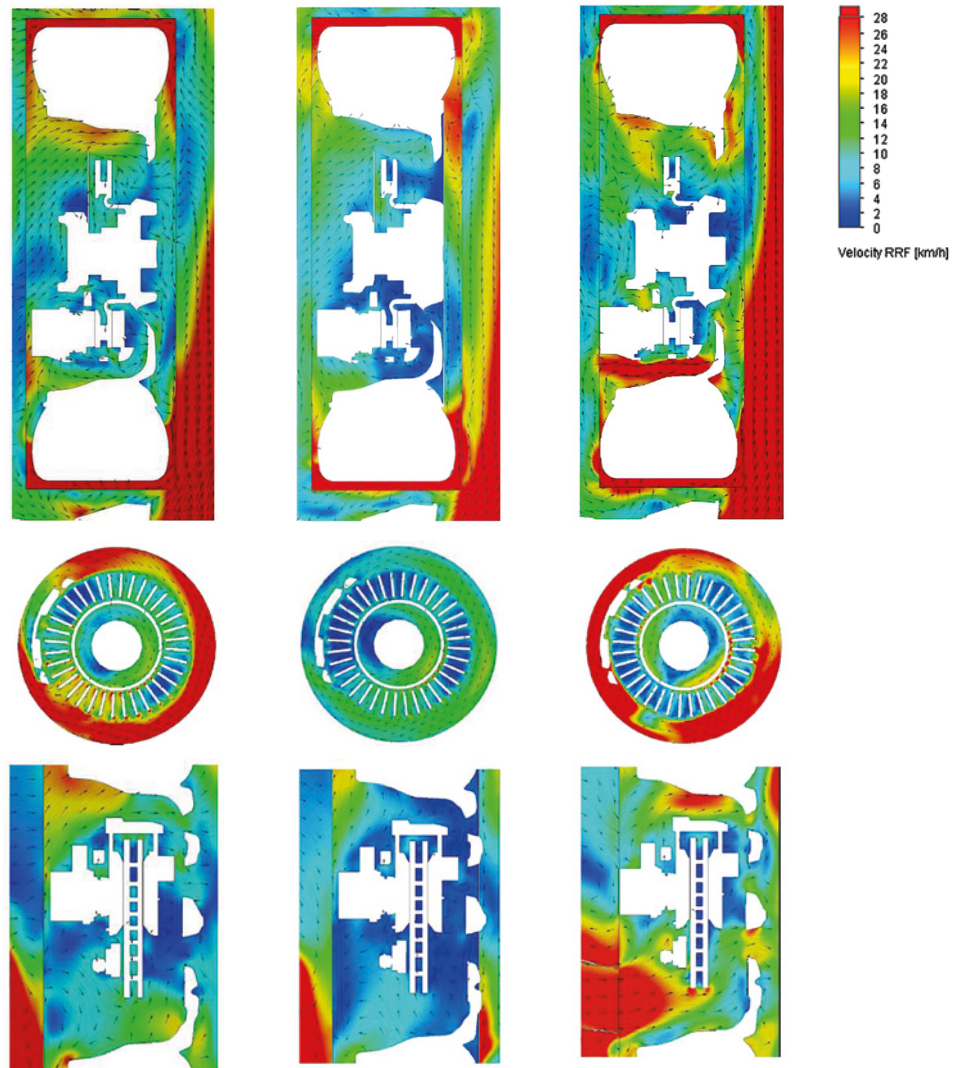


Figure 12. Variant 01, 02 und 05 (from left to right); section XY, YZ, ZX von (from top to bottom)

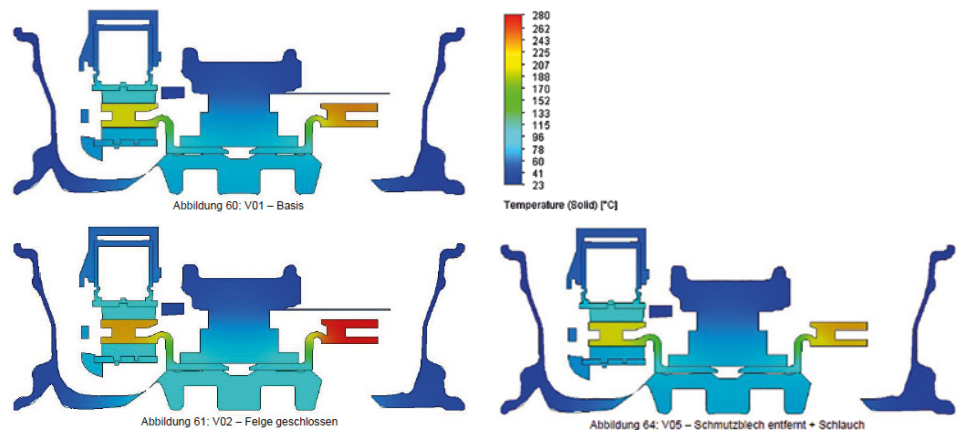


Figure 13. Temperature distribution for variants 01, 02 and 05 (from top to bottom)

Liquid Cooling

turned on its side

The development of Iceotope's KU:L Sistem,
the world's first 1U immersion cooled server

By Dr. Andy Young, Head of Fluids and Thermal Engineering & Jon Halestrap, Business Development Director, Iceotope

In a modern datacenter, for every kilowatt of computing power that is deployed, there are potentially several hundred further watts of power required to support it. The majority of this energy is utilized in moving coolants around the datacenter: for the most part, this means air. Air is a difficult coolant to move to where you need it to be. It is an energy intensive process that also loses a lot of energy along the way. One of the major advantages of liquid cooling is that liquids are generally manageable; liquids fill containers and move around them in a much more controllable and predictable fashion which means you don't have to put as much energy into moving them around as you would have to for air.

In order to address the challenges of the datacenter market, we looked at how we could adapt our current generation technology for this market. This led us to investigate design changes such as 1U form factor, horizontal deployment, and backward compatibility for rack designs where immersive liquid cooling technology can have the most benefit.

This posed significant design challenges for our engineering team, mainly around moving from our vertical, blade-based system to a horizontal, retrofittable, rack mounted design. All these challenges we met and were overcome using CFD techniques.

We needed tools to enable us to take an approach to our problem solving and design that maximized the use of our computational resources and shortened execution timeframes. By employing the concept of the "digital twin" it enabled Iceotope to examine multiple variables across a wider range of design scenarios and achieve optimal system and component design. This strategy was supported by the use of Mentor's 1D CFD software, FloMASTER and helped us overcome major design obstacles during the development of our new product: KU:L Sistem, the world's first 1U immersion cooled server.





As previously mentioned, moving air around with a fan wastes a significant quantity of energy. The same applies for pumps used to move liquid if designed inefficiently. A liquid cooled server has to deliver the coolant to all of the IT components and the major heat sources, the heatsinks and other devices on the board. You have to bring the right amount of coolant to the right components but without over engineering. Over engineering adds costs both in terms of hardware and energy required for operation.

For this part of the design we were able to use FloMASTER to determine the pressure drop in the system for a range of potential flow rates also called a system curve. We used the design of experiments functionality to create the design space and the simulations were automatically run. This allowed us to create Figure 2 which plots the system curve against several pumps we were considering for the blade. This helped us understand which one to choose based on the flow rate along with the power rating of each pump.

After developing a working prototype to prove our concept, we used FloMASTER (Figure 3) to digitally calculate, tune and balance flows so that the correct amount of fluid would be delivered to each major heat source without complex over engineering.

In addition to balancing the flow in the blade we needed to balance all the other components that make up a datacenter rack. FloMASTER was used to balance flow to

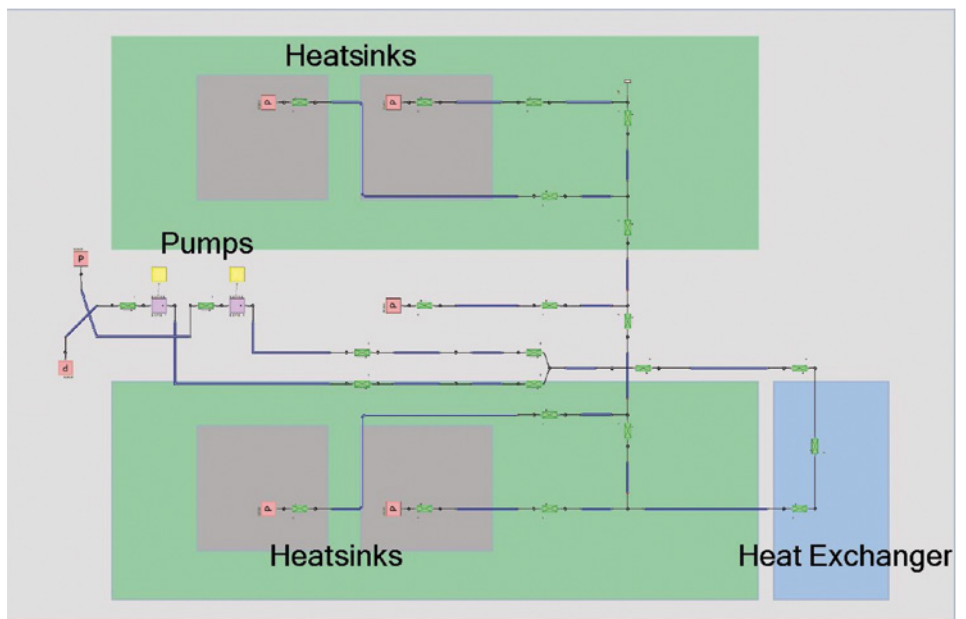


Figure 1. FloMASTER simulation model of KU:L Sistem Server Blade

each component of the rack, both individually and as a whole system. We needed to build a 'system of systems', flow balancing at each stage, to ensure every 1U of technology in the rack has the right amount of coolant flow so that the demands on building services are minimized and the temperatures in the system are acceptable as shown in Figure 3.

One of the other complexities of air cooling is you have to condition the air; you have to add moisture to the air to control electrostatic charge generation. While you can recover some of the liquid used in this process, a lot

of it is lost. By using liquid cooling, you might think that is going to involve lots of liquid consumption and a higher rate of leaks – that is where the analysis software comes in. We designed the risk of leaks out of our system using FloMASTER. By designing a network of pipes to deliver coolant to the server chassis inside the rack without having any pressure spikes, or any stresses over joints or connections, leaks can be eradicated from the server room, Figure 4. This is great for the environment in terms of less water being wasted but it is also ideal for datacenter management.

At a more prosaic level, we had to acknowledge that any datacenter rack system would have to allow the hot swapping of blades. We already use dripless, blind-mate connectors to ensure this operation is fundamentally sound, but it was essential that we engineered the complete solution so that any pressure spikes were removed. This was an interesting engineering challenge that needed advanced “out-of-the-box” thinking to overcome: without the ability to balance the flow, which is a fundamental part of FloMASTER, this would not have been possible without considerable time and resources.

Commenting, Dr Andy Young said “FloMASTER delivers great insight into how to develop a design to maximise value and utility. This combined with much reduced model set up time, extremely fast simulation speed and simplified work-flow will make a big difference to our team.”

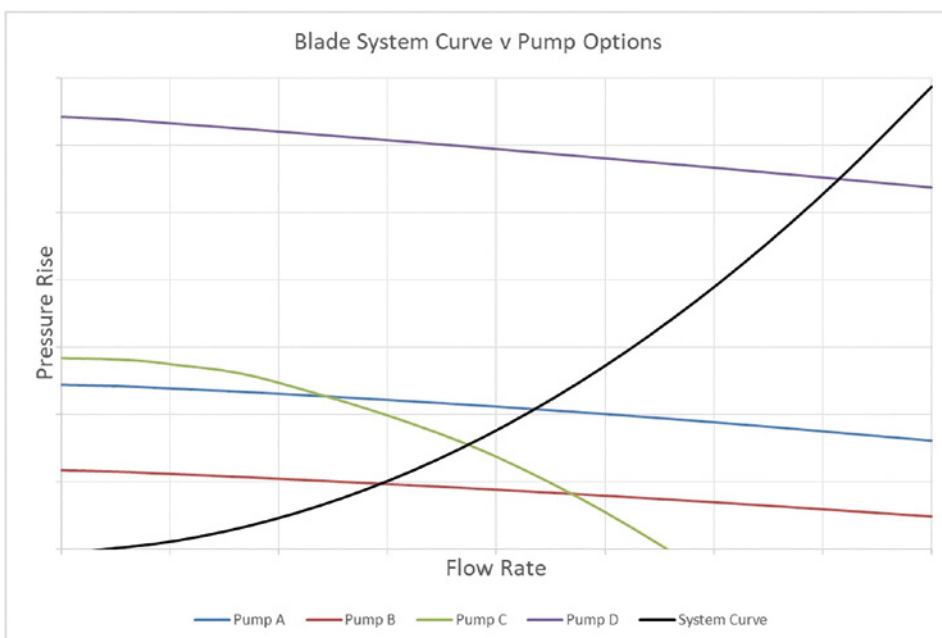


Figure 2. KUL Sitem Server Blade System curve versus several pump options

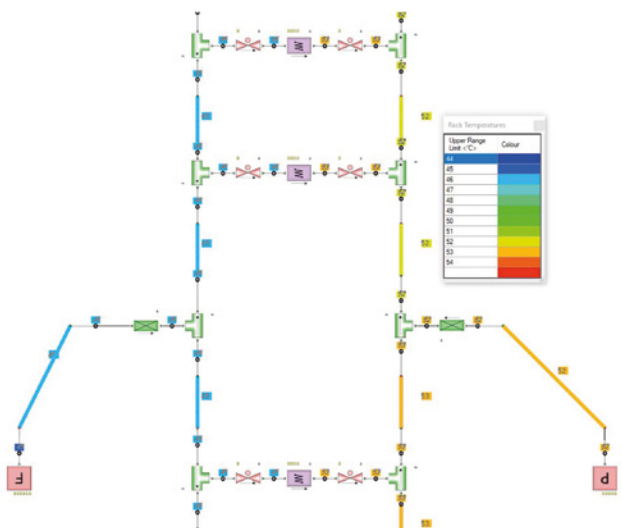


Figure 3. Thermal model of the server chassis using FloMASTER

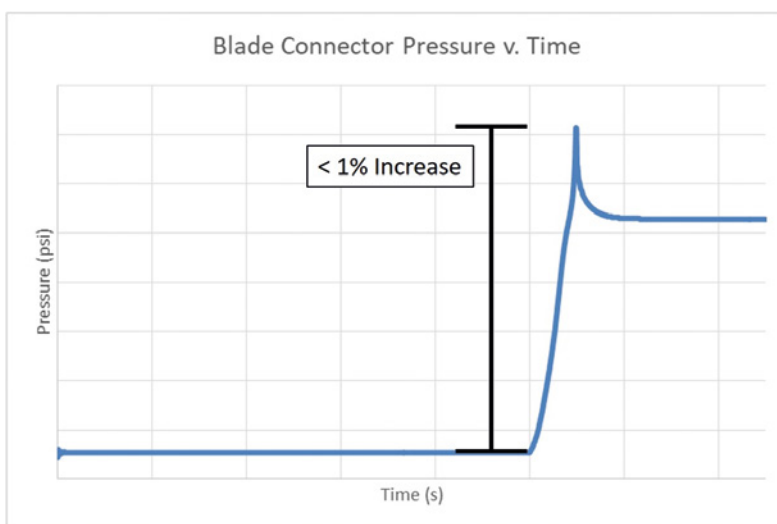
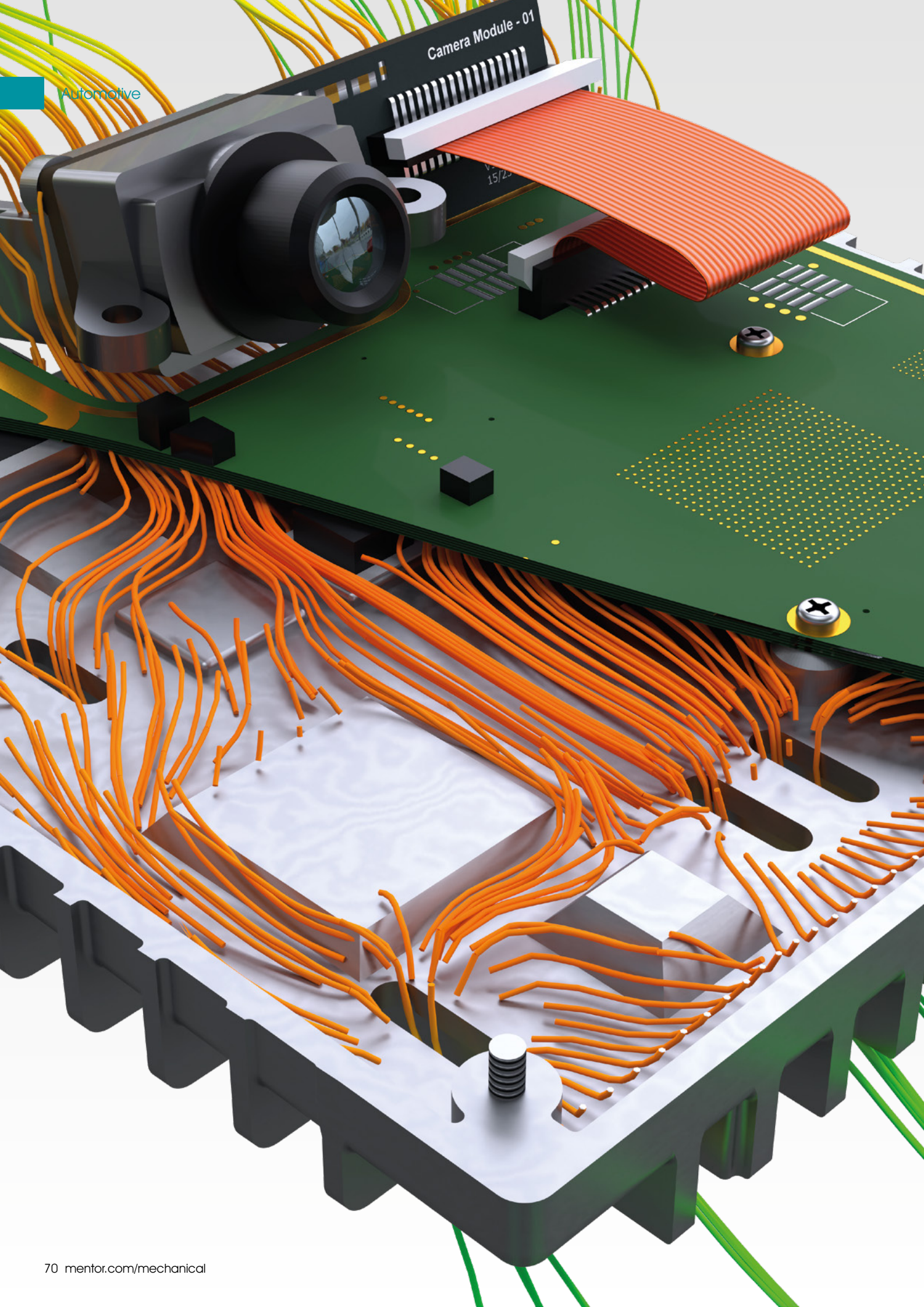


Figure 4. Relative pressure spike due to blade removal as predicted in FloMASTER



Thermal Analysis of an ADAS Camera in FloTHERM XT

By Vladimir Kirichenko, Student Intern, Mentor, a Siemens Business

As the world continues to evolve, autonomous vehicles suddenly have stopped being seen as something from the future. In fact, both world leading companies and new start-ups are getting involved in the automotive world with the aim of not only providing simple driving assist features, but enabling full control of the vehicle to drive its passengers to their destination of choice. While humans mainly rely on their eyes to navigate, autonomous vehicles have to depend on cameras and other sensors to analyze the outside world to familiarize themselves with their surroundings.

Inaccurate data from these devices could have catastrophic consequences and cost lives of passengers and pedestrians. One of the factors that affect image quality is the thermal performance of the optical cameras, resulting in a challenging task of keeping the temperatures at sensible levels.

Challenges

As can be seen from Figure 1, the temperature of the image sensor chip plays a large role in image quality, as higher temperatures dramatically raise noise levels in the Complementary Metal-Oxide-Semiconductor (CMOS) circuitry. Consequently machine vision algorithms may struggle to distinguish objects from the background. To make autonomous vehicles safer and more trustworthy, the camera complexity has increased, and may also incorporate radar, lidar or ultrasonic sensors. Combining such power-intensive devices in one package leads to problems with heat dissipation, therefore serious consideration should be given to virtual thermal analysis during iteration of the design of the cameras used for autonomous driving to develop a final product that will give satisfactory and reliable operation.

Modeling

To analyze thermal dissipation of the automotive cameras in the current market, Mentor kindly provided to me one of the top of the range ADAS cameras available on the market today to disassemble and

examine. Based on the research and the physical device, I created a model, using Siemens NX 10.0, as that was the CAD software I had the most experience with, allowing me to spring into action as soon as possible. It was also a great opportunity to do my primary job role, which was to test FloTHERM XT 3.2 using different import formats to ensure every feature worked correctly. An exploded view of the model I built is shown in Figure 2.

The camera is housed in a plastic shell, apparently for purely aesthetic reasons with cut-outs to provide airflow. The casing of the camera was modeled in a way that the bottom of the casing acts like a heatsink, dissipating most of the heat from major image-processing components in a convective manner. To encourage airflow inside the metal casing, multiple cut-outs have been made to the bottom and top of the casing. This design allowed for the air to circulate inside of the casing, removing the heat from the rest of the components. Any cables and connectors that could restrict the airflow were modeled for increased accuracy of the simulation.

Simulation

Once complete, the model was easily transferred to FloTHERM XT, which meant there was only one part missing before I could perform a thermal analysis on the camera - the main PCB. It was created using FloEDA Bridge, which allowed for a

complex shape of the board and detailed manipulation of necessary parameters. However, if I had the EDA file, it could have been easily imported. Overall, the camera was modeled with eight thermally-significant components assumed to have a total heat dissipation of 6W. The main SoC was dissipating 2.5W of power at the maximum load and has been modeled in detail. All of the power values were assumed based on the research of vision computing SoCs available on the market and engineering judgement. To speed up the simulation, the remaining components were modeled as simple cuboids with an appropriate material attached. For the same reason, compact modeling level of the PCB was chosen instead of detailed or explicit.

Cases

In order to perform a thorough thermal analysis, three different simulations were run. One of the places where autonomous driving technology becomes very useful is the highway, as most of the time the trip becomes monotonous and some drivers can lose concentration. Therefore, to simulate the worst case conditions and analyze a case where, if the limit of 85°C was exceeded when the vehicle is in fully autonomous mode and the camera is functioning at full power, a steady state simulation was created. The vehicle was assumed to be driven at 50 mph on a warm sunny day, consequently, 1000 W/m² of solar radiation was applied at a right angle to the windscreen. To make the simulation more realistic, 20% of the radiation has been absorbed by the windscreen by using a thermal planar source, 60% was applied as a simulated solar radiation and the remaining 20% of the solar radiation was assumed to be reflected and therefore ignored. Further to this, the heat from the camera has been removed solely by natural convection without the presence of forced airflow inside of the cabin. The absolute maximum temperature on the main SoC reached 82°C, while the air inside of the vehicle was simulated at 22°C and the outside temperature levelled at 35°C. From these results, it becomes apparent that although these are absolute extreme conditions and can be considered as a torture test, the camera components are close to their limits.

Problems

Having tested the thermal limits of camera components, two transient simulations were performed to simulate a more realistic scenario. The main problem with the current model was the excess level of detail. Therefore, to improve simulation times, I have made several adjustments. The main

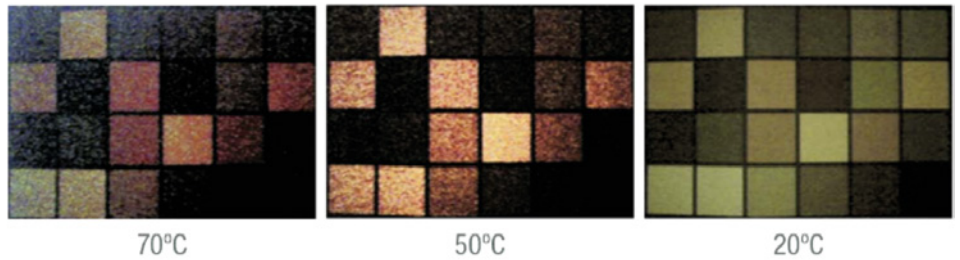


Figure 1. High dynamic range camera image sensor noise under low light for different ambient temperatures (Ref. 1)

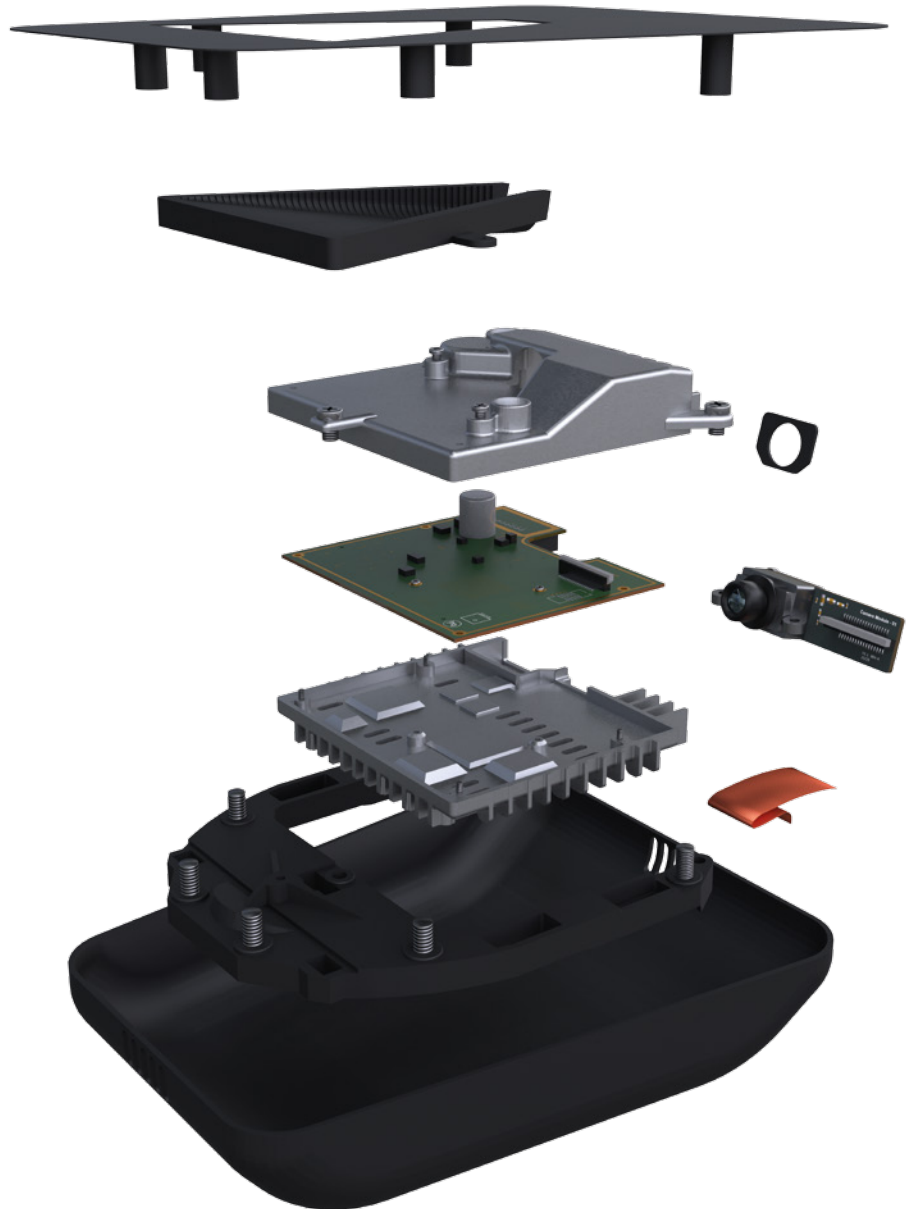


Figure 2. Exploded view of ADAS camera model

SoC was simplified to a simple cuboid with the same thermal properties and a heatsink for the camera module was replaced by a Heatsink Smart Part available in FloTHERM XT 3.2. This led to a dramatic decrease in the number of cells, allowing for significantly reduced simulation times. Even though the mesh number has decreased significantly, I

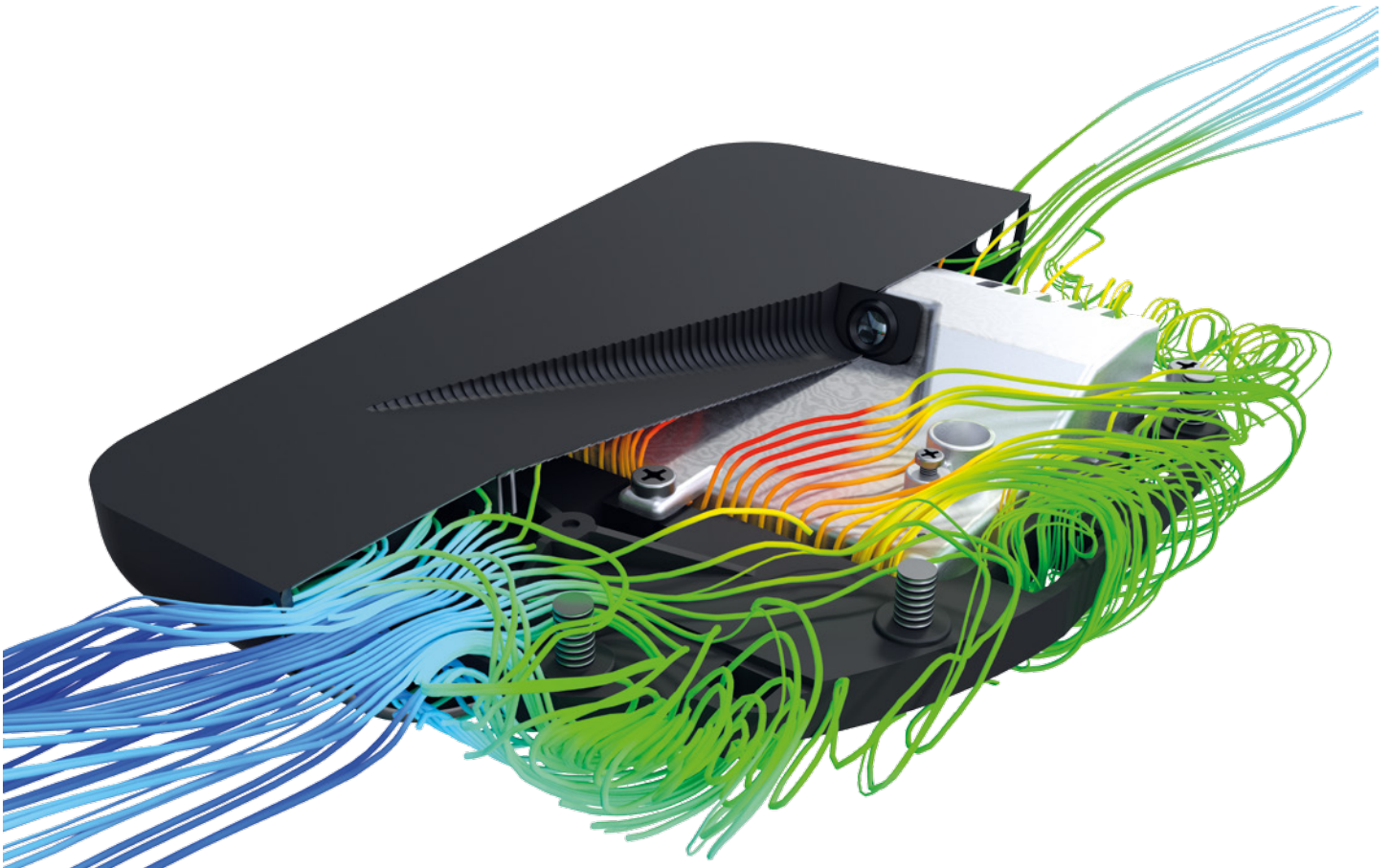


Figure 3. Predicted airflow inside the camera housing

was still unsatisfied with the amount of time it was going to take to perform the thermal analysis. To further optimize the simulation, manually-variable time steps were used.

To further limit the time needed for the simulations, the overall calculation domain was restricted to a box 180x190x135 mm, which worked perfectly for the simulations in still air. However, after an introduction of wind the problems started to appear. As the moving air created turbulence, this solution domain size was not large enough to resolve the flow. Therefore I increased the domain size by approximately 2.5 times.

Transient results

Continuing with the theme of testing the thermal limits of the camera, one of the transient simulations was performed as a cool-down case. I assumed the vehicle was parked under the sun at 30°C with a solar radiation of 750 W/m², 50% of which was applied as radiation, 10% being absorbed by the windscreen and another 40% was reflected, and after that it is driven at 30 mph in a city area.

To ensure the correct starting point of the transient simulation, I have performed a

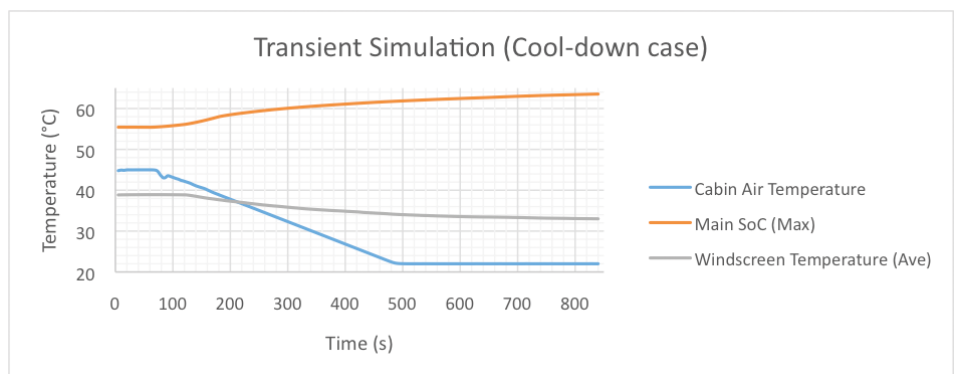


Figure 4. Key temperatures during transient cool-down simulation

steady state simulation with static air first. This allowed the interior of the vehicle to warm up due to solar radiation and stabilize temperatures of the camera components. These results determined the starting point for the cool-down transient case. The temperatures inside of the cabin stabilized at 45.0°C and the temperature of the main SoC in the camera stabilized at 55.4°C.

The overall time of the transient simulation was 14 minutes, from the first to the eighth minute the AC was turned on to cool the

cabin air down to 22°C and keep it at this temperature until the end of the simulation. From the second minute the vehicle accelerated from 0 to 30 mph in 10 seconds and then continued at this speed. The camera itself was powered at 25% while the vehicle was stationary and the AC was on. As soon as the vehicle started moving, the power was increased to 75%, which was assumed to be sufficient to provide advanced driver-assistance systems. From Figure 4 it is apparent that the maximum temperature of the main SoC of the camera stabilizes at 64°C, which is an acceptable result, as in reality the solar radiation would tend to vary due to the surroundings and the power consumption of the camera unit would be altered by traffic conditions.

Turning to a warm-up case, it was assumed that the vehicle was parked outside at -10°C and there is no solar radiation. Similarly to the cool-down case, a steady state simulation was performed first and the vehicle was assumed to be driven at 30 mph. As the changes were not as dramatic as with warm-up case, the simulation had to be run for much longer for the temperature of the main SoC to stabilize.

Eventually, main SoC temperature levelled out at 19.5°C, which puts the camera assembly at a very comfortable level in terms of working temperatures. In this case the temperature of the cabin air had to be raised to a comfortable temperature for the driver and passengers.

Conclusion

With a rapid growth of the automotive industry, there will be increasingly higher demand for cameras and radars that are required to work for longer periods of time without failures in varying weather conditions. As this article has shown, thermal analysis is extremely important to ensure that the design of the Advanced Driver Assistance Systems (ADAS) camera is effective at removing excessive heat from the internal components.

To improve the design of the device, it will be worth considering several materials before production, as well as, simulating the whole camera assembly with the casing and inside of the vehicle’s interior. This would help to identify critical locations for the cut outs in the casing to optimize the airflow. It is important to mention, that while regular processors in a PC or a laptop can be thermal-throttled to reduce the temperatures, this approach is highly undesirable as this would slowdown the processor frequency and reduce

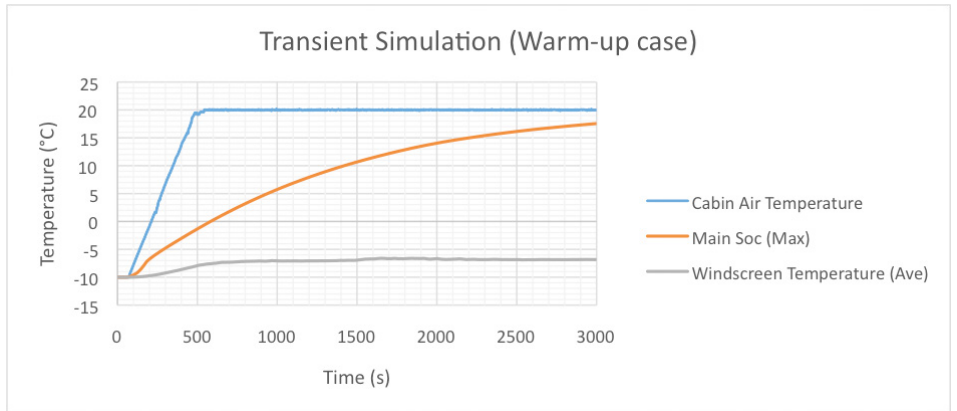


Figure 5. Key Temperatures During Transient Warm-Up Simulation

Power	“Climate Control” temperature	speed
0-1 mins: 0 %	0-1 mins: not set	0-2 mins: 0
1-2 mins: 0-25%	1-8 mins: from cabin ambient to 22 degC	2-2:10 mins: 0-30 mph
2-3 mins: 25-75 %		
3-13:50 mins: 75%	8-13:50 mins: 22 degC	2:10-13:50 mins: 30 mph

Power	“Climate Control” temperature	speed
0-2 mins: 0 %	0-1 mins: not set	0-4 mins: 0
1-2 mins: 0-25%	3-8 mins: from cabin ambient to 22 degC	4-4:10 mins: 0-30 mph
2-3 mins: 25-75 %		
3-50 mins: 75%	8-50 mins: 22 degC	4:10-50 mins: 30 mph

the performance, which consequently reduces the speed of image-processing and may affect how efficiently and safely an autonomous vehicle reacts to the road conditions.

Reference:

[1] “Comparing Ethernet and SerDes in ADAS Applications”, Dave Lewis, Texas Instruments. <http://artsdocbox.com/Television/66316313-Comparing-ethernet-and-serdes-in-adas-applications.html> (downloaded 07 March 2018)

Thermal Design Leading the Charge

By Ferdinand Sluijs, Technology Manager, NXP Semiconductors – Smart Power



Quite a lot has been written about the benefits of moving the thermal design activity higher up the product development workflow to cut down the amount of rework needed later on, eliminate physical prototyping for thermal reasons, etc. That said, thermal considerations are normally indicated as advice, or constraints on the main electrical and mechanical design flows.

In the case of the power adapters that NXP Semiconductors' Smart Power Division are developing thermal considerations have really come to the fore, driven by the trends we see in mobile power adapters, which are getting smaller and have a higher output power. Thermal limits are now constraining all aspects of the design.

A recent project involved fitting a 25W charger into the smaller casing previously used for an 18W charger, some 26% smaller, while still meeting the thermal limits which constrain the casing temperature to a maximum of 50°C averaged over an area not exceeding 2cm x 2cm, against an ambient temperature of 25°C. Increasing the size of the charger, while thermally desirable, would make the charger inconvenient to use. Airflow through the charger, while again thermally desirable was ruled out for safety concerns due to the mains voltage inside.

The first question is "what is possible?" This can be answered by finding out how much power dissipated within the device gives this maximum case temperature condition. By building a simple block representation of the adapter consisting of just two blocks for the body and two for the pins, with a uniform internal power distribution, the power dissipation can be increased until the temperature limit is reached. The adapter casing, and the thermal model of this the ideal case with no hot spots is shown in Figure 1.

This simulation showed that in theory, the adapter could dissipate maximal 2.7W. Given that the output power needs to be 25W, the minimum efficiency, η needs to be:

$$\eta = \frac{25W}{25W + 2.7W} = 90.3\%$$

Providing a performance constraint on the electronic design.

The next step is to model the initial design of the new adapter to see the surface temperature distribution and where the temperature would exceed the limit. At 2.91W the initial design will certainly exceed the maximum temperature, but an insight into the temperature distribution in this design will help identify hot spots and so guide design improvements.

To build this model components that have a significant power dissipation were included in the model, along with electrolytic capacitors as these are both large, influencing the overall thermal behavior and also temperature sensitive. One key aspect of the electrical design is the need to isolate the high voltage mains supply from the low voltage output stage. This is achieved by leaving a large distance on the main PCB between the mains connected high voltage primary side, and the output connected low voltage secondary side. A small second PCB was added as not all secondary side components fit on the main PCB.

Each of these PCBs were expected to have four layers – two 35 μ m outer signal layers, and two 70 μ m internal power planes (mainly used for internal low voltage supply and ground). These boards were modeled with discrete layers, but with averaged material properties for each layer, assuming 30%



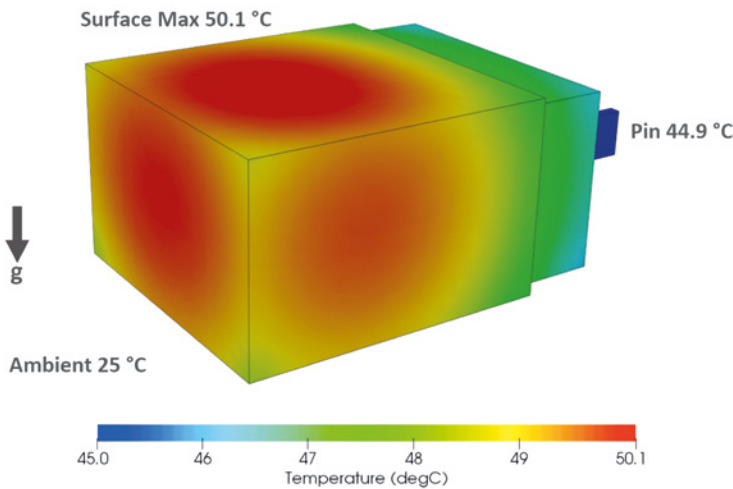


Figure 1. 18W Charger (inset) and simple block model of to determine maximum power dissipation for 25W charger

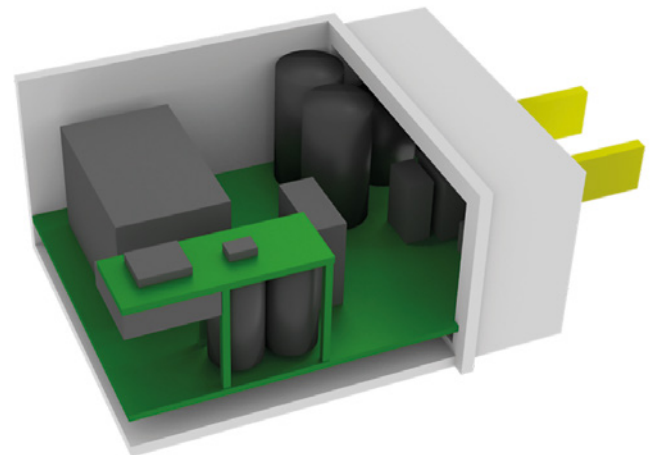


Figure 2. Initial Design

copper coverage for the signal layers and 70% for the power planes. A key decision in early design is how to model the components. Most components were modeled as discrete blocks having a uniform internal power dissipation and material properties, with values chosen based on the primary material for the part.

As expected, the case temperature exceeded 50°C in several places due to local hot spots inside the adapter, with a maximum surface temperature of 61°C.

Two key hot spots inside the adapter were the primary MOSFET on the main board, and the SyncRec MOSFET on the small second board, as shown in figure 4. Next to these two components, also the transformer has a high dissipation and gets warm, but has better cooling because of its larger size.

Rectifying these issues to achieve an acceptable thermal design within the deadline our customer required was very much a team effort, requiring close collaboration between the application engineers working on the sizing of the components, and providing power estimates; the layout engineer working on the PCB layout; and myself as the thermal engineer to also suggest thermal improvement suggestions and to investigate the thermal impact of these by performing FloTHERM simulations. The process involved sitting together and listing ideas, which I then tried out in FloTHERM, and based on the results we decided which ideas to accept and which to reject. We went through that cycle several times, described in more detail below, resulting in the final PCB layout that was simulated, and later assembled.

As the power dissipation was known to be too high, optimization of the circuitry and control was started, focusing mainly on reducing the

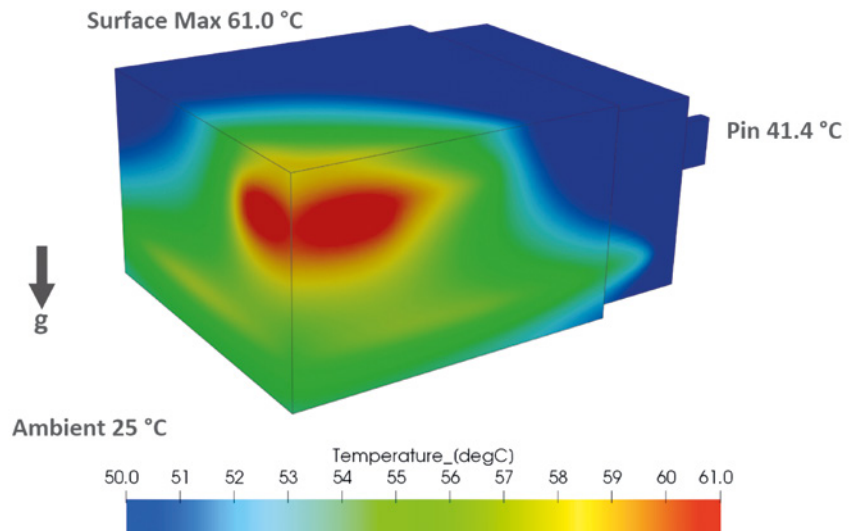


Figure 3. Initial design surface temperatures

power dissipation in the primary MOSFET, the transformer, and the Synchronous Rectifier MOSFET which was used in preference to a rectifier diode as it dissipates less power, but requires a drive signal provided by the Synchronous Rectifier IC. This work resulted in a total power dissipation of 2.2W, giving a 91.9% efficiency. As this is below the 2.7W theoretical maximum, cooling this should be possible provided hot spots on the casing can be reduced, so as well as forcing a redesign of the circuitry and control, thermal constraints also necessitated a significant redesign to alter the layout of the components to better spread the heat dissipation throughout the adapter.

Key changes were to move the primary MOSFET from the top of the main board to the bottom, and away from the transformer to separate these dissipating sources. The primary MOSFET was mounted flat onto the PCB to conduct away more of its heat. The four bridge diodes were then moved to the top of the main board. These changes meant

that one the large cylindrical capacitors on the main board also had to be moved. This was mounted on its side and raised off the main board.

The size of the small second board was increased to improve heat spreading, and the location of the connecting wires changed. Between the transformer and the secondary board a vertical plastic wall is added to help conduct heat from the secondary PCB down into the main board and into the transformer to help remove heat from the Synchronous Rectifier MOSFET. The final change was to move the USB connector to the main board, as the cable, which will be present when the adapter is charging, and so dissipating heat, will help remove heat from the adapter, as will the pins supplying mains power to the unit as these will conduct heat into the mains socket.

These changes dropped the temperature of the casing adjacent to the Synchronous Rectifier MOSFET by 10°C and with the maximum casing temperature averaged over a 2cm x 2cm area of 48.8°C, as measured by a FLIR infrared camera with a USB cable attached, thereby meeting the design requirements. This work illustrates the importance of thermal design for electronic products and the insights possible using FloTHERM. The simulation results of the final adapter design are in close agreement with the surface temperature maximum and distribution measured on the casing after the adapter had been fabricated, so no further design rework was necessary.

Had this design not met the requirements we still had the opportunity to increase the size of the charger slightly to improve the external cooling, and use more expensive electronic components internally, or increase the copper content of the PCB. All of these would have added cost to the final product and FloTHERM helped us to find what we believe is the lowest cost cooling solution for the product.

Acknowledgements:

The author would like to thank Frank van Rens for the optimization of the adapter's circuitry and control, and Thady Bruton for the thermal measurements performed on the adapter.

Reference:

[1] Ferdinand Sluijs (2017), "Thermal Modelling to Optimize Design in Mobile Charging Applications", Proc. of 23rd THERMINIC Workshop, Amsterdam NL, September 2017, pp. 1-5. ISBN 978-1-5386-1928-8

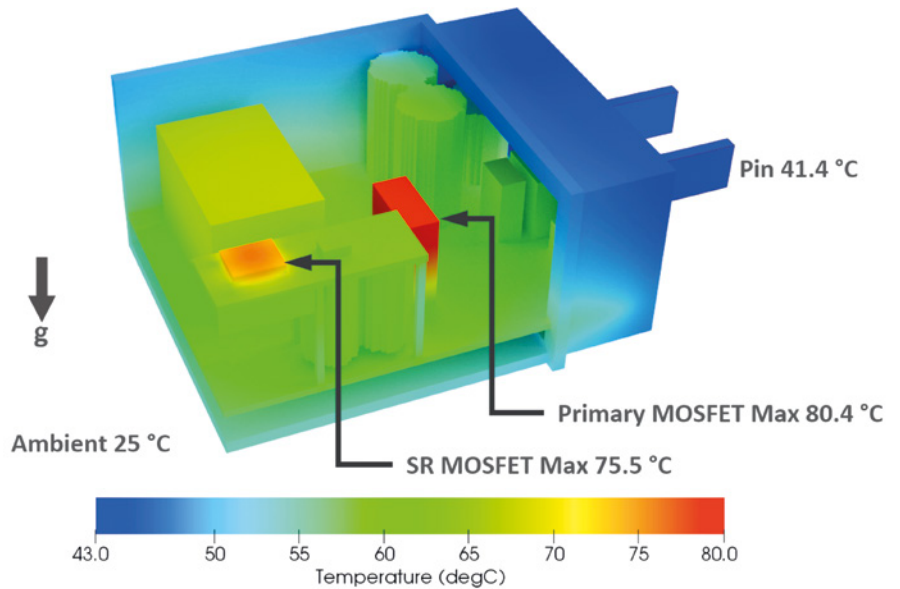


Figure 4. Initial design showing internal hot spots

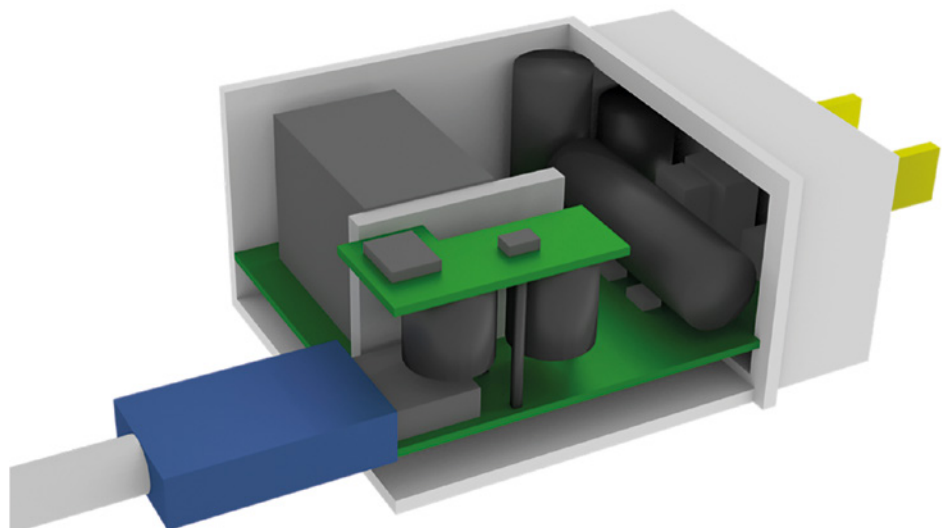


Figure 5. Final design

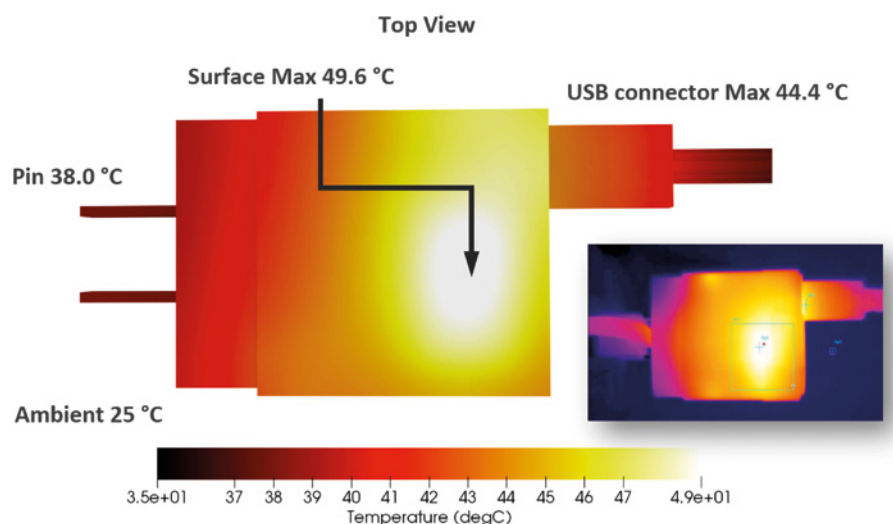


Figure 6. Final design showing surface temperature comparison with measurement

Understanding Die Attach Thermal Performance

By John Parry, Senior Industry Manager, Mentor, a Siemens Business
and Sujay Singh, Principal Reliability Engineer, ON Semiconductor

Power electronics components improve the energy efficiency of electric machines and motors across all industries and applications. Increasingly these power electronic components are being more densely packed together, positioned close to or on the motor itself, and so are affected by harshness and vibration in the application. Heat dissipation from these components has to be removed efficiently to prevent the premature failure of the device, or in the most serious cases thermal runaway as leakage currents increase with increasing temperature, further adding to the heat dissipation until the semiconductor die actually melts.

As part of ON Semiconductor's commitment to delivering the highest quality of product to its customers it is essential to understand how the new technologies such as wide band gap semiconductors can be introduced and produced with the lowest possible defects to achieve improved device performance and reliability in service, when the part experiences temperature swings.

These temperature swings can cause cracking of the solder die-attach or delamination between the die attach and the die, or the die-attach and the substrate. This in turn leads to an increase in the die temperature, as the heat flow path from the die to the ambient is disrupted, further elevating the magnitude of the temperature swing which further speeds up the rate of damage. Device lifetime is dependent on many factors, but based on the operating temperature of the die, ON Semiconductor know that a 10°C increase in temperature roughly corresponds to a two to threefold decrease in lifetime for the same duty cycle.

Voids that can occur in the solder die attach have the combined effect of making the die attach less thermally conductivity and act as sites where cracks can form, so solder die-attach voids are one of the major reliability concerns in power electronics packages. The impact of die-attach voids depends on the void type, pattern, and location of the voids within the solder, making it critical to really understand the influence these have

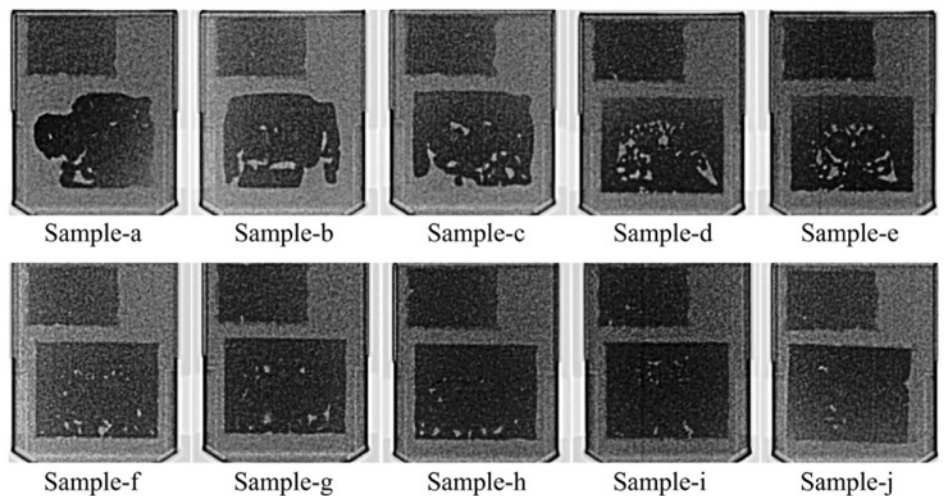


Figure 1. Samples in decreasing order of die-attach voiding under IGBT die

on the thermal impedance of the die attach.

To investigate this, ON Semiconductor selected an insulated gate bipolar transistor (IGBT) co-packaged with a diode in a TO-247 package. Ten samples were selected having differing amounts of voiding in the die attach, detected using X-ray imaging, as shown in Figure 1.

These were categorized both in terms of the total amount of voiding, as a percentage of the area of the die, and in terms of the size of the largest void, typically caused by coalescence of voids around the periphery of the die.



Figure 2. MicReD Industrial 1500A Power Tester

Measuring the effect of the voids on the thermal impedance of the die-attach require a highly sensitive measurement system, and a means of identifying the contribution of the die-attach to the overall thermal resistance measured. That meant following the JEDEC JESD51-14 standard to measure the junction-to-case thermal resistance, Θ_{JC} , using the transient dual interface measurement (TDIM) method. The thermal impedance Z_{th} measurements were performed using Mentor's MicReD Power Tester 1500A showing in Figure 2, which provides the necessary measurement fidelity, combined with inbuilt structure function analysis of the Z_{th} curve to identify the partial thermal impedance due to the die attach.

The structure function is a 1D representation of the heatflow path and provides information regarding the spatial distribution of thermal properties in a system, presenting this information as a graph of the cumulative thermal resistance versus the cumulative thermal capacitance the heat experiences as it passes from the source on the die surface out to the cold plate on which the part is mounted in the Power Tester 1500A. The method, which fully conforms to the JEDEC JESD51-14 standard is non-invasive as it uses the electrical test method described in JEDEC JESD51-1 to both electrically heat the die and sense the die temperature during the measurement.

Figure 3 (a) and (b) show the electrical schematic for heating and sensing of the junction temperatures of the IGBT and diode respectively. The Z_{th} measurements on the IGBT were done in saturation mode. Figure 3(c) shows the experimental fixture for the IGBT measurement. The fixture is clamped on the cold plate by a clamping torque of 6"/lb to ensure good thermal conduction. Figure 3(d) shows the package construction and the physical separation of the IGBT and diode which are both mounted on the leadframe. While the Power Tester 1500A is capable of delivering up to 1500A to a single package, the heating current used for the measurements was 20A. All measurements were done at a cold-plate temperature of 25°C with data automatically captured during the measurement by the Power Tester. Analysis of the data was done using the MicReD T3Ster Master software. The electrical transient that occurs during the first few microseconds of the measurement caused by the power being switched down from the 20A heating current to a measurement current of 0.1A was corrected by using the in-built "square-root" method that replaces

the initial/parasitic transient with a curve extrapolated using a square-root fit within an appropriately selected time window.

The measurement of Θ_{JC} using JESD51-14 involves performing the measurement twice, once with the sample mounted to the cold plate without grease between the sample and the cold plate, and again with grease.

The microscopic roughness of the fixture and the package resists the heat flow for the dry case, whereas the TIM/grease minimizes the surface roughness and decreases the interfacial thermal resistance. Therefore, the separation between the two curves is due to the difference in the thermal path for the two measurements. The two curves start to separate as soon as the heat flux reaches the package-fixture interface, i.e., when flux leaves the case of the package. The splitting point of the two curves indicates Θ_{JC} . However, the two curves separate gradually rather than on a well-defined point, as shown in Figure 4(a). Therefore, it is necessary to define the point of separation in time more precisely. The task is relatively easier if the derivative of the curves is used, as shown in Figure 4(b). Noise on the graph is accounted for by fitting a resistor-capacitor ladder to the experimental response and noting where that intersects the trend line fitted to the difference in the derivatives at the start and end of the transient.

Using this method the separation point corresponding to the junction-to-case thermal resistance is 0.18K/W for Sample-a. T3Ster-Master software, used to post-process the temperature versus time response of the sample provides an alternative way to assess the junction-to-case thermal resistance using a structure function. The structure function is a graphical representation of the total, cumulative thermal capacitance as a function of the total, cumulative thermal resistance measured from the heat source or driving point (junction), that the heat encounters as it passes through the package to the ambient, in this case the cold plate. The structure function is computed by the mathematical transformation of the measured transient response that involves several steps not described here.

For a 1D heatflow path, the thermal structure function provides information about the thermal properties of the individual layers inside a packaged device. A change in the heat flow due to defects in the packaged device would change the

Thermal Structure Function analysis offers an effective and a non-invasive method to identify physical characteristics of the individual layers of a packaged device. This technique complements other non-destructive failure analysis techniques such as X-ray and C-SAM that visibly identify defects, however, these techniques do not provide any information regarding the impact of these defects on the thermal behavior of the part.

Sujay Singh, Principal Reliability Engineer, ON Semiconductor

structure function. In other words, a change or shift in cumulative thermal resistance or cumulative thermal capacitance would correspond to a change in the thermal structure or material properties within the heat flow path. For example, if the thermal interface between the case and the fixture is changed from a dry contact to grease, then the structure functions for these two measurements would separate at the corresponding point with the thermal resistance at the separation point indicating the value of the junction-to-case thermal resistance, providing an alternative approach to its measurement.

One challenge, with either approach, is clearly determining at what point the curves have separated. In the case of the structure function approach, the difference in the cumulative structure functions also has some noise, so again there is no unique point at which the curves suddenly deviate from one another. While the method is standardized and documented in the JEDEC JESD51-14 standard, it does not contain clear guidelines for choosing the value of the difference in thermal capacitances at which the curves are judged to have separated. The difference is taken to be 5% of the capacitance value at which the curves appear to separate. Using a lower value leads to larger variations in the junction-to-case thermal resistance.

According to JESD51-14, the junction-to-case thermal resistance obtained through the structure function difference method for low thermal resistance packages is often impeded by numerical effects; therefore, the derivative delta method seems to be more reliable in this case as the TO-247 package has a low thermal resistance.

Having selected the most reliable way to measure the junction-to-case resistance, ON Semiconductor were able to turn their attention to examining the impact of voids in the die attach layer on the junction-to-case resistance. Previous studies have found that large coalesced voids that are hot in nature affect the thermal dissipation more severely when compared with distributed or random voids. To deliver high quality and cost-effective products it is essential to understand exactly how the size, position and distribution of voids affects the package's thermal performance.

The ten packages, Sample-a to Sample-j were measured and the junction-to-case resistance measured using the temperature versus time derivative method and the results were correlated with both the

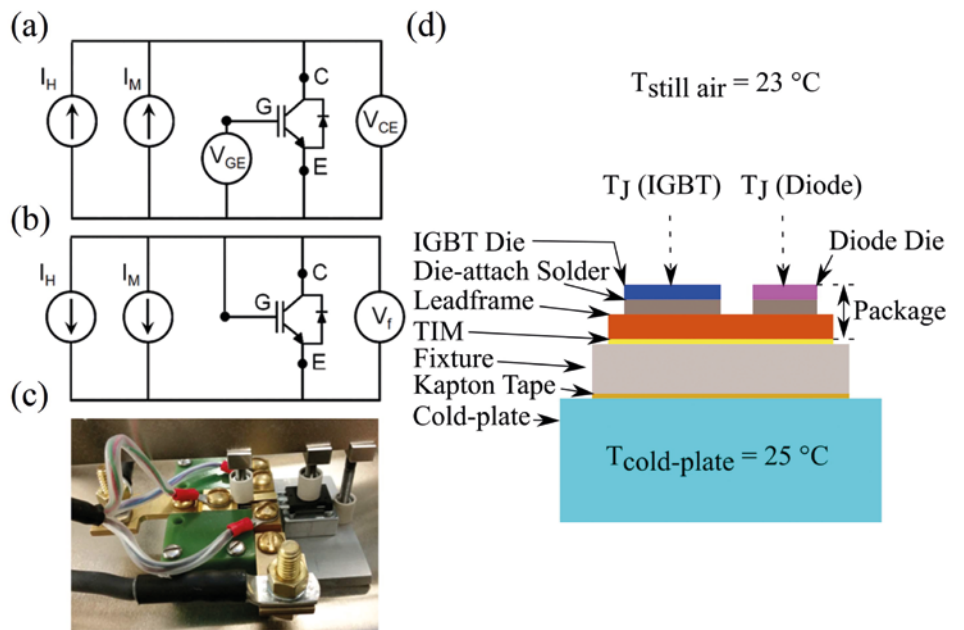


Figure 3. (a) and (b) Schematics for Θ_{j-c} (IGBT) and Θ_{j-c} (Diode) measurement, respectively. (c) Experimental setup for Θ_{j-c} (IGBT) measurement. (d) Schematic showing the cross section of different layers and boundary conditions.

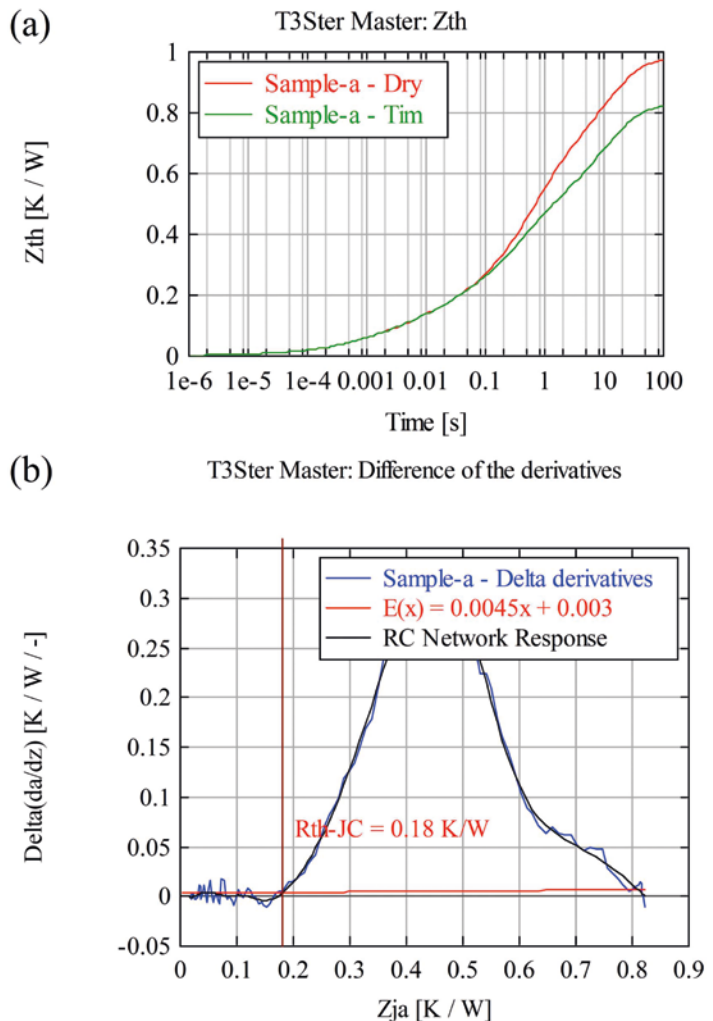


Figure 4. (a) Zth curve for Sample-a measured with and without grease. (b) Θ_{j-c} evaluation following derivative delta method for Sample-a. The x value of the point of intersection between the fit curve based on RC-network response and the trend line defines Θ_{j-c} .

percentage area corresponding to the largest void and the total void percentage. The results of this are shown in Figure 6.

From the results it is clear that below about 10% total void area the junction-to-case resistance is not appreciably increased by the presence of voids. The conclusion from this is that the distributed voids included in the total void percentage do not significantly affect thermal dissipation severely. The largest void size, as a percentage of the total area has a more marked impact on the junction-to-case resistance.

The behavior of junction-to-case thermal resistance with increasing largest void percentage can be described by an exponential fit as shown in Figure 6(a). The reason for choosing an exponential function is to assess the nature of the acceleration behavior.

It is clear that the increase in void levels would decrease the effective area for heat conduction and that will lead to an increase in junction-to-case resistance. The change in resistance with an increase in void percentage could be dramatic for a higher void level, and the exact behavior is hard to predict as it depends on how these voids are distributed. Thermal dissipation of packaged device is severely affected by die-attach voids, and minimizing these voids is important from a reliability standpoint. The largest void percentage has greatest impact on the thermal impedance of the devices. Measurements on the diode junction-to-case resistance showed this is unaffected by voiding in the IGBT die attach, implying that the diode heat path is independent of the IGBT heat path.

Reference:

[1] Sujay Singh, Jifa Hao, Daniel Hoffman, Thomas Dixon, Andrew Zedolik, Joe Fazio, and Thomas E. Kopley (2017) "Effects of Die-Attach Voids on the Thermal Impedance of Power Electronic Packages", IEEE Transaction on Components, Packaging and Manufacturing Technology, Vol. 7, No. 10, October 2017, pp. 1608-1616.

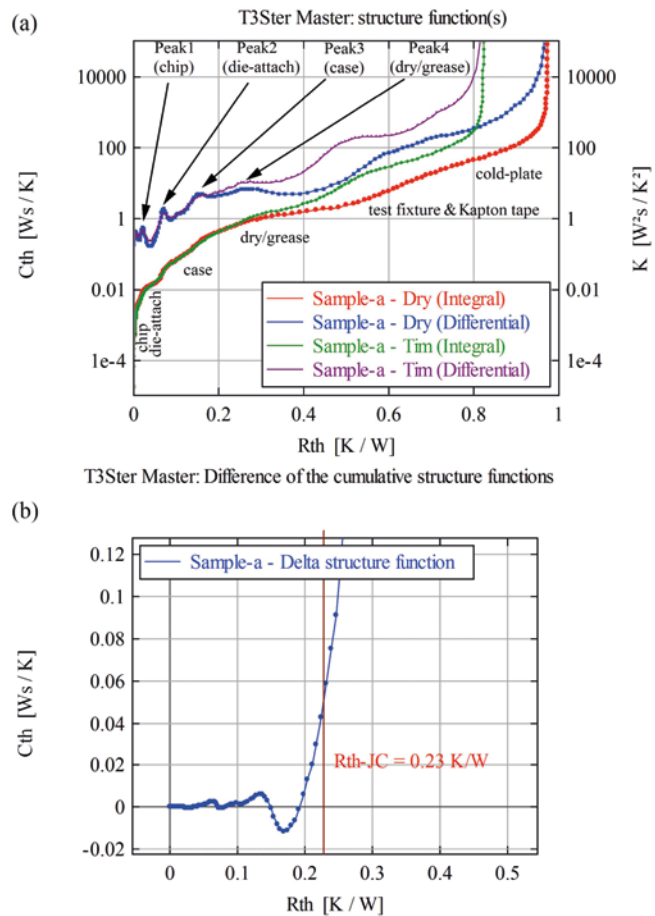


Figure 5. (a) Thermal capacitance versus thermal resistance for Sample-a showing difference in thermal paths due the change in the interface between the case of the package and

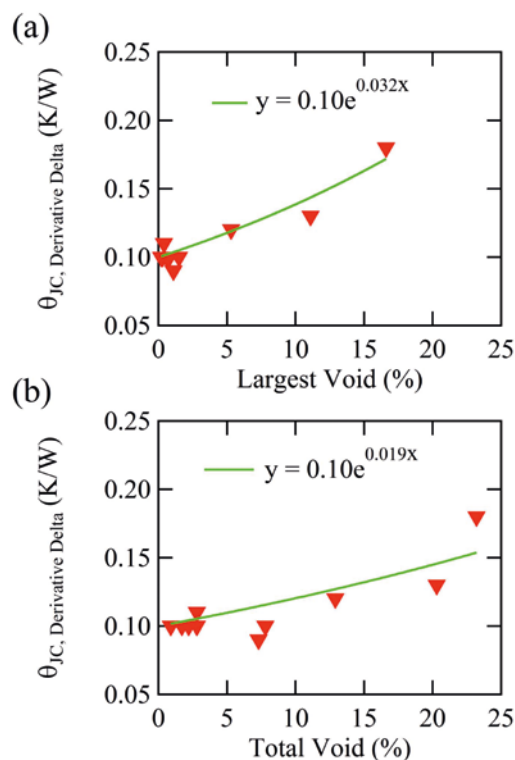


Figure 6. (a) and (b) Junction-to-case thermal resistance (for the IGBT dies) as a function of largest void as a percentage, and the total void percentage, respectively.

Rapid Beverage Cooling Analysis

By Jay Chien and Hank Chung, EFD Corporation

There is an increasing market for appliances that are designed to cool beverages many times faster than a conventional refrigeration approach. When the liquid is prepackaged in a can or bottle, there are cooling approaches that aren't possible when cooling items of arbitrary shapes and sizes. The same is true for beverage coolers that are designed with an integrated barrel or tank for the liquid as shown in Figure 1.

There are many cooling options to consider early in the design phase depending on the performance requirements. The design may involve thermoelectric coolers (TEC) that use the Peltier effect to extract heat from the fluid. Other options to absorb heat from the fluid could include liquid cooling loops or cold plates. Rejecting the heat to the environment might include a liquid to air heat exchanger or fan cooled heatsinks. The fluid within the barrel might also be mixed to improve the rate of liquid cooling. The thermal design tool used to consider all of the possible options must be able to model each of the approaches. FloTHERM XT was used to explore some of the cooling strategies used when designing a rapid beverage cooler.

Two designs with an integrated barrel were considered in FloTHERM XT to explore some of the alternatives for rapid beverage cooling. The two designs considered both use TECs to extract heat from the fluid.

The first design scenario used an air cooling strategy with three cooling assemblies and is shown in Figure 2. Each cooling assembly, as shown in Figure 3, consists of a fan, plate fin heatsink and two TECs. The cooling assemblies are connected together with four heat pipes. The TEC chosen for this design can pump up to 57W of heat and are colored pink for clarity in Figure 3.

The second design scenario used a liquid cold plate with an air cooled heat exchanger as shown in Figure 4. The cold plate is mounted to three TECs that pump up to 145W of heat each. The barrel in Design 2 also included internal fins and a rotating impeller, rotating at 60RPM, as shown in Figure 5.



Figure 1. Rapid beverage cooler with integrated barrel

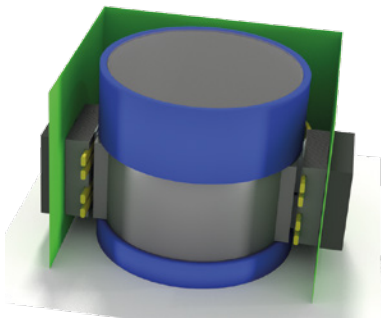


Figure 2. Design 1 cooling strategy

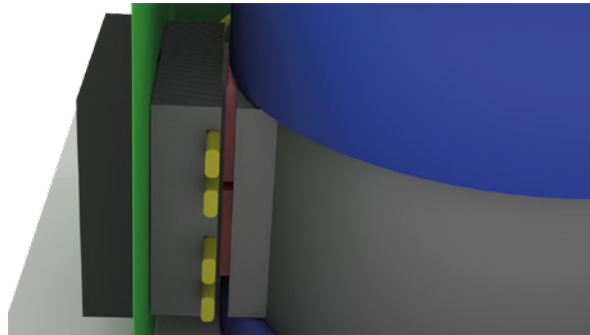


Figure 3. Design 1 cooling assembly with TEC

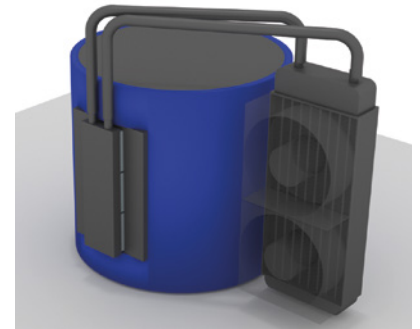


Figure 4. Design T cooling strategy

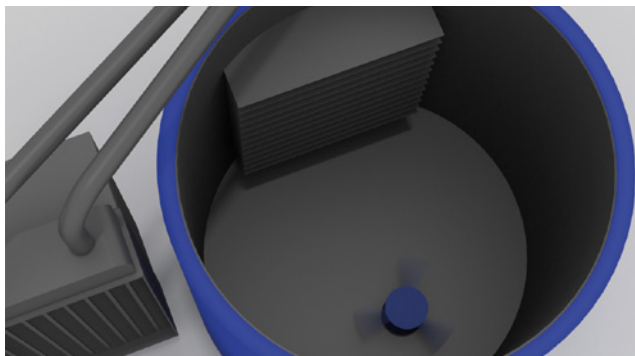


Figure 5. Design 2 internal fins with impeller

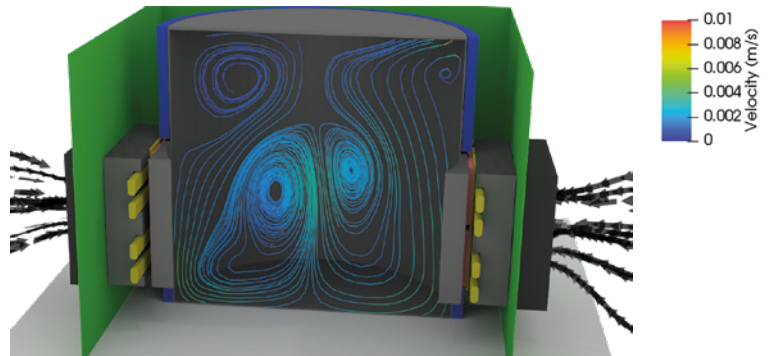


Figure 6. Design 1 flow streamlines at 30 minutes

Each design was simulated for a transient duration to assess the quality of each design in terms of rate of fluid temperature decrease. Figure 6 displays the flow streamlines for Design 1 at the end of the transient simulation. The fluid travels downwards near the cooling assemblies, along the bottom of the barrel and rises in the center. The average velocities in Design 1 are well below 0.01m/s. Design 2 included a rotating impeller and had peak velocities in the 0.4m/s range as shown in Figure 7. Also shown in Figure 8 is the cooling loop fluid temperatures with the return temperature from the heat exchanger at about 40°C.

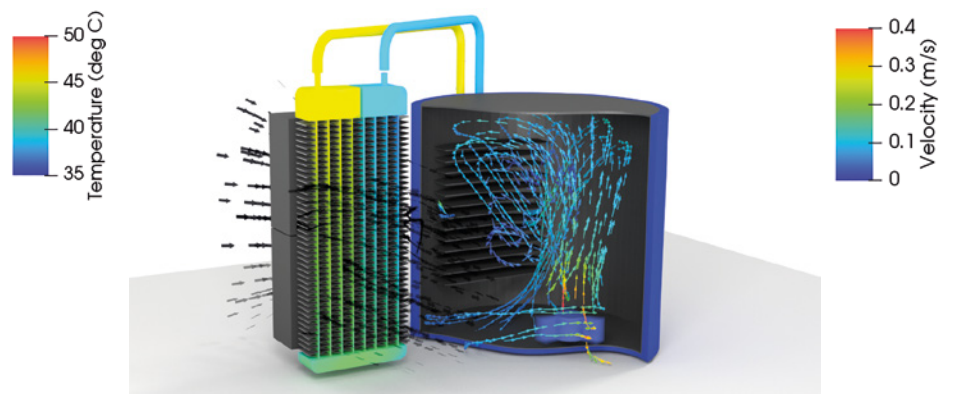


Figure 7. Design 2 Flow streamlines and cooling loop fluid temperature at 30 minutes

Figure 8 shows the rate of temperature decrease at the center of the barrel as a function of time. Though Design 2 had a higher maximum possible TEC heat removal rate and impeller, the rate of temperature decrease was less than Design 1.

When designing a rapid beverage cooler there are many cooling strategies that need to be explored early in the design process to determine the most effective approaches to be considered for prototyping. FloTHERM XT is an easy to use design tool that allowed us to quickly consider design choices that could be used to develop an effective rapid beverage cooling design.

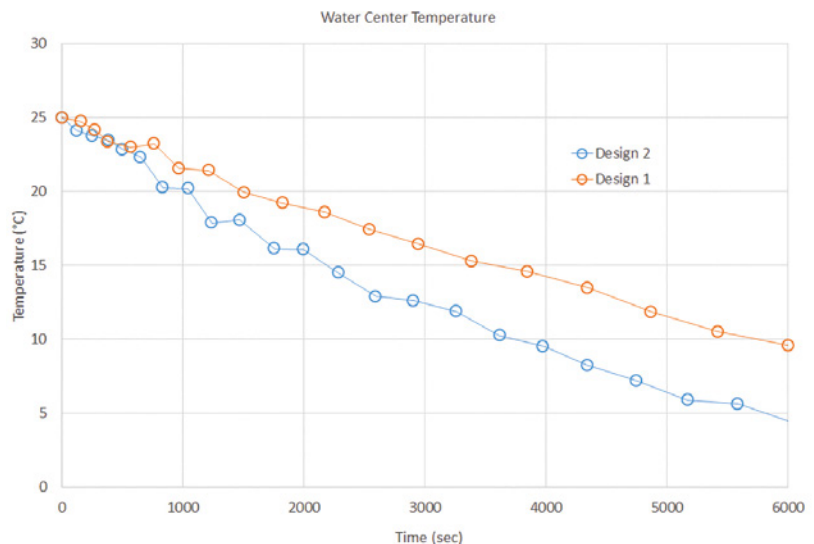


Figure 8. Water center temperature vs. time

Bitcoin Mining: A Thermal Perspective

By John Wilson, Technical Marketing Engineer, Mentor, a Siemens Business

Bitcoin is arguably the most well-known of the crypto-currencies in part because it has been around for nearly 10 years and has increased in value dramatically over the last few years. Another reason Bitcoin is in the news has to do with the high energy usage of the crypto-currency mining industry. For example, Iceland is a popular destination for Bitcoin mining because energy costs are very low, temperatures are cool, and internet speeds are high. It is estimated that the Bitcoin mining industry in Iceland will use about 840 gigawatt hours of electricity in 2018, which is more than all of Iceland's homes did in 2017 (Morris, 2018). Why does Bitcoin mining consume such large amounts of electricity and how is that related to thermal engineering?

What is Bitcoin Mining?

Simply put, Bitcoin miners run a hashing algorithm on computer hardware to determine the correct hash, a fixed length 64 character(256-bit) string, which represents a block of Bitcoin transactions. Once a miner has determined the correct hash, as verified by other miners, that block of data is added to the Bitcoin blockchain, which is an encrypted ledger of all Bitcoin transactions. The miner that determines the correct hash is rewarded Bitcoins (BTC), currently 12.5 BTC. The Bitcoin block mining reward halves every 210,000 blocks or about every 4 years.

The total number of Bitcoins that will ever be produced is 21 million, of which about 80% have been mined. It is estimated that the last Bitcoin will be mined in 2140. The time estimate should be accurate since the Bitcoin mining difficulty of generating the correct hash is managed such that a new block is added to the blockchain about every ten minutes. As the rate of block solutions, or hashes, increases, so does the difficulty of generating the correct hash. The current hash rate of the Bitcoin mining network is about 25 EHash/s (1018 Hash/sec).

Evolution of Bitcoin Mining

From 2009, when the first Bitcoins were



mined, to 2012, the Bitcoin mining network hash rate increased from MHash/s (106) to THash/s (1012) to today's EHash/sec (1018) and as a result mining hardware has evolved. In the early days miners could use their CPUs to mine at a hash rate on the order of MHash/s. Desktop computers could also be used to mine or dedicated custom mining rigs like the one shown in Figure 1. Note the excessive use of cooling fans on each chip. Many mining rigs are simply a collection of existing systems with little redesign with respect to cooling efficiency.

As the hash rate of the network has increased, two important metrics have emerged. The first metric is simply the hash rate of the mining hardware. Similar to a single ticket in a raffle, the odds of winning are greatly increased with more than one ticket, but it only takes one to win. The greater the hash rate the greater the chance of calculating the correct hash. It is therefore much more likely that many calculations will be required, so in addition to the hash rate it is important to consider the efficiency of each calculation, or the energy required to produce the hash. The second metric that is used when comparing mining hardware is the energy consumed per hash.

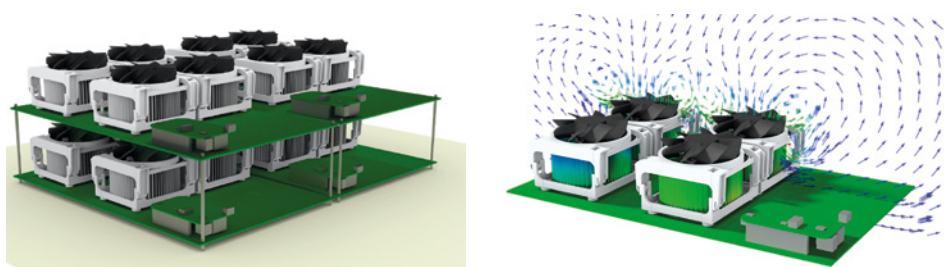


Figure 1. CPU mining rig

Because of low hash rates as compared to the Bitcoin network and efficiencies in the J/MH (Joule per Mega-Hash) range CPU, mining using CPUs became financially unviable (Mining - Bitcoin Wiki, 2018) and evolved to the use of GPUs. The popularity of GPUs was presumably aided by the availability of off-the-shelf graphics cards with integrated cooling solutions, as shown in Figure 2, and the ability to scale up to an entire mining rig fairly easily.

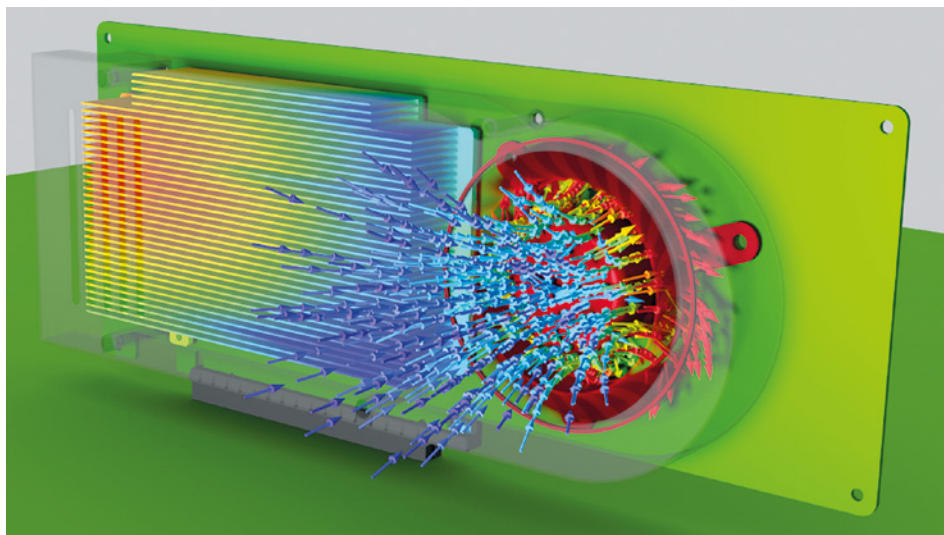


Figure 2. GPU graphics card

Bitcoin mining subsequently evolved to the use of FPGAs that offer hash rates similar to a GPU with increased efficiency due to lower power consumption as compared to a GPU. In 2013, the first ASIC specifically designed for Bitcoin mining was released (Mining - Bitcoin Wiki, 2018). The year the ASIC was introduced the Bitcoin mining network hash rate increased from THash/s (1012) to PHash/s (1015) range and BTC increased in the open market from about \$100/BTC to around \$1000/BTC by the end of the year (Bitcoin.com Charts, 2018). Note that it peaked at \$20,000/BTC in December 2017 but has fallen to the \$7,000/BTC mark recently.

a miner might invest in a USB miner, as shown in Figure 3. At the higher end there are mining rigs available like that shown in Figure 4 (from companies such as Bitmain with its AntMiner units).

For Bitcoin miners looking for an off-the-shelf solutions that use ASICs there are a number of options available that address varying investment comfort levels. At the lower end,

The USB miner is clearly a low power solution that is limited by the USB port capability. Even at the 2.5W maximum power supplied by the USB port, the heatsinked ASICs on the device can get very warm. The ASIC temperatures are well within typical

operating limits but the heatsink would feel hot to the touch. You often see these devices operating with one or more fans directing air across them. USB miners offer hash rates in the 1GH/s range with efficiencies of about 1 J/GH, easily outperforming the CPU based miners from the early days of 2009. The ASIC mining rig will have multiple PCBs filled with Bitcoin-hashing ASICs and will consume about 1 KW. Rather than a collection of existing systems this type of rig has more of a holistic cooling approach. The cooling strategy might therefore involve forced convection with two fans in a push-pull arrangement. The ASICs will have heatsinks, either a monolithic approach as shown in Figure 5, or simply a small heatsink mounted on each ASIC with thermal adhesive. Mining rigs offer fantastic performance with hash rates in the 1TH/s range and efficiencies of 0.1 J/GH although they do require a significant initial investment of ~\$1,000 - \$3,000 in equipment.

On an even bigger scale of Bitcoin mining there are mining farms. These large mining operations are located in regions that have low energy costs like Iceland (with its cheap geothermal energy and cold air cooling climate), or central Washington State in the United States (with its cheap hydropower). The buildings used in mining farms (Figure 6) are typically much more like a barn or warehouse or shipping container than a datacenter. These operations clearly use megawatts of electricity and cost \$10,000,000s to build and millions of dollars a month just to maintain.

The Bitcoin farms in places like Iceland also benefit from the year-round cool air that can be drawn in via vents on the building exterior, and across the mining equipment, exhausting from the roof of the building (Figure 7).

Challenges and Opportunities

Nearly all of the technical innovation in the Bitcoin mining industry has happened at the IC package level with the development of the Bitcoin mining ASIC. Innovations continue at the IC package level that will no doubt provide higher hash rates but presumably at an increased power. Other areas of innovation will involve submerging the mining rigs in oil or engineered fluids suitable for electronics (i.e. liquid cooling). The advantage of this approach is the ASICs could be more densely packed and could operate in a much smaller facility than the current Bitcoin farm approach.

It was much easier to mine for Bitcoin when they had essentially no value. Now today BTC trades for thousands of dollars and the

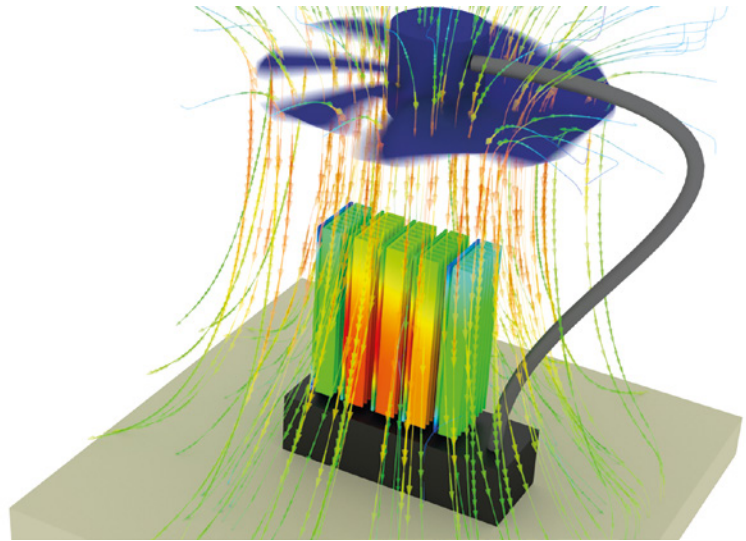


Figure 3. Typical Bitcoin ASIC USB miner

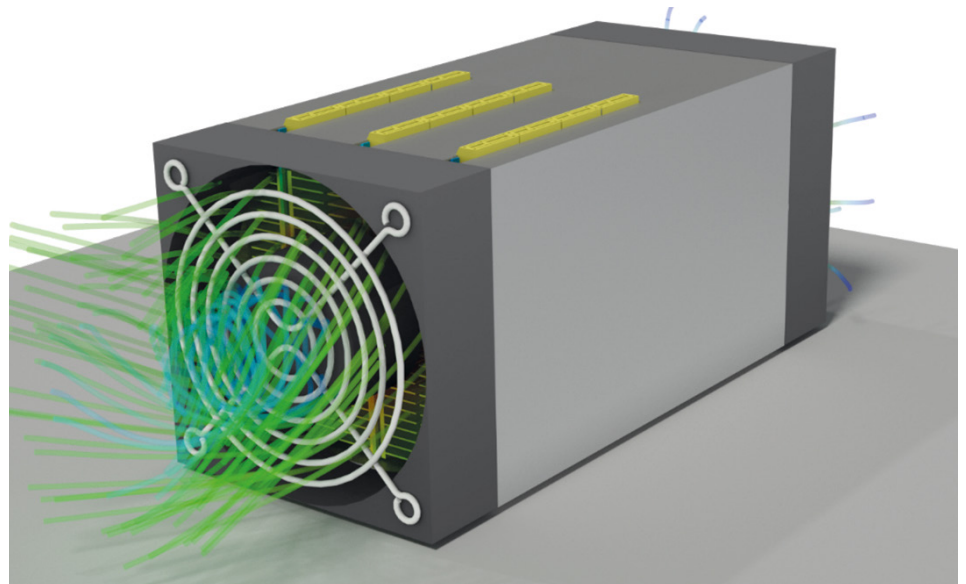


Figure 4. Typical Bitcoin ASIC mining rig

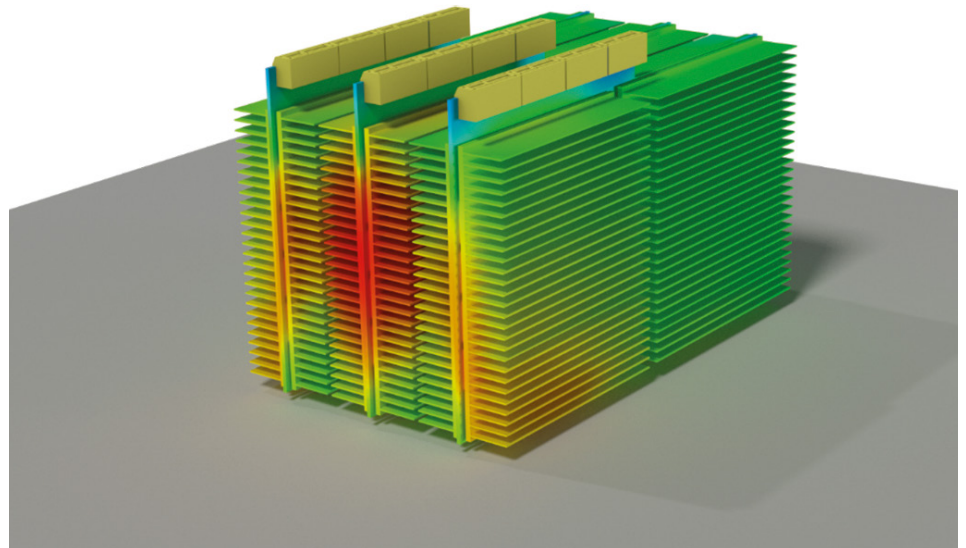


Figure 5. Typical Bitcoin ASIC mining rig internals

mining network hash rate is at the EHash/s level which makes it very difficult for a small mining operation to compete, or even turn over a profit. As a result individual miners join mining pools where resources are pooled and rewards are split.

Our conclusion from a thermal perspective is that the cost of mining for cryptocurrencies in terms of electronics cooling capital costs and 24/7 electricity usage and maintenance costs are such that it might be a better use of your cash to buy a lottery ticket especially as the gold rush and diminishing number of coins to be mined accelerates. Moreover, there is a major ethical question over the use of our planet's power generation resources (which are stretched as it is) for something that essentially appears to be speculative mining to gain a fortune in cryptocurrencies in what may turn out to be a commodity bubble. Indeed, cryptocurrencies are known to be used extensively in the dark web, money laundering and drug deals. Only time will tell on the cryptocurrency mining boom, and of course the big traditional banks are actually better placed today with their massive datacenters to do hashing calculations for block chain creation than rough and ready mining operations. However, we do think that there will definitely be a place in the cashless world and banking sector of the future for block chain creation algorithms and computer datacenters because of its secure encryption capabilities.

References:

- [1] Bitcoin.com Charts. (2018, March 28). Retrieved from <https://charts.bitcoin.com/chart/hash-rate>
- [2] Mining - Bitcoin Wiki. (2018, February 2018). Retrieved from <https://en.bitcoin.it/wiki/Mining>
- [3] Morris, C. (2018, February 13). Bitcoin Mining Uses More Energy Than Homes Do in Iceland. Retrieved from Fortune.com: <http://fortune.com/2018/02/13/iceland-bitcoin-mining-electricity/>

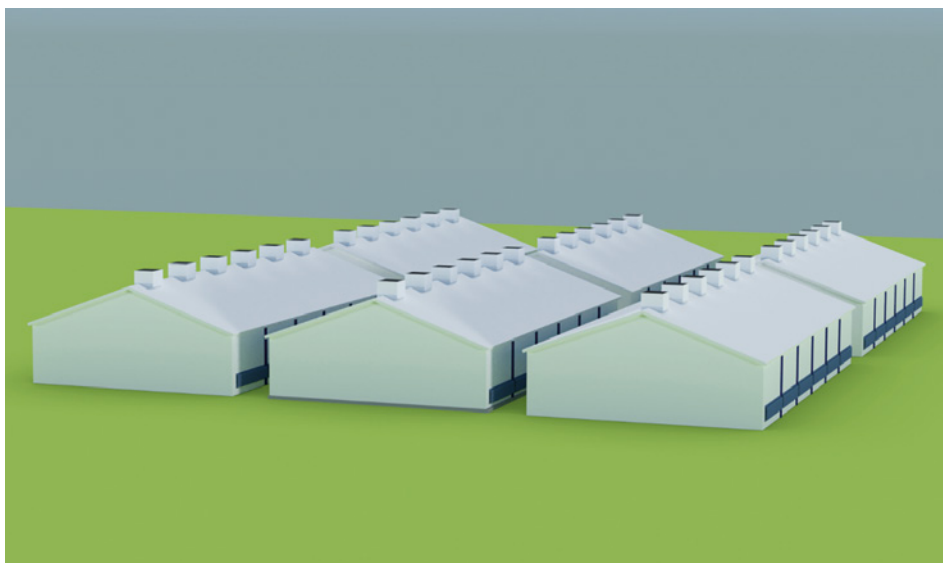


Figure 6. Typical Bitcoin mining farm (effectively a Datacenter)

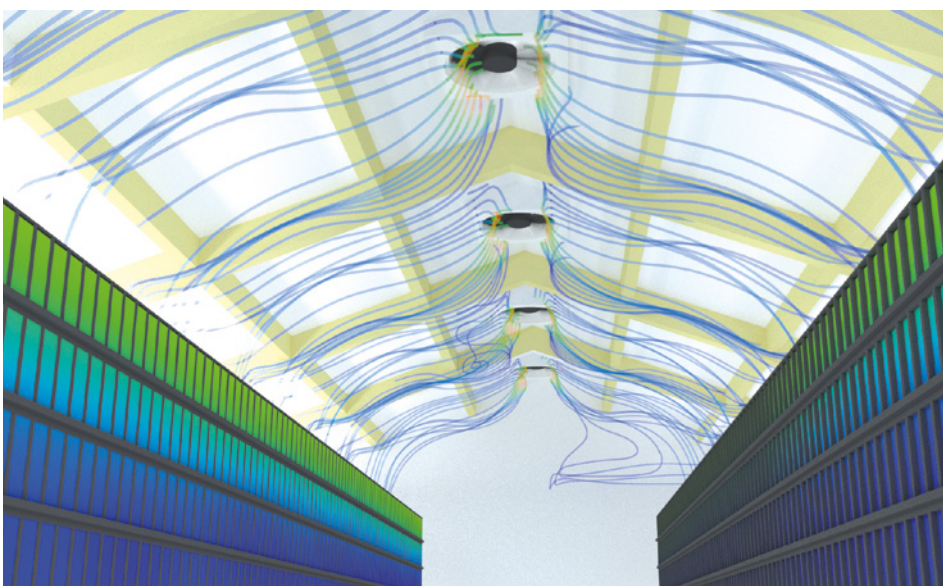
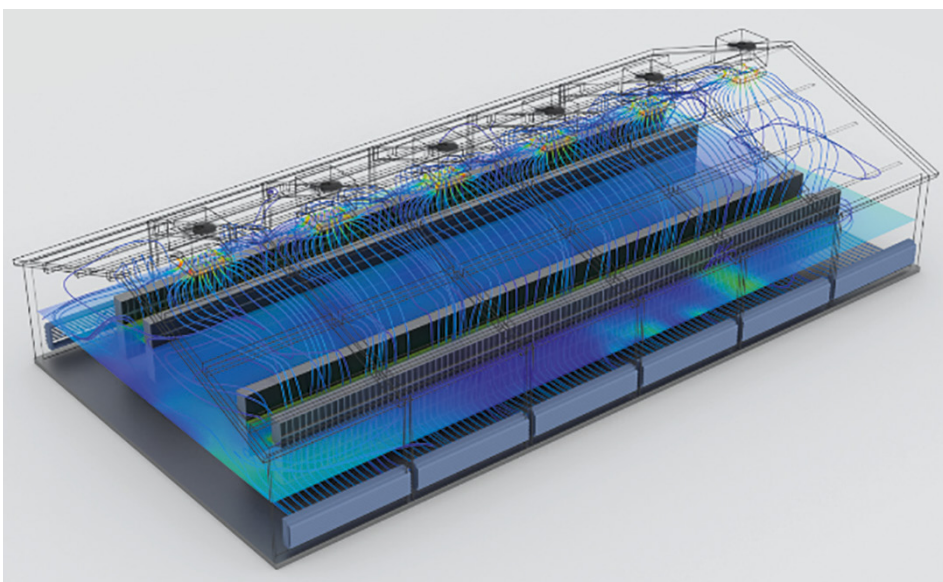


Figure 7. Typical Bitcoin Farm Ventilation Flow and Exhaust System

Simulation is Key to Design of High-Efficiency, Low-Cost **Synchronous Reluctance Motor**

By George Holling, Technical Director, Rocky Mountain Technologies

Synchronous reluctance motors are increasingly being used in a wide range of industrial applications because of their unique combination of high efficiency, high power density and low manufacturing costs. In designing this motor, the ability to accurately simulate the performance of a given design point was critical because each motor prototype can cost \$15,000 to \$20,000.

“We have evaluated all of the major motor simulation tools and Mentor’s MagNet simulation environment is the only one we have found that meets our goal of 0.5% accuracy in predicting efficiency,” said George Holling, Technical Director at Rocky Mountain Technologies. Rocky Mountain Technologies engineers modeled the motor using MagNet, modeled the motor drive in Mathworks’ Simulink and developed a custom optimization routine that choreographs a co-simulation of the two models to explore the design space. “Our engineers started with an initial design concept that produced 400 watts at 19.5% efficiency and iterated to a final design that produces 1 kilowatt at 94.5% efficiency,” Holling said.

The advent of synchronous reluctance motors

The synchronous reluctance motor is one of the simplest of all electric motor designs but it has rarely been used in industrial applications until recently because modern digital electronics has reduced the cost of the complex control circuitry required with this type of motor. The operating principle of the motor is that magnetic material in a magnetic field will orient itself towards the magnetic pole so as to minimize the reluctance of the magnetic circuit. The stator is usually similar to a permanent magnet brushless DC motor with multiple projecting electromagnet poles. The rotor,

on the other hand, has neither windings nor permanent magnets, instead consisting of a magnetic material with multiple projections acting as magnetic poles through magnetic reluctance. When a stator pole is energized, the nearest rotor pole is pulled into alignment with it. The stator field then rotates in advance of the rotor poles to spin the motor.

Rocky Mountain Technologies engineers were confident that if they could deliver a less-expensive synchronous reluctance motor in the same footprint with the same level of efficiency as the older motor then they would get the order. “We knew upfront we would need to evaluate a large number of design points in order to meet the customer’s requirements,” Holling said. “Building several iterations of prototypes was not affordable so we needed the ability to accurately predict the performance of the proposed design. A few years ago we worked with the Navy to evaluate the performance of the leading motor simulation software packages. We found that the torque and losses predicted by MagNet and one other package matched closely the physical results that we measured on an actual motor design. We selected MagNet because it simulates a wider range of designs including the ability to simulate the 6 degrees of freedom in motions of magnetic bearings which are increasingly being used in electric motors.”

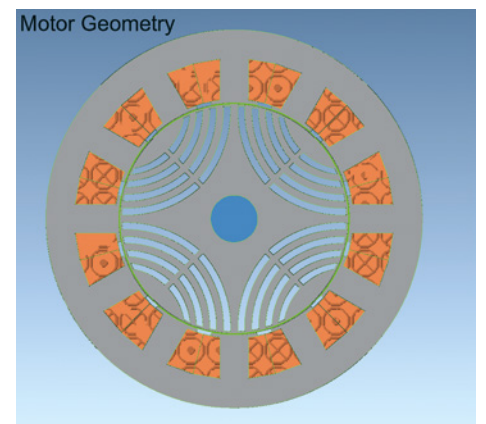


Figure 1. Motor geometry

Simulating the new motor design

Rocky Mountain Technologies engineers have found using idealized waveforms such as sinewaves to simulate the drive has a negative impact on motor simulation accuracy. So in this case they simulated the drive including filters, current limiting algorithms and pulse width modulation (PWM) frequencies in Mathworks Simulink software and applied the resulting realistic waveforms to the transient motor model. The motor model responds to these voltages and calculates the motor position, speed and current. These values are fed back to the control model which takes them into account in determining the voltages to be applied to the motor at the next time step. Since this was a four-pole machine, an electrical cycle consists of half a revolution and the co-simulation for each design point was run for one complete electrical cycle after stabilization.

The air gap diameter, shaft diameter and outer diameter of the motor were fixed by the customer’s requirements while others such as number of stator poles were determined during the design optimization. Engineers modeled their initial concept design in MagNet by selecting the rotor pole and slot combinations, rotor and stator dimensions, material choices, stator winding details such number of turns, and electrical parameters such as phase vector control and drive current. They took advantage of the symmetry and needed to only model 1/4 of the motor, which helps to reduce the computational time for each iteration. The simulation of the initial design in MagNet revealed substantial losses in both the windings and the core of the stator. Rocky Mountain Technologies engineers used a custom optimization routine that they developed in MATLAB to drive the simulation of the motor through many iterations while modifying 20 different design parameters with the goal of maximizing motor efficiency while achieving the required 1 kilowatt power output and reducing the volume of the motor to control manufacturing costs.

Increasing efficiency to 94.5%

The engineers started the optimization process with a design that produced only 400 W at 26.2% efficiency. The software automatically optimized the motor design until its efficiency could no longer be improved. The final design achieves 1 kilowatt at 94.5% efficiency, meeting all the customer’s requirements. Only at this point did Rocky Mountain Technologies build a physical prototype. Testing of the prototype showed that its performance matched the

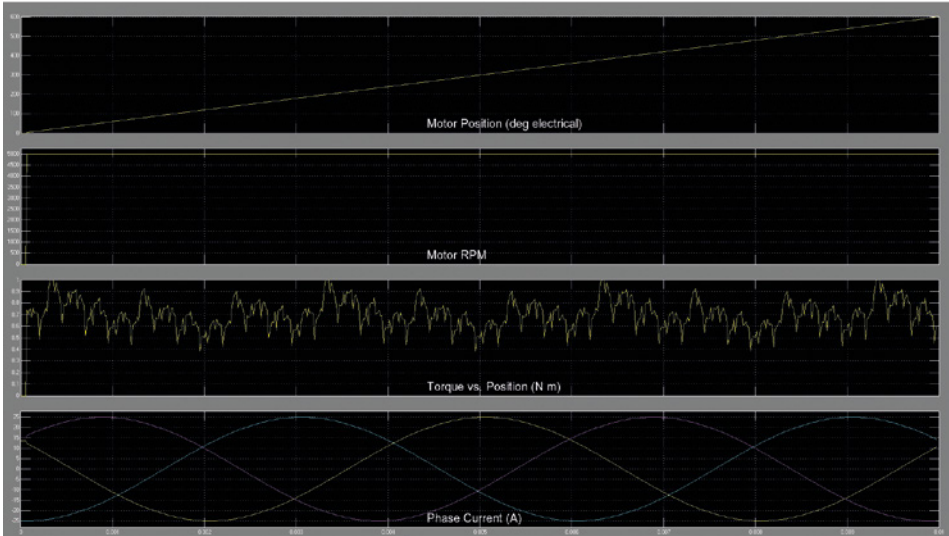


Figure 2. Modeled motor waveforms

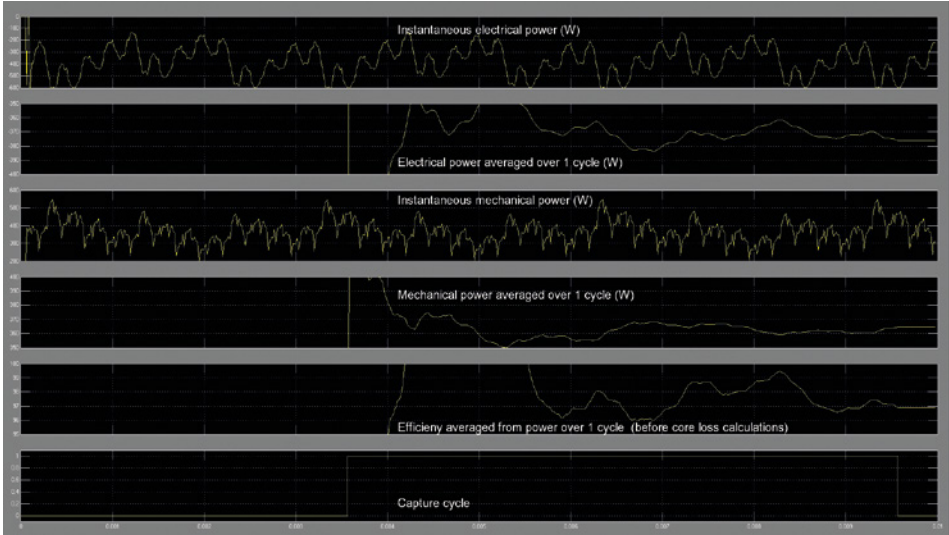


Figure 3. Modeled system performance

simulation nearly perfectly. Rocky Mountain Technologies won the order based on the fact that it can deliver synchronous reluctance motors at a considerably lower cost than permanent magnet motors of the same capacity.

“The ability of the MagNet software to accurately predict efficiency and other key performance parameters made it possible to optimize the performance of this motor to levels that would have been impossible to achieve with synchronous reluctance motors just a few years ago,” Holling concluded. “At the same time, simulation has enabled us to reduce the number of physical prototypes for the vast majority of motors we design to just one, which saves money and makes it possible to get new motors to our customers in less time and at a lower cost.”

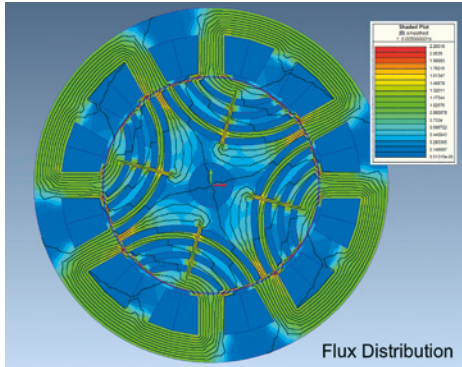


Figure 4. Flux distribution

Delphi4LED - From Measurements to Standardized Multi-Domain **Compact Models of LEDs**

A Report on the Thermal Modeling Aspects

By Genevieve Martin, Phillips Lighting



The rise of LED technology is changing the ecosystem of the lighting industry. With the commoditization of LED, Delphi4LED, a European Union consortium, is providing a solution to this dynamic market. It is providing the EU LED Lighting industry with a set of methodologies and standards to enable the design and production of more reliable, cost effective and market-leading LED-based lighting solutions.

Although LEDs are very efficient, and therefore dissipate much less heat than conventional light sources such as incandescent, halogen or high-intensity discharge lamps, their efficiency is dependent on the LED temperature. This temperature depends on how effectively the LED dissipates its power to the surrounding environment, the amount of heat dissipated by the device and the effectiveness of the heat transfer paths inside the LED component. Thermal-optical-electrical parameters are inter-related but incomplete or even erroneous in datasheets of LED suppliers.

At luminaire developers, this results in considerable reverse engineering effort to get the proper product information about packaged LED. Ways to do this include material analysis, cross-section analysis, computer simulation and measurements. All these reverse engineering techniques combined lead to reasonable results but require long development time and cost a lot of money. For example the exact package dimensions and materials properties – specific features and parameters of the LED chip and phosphors – are unfortunately proprietary information of LED suppliers and cannot be expected to be publicly shared.

The Delphi4LED consortium includes 15 partners from seven countries and seeks to identify and exercise methods to extract

and use multi-domain compact models of LEDs. A modular approach to such compact models [1], [2], [3], [4] would then be employed to enable lighting designers to meet both thermal reliability and optical design goals (Figure 1).

Such models take forward current as an input, and calculate emitted optical properties such as luminous flux as well as operating junction temperature for each LED in a design. The temperature dependence of the conversion of electrons to photons is considered, which impacts the resulting thermal power dissipation which in turn affects the temperature etc. It is this electro-optical-thermal coupling that necessitates all three domains to be considered concurrently in a single multi-domain modular compact model.

From the thermal perspective, although methods such as DELPHI exist to extract compact thermal models (CTMs) of monolithic single heat source IC packages, LEDs can have multiple heat sources. This is the case for White LEDs where additional heat is dissipated in phosphor layers due to Stokes shift light conversion losses. In addition LED packages may have multiple LED chips within them as is the case for Chip on Board (CoB). Temperature prediction at each chip junction, in each phosphor layer and also at solder points is required to ensure reliability in operation.

Dimming behavior and operation under AC conditions also necessitates that these CTMs are capable of dynamic prediction, i.e. dynamic compact thermal models (DCTMs).

To extract such DCTMs, Delphi4LED is determining a methodology that starts with a physical LED sample, performs a transient thermal measurement, uses that to calibrate a 3D detailed thermal model and from that a DCTM with an assumed nodal topology may be extracted (Figure 2).

T3Ster and TeraLED are used to perform the transient thermal response measurement in compliance with the latest JEDEC LED testing standards and recommendations of CIE, such as JESD51-51, JESD51-52 and CIE 225:2017 [5], [6], [7]. The total emitted optical power is measured by the TeraLED integrating sphere, the resulting thermal power dissipation (the difference between the electrical supplied power and the optically emitted power) is used to correct the resulting Zth profiles ((Tj-Ta)/ thermal dissipated power) vs. time. An important aspect of these combined thermal and optical measurements is that the LEDs' junction temperature is kept at known, constant value as also recommended by the CIE 225:2017 technical report. As a side product of such a test procedure, the temperature dependence of the light output properties of the LEDs can also be measured.

A FloTHERM model of an LED package is then constructed of the same configuration used for the T3Ster+TeraLED measurement (Figure 3).

FloTHERM's calibration feature is then used to fine tune material properties along the heat flow path until such time as simulated Zth responses (and corresponding structure function profiles) match the measurement. This entails nomination of those materials properties that are both most unknown and contribute most to the overall thermal resistance. In this case the chip submount, bottom die attach and FR4 thermal conductivities. Upper and lower bounds of those parameters are defined, a (computational) design of experiments set and solved then a gradient based optimization used to determine which parameter values result in the smallest deviation between measured and simulated transient thermal response curves (Figure 4).

Unlike the measurement that was limited to only being capable of recording the

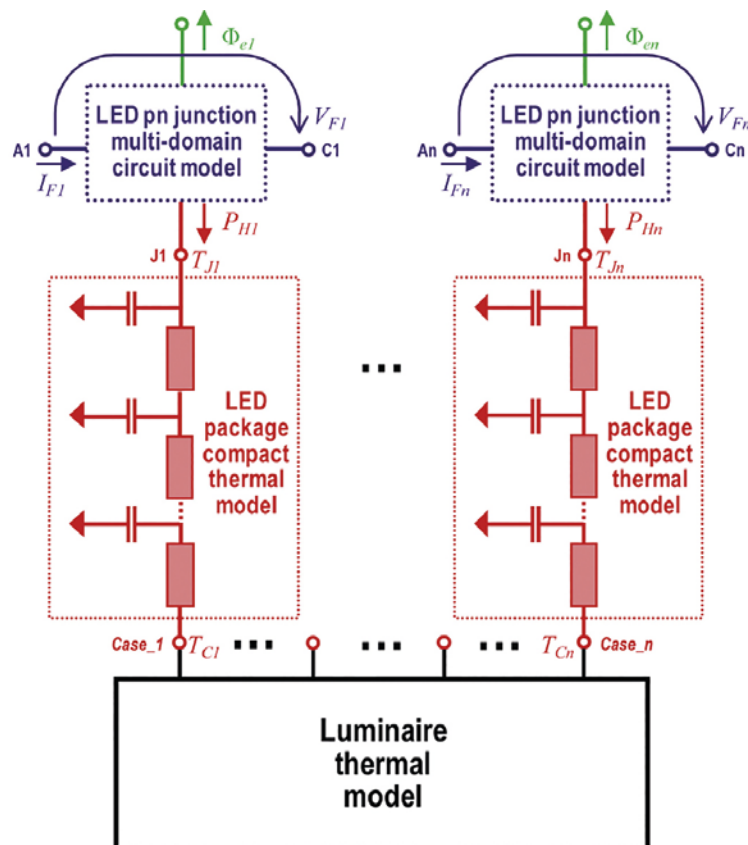


Figure 1. Multi-domain compact model of Multiple LEDs within their Operating Environment [3], [4]

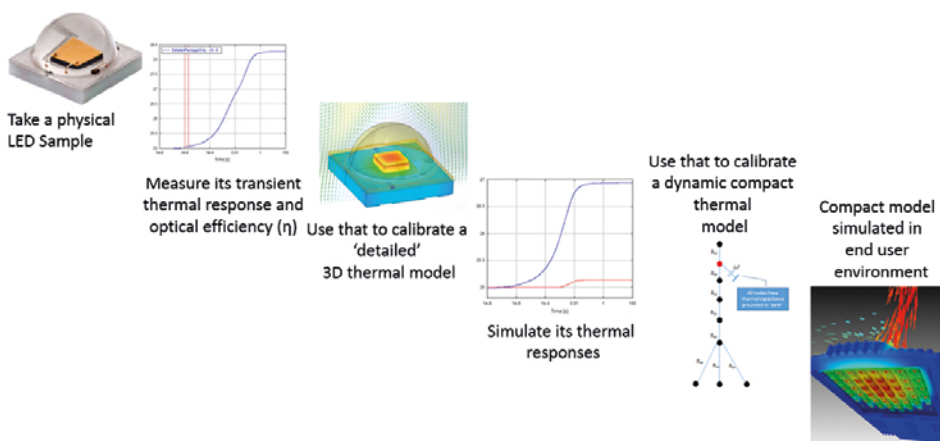


Figure 2. Dynamic compact thermal model extraction process

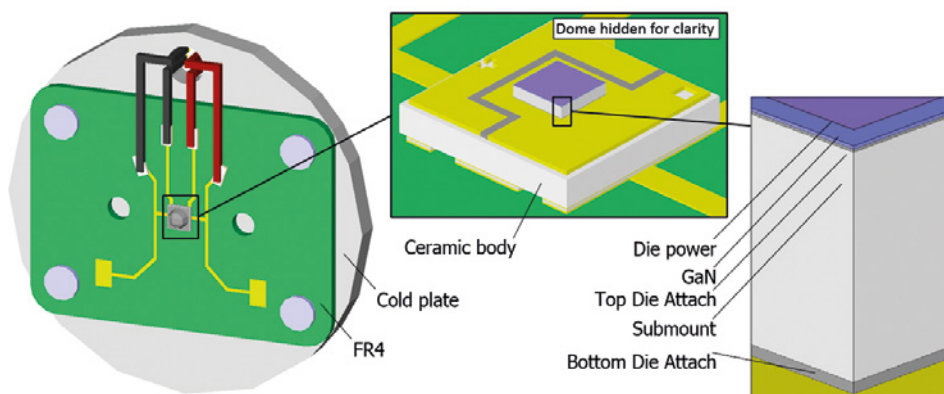


Figure 3. Cree XP-E2 Blue LED on FR4 on coldplate [8]

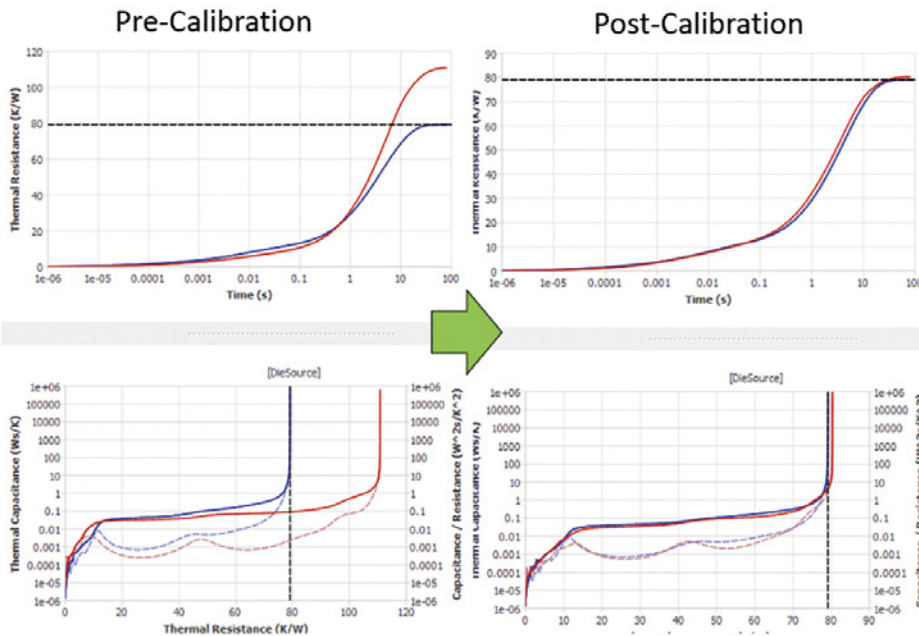


Figure 4. Pre- and post-calibration Zth (top) and Structure Function (bottom) comparisons. red = Simulated response. Blue = Measured response.

chip junction thermal response, the 3D FloTHERM model is capable of predicting temperature and 1000s of points. This additional simulated thermal response behavior is subsequently used to calibrate the thermal resistance and capacitance values at certain points in a nodal DCTM.

The topology of the DCTM has been determined having enough points so as to capture the dominant thermal time constants experienced along the heat flow path (Figure 5)

The heat flow path within the package, away from the package periphery, is boundary condition independent and can be represented with thermal resistance (R) and thermal capacitance (C) values taken directly from the measured structure function. The R and C values nearer the package periphery have to be determined so that the thermal response of the DCTM at both junction and solder point nodes match with the corresponding points of the 3D detailed model. The same calibration methodology is applied to achieve this, considering the DCTM in isolation with representative boundary heat transfer coefficients applied on top and bottom surfaces. In this case there are two pairs of curves that need to match, the driving point impedance at the junction as well as the transfer impedance of the solder point. The results of the DCTM calibration are shown in Figure 6.

A verification of the accuracy of the DCTM can be ascertained by comparing the resulting thermal response when the

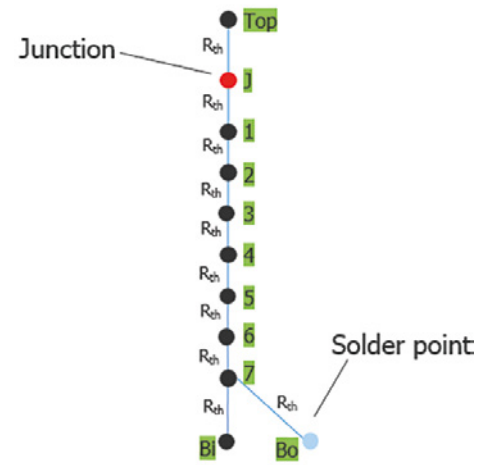


Figure 5. Nodal DCTM topology (thermal capacitance values at each node, not shown for clarity)

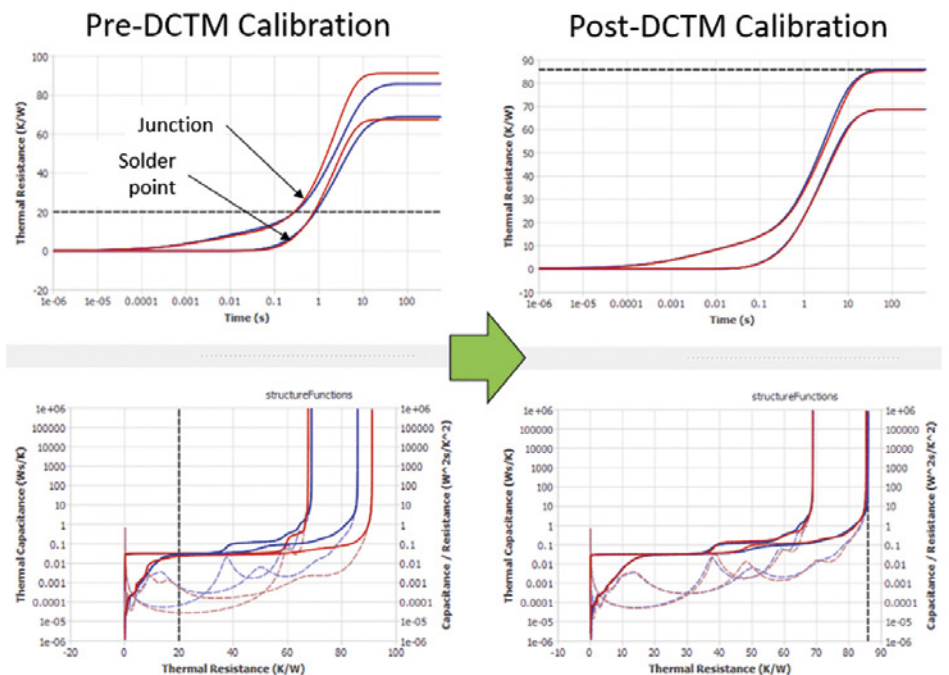


Figure 6. Pre- and post-DCTM calibration Zth (top) and Structure Function (bottom) comparisons. Red = DCTM response. Blue = 3D Detailed model response.

DCTM is placed back into the full system level model representing the original T3Ster+TeraLED measurement (Figure 6)

A maximum error of 4.5% in dT prediction is noted, but only during 1-10s of the transient thermal response. Steady state temperature prediction is highly accurate.

The same methodology is being extended in the Delphi4LED project to extract boundary condition independent DCTMs by calibrating

R and C values so that all thermal response at all points of interest are accurate over a set of differing top and bottom heat transfer coefficient values. The number of points of interest may be extended to incorporate other dissipating nodes (i.e. nodes representing phosphor conversion) and additional solder point temperatures.

Coupled with a chip level model of LEDs (extracted directly from measurement) describing the temperature dependent electrical and optical characteristics, the DCTM forms part of the multi domain compact model. An accurate representation of the LED capable of providing thermal and optical information quickly and easily so that lighting designers may meet both functional and reliability product specifications.

References:

- [1] R. Bornoff, V. Hildenbrand, S. Lugten, G. Martin, C. Marty, A. Poppe, M. Rencz, W. Schilders, J. Yu, Delphi4LED - From Measurements to Standardized Multi-Domain Compact Models of LEDs: a New European R&D Project for Predictive and Efficient Multi-domain Modeling and Simulation of LEDs at all Integration Levels Along the SSL Supply Chain, Thermnic 2016, Budapest, Hungary
- [2] www.delphi4LED.org
- [3] A. Poppe, J. Hegedűs, A. Szalai, R. Bornoff, J. Dyson, "Creating multi-port thermal network models of LED luminaires for application in system level multi-domain simulation using SPICE-like solvers", In: Proc. of the 32nd IEEE SEMI-THERM Symp., 14-17 March 2016, San Jose, USA, pp. 44-49, DOI: 10.1109/SEMI-THERM.2016.7458444
- [4] A. Poppe, "Simulation of LED Based Luminaires by Using Multi-Domain Compact Models of LEDs and Compact Thermal Models of their Thermal Environment", MICROELECTRONICS RELIABILITY 72:(5) pp. 65-74. (2017), <http://dx.doi.org/10.1016/j.microrel.2017.03.039>
- [5] JEDEC JESD51-51 Standard "Implementation of the Electrical Test Method for the Measurement of Real Thermal Resistance and Impedance of Light-Emitting Diodes with Exposed Cooling" (2012), <https://www.jedec.org/system/files/docs/JESD51-51.pdf>
- [6] JEDEC JESD51-52 Standard "Guidelines for Combining CIE 127:2007 Total Flux Measurements with Thermal Measurements of LEDs with Exposed Cooling Surface" (2012),

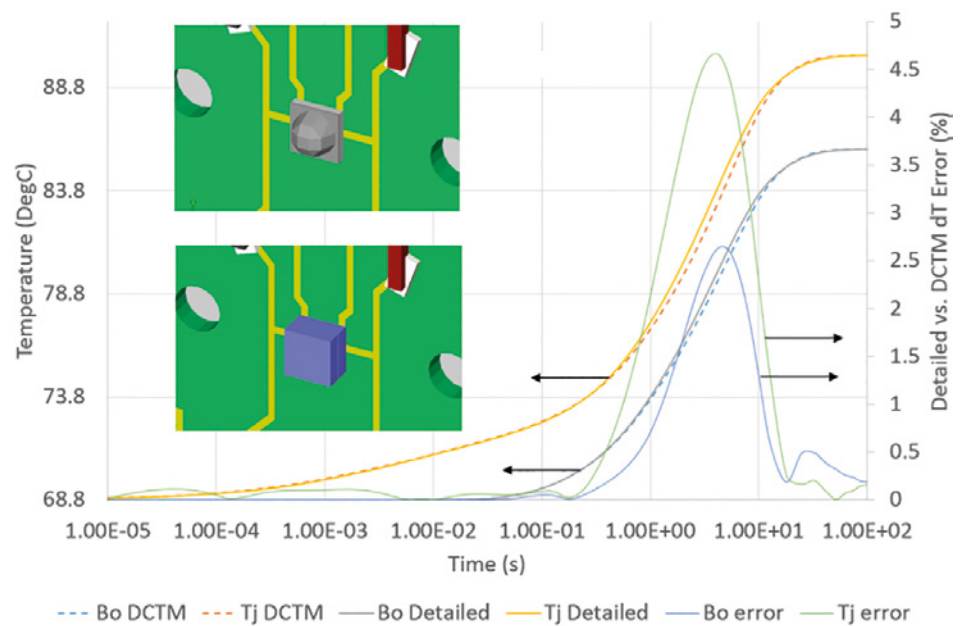


Figure 7. DCTM vs. 3D Detailed model comparisons

<https://www.jedec.org/system/files/docs/JESD51-52.pdf>

- [7] Y. Zong, P-T. Chou, P. Dekker, R. Distl, K. Godo, P. Hanselaer, G. Heidel, J. Hulett, K. Oshima, A. Poppe, G. Sauter, M. Schneider, H. Shen, M.M. Sisto, A. Sperling, R. Young, W. Zhao, "Optical Measurement of High- Power LEDs", CIE 225:2017 (Technical Report) ISBN 978-3-902842-12-1, DOI: 10.25039/TR.225.2017
- [8] R. Bornoff, G. Farkas, L. Gaal, M. Rencz, A. Poppe, "LED 3D Thermal Model Calibration against Measurement", In: Proceedings of the 19th International Conference on Thermal, Mechanical and Multiphysics Simulation and Experiments in Microelectronics and Microsystems (EuroSimE'18), 15-18 April 2018, Toulouse, France

A COOL Emulator

By Jean Paul Prevot, Mentor, a Siemens Business, Emulation Division



Mentor, a Siemens Business, Emulation Division designs, manufactures and sells a hardware emulation system under the Veloce® registered trademark. A wide range of semiconductor and systems manufacturers around the world verify their chip and system designs with the Veloce emulator.

They use the Veloce emulator because it is tens of thousands times faster than the alternative software simulation approaches thus boosting productivity in the verification of SoC and Intellectual Property (IP)-based designs. Veloce also accelerates block and full SoC RTL (Register Transfer Level) and gate-level simulations during all phases of the design process, and enables pre-silicon testing and debug at hardware speeds, using real-world data, while both hardware and software designs are still fluid.

The Veloce Strato platform, is the current generation of the Veloce platform (Figure 1).

Mentor's emulation division has been a leader in the development of emulators designed for the best energy use profile possible making the Veloce Strato emulator a very efficient and datacenter friendly tool. Despite this, tens of kW's in thermal energy, in total, are generated by the emulator's boards and AC/DC power modules during normal operation which need to be removed.

Since 2004, the Mentor Emulation Division has been using the FloTHERM® electronics cooling CFD product to optimize internal airflow and cooling for the Veloce emulation platform.

The development of the Veloce StratoM configuration presented a number of mechanical engineering challenges. One was to fit the Veloce StratoM into the same system layout as the previous generation Veloce2 (same external dimensions) even though it has longer logic boards and increased logic board pitch. Another challenge was to define a unique logic board pitch compatible with cooling and midplane connector positioning rules dictated by the use of mixed technologies.

Increasingly, numerous constraints needed simultaneous management to comply with all macropackaging requirements in terms of:

- boards interconnect
- cabling
- accessibility
- mechanical strength and stability
- AC and DC powering
- cooling, sub-assemblies positioning
- audio noise control
- pressure drop limitation
- air inlet and air outlet locations
- EMC shielding
- safety norms compliance
- customer site access capability
- aesthetic
- system configurations, etc.

All while complying with manufacturing requirements in terms of design for manufacturing, parts commonality, cost optimization, etc.

Regarding cooling aspects, several complementary explorations were used to deal with cooling of both the chip package, logic boards, board module sub-assemblies and global system.

The team started with rough estimations for the global airflow needed to insure global heat dissipation, and manual calculations to determine fan types, to pre-dimension grid air inlets and outlets, and to consolidate board pitch and package heat-sink draft design. Because of the wide range of inputs, we were quickly led to build several CFD models using FloTHERM software modules.

By using FloTHERM PACK at the package level, we were able to easily obtain a compact thermal model of our chip package enabling us to integrate it into our logic board CFD model and to obtain a good estimation of junction temperature. (Figure 2)

The compact model provided the advantage of being computationally less



Figure 1. The Veloce StratoM emulator

expensive while still insuring reliability and accuracy. Both “2 resistors” as well as “Delphi” compact models, currently being standardized by the industry standards body JEDEC, were generated and used.

By using FloTHERM PCB at the board level, we were able to build our logic board CFD model using data imported directly from Expedition®. PCB layers, components and DC/DCs connectors were automatically built and then parameters were detailed to “dress” the model. Identification of a sufficiently accurate power dissipation estimate for each key component is a crucial phase and results are dependent on this data. Once the board’s model was available, we studied the central board assembly located in a “three pitch boards” model. This allowed us to perform package heatsink optimization in terms of efficiency and pressure drop and DC/DCs or component repositioning on PCB layout.

One of the numerous advantages of FloTHERM is the ability to detail, in exacting granularity, some components as package or heatsink and decide to use them with a simplified representation to save computation time while keeping a reliable model. We could also add dissipative zones to represent the heating effect of any deliberately missing components. In addition, the use of localized grids sped up the calculation.

We were able to determine the optimal temperature sensor positioning on PCB’s (numbered 1 to 3 in Figure 3); thermal sensors used to monitor fans’ speed while emulation is running, enabling us to manage audible noise levels.

We were able to study temperature at both PCB level and component level using the cross section thermal planes shown in Figure 4.

By using FloTHERM at the chassis level, we were able to optimize sub-assembly positioning inside the chassis—primarily board modules, air inlets, lower and upper fan drawers and fan positioning inside the drawers.

It was important to balance the air intakes, taking into account the front and rear areas for both lower and upper levels. We needed to prevent dead air zones inside the system due to the excessive air velocity at inlet, and lack of air plenum between fans and the board’s edge.

The last step was to build the entire system model to validate global heat transfer

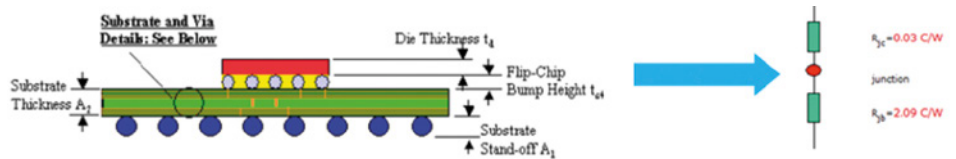


Figure 2. Example of compact model creation for one of Mentor’s packages

and verify the absence of dead areas or deleterious air recycling zones (inducing hot spots and/or audio noise disturbances) for different system configurations (board population, failed fans, etc.).

FloTHERM also helped us to dimension our copper DC busbar enabling us to take into account the Joule effect inside copper as it is carrying several hundreds of amperes, and to deal with current distribution all along the midplane.

Another highlight of our work was the use of FloVENT that let us study different system layouts at customer sites and analyse the benefits of using hoods to manage air exhaust through the ceiling.

To conclude, from the beginning of the Veloce Strato design, each step was taken to optimize air path, optimize air velocity and minimize pressure drop. Continuous effort was applied from the package to global system.

The main goal of using FloTHERM CFD software was to ensure optimum package junction temperature to reach the optimal electronic performance and reliably while using the minimum airflow. Thus allowing the system to operate within a reasonable temperature range.

FloTHERM CFD software is a great help in showing trends associated with parameter variations. Moreover, the “smart” pre- and post-processors offered by FloTHERM CFD modules help you understand your product so you can detect unexpected physical behavior and optimize the design. FloTHERM is like a bike; you never forget how to use it.

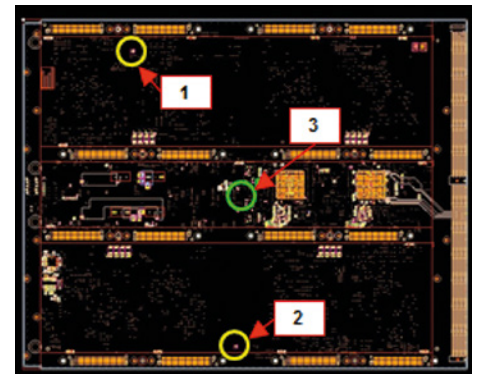


Figure 3. Mentor’s logic board thermal sensors positioning

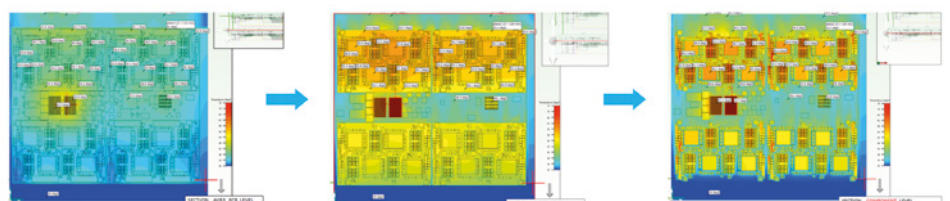
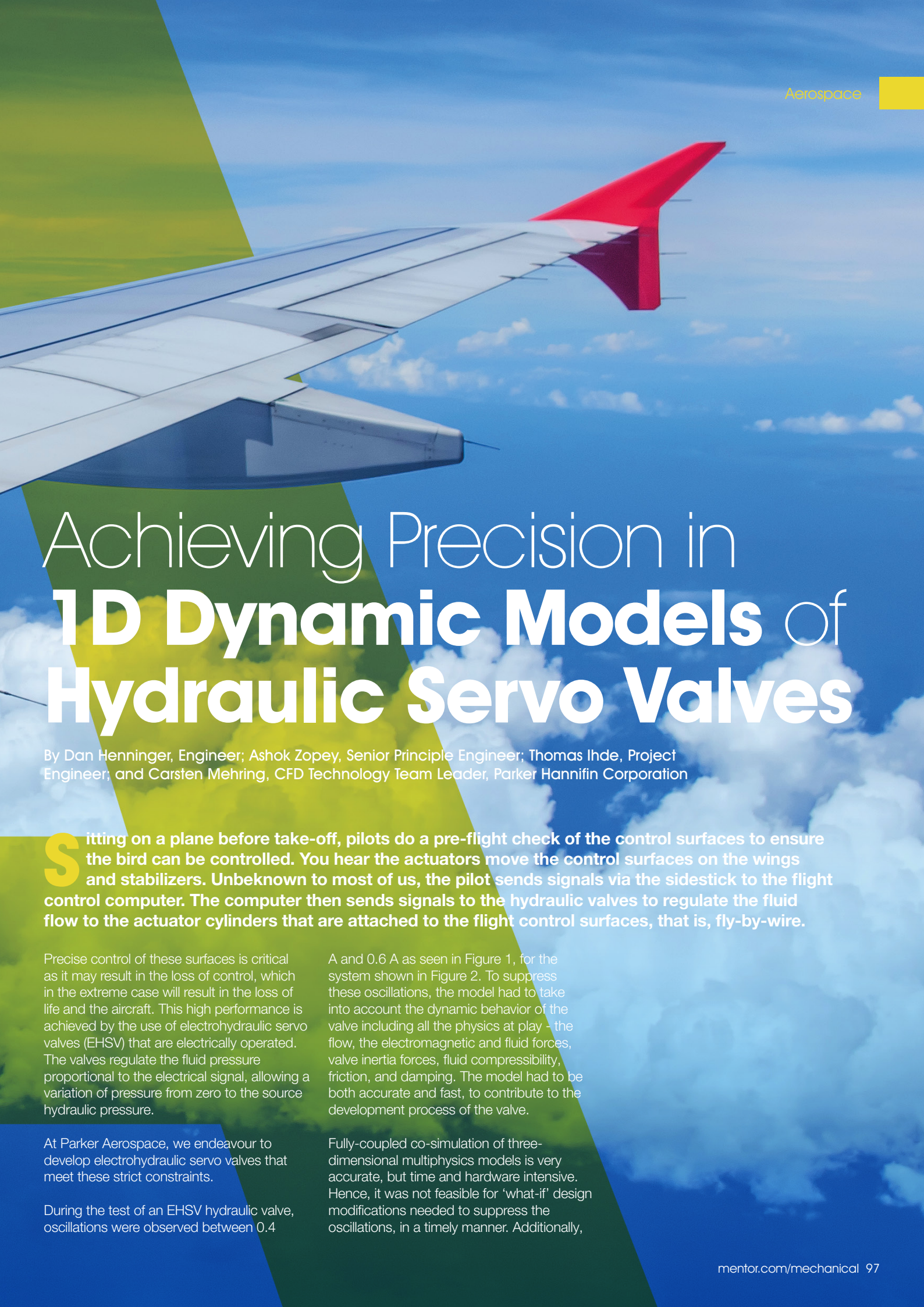


Figure 4. Mentor’s logic board thermal study - PCB / Components sections

Without the accuracy of MagNet in the computation of electromagnetic forces, it would have been very difficult to develop a dynamic 1D model. To be of use in the detection and suppression of valve oscillations, the model had to be able to detect minute changes in the force balance on the valve

Ashok Zohey, Senior Principle Engineer, Parker Aerospace



Achieving Precision in 1D Dynamic Models of Hydraulic Servo Valves

By Dan Henninger, Engineer; Ashok Zopey, Senior Principle Engineer; Thomas Ihde, Project Engineer; and Carsten Mehring, CFD Technology Team Leader, Parker Hannifin Corporation

Sitting on a plane before take-off, pilots do a pre-flight check of the control surfaces to ensure the bird can be controlled. You hear the actuators move the control surfaces on the wings and stabilizers. Unbeknown to most of us, the pilot sends signals via the sidestick to the flight control computer. The computer then sends signals to the hydraulic valves to regulate the fluid flow to the actuator cylinders that are attached to the flight control surfaces, that is, fly-by-wire.

Precise control of these surfaces is critical as it may result in the loss of control, which in the extreme case will result in the loss of life and the aircraft. This high performance is achieved by the use of electrohydraulic servo valves (EHSV) that are electrically operated. The valves regulate the fluid pressure proportional to the electrical signal, allowing a variation of pressure from zero to the source hydraulic pressure.

At Parker Aerospace, we endeavour to develop electrohydraulic servo valves that meet these strict constraints.

During the test of an EHSV hydraulic valve, oscillations were observed between 0.4

A and 0.6 A as seen in Figure 1, for the system shown in Figure 2. To suppress these oscillations, the model had to take into account the dynamic behavior of the valve including all the physics at play - the flow, the electromagnetic and fluid forces, valve inertia forces, fluid compressibility, friction, and damping. The model had to be both accurate and fast, to contribute to the development process of the valve.

Fully-coupled co-simulation of three-dimensional multiphysics models is very accurate, but time and hardware intensive. Hence, it was not feasible for 'what-if' design modifications needed to suppress the oscillations, in a timely manner. Additionally,

the co-simulation transient time-step is determined by the least time constant of the relevant physics phenomena. In this case, it is governed by the time-accurate spatial resolution of the local flow, which had to be realized by the Computation Fluid Dynamics (CFD) solver. Therefore, multiphysics co-simulation although highly accurate, loses one of the key simulation advantage - short analysis time needed to make decisions during product development. Lower-order models or simplistic handbook correlations are the fastest but of low dynamic fidelity.

A high-fidelity one-dimensional model of an electrohydraulic servo valve meets the need for dynamic analysis that includes all the physics, and fast analysis time. These models are invaluable in product development for what-if analysis during preliminary analysis, troubleshooting during qualification testing, and design optimization during the detailed design phase. At the system-level, these models capture the local transient phenomena that may have a decisive effect on the overall system behavior, and at the local level, the dynamic system-level interaction is considered.

Before delving into the development of the accurate 1D model, let us look at how the operation of the electrohydraulic servo valve.

Electrohydraulic Servo Valve (EHSV) System

The electrohydraulic servo valve system is shown in Figure 2. Figures 2 (a), (b) and (c) show the entire system including the controls, the details of the valve and the spool, respectively. The valve motion is controlled using two linear solenoids. Energizing Solenoid 1 moves the plunger-spool assembly linking the pressure supply (P_{supply}) to the extend side of the actuator (P_{extend}), and the retract side of the actuator ($P_{retract}$) to the return pressure (P_{return}), moving the actuator piston to the right. To move the actuator piston to the left, Solenoid 2 is energized. The speed of the actuator is controlled by the effective flow area of the servo valve (extend and retract), piston area, external load, and the supply or return pressure.

The actuator stroke is controlled by sensing the position via the linear variable differential transformer (LVDT) and comparing it to the commanded position ($X_{command}$). The resulting error signal is sent as a current command to either solenoid. The sign of the error determines which solenoid is energized, while its magnitude determines the valve opening and actuator velocity. The suppression of valve oscillations therefore requires the

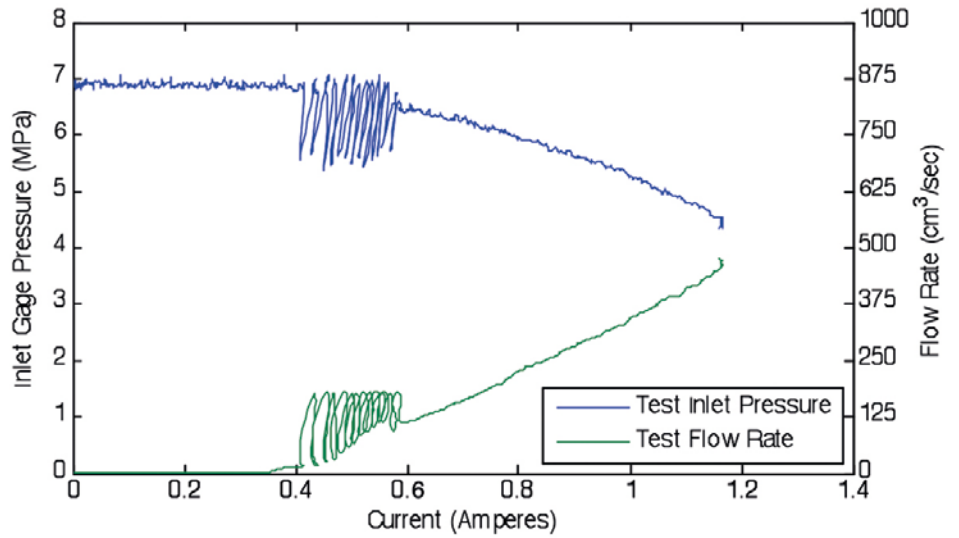
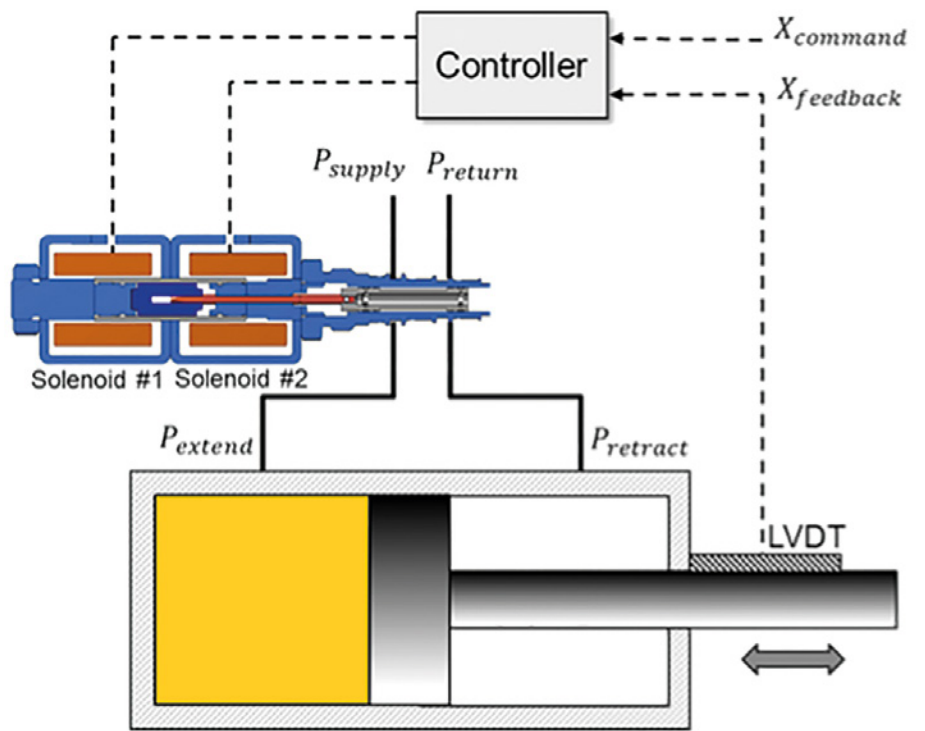
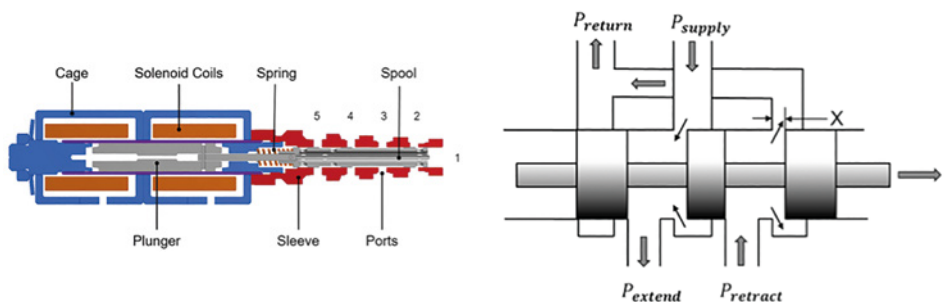


Figure 1. Test results of an EHSV hydraulic valve showing oscillations



a) Electrohydraulic servo valve system showing the solenoid and plunger that actuates the spool. The motion of the spool regulates the fluid flow to the cylinder through the ports.



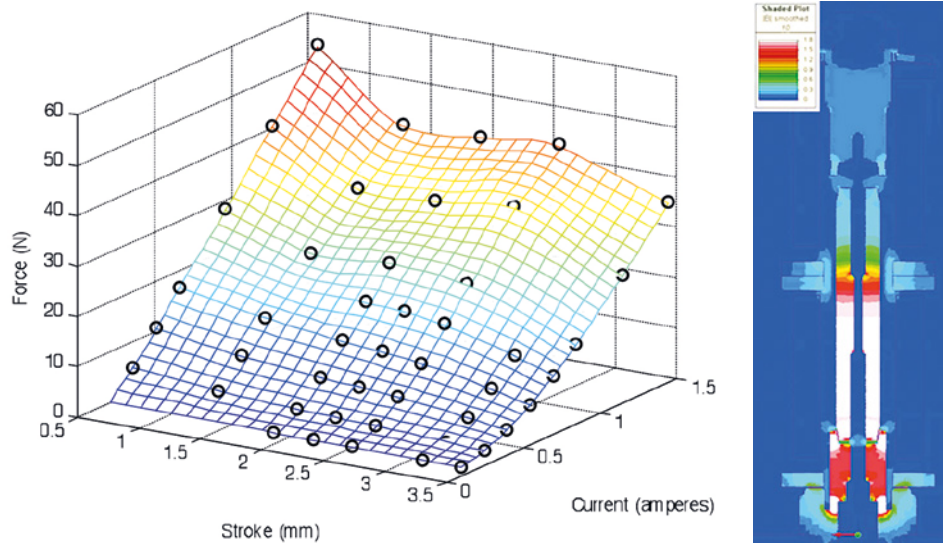
b) Details of the valve
c) Details of the spool [1]
Figure 2. Electrohydraulic servo valve (EHSV) system

accurate modeling of the forces experienced by the system.

The oscillations are caused by minute changes in the force balance on the moving valve body. Therefore, accurately predicting the solenoid's electromagnetic and the spool's fluid forces are critical in order to understand and remedy the oscillations. The same is true for any additional forces such as damping, which was included in the model but challenging to account accurately. Friction which was neglected.

Development of the 1D Dynamic Model

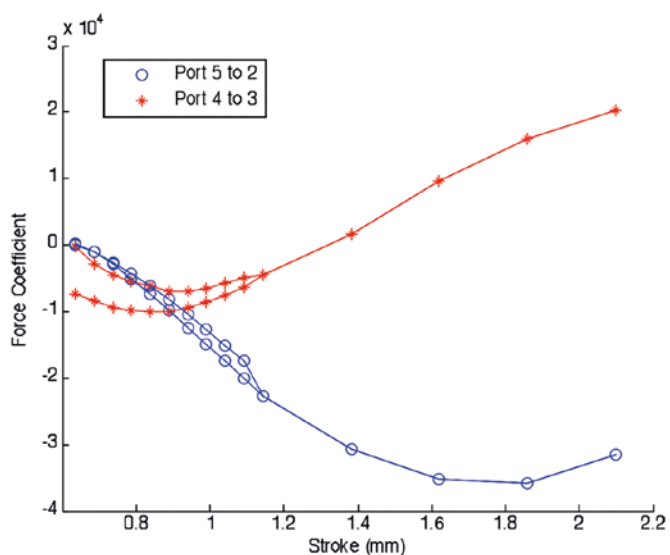
Development of the highly accurate dynamic model was completed in phases. First, simple sub-models that use empirical or handbook information in representing complex electromagnetic and fluid forces, were used. Comprehensive 3D analysis of complex electromagnetic fields and fluid flow



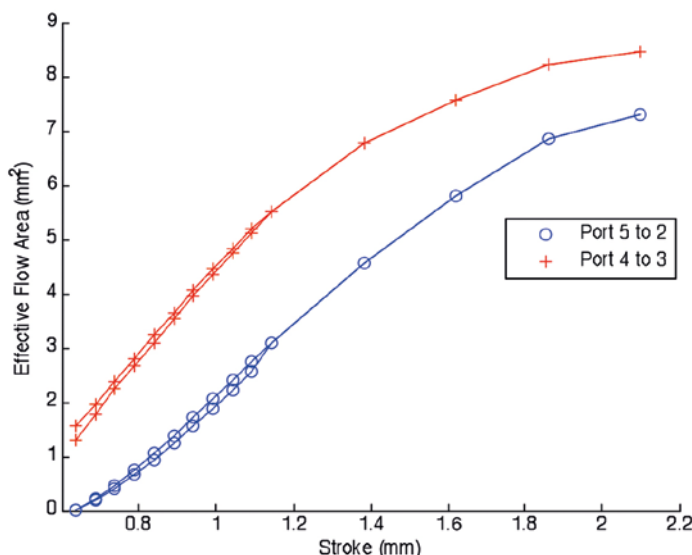
a) Electromagnetic forces as a function of current and plunger positions

b) Magnetic flux-density distribution

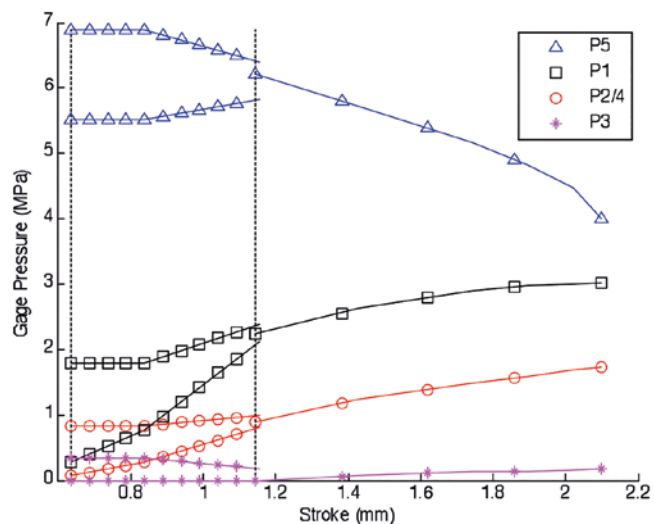
Figure 3. Electromagnetic forces and flux-density distribution derived from MagNet 3D FEA



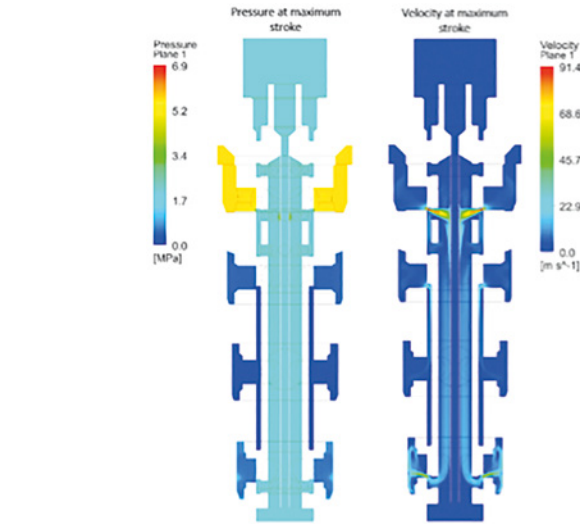
a) Force coefficient, C_f



b) Effective flow area, A_e



c) Effective flow area, A_e



d) Pressure and fluid velocity distribution at maximum stroke

Figure 4. Fluid parameters and pressure and fluid velocity distributions determined from 3D CFD

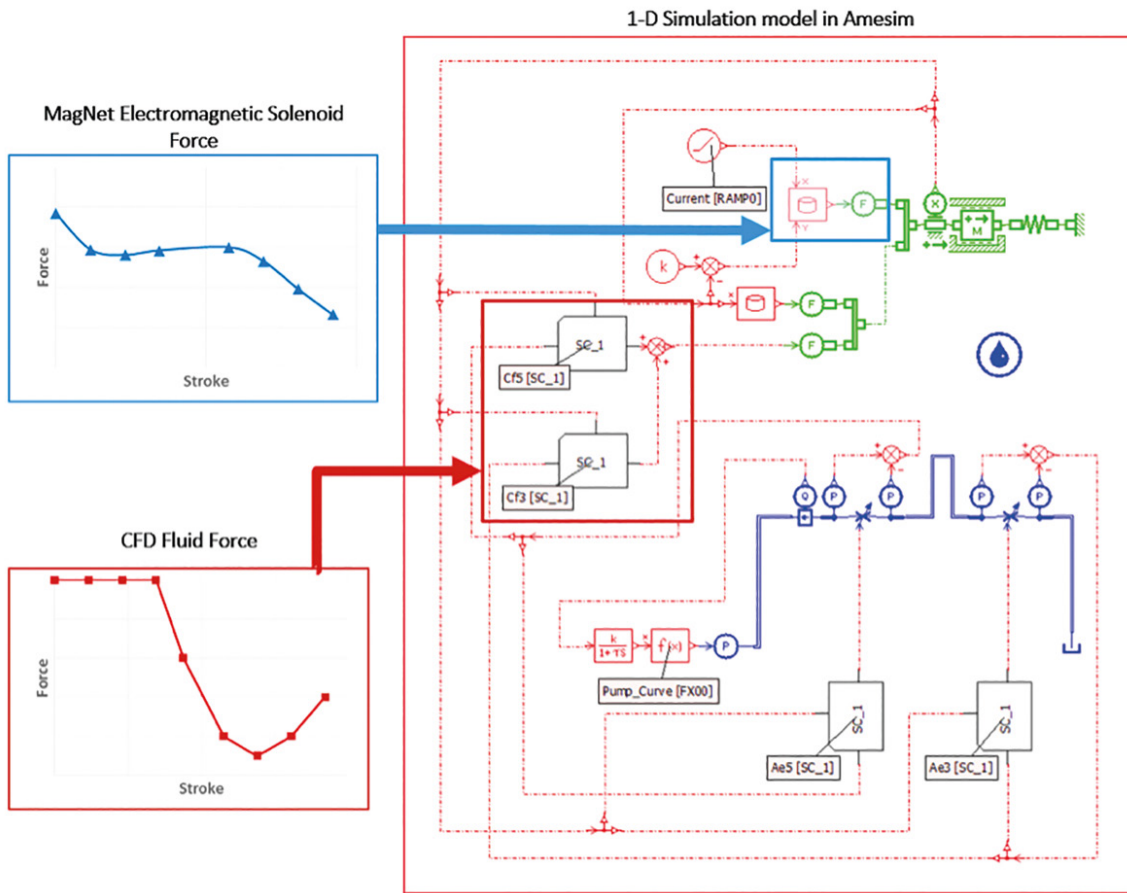


Figure 5. The implemented 1D model of an EHSV hydraulic valve system in Amesim

fields for a set of preselected conditions were then used to improve the accuracy of the 1D models to describe the dominant physics. This concurrent development of 1 and 3D models allowed stepwise improvement of the 1D model.

The forces acting on the valve are described by Newton's second law of motion as:

$$m \frac{d^2x}{dt^2} = F_{solenoid} + F_{fluid} - F_{preload} - K_{spring}x - c \frac{dx}{dt} \quad (1)$$

where m is the effective moving mass of the spool, solenoid plunger and spring, $F_{solenoid}$ is the electromagnetic solenoid force, F_{fluid} is the fluid forces on the spool, $F_{preload}$ is the force exerted by the preloaded spring on the spool, K_{spring} is the spring constant, c is the viscous damping coefficient and x is the position of the plunger-spool assembly.

The electromagnetic forces generated by the solenoid are a function of current and plunger position. A series of force-vs-stroke curves at various currents were generated in MagNet using the 3D magnetostatic solver. The solver accounted for the non-linear behavior of the material B-H curve. The surface map shown

in Figure 3 (a) was generated by interpolating the MagNet FEA results. Figure 3 (b) shows the flux density distribution.

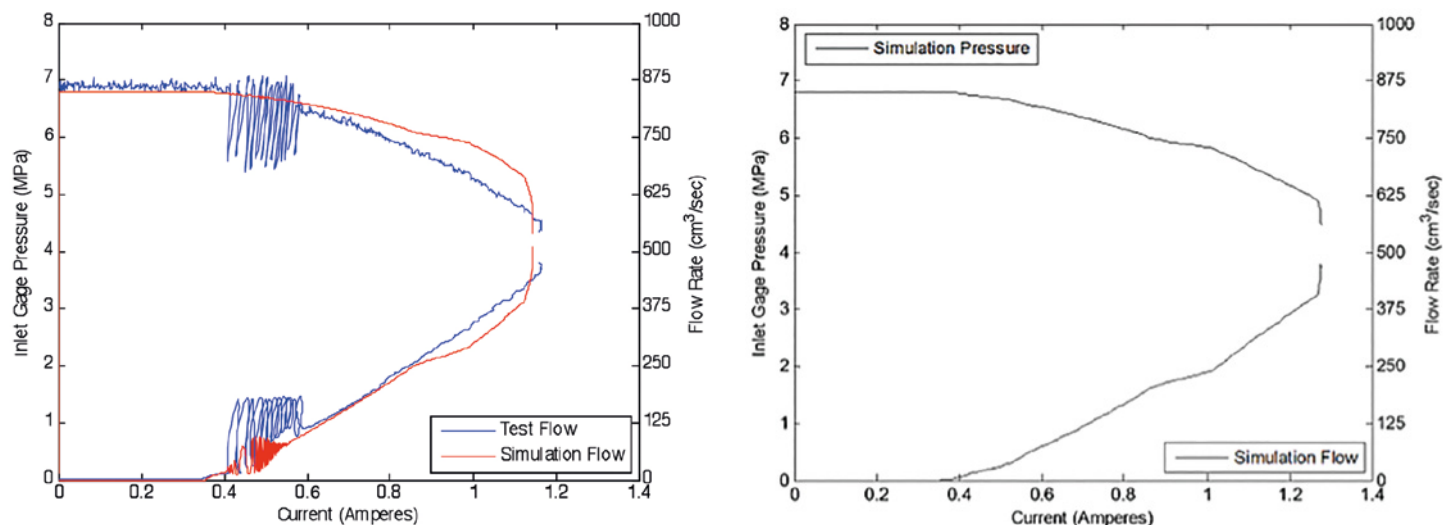
The MagNet FEA model was also instrumental in evaluating the different force responses between the push and pull directions, due to the asymmetry in the design. These results are not shown in this article.

Quasi-steady state CFD analyses were done at various spool positions and pressure conditions to accurately map a given set of valve operating conditions and the resulting fluid forces on the spool.

The fluid forces were described by a non-dimensional force coefficient C_f and effective flow area A_e as:

$$C_f \frac{F_{fluid}}{A_{ref} dp} \text{ and } A_e = \frac{Q}{\sqrt{2} \frac{dp}{\rho}} \quad (2)$$

Q is the volumetric flow rate through the ports, ρ is the fluid density, dp is the port differential pressure, and A_{ref} is an arbitrary reference area set to 1 mm^2 . The values of C_f , A_e and dp were derived from 3D CFD assuming steady-state conditions for spool positions ranging just as the port starts to



a) Comparison of the experimental and simulated flows before modifying the spool geometry

b) The simulated flow after modifying the spool geometry

Figure 6. Applying the developed 1D dynamic model in the development of an EHSV hydraulic valve

open, to when it is closed; with most cases being around the oscillatory region. The plots for these parameters are seen in Figures 4 (a) to (c), with Figure 4 (d) showing the pressure and velocity distributions at maximum stroke.

The fluid forces-vs-stroke curve was then derived from C_f , A_e and dP plots, and incorporated into the 1D model, together with the MagNet derived electromagnetic force-vs-stroke for different currents map (Figure 5 (a)). For electromagnetic forces, there was no need for a force conversion coefficient.

Figure 5 shows the implementation of the 1D model in Amesim.

Valve Oscillation Analysis

The developed dynamic 1D model was able to capture the valve's flow oscillations as shown in Figure 6 (a). To suppress these oscillations, the spool geometry was modified and analyzed using the 1D model after updating it with new force maps. Both test data and simulation results of the modified spool geometry provide significant performance improvements. The simulation results are shown in Figure 6 (b), which shows the complete elimination of the oscillations.

Conclusion

An electrohydraulic servo valve was tested and found to have oscillations. The suppression analysis required a highly accurate dynamic model. Fully-coupled co-simulation of 3D multiphysics models is very accurate but time and hardware intensive. Hence, it loses on the short analysis time needed to make decisions during the development of the valve.

Lower-order models or simplistic handbook correlations are of very low dynamic fidelity. Therefore, there was a need to develop a highly accurate 1D model that captures the dynamic instability of the valve. This required the precise computation of the forces at play.

The increased model accuracy could not have been achieved without the detailed 3D electromagnetic analysis of the solenoids using MagNet 3D, in addition to the flow through the spool valve body. This allowed the precise mapping of magnetic forces and flow on the moving valve body.

The 1D model was implemented in Amesim and used to identify the valve oscillations. The spool geometry was then modified to eliminate oscillations. The dynamic 1D model allowed quicker computational times than fully-transient 3D analysis and can be used to analyze multiple operating systems and conditions.

So, the next time you are in a plane, think about how the bird flaps its wings and moves its tail!

References:

- [1] H. E. Merritt, *Hydraulic Control Systems*, John Wiley and Sons Inc, 1967.
- [2] D. Henninger, A. Zopey, T. Ihde and C. Mehring, "High-Fidelity 1D Dynamic Model of a Hydraulic Servo Valve Using 3D Computational Fluid Dynamics and Electromagnetic Finite Element Analysis," *International Journal of Mechanical and Mechatronics Engineering*, vol. 11, no. 8, pp. 1476-1482, 2017.

Using FloEFD as an Engineering Tool

By Karl du Plessis, Senior Engineer, ESTEQ

What do you do when faced with analyzing a shell and tube heat exchanger as in the model shown in Figure 1? I can already hear you saying “you want to ‘C..F.D’ this thing!? There’s like a thousand meters worth of piping..?” Quite literally in fact, approximately 1km in total with a 1mm wall thickness and 800 bends. Thoughts that run through my mind are: “How big is this mesh going to be? How long is it going to take to solve? I only have a quad core laptop (at least with 32GB of memory which helps)”. And if I were to use anything other than FloEFD I’d also think with all those bends I’m probably going to have to remodel the piping so that I can HEX-mesh it... It seems overwhelming at first because most of the time, us engineers simply don’t have time for all that, we need answers and we needed them yesterday!

Fortunately this is exactly where FloEFD starts to make a lot of sense, especially for the internal pipe flow, where the SmartCells™ technology within FloEFD really comes into play. SmartCells will recognize directly from the CAD geometry if it is a pipe or a channel, and decide based on the number of cells across this pipe or channel to apply a textbook or engineering calculation (1D) for the pressure drop and heat transfer when there is insufficient cells across the pipe to numerically resolve the flow. Alternatively, when there is indeed a sufficient number of cells across the pipe, SmartCells will then automatically switch to resolving the flow (3D) with the numerical grid. But, if you’ve ever wondered exactly how well FloEFD performs in this regard, perhaps the following observations may be very beneficial.

Part I: Internal Pipe Flow

Consider for example the internal flow of a single 10-pass pipe layout as relevant to the heat exchanger at hand. The FloEFD model of the pipe is shown in Figure 2. Heat transfer to the fluid is modeled with an external HTC applied to the outer wall, to allow for the calculation of conduction through the wall along with the conjugate heat transfer at the fluid-solid interface on the internal pipe surface. Radiation is neglected for this example. The mesh was generated such that the characteristic number of cells across the diameter of the pipe was gradually increased, starting with as little as 2x2 cells across the pipe diameter up to 6x6 cells.

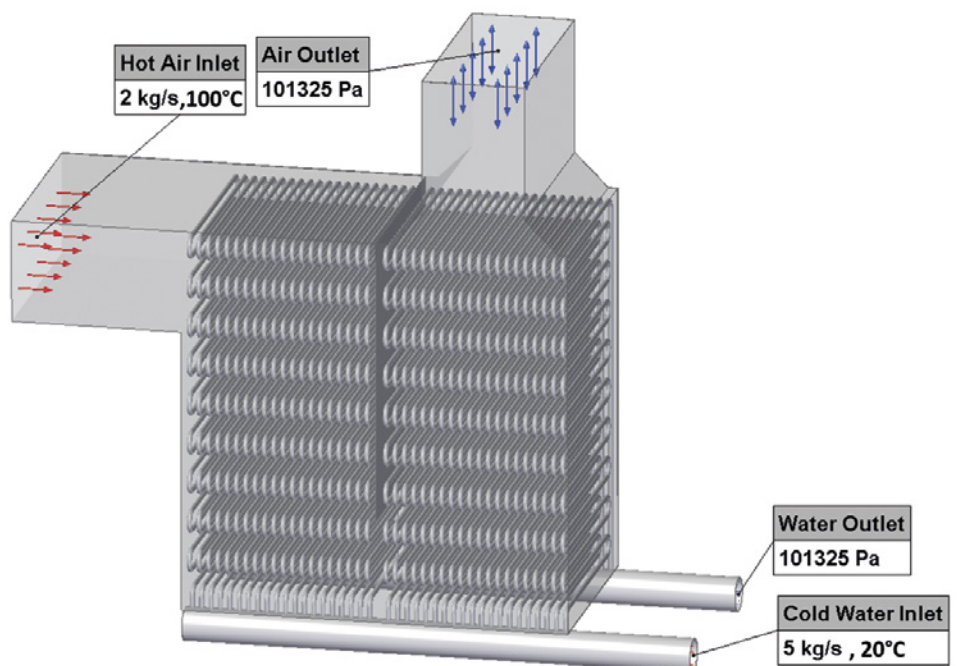


Figure 1. Shell and Tube heat exchanger

Now let us compare the results from FloEFD with that of the very reliable 1D thermal hydraulic system solution called Flownex (developed locally here in South Africa). The Flownex model of the same pipe layout is shown in Figure 4. Graphs of the pressure drop and total heat transfer are presented in Figure 5. The FloEFD results are displayed with respect to the increasing mesh density and compared to the Flownex result. A band of +10% and -10% about the Flownex result

is also shown to add some perspective to the comparison.

Consider first of all the pressure drop comparison. One can see a very good agreement between FloEFD and Flownex, albeit a slightly lower pressure drop being predicted by FloEFD. Please note that for the sake of brevity I only display the results for meshes up to six characteristic cells, since further investigations showed that the FloEFD pressure drop result becomes mesh independent from around six cells for this example and eight to ten cells for an example with air at much higher flow velocities. Furthermore, it was also established that there seems to be a consistent difference in pressure drop prediction between Flownex and FloEFD, which is mainly attributed to the possible differences in the calculations for both primary (wall friction) losses and secondary (bend) losses used within Flownex and FloEFD, so we will not focus our attention on this.

What I would rather prefer to focus on is the much more fascinating heat transfer result. It runs out that for this example the heat transfer prediction by FloEFD is always within the +/-10% band compared to Flownex, regardless of the mesh density.

Again I am only showing one example here, but an extensive study of first comparing 1-pass, 2-pass and then 10-pass pipe layouts, with flows at varying Reynolds numbers (as high as $Re=600,000$ with air at 45 to 50m/s), all produced very similar behavior. For the sake of everybody's curiosity I want to make the following interesting observation: It seems the switch

over point from the engineering calculation to the fully resolved pure CFD calculation, happens at around eight to ten cells. Beyond this point one could see a sudden jump in heat transfer prediction as the mesh resolution is increased, all the while remaining within the +/-10% band compared to Flownex, see Figure 6.

Part II: External Flow over Heated Cylinder

So, what about the flow on the outside of the pipes, i.e. the shell side of the heat exchanger in question? To represent the 'shell side' flow we will consider the standard validation example of external flow over a heated cylinder. In this analysis only the heat transfer behavior is considered, and not the drag, per sé. Again the mesh is set up

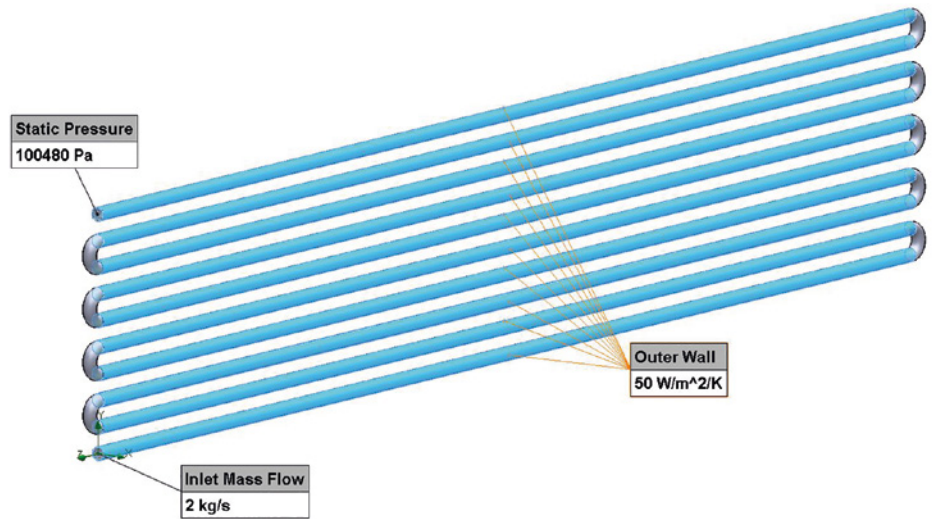


Figure 2. FloEFD model of 10-pass pipe layout

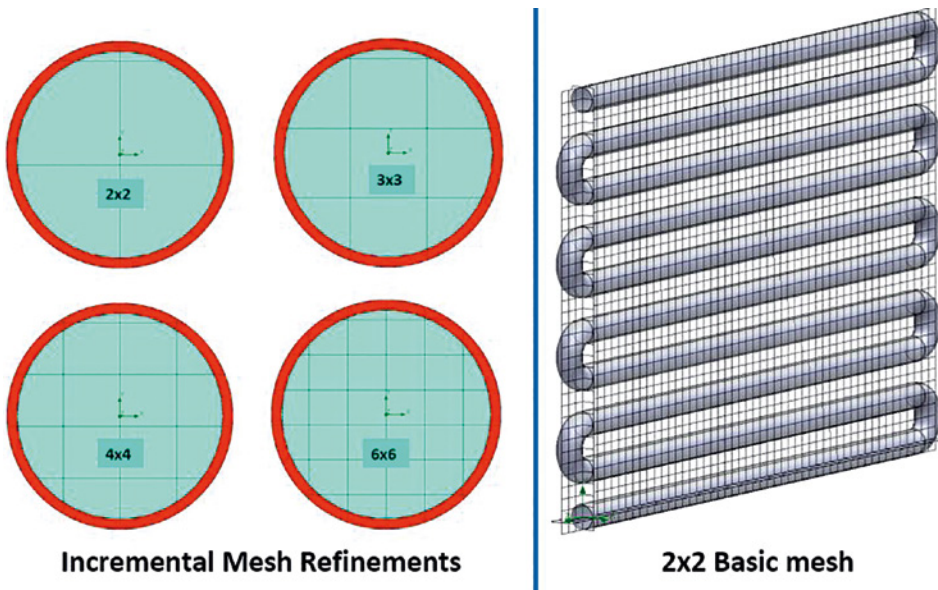


Figure 3. FloEFD mesh resolution

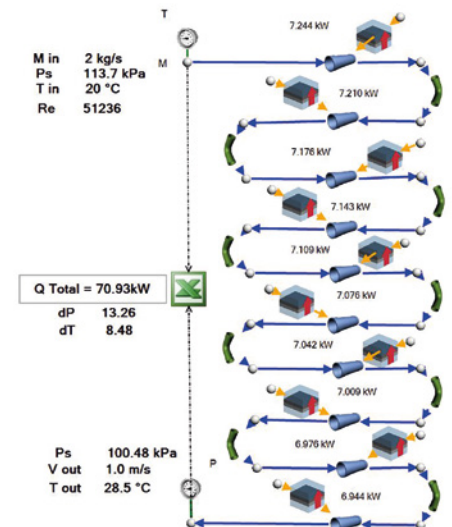


Figure 4. 1D Flownex model of 10 pass pipe layout

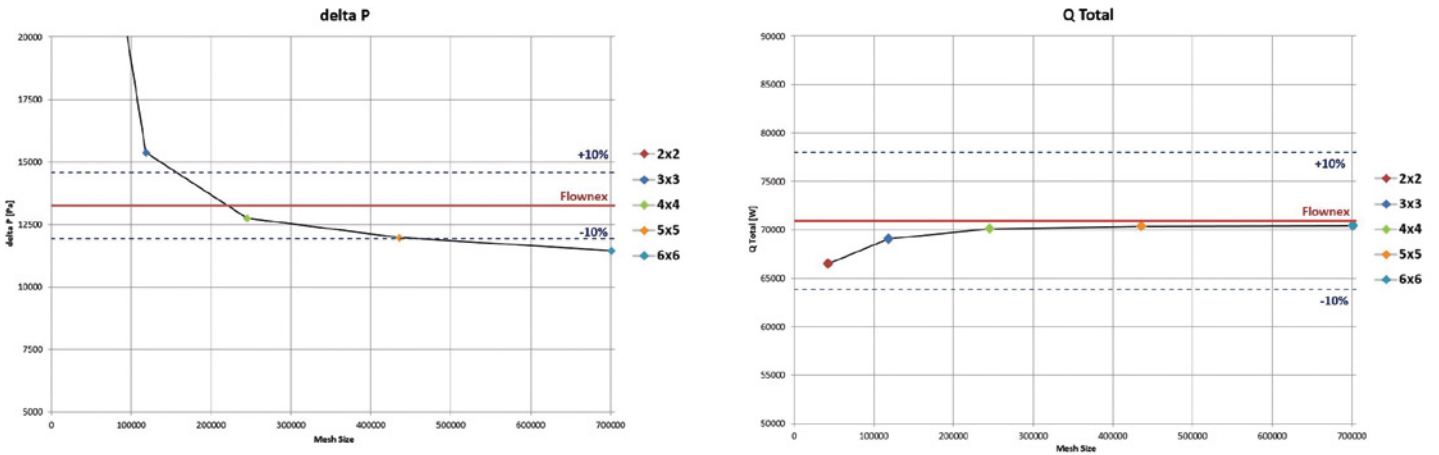


Figure 5. FloEFD versus Flownex results comparison.

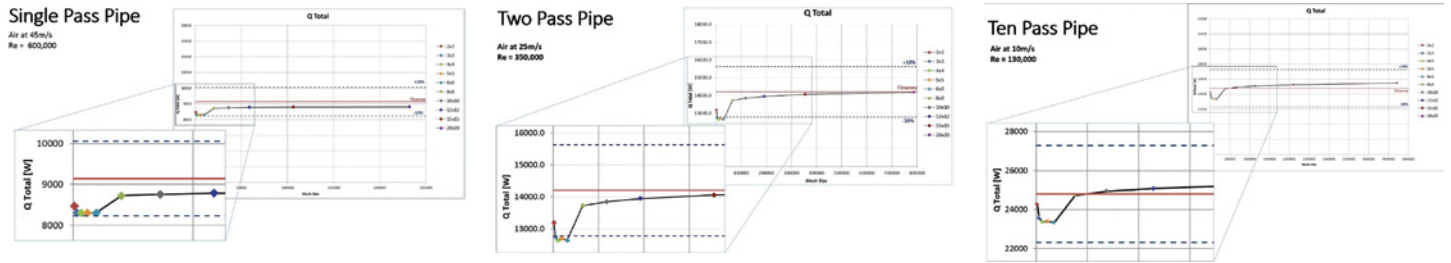


Figure 6. FloEFD versus Flownex results comparison: High Reynolds number example

such that the characteristic number of cells across the diameter was varied incrementally. Consider the graph in Figure 7 which shows the Nusselt number prediction for several mesh densities across a range of Reynolds numbers. It is evident from the graph that regardless of the mesh density the FloEFD prediction is very good, always within the scatter of the experimental data, even for extremely coarse meshes in CFD terms (four to ten cells per diameter). See especially the close-up image showing the 4x4 and 6x6 mesh results. This observation fortunately aligns very well with that of the internal flow results in that one should be able to generate very useful engineering results with meshes as coarse as just four characteristic cells across the pipe diameter (six cells would be ideal for this 'engineering' approach).

Part III: Full Heat Exchanger

The reason for all of this is basically to establish just how coarse a mesh one could dare to use when having to analyze large or complex heat exchangers like this. Since, you might find yourself in the same position as many engineers in South Africa, usually required to make do with limited computer resources. Therefore, it would be very beneficial if you can use CFD software that can double-up as an engineering tool to solve large problems on your standard issue laptop or desktop machine. And this is exactly where FloEFD starts to make a lot of sense.

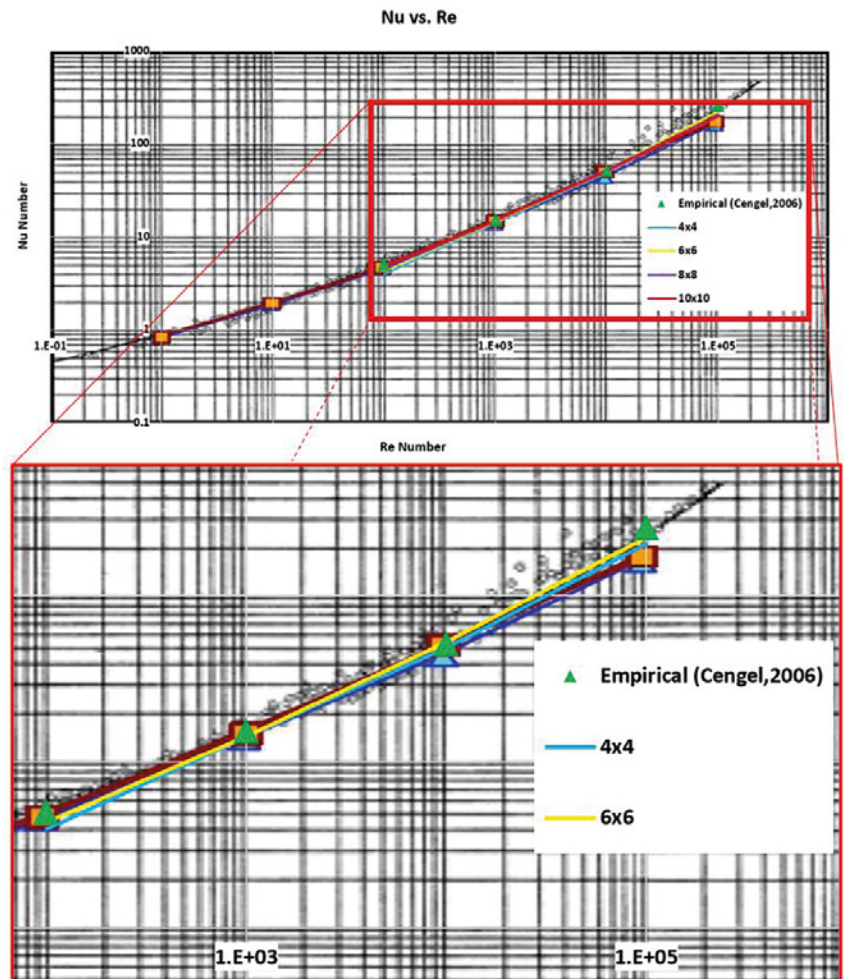


Figure 7. External Flow over a heated cylinder - Nu number comparison.

In order to analyze the heat exchanger in question the only limitation would be the computer memory. By applying the knowledge gained from the preceding discussions, one could generate a mesh with four characteristic cells across the tube diameters and still have a high level of confidence in the 'engineering' answer. With the limit of 32GB memory, some stretching of the cells had to be applied to save a little on the memory requirements, thus stretching the cells away from the bends which resulted in a mesh size of approximately 5.7 million cells in total. See the resulting mesh on the tubes in Figure 8. Furthermore, on the question of the required calculation time, this particular model solved in a very respectable ten hours per travel with a mere quad core CPU, with the respective outlet temperatures already converged by 1.5 travels (flow freezing enabled). The resulting outlet temperatures obtained were, $T_{\text{air,out}} = 51.6^{\circ}\text{C}$ and $T_{\text{water,out}} = 24.6^{\circ}\text{C}$. See the tube internal and shell temperatures in Figures 9 and 10. Based on the merits of the previous discussions, this result would already be very useful to base decisions on, especially when doing comparative studies of various baffle plate designs. It must also be stated that the solution runs very stable and convergence just happens. Quite astonishing considering the type of problem.

Conclusion

I have long since realized the value of FloEFD whenever it comes to solving heat transfer problems. However it has only now also become evident that FloEFD has made it possible for engineers to solve large problems like shell and tube heat exchangers with the minimum amount of effort and resources required, compared to 'old school' CFD programs, thanks to the underlying SmartCells technology and the ever-so-fantastic thin boundary layer approach. The only demand being placed on computer memory which limits the mesh size of these models. It is not just the ease of use and the minimal effort of setting up the model including the meshing, all of this would be useless were it not for the stability and robustness of the solver. FloEFD is simply the most reliable CFD software out there. From an Engineering in South Africa perspective, i.e. to be as resourceful as possible, FloEFD really resonates well with our kind of thinking.

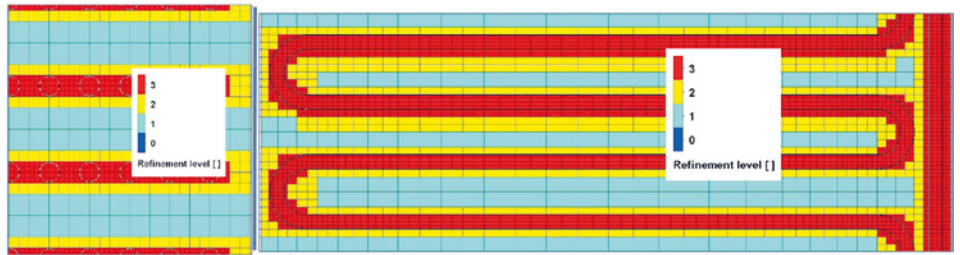


Figure 8. Heat exchanger tubes mesh refinement

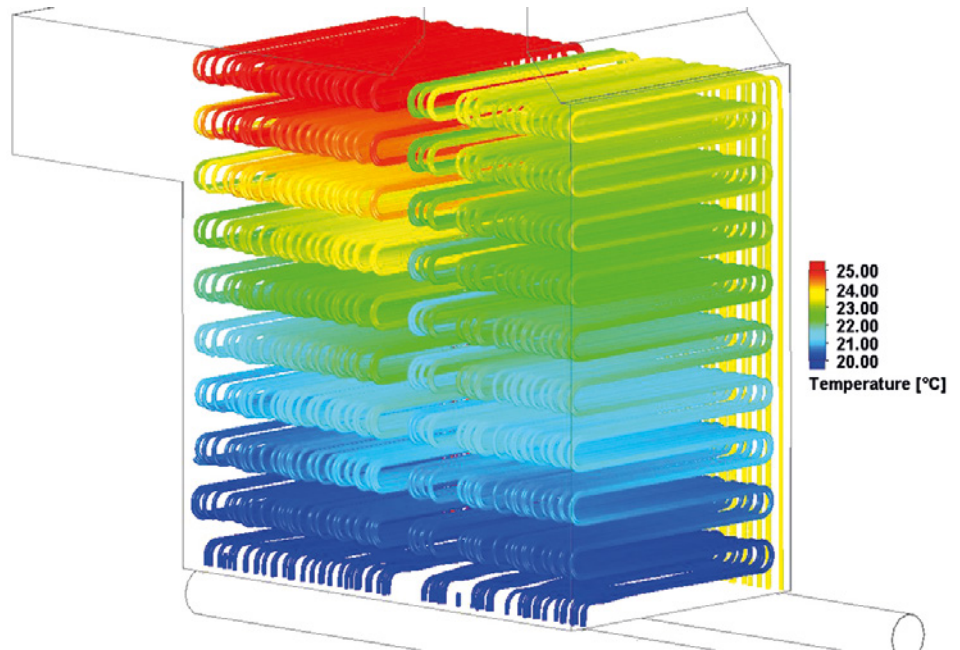


Figure 9. Tube-side water temperature flow trajectories

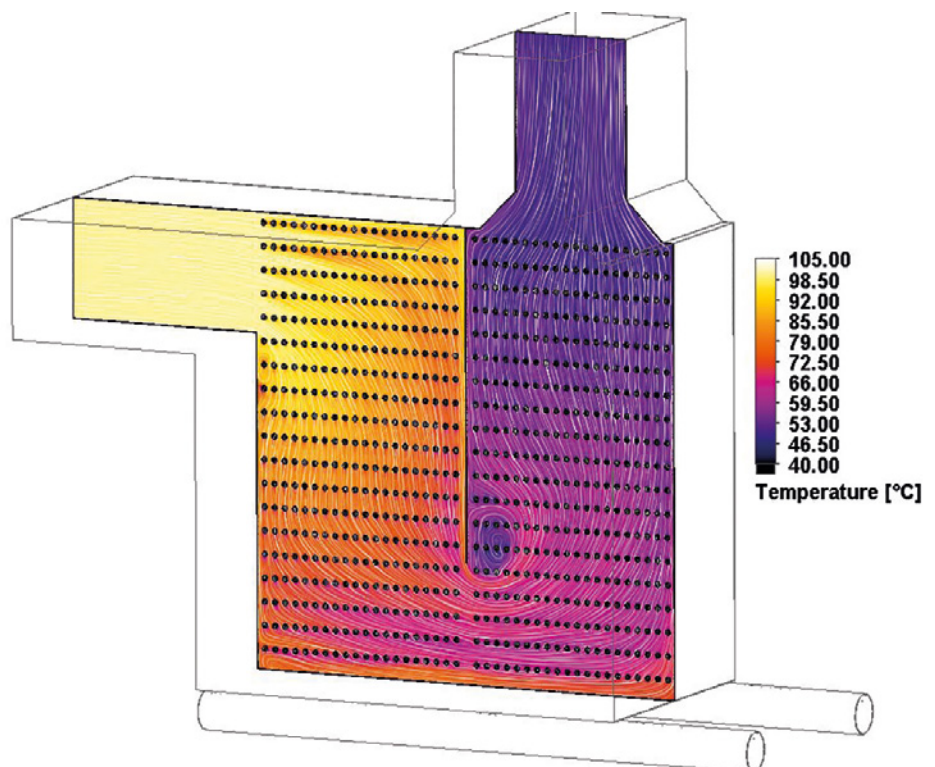


Figure 10. Shell-side air temperature cut plot

Comparison between Experimental & Computational Results

For The Transition to Turbulence in Flat Plate Channel Flow

By Mircea Dinulescu, Founder & Jens Kitzhofer, R&D Manager, APEX Group



APEX Group specializes in developing, marketing and manufacturing high-performance heavy-duty equipment for heat recovery and gas handling projects. APEX Group's main products are plate-type and tubular heat exchangers for large volumes of gases, in petrochemical, power, metallurgical, pulp and paper, cement, DENOX and general environment applications. For corrosion protection, heat exchangers with glass-enameling protection are available. A typical example, with the dimensions of 6 x 5 x 8 m is shown in Figure 1 for a combustion air preheating system. The use of these heat recovery systems is mandatory for plants with long operating times and high thermal output. Each individual unit is designed according to the customer's specifications in terms of pressure drop, heat transfer performance and space constraints.

APEX-Research B.V., in The Netherlands, has a modern laboratory equipped with state of the art measurement equipment, such as advanced laser equipment (Particle Image Velocimetry and Laser Doppler Anemometry). The combination of CFD simulations and laboratory measurements is essential for the successful development of cutting-edge equipment. One component of the applied software package is the CFD software FloEFD™.

A basic design of a plate-type heat exchanger system is shown in Figure 2, which consists of one pass in z-configuration and one pass in x-configuration. The cold air, first enters the x-configuration heat exchanger and is redirected into the z-configuration heat exchanger. The air travels through the heat exchanger from the bottom to the top, where it leaves the heat exchanger preheated. The hot flue gas, for example from a combustion process, is directed in the opposite direction. The inlet is at the top

of the z-configuration heat exchanger, the flow direction is from top to bottom and the outlet of the cooled flue gas is at the bottom of the x-configuration heat exchanger, which is frequently described as the cold end.

The heat is exchanged between the hot flue gas and the cold fresh air through metal plates of different thicknesses (Figure 3) depending on the application. The system has to be gas-tight; the two gas streams may not mix. A modular design is shown in Figure 4.

Depending on the project specifications, there are numerous geometrical and fluid-mechanical parameters that influence each other. The channel height can vary, for example between 6 and 20 mm. Other geometrical parameters are: cross section area, number of channels, or flow configurations. Fluid- and thermo-mechanical properties are volume flow rate, Reynolds number, gas compositions, or inlet and outlet temperatures. All these variables result in

We at APEX-Research successfully used FloEFD for many years and now we have the increased confidence in its results through our own modeling experiment

**Mircea Dinulescu, APEX Group
Founder**



Figure 1. Heat Exchanger for combustion air preheating

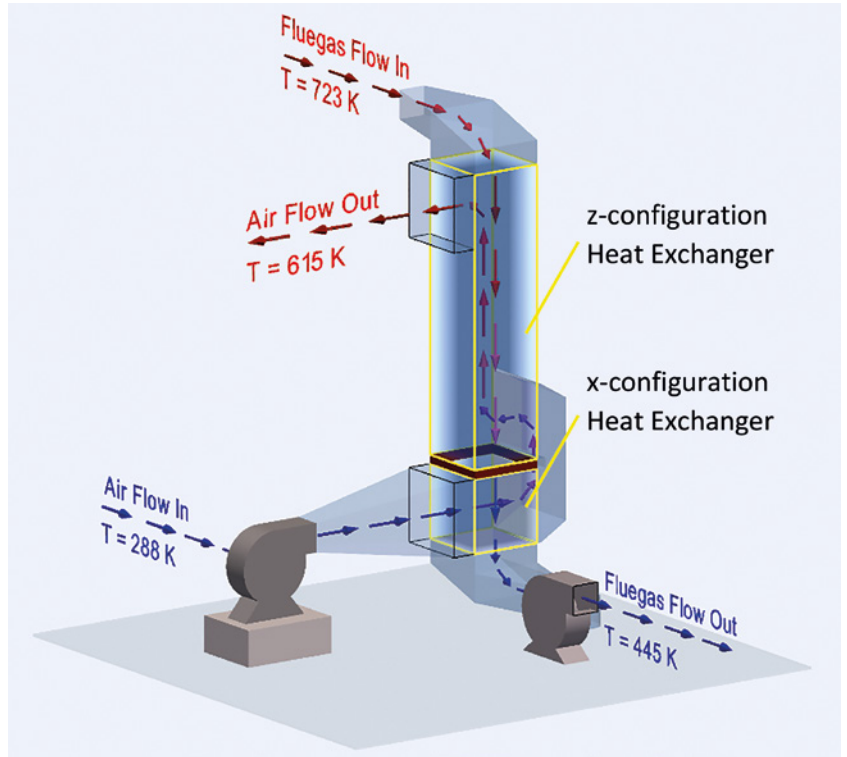


Figure 2. Basic design overview

APEX Heat Transfer Concept

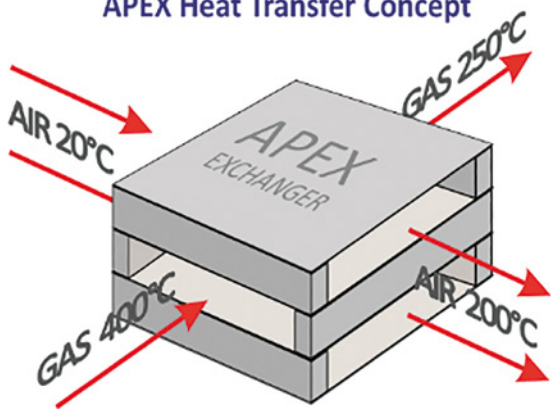


Figure 3. Principle heat exchange metal plates

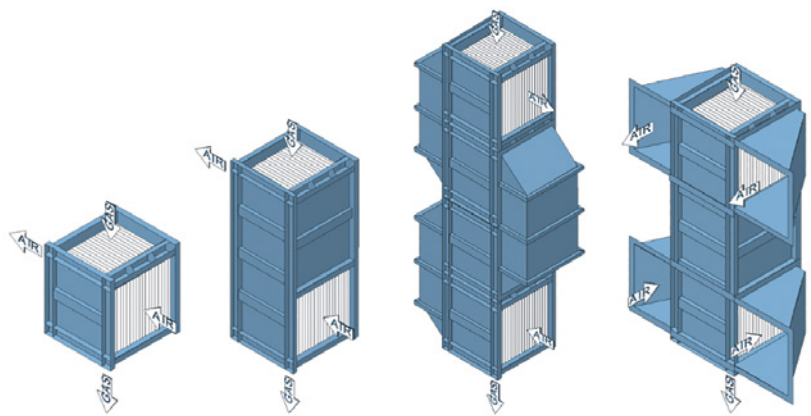


Figure 4. Modular design

a variety of possible design configurations, that make it almost impossible to establish experimental or empirical data for each individual parameter variation.

A good pressure drop to heat transfer relation is crucial for these applications to save energy or to fit into existing plant configurations.

The design criterion often demands that the flow must be in the lower turbulent Reynolds number range (Figure 5). A higher velocity allows a higher heat transfer, but at the same time, the pressure drop increases rapidly proportional to the square to the velocity. Therefore, it is important to find the appropriate design compromises.

I appreciate the straightforward and fast simulations with FloEFD

**Dr.-Ing. Jens Kitzhofer, R&D Manager
APEX-Research B.V.**

A large variety of possible configurations (Figure 6) for the gas flow arrangement must be investigated with regard to the pressure drop, heat transfer performance, and recirculation zones. For one of these configurations, the highlighted z-configuration, APEX-Research B.V., a company of APEX Group, conducted a calibration between simulation and measurement.

A detailed description of the flow conditions in a z-configuration channel is shown in Figure 7. The blue arrow indicates the air inlet flow. Two recirculation areas are generated at the first bend downstream of the inlet, followed by a specific velocity profile and finally by the same recirculation areas in the second bend as appeared at the first bend. The flow through the z-configuration channel is associated with a certain pressure drop. On the other side of

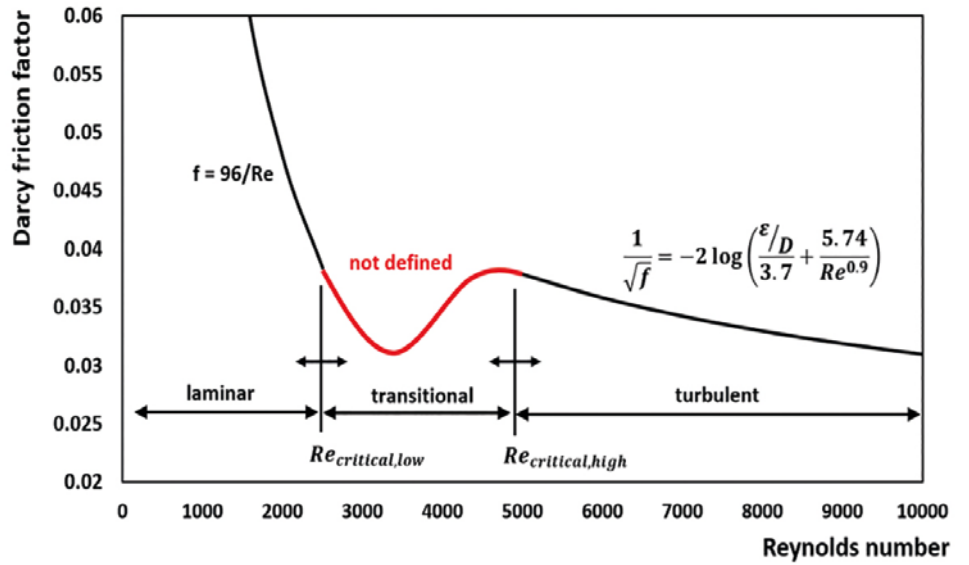


Figure 5. Re number ranges

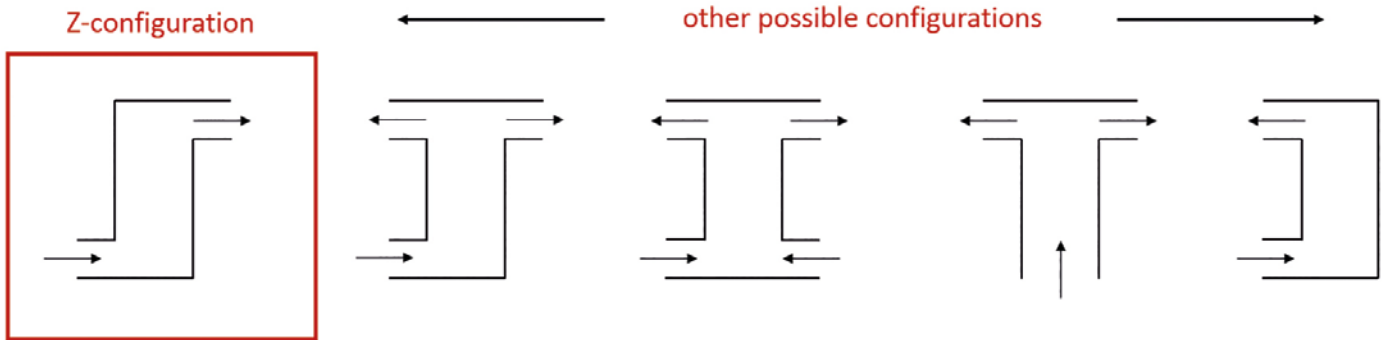


Figure 6. Possible configurations for gas flow arrangement

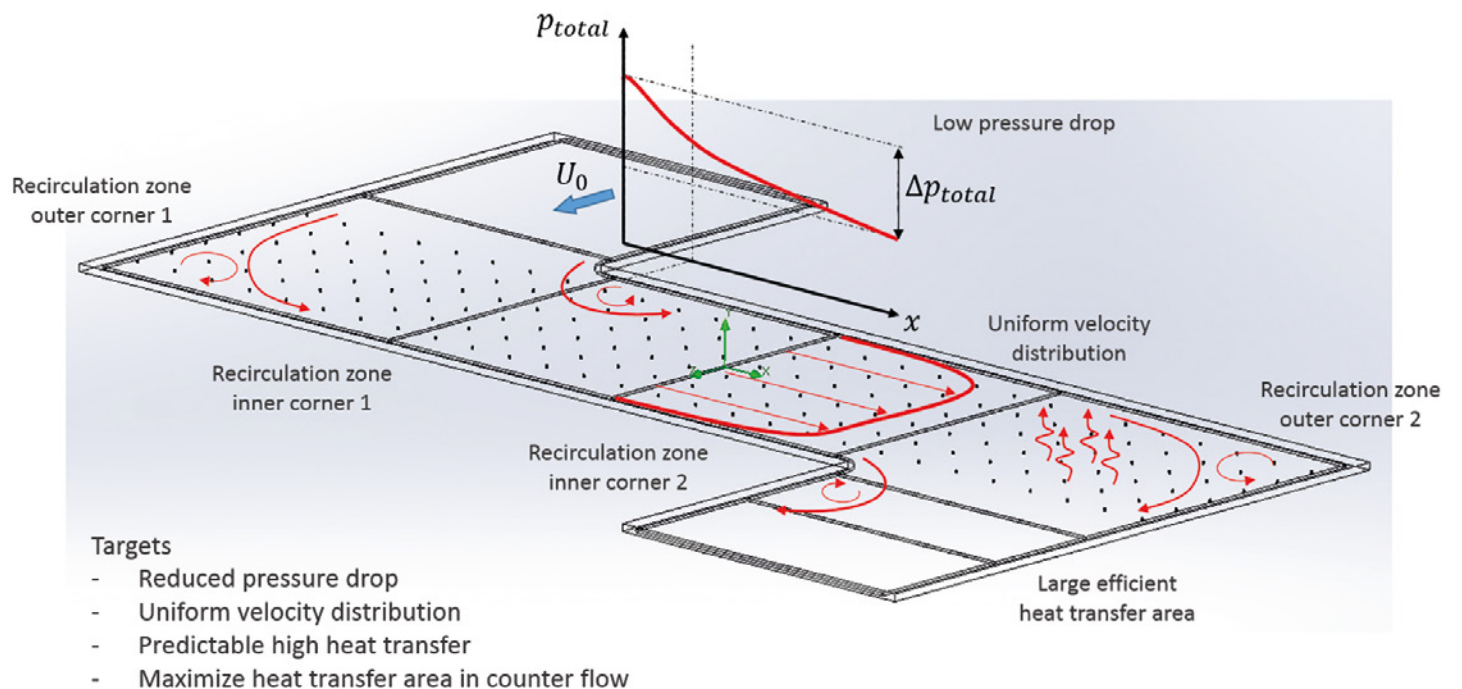


Figure 7. Flow conditions in a channel

the channel (below and above, not shown in the figure) flows the hot flue gas. The highest heat output is achieved with straight counter-flow and as such cross-flow areas should be minimized.

APEX-Research established an experimental set-up to validate the simulation results and to calibrate the CFD software for the application of plate-type flow configurations. The experimental set up is shown in Figure 8. The scaled 1:1 model is made of Plexiglas for optical access. A centrifugal fan is placed at the inlet. The flow is guided through the diffuser duct and the distribution duct to enter into the z-configuration channel. The measurements for volume flow rate, velocity and turbulence distribution are carried out by Laser Doppler Anemometry (LDA) and pressure drop measurements are collected by static pressure sensors.

For the FloEFD simulations, a 1:1 scaled z-configuration example was used, with symmetric conditions and the use of half of the model, see Figure 9. Approximately 4.3 million cells were created by the automatic mesh generation to have a high spatial resolution in the computational domain. The boundary conditions for the simulation were set with respect to the measured values in the physical values.

The volume flow rate, the static pressure distribution, and the velocity as well as the turbulence intensity profile were measured



Figure 8. Experimental set-up

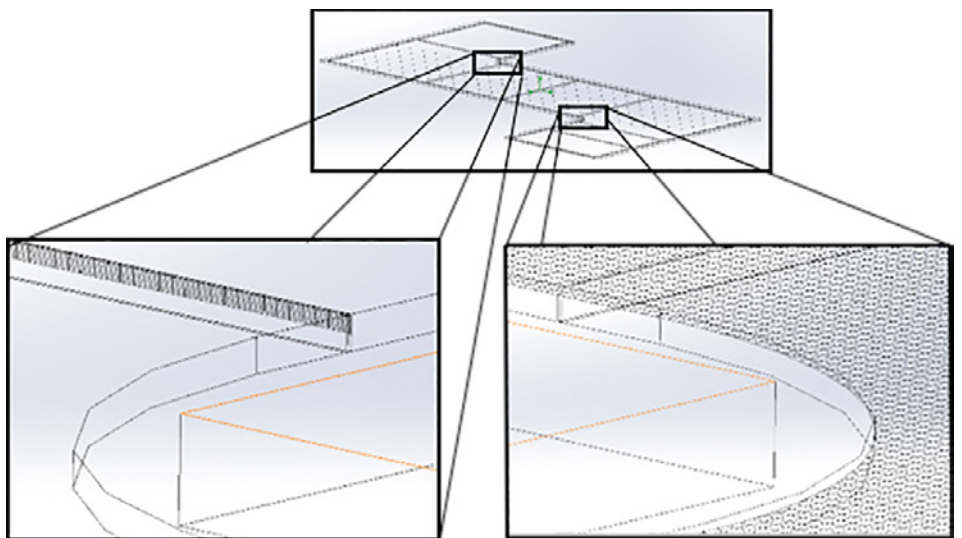


Figure 9. FloEFD simulation model

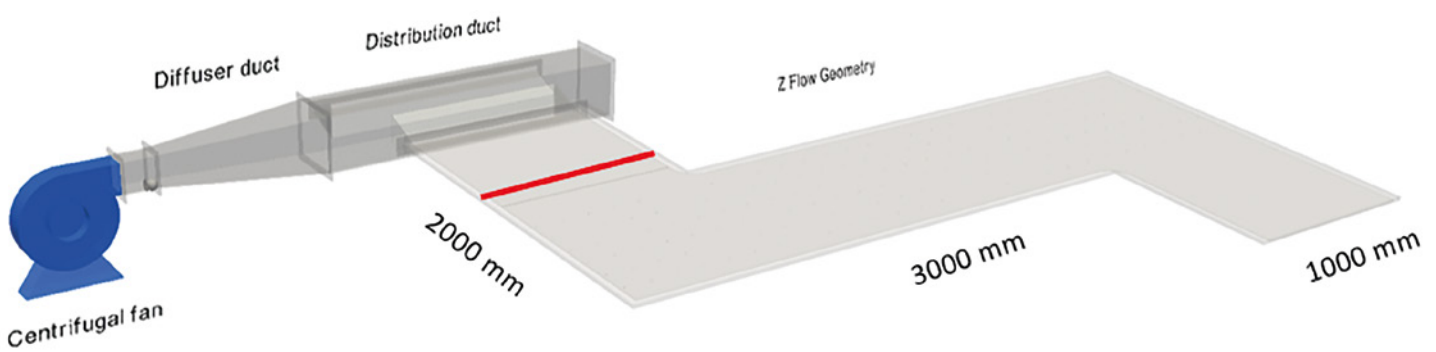


Figure 10. Physical flow model

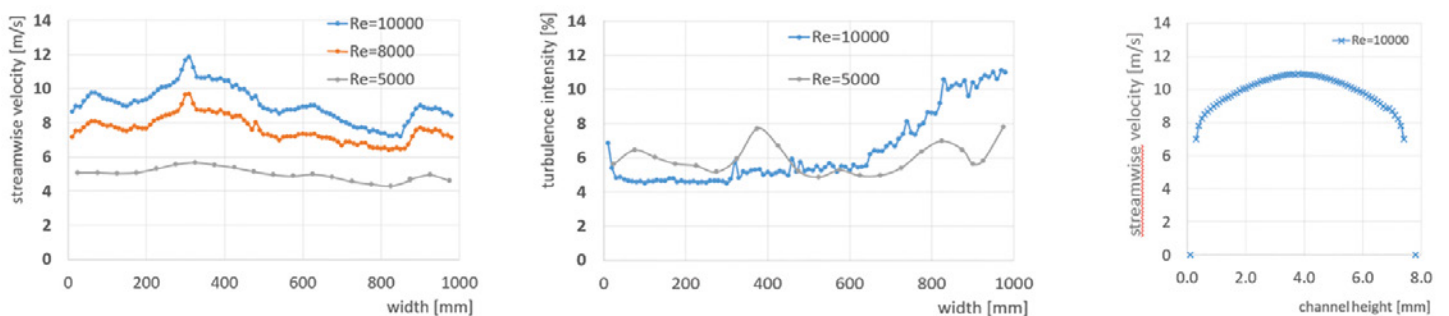


Figure 11a, b, c. Measurement results

in the physical flow model, see Figure 10. Figure 11a shows the measured streamwise velocity in the center of the channel for three different Reynolds numbers (lower turbulent Reynolds number range) as a function of width (along the red line in Figure 10). Figure 11b shows the measured turbulence intensities in the center of the channel as a function of width and Figure 11c shows the velocity profile as a function of channel height. The integration of the velocity along the height, and following integration over the width, yields the volume flow rate.

The FloEFD results were compared with the experimental data. One of the main findings was the importance of the correct boundary condition definition. The centrifugal fan and intake geometry generate an inhomogeneous velocity profile at the inlet. The definition of the real velocity profile and turbulence intensity, measured in the laboratory, significantly increased the simulation results accuracy. Figure 12 shows the comparison with respect to overall total pressure drop. The deviation decreased from approximately 10 % to 2 %, only on the basis of the realistic boundary conditions definition.

In Figure 13, some comparisons of the test results with the simulation at different measuring positions are presented for the overall static pressure distribution. The good agreement between simulation and experiment can be seen by the identical color coding.

Also the comparison of exact values of the static pressures at identical positions (red

line in Figure 14) shows a good agreement between simulation and experiment.

The comparison of the velocity profile is shown in Figure 16 for different Re numbers at the position of the red line, which crosses the recirculation area in the inner corner. The simulation of the flow fields, are very close to the experimental results. This allows the reliable prediction of flow field characteristics like pressure drop or flow uniformity in the plate-type heat exchangers with the calibrated simulation.

The simulation results are confirmed by the measurement results, using state of

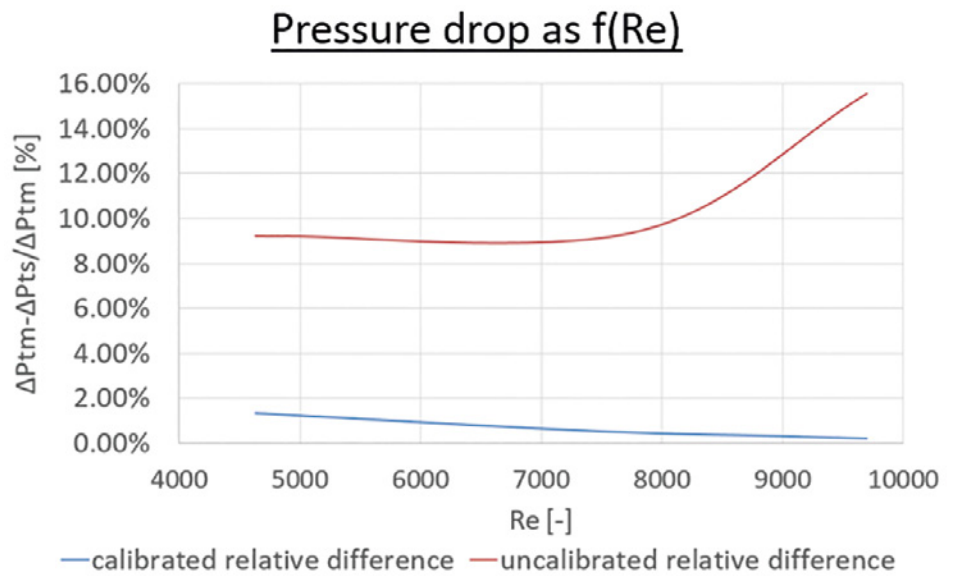


Figure 12. Deviation comparison for different boundary condition definitions

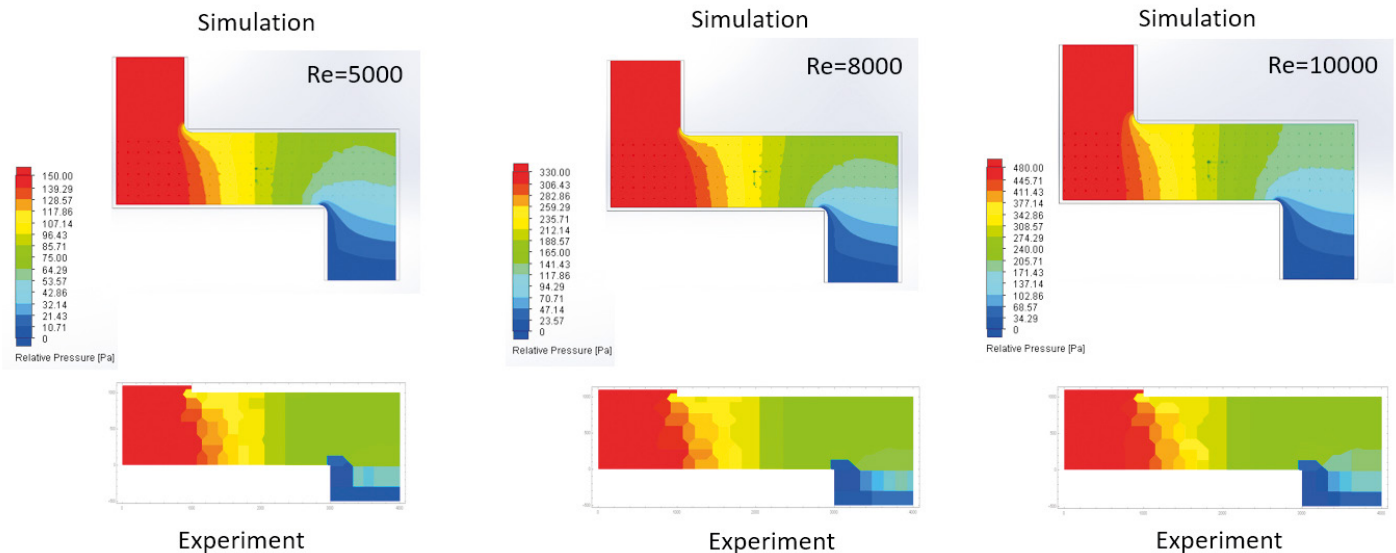


Figure 13. Comparison of test results with simulation results

the art technology for measurement, such as Laser Doppler Anemometry (LDA), Particle Image Velocimetry (PIV) and static pressure measurements. As a result of the confidence achieved by the calibration of simulation with experimental data, numerous configurations can be simulated. With FloEFD many different geometries can be investigated according to specific project specifications, such as heat transfer output, pressure drop limitations and space requirements. The optimized configuration can be designed for production with the collaboration of simulation and experimental measurements.

References:

- [1] www.apexgroup.eu
- [2] https://www.apexgroup.eu/admin/uploads/_pdf/Short_Note_CFD.pdf
- [3] <https://www.dantecdynamics.com/laser-doppler-anemometry>

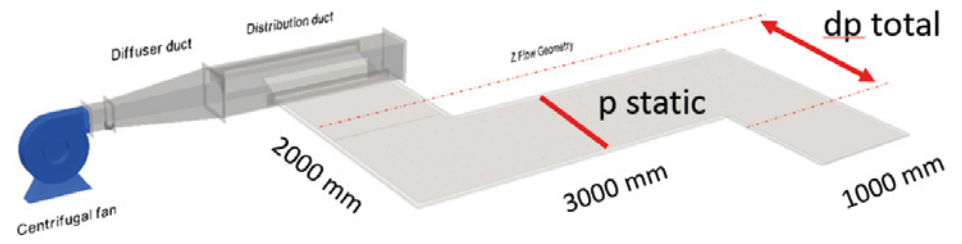


Figure 14. Position for static pressure measurement

Static pressure profile

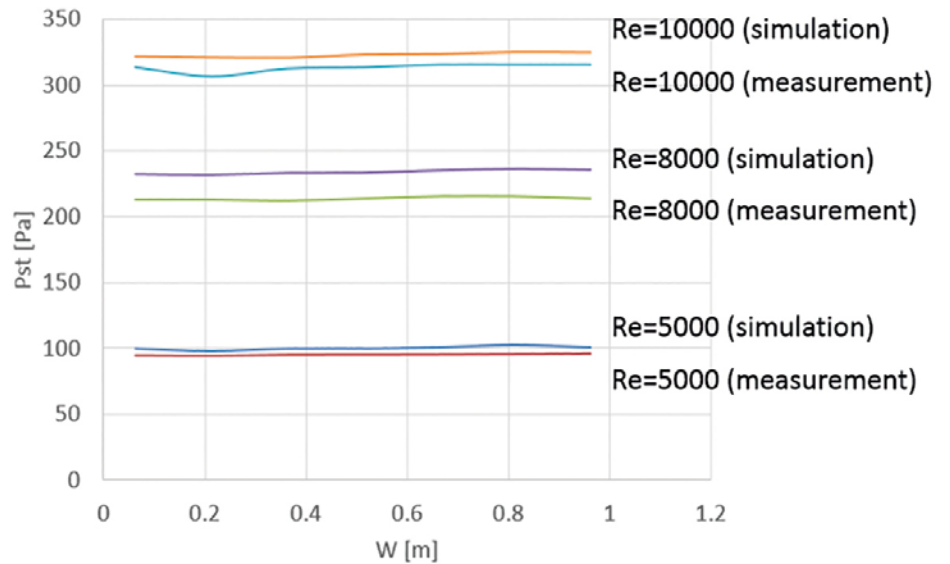
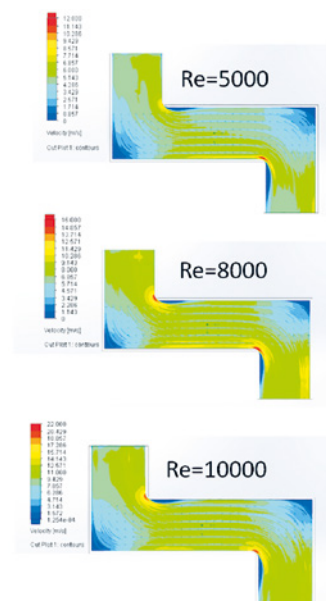


Figure 15. Comparison of measurement and simulation



Extraction of velocity profile

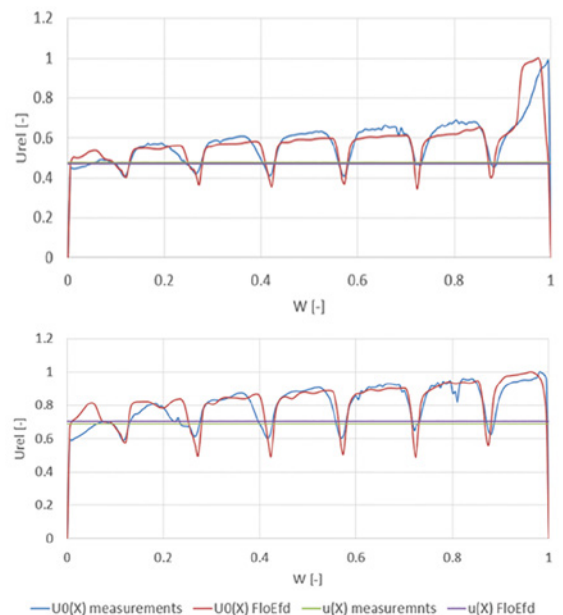
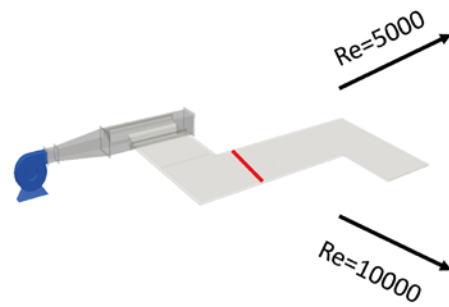


Figure 16. Comparison of the velocity profile

Design of a High Speed Decoy UAV

By Umut Baycara, Middle East Technical University

Drone aircraft and their uses have been evolving very quickly and there is a great deal of research that is occurring on an ongoing basis. One area of increased interest is in the decoy drone. These drones are designed to mimic the radar and heat signature of an actual aircraft. They are intended to confuse or mislead anti-aircraft defense systems. If operating as designed, one or more drones are launched from an actual aircraft as it enters airspace that is being monitored by anti-aircraft systems. The system picks up the signature of the drones and attacks them while the actual aircraft can be hidden with the swarm of drones.

The work conducted by Umut Baycara, is the design and CFD analysis of one such decoy UAV. The mission requirements for the high speed decoy were chosen to be: Maximum altitude of 15000 ft, maximum speed of 450 kts and an endurance of at least 1 hour.

The decoy UAV is launched from a pneumatic catapult and lands via a parachute system. It is a highly agile aircraft having a high maneuverability capability. The aircraft has a 6g sustained and 9g instantaneous load factor. Required payload capacity is set to be as 22 lbs, consisting of a smoke dispenser, a passive radar cross section augmenter (luneberg lens), a chaff and IR dispenser and a miss distance indicator.

Since, the aim of this study is to design an optimized high speed decoy that surpasses its predecessors, FloEFD CFD tool is used to achieve the high speed decoy configuration which gives the best aerodynamic performance. Baseline design and other configurations were created according to their vertical wing and tail geometry designs. All models were created in CAD environment and analyzed for different flow regimes and envelopes. Finally, configuration is selected considering various design and performance criteria.

Once the baseline design of the UAV was created in CAD, there were nine variations generated with the different wing / tail design combinations as shown in Figure 1. CFD analyses of each of these combinations was then run to find the optimum combination that

would best meet the mission requirements of the drone. These nine variations were derived from three wing and three tail options which included:

Wing vertical location effect the performance directly. It alters the C.G of the aircraft and therefore, the stability.

Baseline high speed decoy UAV has been designed as mid-wing due to reasons stated in the full paper [1]. In this section, low and high wing configurations have been designed.

- Low Wing – has less ground clearance and is not as laterally stable but enables better lateral control. It also produces less lift and induced drag. It has less downwash on the tail thereby making the tail more effective and finally it is structurally lighter than a high wing configuration.
- High Wing – has the most ground clearance, and is the most stable laterally though has less lateral control. They also tend to produce more theoretical lift and therefore more induced drag. They are also the heaviest structurally of all the designs.
- Mid Wing – As the name implies is in between both the high and the low design and the characteristics are as well.
- Conventional tail – Has a vertical tail that is the lightest structure of all three tail combinations because vertical tails do not need to carry the horizontal tail. The wing wake can disturb the horizontal tails in this tail configuration, especially with high wing combination.

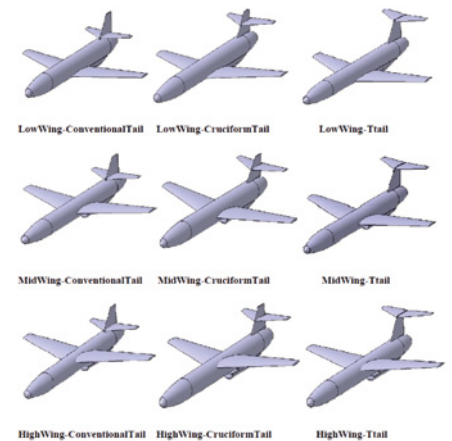


Figure 1. Drone test configurations

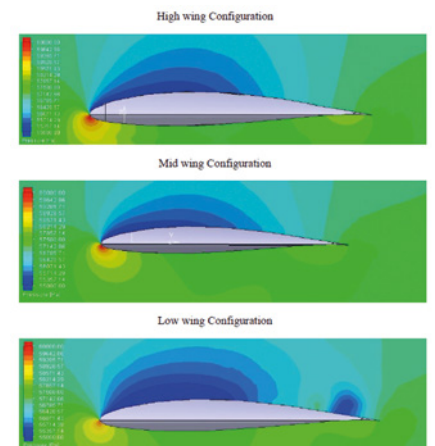


Figure 2. Pressure Contours 0.13m from centerline for High Wing, Mid wing and Low wing Configurations at $\alpha=60$

- T-tail - Offers the advantage to have a wake free horizontal tail since it is positioned the furthest distance vertically from the wing in any configuration. The downside is that it requires a heavy vertical tail structure to carry the horizontal tail.
- Cruciform tail is the combination of the T-tail and the Conventional tail. Cruciform tail enables lighter tail and helps in preventing deep stall.

For the initial analyses, high wing, mid wing and low wing Configurations were compared. With the tail configuration kept as T Tail. CFD analysis showed that the fuselage effect negatively affects the low wing and forces the flow to separate and makes the low wing prone to stall and reduces its lift efficiency making it the worst wing position among all configurations. High wing and mid wing showed similar performance but the high wing had more advantage for high angles of attack.

FloEFD revealed that for low angles of attack, mid wing configuration had lowest drag and highest L/D values. Whereas for higher angles of attack, high wing configuration yields lowest drag coefficient, highest maximum lift coefficient and gave highest L/D values. Unlike theory, the high wing configuration model yielded the lowest drag at higher angles of attack compared to other configurations. Therefore, high wing was selected for wing configuration.

Three different tail configurations were then analyzed while holding the high wing configuration constant. This showed that the T-tail seems to be wing wake free and the most lift. Since, deep stall is very important phenomena, the stall angle $\alpha=16\text{Deg}$ should be discussed in a higher detail to prove that deep stall will not occur.

In order to see occurrence of the stall phenomena completely, 3D flow trajectories were plotted. 200 pipe lines were used to show the flow trajectories through wing. 3D Flow trajectories finally confirms that the T-tail configuration horizontal tail tips are not significantly affected by stall wing wake.

Finally, decoy UAV has been tested in FloEFD during maximum velocity, corner velocity and cruise velocity. CFD results shows that the aircraft will be able to fly at the required maximum velocity without strong shock occurrence. Optimum cruise velocity has been found as 0.38 M from drag polar curves. Then, Optimum corner velocity is found from CFD result CL max.

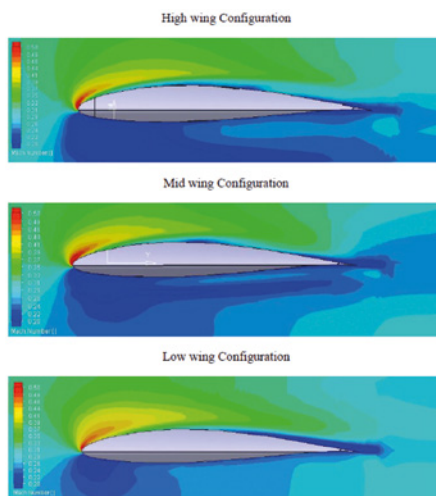


Figure 3. Mach Number Contours 0.13m for centerline for High wing, Mid wing and Low wing Configurations from at $\alpha=14^\circ$

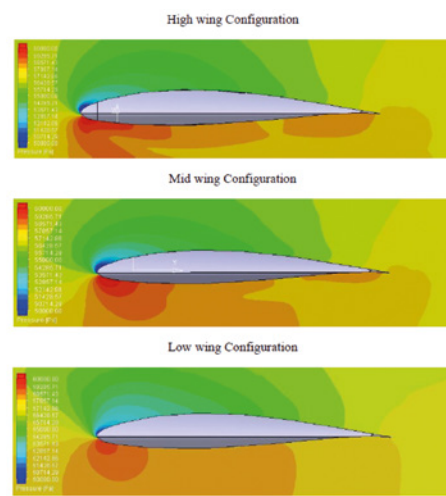


Figure 4. Pressure Contours 0.13m from centerline for High wing, Mid wing and Low wing Configurations at $\alpha=14^\circ$

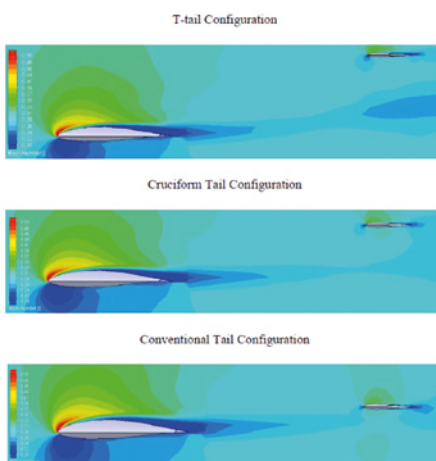


Figure 5. Mach Number Contours Cut plots 0.231m from centerline of T-tail, Cruciform tail and Conventional Tail at $\alpha=14^\circ$

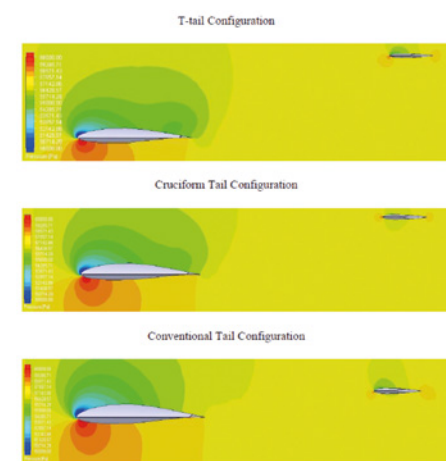


Figure 6. Pressure Contours Cut plots 0.231m from centerline of T-tail, Cruciform tail and Conventional Tail at $\alpha=16^\circ$

Wind tunnel testing is considered indispensable for getting the most accurate aerodynamic performance. However, creating prototype of every configuration and testing all of them in a wind tunnel is too time consuming and expensive for a designer. Therefore, high tech FloEFD CFD software is very helpful to reduce the prototype number. In this study, Catia-v5 embedded FloEFD software was used to successfully optimize the aircraft and test the aircraft performance during different operations such as cruise, maneuverability and maximum speed.

Reference:

[1] Design of a High Speed Decoy Uav a thesis submitted to the Graduate School of Natural and Applied Sciences of Middle East Technical University. By Umut Baykara, June 2016, <http://etd.lib.metu.edu.tr/upload/12620011/index.pdf>

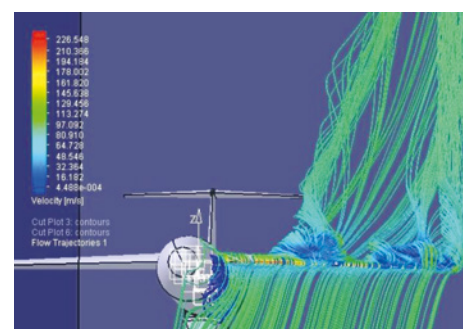


Figure 7. 3-D Flow Trajectories at $\alpha=16^\circ$ of T-tail

Thermal Interface for Pluggable Optics Modules

By Bonnie Mack, Senior Thermal Engineer and Terence Graham,
Senior Thermal Engineer, Ciena Corporation



Power on pluggable optics modules (POMs) such as SFP+, QSFP+, QSFP28, CFP2, CFP8 has increased along with the demand for higher bandwidth. POMs give access at the faceplate to an optical signal. Existing Multi-Source Agreements (MSAs) specify physical form factor and electrical interfaces, which allow multiple manufacturers to make physically compatible products to promote competition, interoperability and multiple sources for systems vendors and end users. These MSAs also define power classes for POMs that are based on the supplied power and correspond to different internal processing levels and optical signal reach. POMs are designed to support various communication standards and their data rates range from ~1 Gb/s to 400 Gb/s with many data rates available in each form factor.

POMs are difficult to cool; all but the CFP, are housed in a cage which guides the modules to the connectors and contains EMC solutions for the faceplate ports. The modules extend through the faceplate, and can be hot swapped. There are air gaps, ~0.2mm to 0.3mm nominal, between the module case and the cage, and between the cage and PCB. This provides an inconsistent thermal resistance due to tolerances. The cages generally have small openings on the sides to allow ingress and egress of air for cooling purposes. With high power POMs, these openings do not provide sufficient cooling so an opening on the cage top is added which gives access for a spring-loaded riding heatsink. To date only a dry thermal interface between the two surfaces has been available because the pluggable feature has precluded the use of thermal interface materials between the heatsink and the POM case. The thermal interface between POM and heatsink is not consistently defined or controlled in the MSAs. The challenge is to permit the required sliding while providing a low interface thermal resistance. This is especially important in a telecom environment where equipment in NEBS [1] shelf level products must operate in an ambient of 55°C. POMs temperature case limit is usually 70°C. This results in a 15°C temperature delta to cool the POMs, usually less when pre-heated by other POMs or components. Figure 1 shows typical

thermally-important features of POMs and cages.

Heat transfer routes to and from the POMs are described in references [2,3]. Thermal evaluation requires detailed 3D conjugate heat transfer analysis software. Essential input for the analyses includes detailed geometric, power, and thermal properties of the POM, EMC gasket and cage, and contact interface as described in the OIF thermal interface specification IA# OIF-Thermal-01.0 [4].

IA# OIF-Thermal-01.0 specifies general resistance parameters for the thermal interface as a function of power density. For high power modules, the major path for heat removal is via the heatsink across the contact area with the POM. It stipulates the MSA to define the location and size of contact area for heat removal on the top surface of POM. It also describes factors affecting thermal interface resistance: flatness, surface finish, and heat spreading. Additionally, it defines a calibration method for the internal sensors and includes the requirement to identify the location of thermal monitor point(s).

The initial work done in support of IA# OIF-Thermal-01.0 IA included a study of the thermal interface resistance between a CFP2 lid and heatsink base including heat spreading effects. The study examined three contact

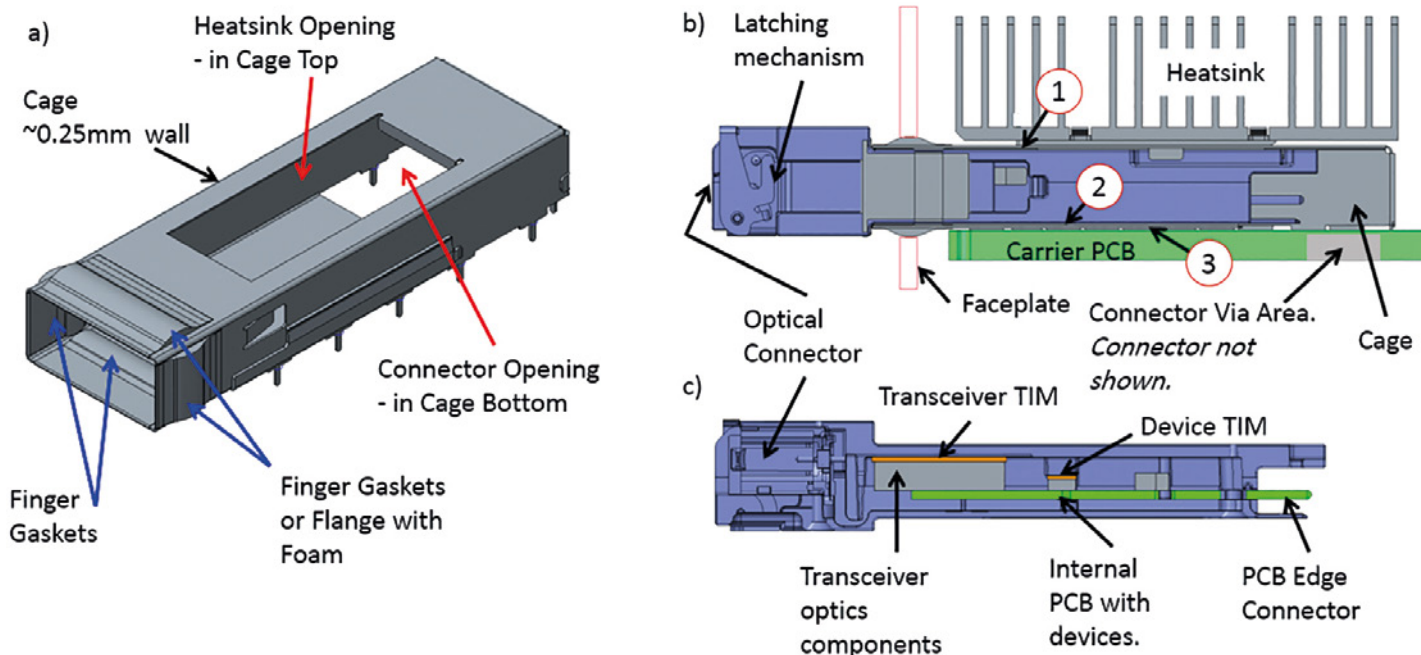


Figure 1. a) A typical POM cage, b) QSFP in cage section at inside edge of cage, c) QSFP section showing typical internal layout. Narrow air gap locations: 1) Module to top of cage, 2) Module to bottom of cage, 3) Bottom of cage to PCB, and not shown 4) sides of module to sides of cage.

scenarios: 1) a transverse bump in the center of the lid, 2) a transverse hollow in the center of the lid, and 3) a transverse contact in the center and ends of the lid. All three scenarios have the same contact area. These simplified contact geometries are depicted in Figure 2 and the contact gap ranges from what would be an extremely fine production surface flatness to 0.3mm, the maximum allowed by the MSA for the CFP2 contact surface for Power Class 1 and 2. It was assumed for the study that both surfaces had the same type of out of flatness so that modeling of the net gap between surfaces was easily implemented in FloTHERM® software used for the analysis.

The resistance in the contact areas between the heatsink and the module was modeled using the method described by Yovanovich et al. [5]. Where:

$$\text{Joint Resistance } h_j = h_{\text{contact}} + h_{\text{gap}}$$

A simplified CFP2 FloTHERM model was created with a T6063 aluminum case and up to six sources that can be set to dissipate power and to contact the lid as shown in Figure 3. Results were obtained for varying gaps due to out-of-flatness and different source locations. Intake air is 55°C at 1m/s across the enclosure cross-section upstream of the module. Total power for the CFP2 is 12W in all cases. Other model details are given in [2,3]. CFP2 lid temperature is monitored directly above the center of each source. Maximum lid temperatures are plotted in Figure 4 versus net flatness over the range

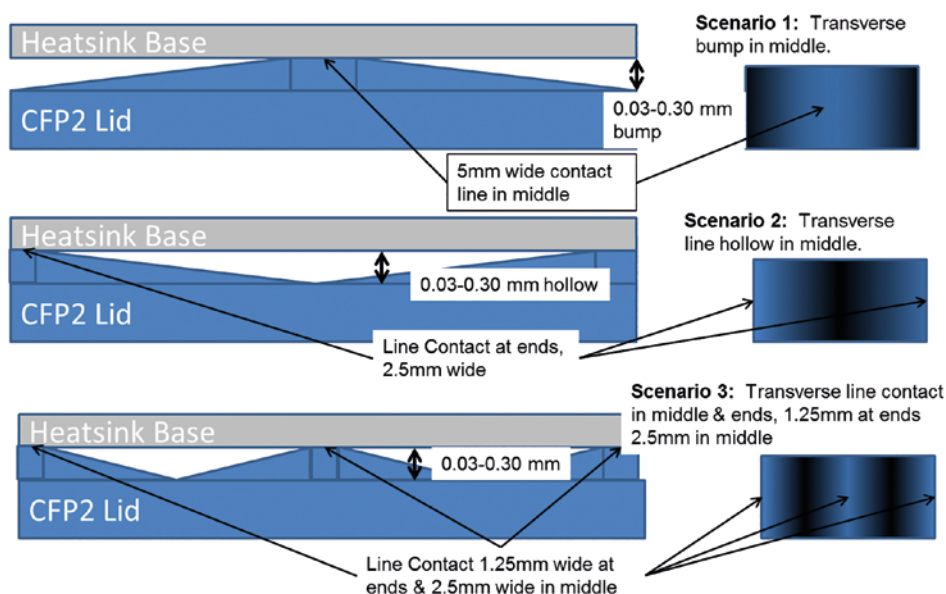


Figure 2. CFP2 Contact Interface Flatness Scenarios

of 0.03 mm to 0.3 mm flatness, for the three scenarios depicted in Figure 2. Defining:

- $T_{\text{Lid max}}$ = maximum lid temperature
- $T_{\text{HS ave}}$ = average heatsink pad temperature
- dT_{Lid} = temperature difference among lid locations A – F (indicative of thermal spreading resistance)
- $dT_{\text{Lid max to HS ave}} = T_{\text{Lid max}} - T_{\text{HS ave}}$

Spreading resistance in the lid was highest for scenario one, a center bump, which is

also effectively a single contact. Spreading resistance varies with the thermal conductivity and thickness of the lid. The interface resistance between the lid and heatsink is shown to be sensitive to the interface flatness. Temperature differences between lid and heatsink base can be reduced by 5°C to 8.5°C with flatness improvement on a CFP2 depending on heat source location and the nature of the out-of-flatness. This is a third to half of the CFP2 temperature budget in a NEBS environment! This is a huge improvement without increasing the size of the heatsink.

QSFP Model – Expanding on the Effect of Spreading Resistance

The QSFP form factor is a common POM that presently has the highest power density of all the form factors. Most of its heat is dissipated close to the faceplate and not directly underneath the heatsink contact area. A numerical wind tunnel study was conducted to explore the internal resistances and develop methods of reducing the QSFP temperatures. The numerical model, detailed in [2,6], was similar to that of [7] having a 5 W QSFP and a power density of 1.34 W/cm², class pd14. Cooling was via a typical aluminum off-the-shelf heatsink. The model was used to predict the effect of changes in the heat source locations relative to the heatsink contact area and surface finish in the interface area. Figure 5 gives the scenario descriptions. For scenario d) the 5mm extension of the heatsink contact area towards the transceivers, the power density decreases 15% to 1.14 W/cm² or to pd12. Two contact resistance values between the case and the heatsink were explored as well for two difference surface roughness and load conditions. Results were calculated for QSFP case material thermal conductivities of 116, 169, 385 and 1000 W/m-K corresponding to a zinc alloy, high grade aluminum casting, copper, and an ultra-high conductivity material respectively. FloTHERM Command Centre was used to solve these scenarios.

The results shown in Figure 6 illustrate the importance of the surface finish of the case and heatsink, and of locating the heat sources and the thermal interface area as closely together as possible. QSFP MSA cage dimensions [8-9] allow an increase in heatsink contact length by up to 5mm. In our model this larger contact resulted in a temperature decrease of more than 1.5°C with the lowest case conductivity and Rc1. If the case material conductivity is increased to 169 or 385 W/m-K, further decreases of 1°C to 2°C respectively could be achieved. While very high case conductivities representing an exotic material was examined, changing QSFP case material to Cu from zinc

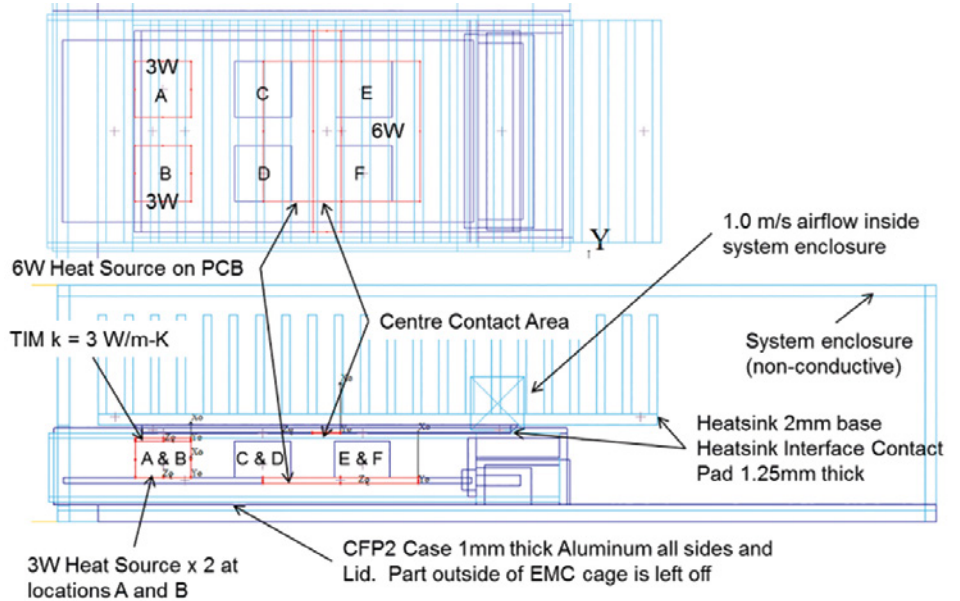


Figure 3. CFP2 flatness model layout showing front device, rear CFP2 PCB heat and central contact location

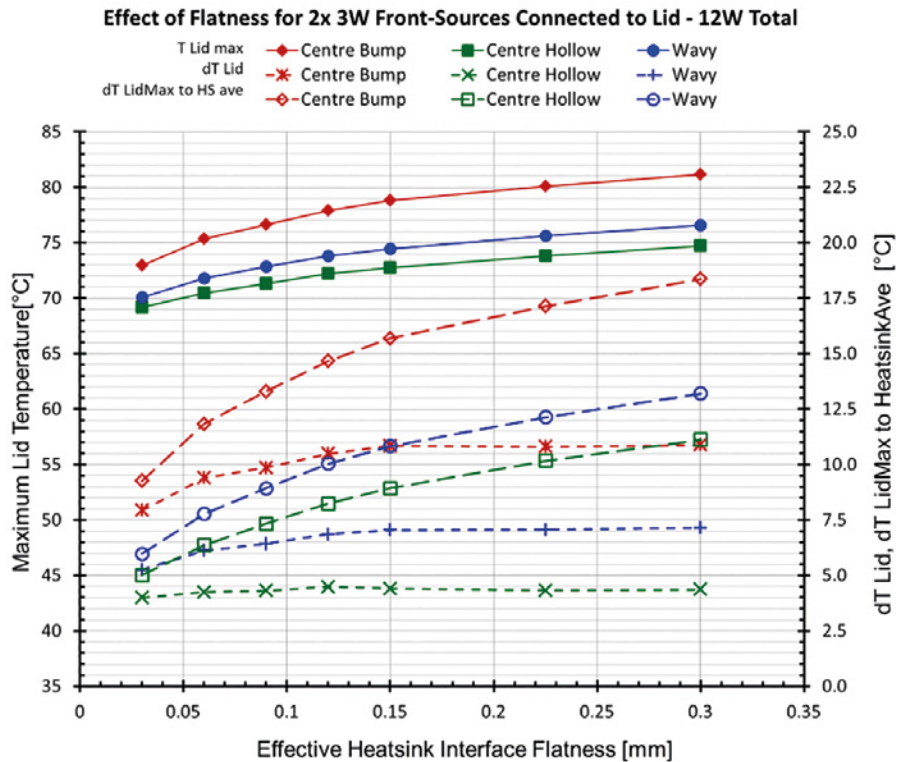


Figure 4. Range of flatness results with front device, and rear PCB heat dissipation and only the devices connected directly to the lid.

alloy can improve performance by 2 to 3°C. Decreasing the contact resistance to Rc2 would bring total improvement to ~5°C. These are significant when the overall ambient to case temperature budget could be 15°C or less.

The expansion of the heatsink opening in the cage has been incorporated into the MSA for the much higher power QSFP-DD modules [10].

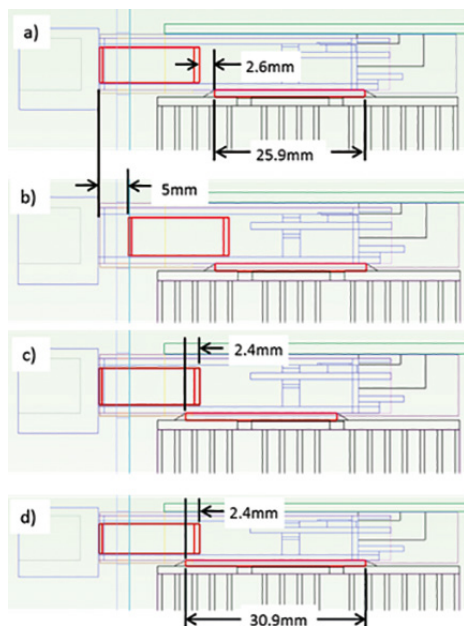


Figure 5. Modeling scenarios for the QSFP a) Original, b) Transceivers 5 mm closer to heatsink contact, c) Heatsink contact 5 mm closer to transceivers, d) Heatsink contact 5 mm longer towards transceivers. Transceiver location is the red rectangle on the left.

Final module thermal assessment is at present only available with a computationally expensive detailed model created from the information specified in [4] and either built by the system designer with information from the module supplier, or is a model supplied by the module vendor, likely under some type of non-disclosure agreement. An alternative to this that has not yet been explored is the development of a Delphi-type resistance network. A model of this type could be used to model the connections to the PCB, surrounding air and heatsink with distributed internal heat sources in a manner similar to that used for multi-junction integrated circuit devices. This could be provided by module vendors without giving internal details of the module.

References:

[1] Telcordia Technologies Generic Requirements, Generic Requirements for Telecommunications Data Center Equipment and Spaces, GR-3160-CORE, Issue 2, July 2013

[2] Mack, B., Graham, T., Thermal Specifications for Pluggable Optics Modules, 32 IEEE SEMI-THERM Symposium, March 2016.

[3] Mack, B., Graham, T., Pluggable Optics Module – Thermal Specifications, Part 1, Electronics Cooling, June 2016.

[4] IA# OIF-Thermal-01.0, Implementation

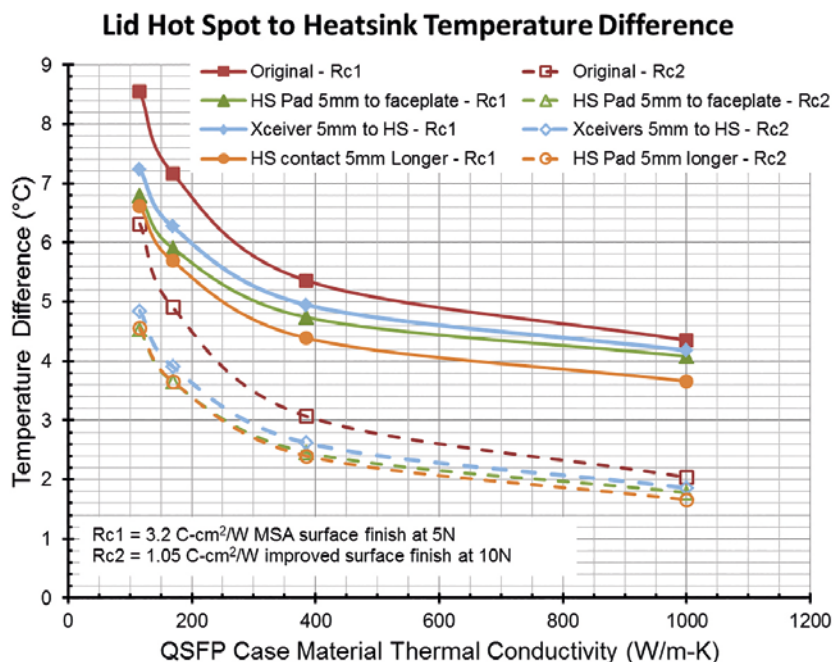


Figure 6. Temperature difference between QSFP hot spot monitor point and heatsink pad. Surface finishes of 0.6 μm Ra and 1.6 μm Ra on both heatsink and case

Agreement for Thermal Interface Specification for Pluggable Optics Modules, Optical Internetworking Forum, May 18, 2015

[5] Yovanovitch, M.M., Culham, J.R., and Teerstra, P., Calculating Interface Resistance, Electronics Cooling, Article 3, May 1997, http://www.electronics-cooling.com/Resources/EC_Articles/May97/article3.htm

[6] Graham, T., Mack, B., Pluggable Optics Module – Thermal Specifications, Part 2, Electronics Cooling, September 2016.

[7] OIF-PLUG-Thermal-01.0, Thermal Management at the Faceplate White Paper, Optical Internetworking Forum, March 2012

[8] SFF Committee, SFF-8663 Specification for QSFP+ 28 Gb/s Cage (Style A), Rev 1.5 April 2014, <ftp://ftp.seagate.com/sff>

[9] SFF Committee, SFF-8661 Specification for QSFP+ 28 Gb/s 4x Pluggable Module, Revision 2.0, February 2014, <ftp://ftp.seagate.com/sff>

[10] Quad Small Form Factor Pluggable Double Density (QSFP-DD) Multi Source Agreement (MSA) Group, QSFP-DD 3.0 Hardware Specification, September 2017 www.qsfp-dd.com

Geek Hub

What do engineers see in coffee grounds?
FloEFD Validation applied to the tasks of geometrical optics

By Dr. Svetlana Shfilkind, Dr. Andrey Ivanov and Maxim Popov, Mentor a Siemens Business

Our life is full of light. Inside or outside, near or far, light surrounds us everywhere and penetrates even in the dark places. Light expresses itself in many ways. One of them is shiny patterns produced by reflection and refraction of rays from complex surfaces (Figure 1).

They are called caustics – the curves or surfaces which are tangent to patches of rays. Caustics outline the boundaries of maximum radiative flux.

The object of our investigation is well-known and one of the most beautiful caustic. Inspired with amazing properties of light, we've focused its rays in the shape of the heart or cardioid in terms of math.

The origins of this work are following to the kitchen and arising on the bottom of a cup (Figure 2).

Side irradiation and cylindrical specular surfaces of cup are necessary conditions to obtain the cardioid. Therefore you can easily observe cardioid inside glasses, cups of coffee, pans and other equal tableware. Let us consider how it appears.

Cardioid is an algebraic curve of 4th order. Its polar equation is $r = 2a \cdot (1 - \cos \phi)$. The coefficient a is based on the geometrical interpretation of curve. On the one hand cardioid can be defined as trace of point M which belongs to the circle of radius a . This circle is rolling without slipping on another circle of radius a , starting from the point O (Figure 3a). On the other hand cardioid is an envelope of circles built on the generatrix circle of radius a with radiuses OP (Figure 3b).

Mathematical substantiation of our simulation is based on the geometrical law: cardioid is an envelope of light rays emitted from the point on the circle and reflected specular from circle's boundary (Figure 4).

In other words cardioid is a caustic of circle with a light source, placed on its boundary. This law defines the distribution of radiant flux after it has been reflected from cylindrical surface (Figure 5).



Figure 1. Caustics produced by a glass [1]



Figure 2. Cardioid inside a cup [2]

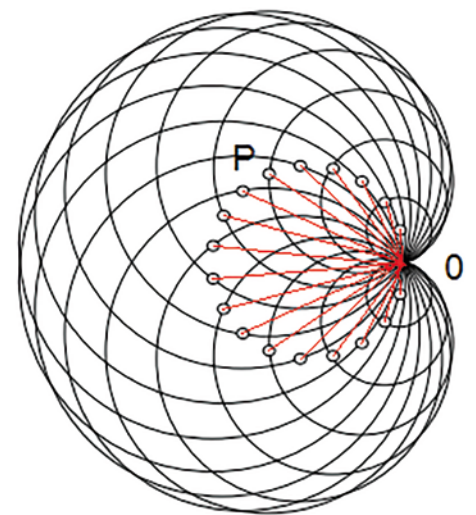
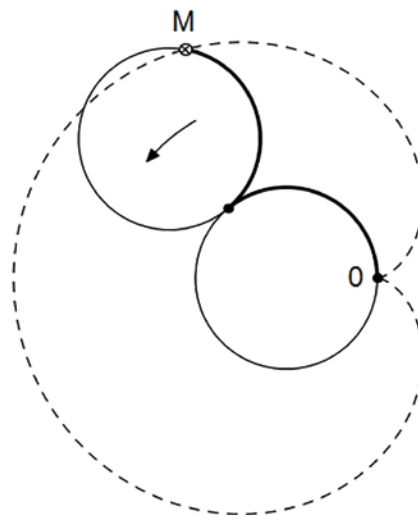


Figure 3. The ways of how the cardioid can be created [2]

The model

For our simulation the real cup with complex conical reflecting surface was chosen (Figure 6).

The model of a cup has been constructed partially filled with some liquid (coffee is preferable), but reflecting and refracting properties of this wasn't taken into account. Its volume was defined like solid, impermeable for light. Walls of cup were also

interpreted as opaque. The surface of liquid was treated like a screen which accumulates incident rays reflected from cup's interior. Rays intensity can be evaluated through distribution of net radiant flux.

The source of light was defined as diffusive. Its size was close to point to exclude the influence on the propagation of light.

Influence of source location

Obviously the location of the source determines the distribution of radiative flux on the screen. To find the location of source on which light will be focused into cardioid, a set of preliminary calculations were performed. The source was examined in 16 positions, differed by horizontal and vertical coordinates (Figure 7).

The growth of both coordinates was started from the point 0 on the cup edge. Spatial step along X was 15 mm, along Y – 40 mm, radius of cup edge – 50 mm. Fig.8 illustrates the results of calculation: distribution of net radiant flux on the screen.

It is easy to see how the location of source affects the distribution of radiative heat flux. When the source is in the low position (Y=0) and far enough from cup edge (X>1), the screen is fully shadowed. But if even small portion of light has reached internal surface of cup, the rays are being focused in the shape of cardioid. The size of cardioid grows as the source moves from cup edge.

To demonstrate the influence of height of reflecting surface into optical image we've simplified our model and explored reflection from cylindrical walls. The two configurations have been explored: at the first case walls height was close to zero – the model abstraction to organize reflection on the plane of bottom only. At the second case reflections took a place along the wall's height. The results of calculations are presented in Figure 9.

It is easy to see how the distribution of radiative flux changes in accordance with height of reflective walls. If rays are reflected from «boundary of the circle» (case a), we've got sharp cardioid. If the reflections occur in different height (case b), the image becomes more complex and includes secondary maximums.

Now we can choose the proper location of source to reproduce the cardioid of desired configuration. The results of calculations are very close to the real observed picture (Figure 10 and 11).

To confirm correspondence between the calculated caustic and cardioid, let us

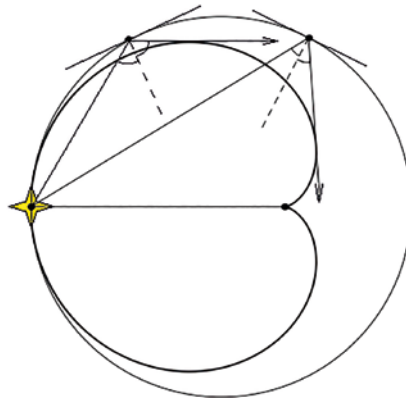


Figure 4. Geometrical interpretation of cardioid [3, 4]

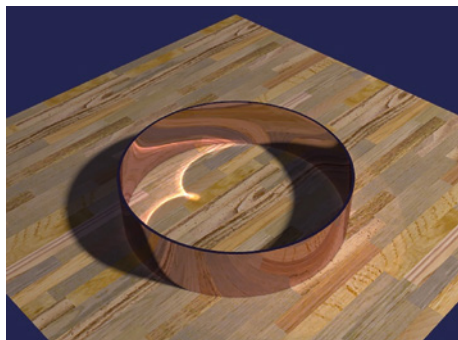


Figure 5. Cardioid produced by cylindrical reflecting surface [3]

compare the maximum of net radiant flux with the curve defined by equation $r = 2a \cdot (1 - \cos \phi)$. The two situations were considered: the source is located at X=2, Y=3, second – at X=0, Y=2. It is easy to see that the first results corresponds to cardioid with coefficient $a=0.0588$, and the second results – to cardioid with $a=0.0480$ (Figure 12).

Both results have reproduced accurately the cardioid of two types, which differs from each other in the source location.

3D cardioid

Starting from the two-dimensional image on the bottom of the cup, let us expand our vision of cardioid in 3D case. The next example presents quite an original diagram of radiation visibility. Radiation is being detected on the far field from the spherical heat source, made from two equal parts with different temperatures (Figure 13).

Let us imagine the circulation around heat source in the far field. The objective of the circulation is to collect the values of radiation flux in each point of orbit. Orbit belongs to the one of three planes: XY, XZ and YZ. The results of such investigation predicted with FloEFD in polar coordinates are shown in Figure 14. Radiation flux detected in YZ plane is a circle, because of uniform impact of each point of heat source. Distribution of energy crosswise source in XY and XZ planes

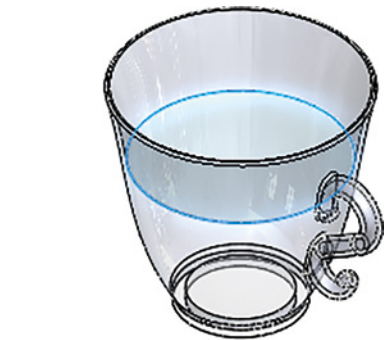
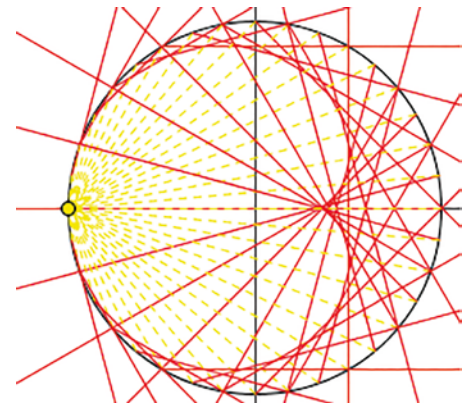


Figure 6. The model of a cup

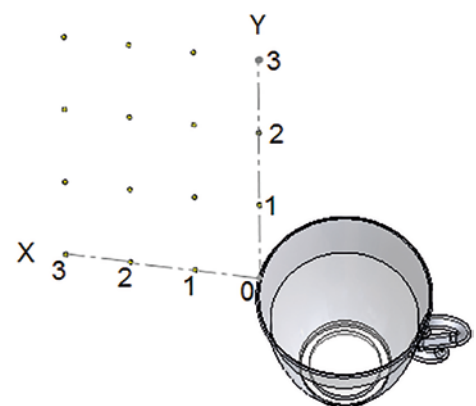


Figure 7. Source locations, gridded in coordinates thXOY

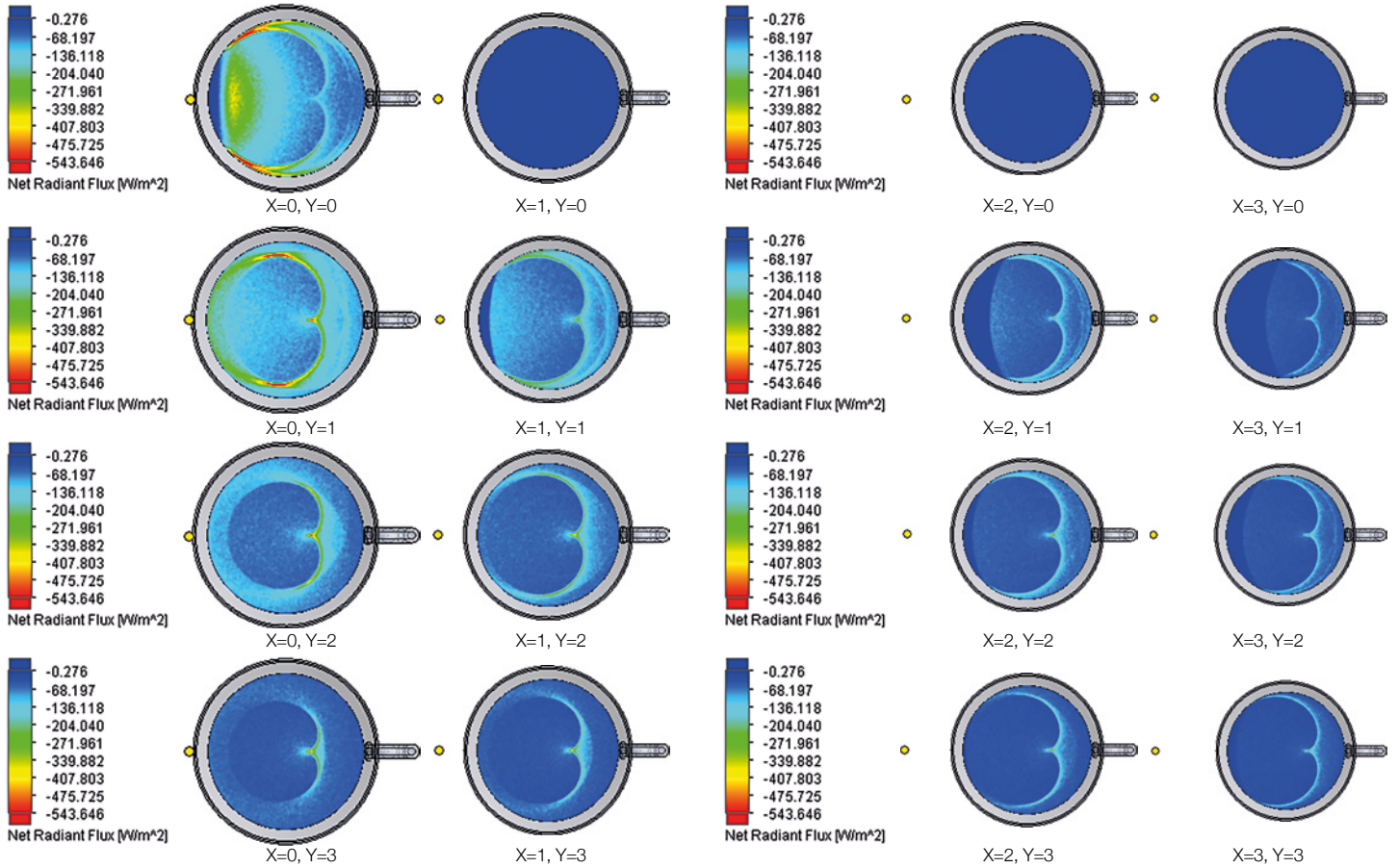


Figure 8. Distribution of net radiant flux on the screen: top view. The location of source is marked with yellow point.



Figure 9a. reflection from the wall: height is close to zero

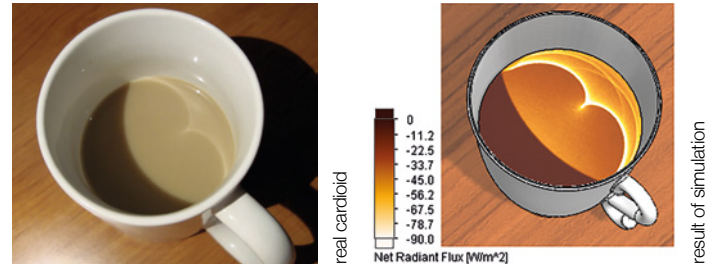


Figure 10. reflection from the wall: height is close to zero



Figure 9b. reflection from the wall: height is nonzero

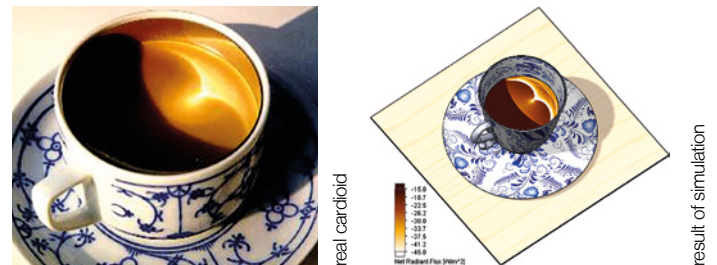


Figure 11. Reality and the results of simulation [5]

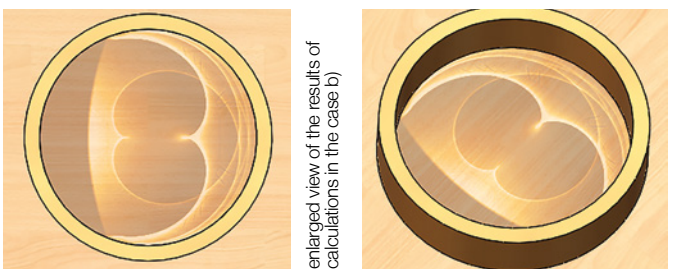


Figure 9. Cardioids produced by the walls of different heights

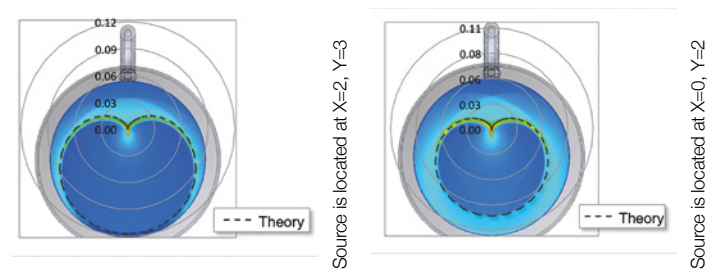


Figure 12. Comparison between the shapes of calculated caustics and analytical curves

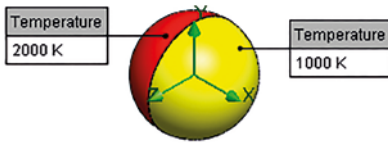


Figure 13. Spherical source with nonuniform distribution of temperature

depends on the angle of view. It changes monotonically from the coldest point ($X=+R_v, Y=0, Z=0$) to hottest point ($X=-R_v, Y=0, Z=0$). Its shape corresponds to cardioid with coefficient $a=0.00057$.

By the way an ordinary example of such a source is a simple lamp. Its radiative flux, measured in the equally-spaced positions, creates a cardioid (Figure 15).

Thereby radiative flux produced by non-uniform heat source, measured on the surface of imaginary sphere and presented in polar coordinates, takes the shape of 3D-cardioid (Figure 16).

3D-cardioid can be a result of propagation not only light rays, but even sound waves (when they are treated as rays – linear acoustics). The cardioid microphone has a special name because of its sound pick-up pattern [6]. Polar pattern graphs visually represent the microphones sensitivity to sound relative to the direction or angle from which the sound arrives. Figure 17 illustrates how sensitive it is to the sounds coming at different angles. Each point of cardioid corresponds to a composition of an angle at which sound enters the microphone and a volume of sound being input.

In our investigation multifunctional CFD-package FloEFD has demonstrated its wide opportunities in the area of precise optics simulation. The models of radiative heat transfer which are taking into account different ways of light propagation enables analysis of complex interference of light. The results of calculations are in perfect agreement with experimental data, theoretical estimates and our living experience.

Taking a look at the bottom of the cup engineers are thinking of the beauty of nature and predictive power of the modern numerical methods. We do believe that calculations with FloEFD can shine a light on the dark issues in engineering.

References:

- [1] <https://ru.wikipedia.org/wiki/%D0%9A%D0%B0%D1%83%D1%81%D1%82%D0%B8%D0%BA%D0%B0>
- [2] <http://prof.pantaloni.free.fr/spip.php?article58>

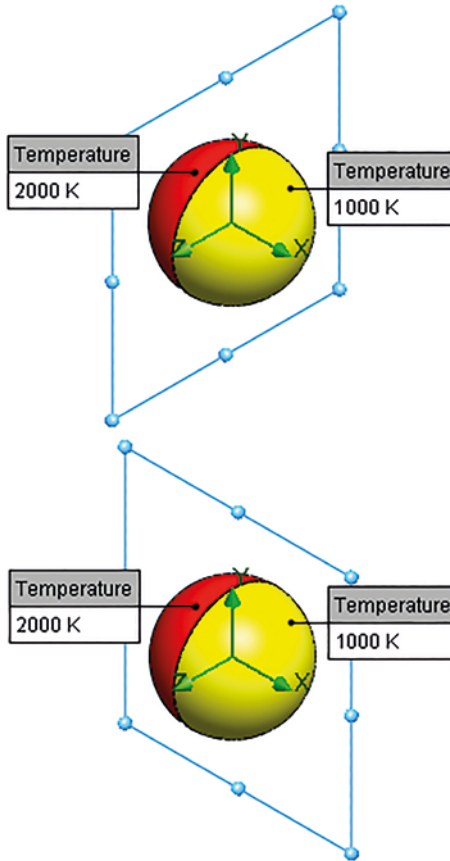


Figure 14. Radiative visibility of the source in different planes

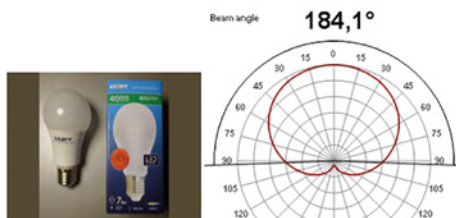
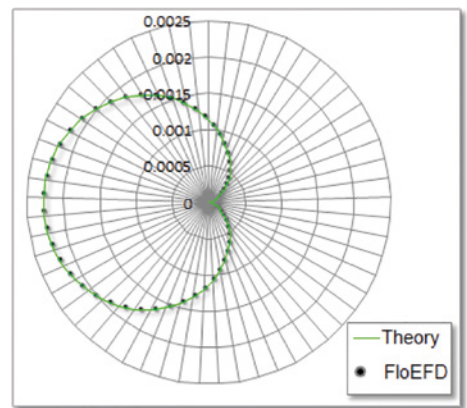
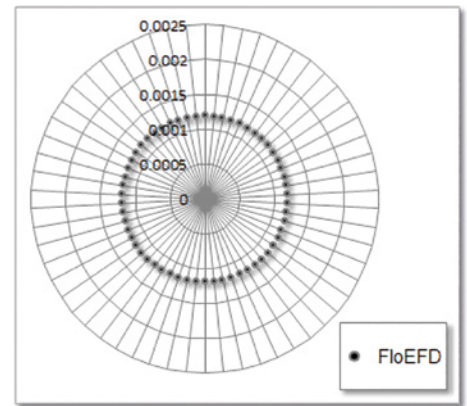


Figure 15. Radiative flux from lamp

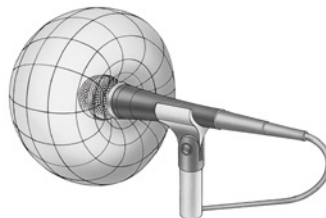


Figure 17. microphone with cardioid pick-up pattern

- [3] <http://graphics.stanford.edu/~henrik/images/metaling.jpg>
- [4] A.V.Akopian. Geometry of a cardioid. KVANT Journal, №3, 2012 (In Russian).
- [5] <http://thatsmaths.com/2014/09/25/curves-with-singularities/>
- [6] <http://mathforum.org/mathimages/index.php/Cardioid>

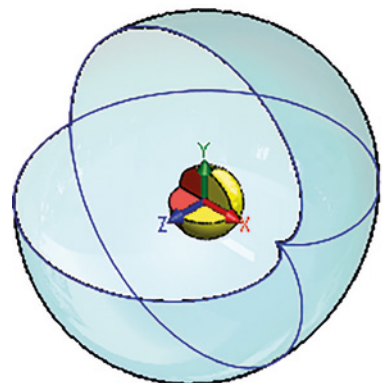
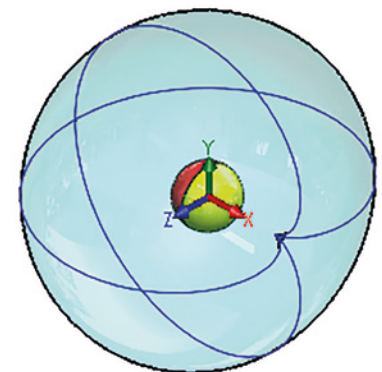
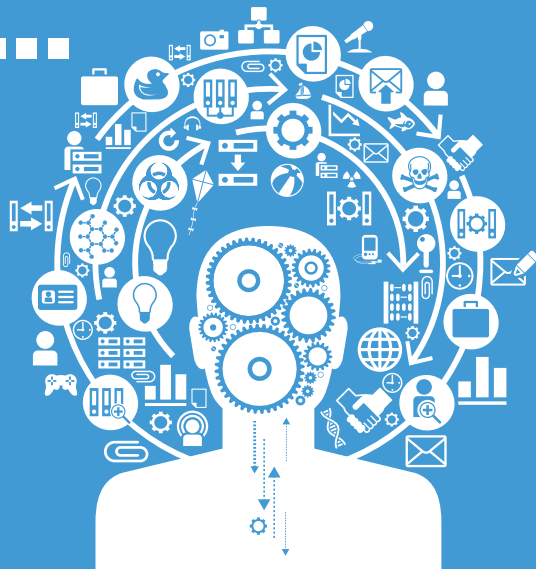


Figure 16. Total radiative visibility of the source

Brownian Motion...

The random musings of a Fluid Dynamicist

Brownian Motion or **Pedesis** (from Greek: πήδησις Πεδε:σις 'leaping') is the presumably random moving of particles suspended in a fluid (a liquid or a gas) resulting from their bombardment by the fast-moving atoms or molecules in the gas or liquid. The term 'Brownian Motion' can also refer to the mathematical model used to describe such random movements, which is often called a particle theory.



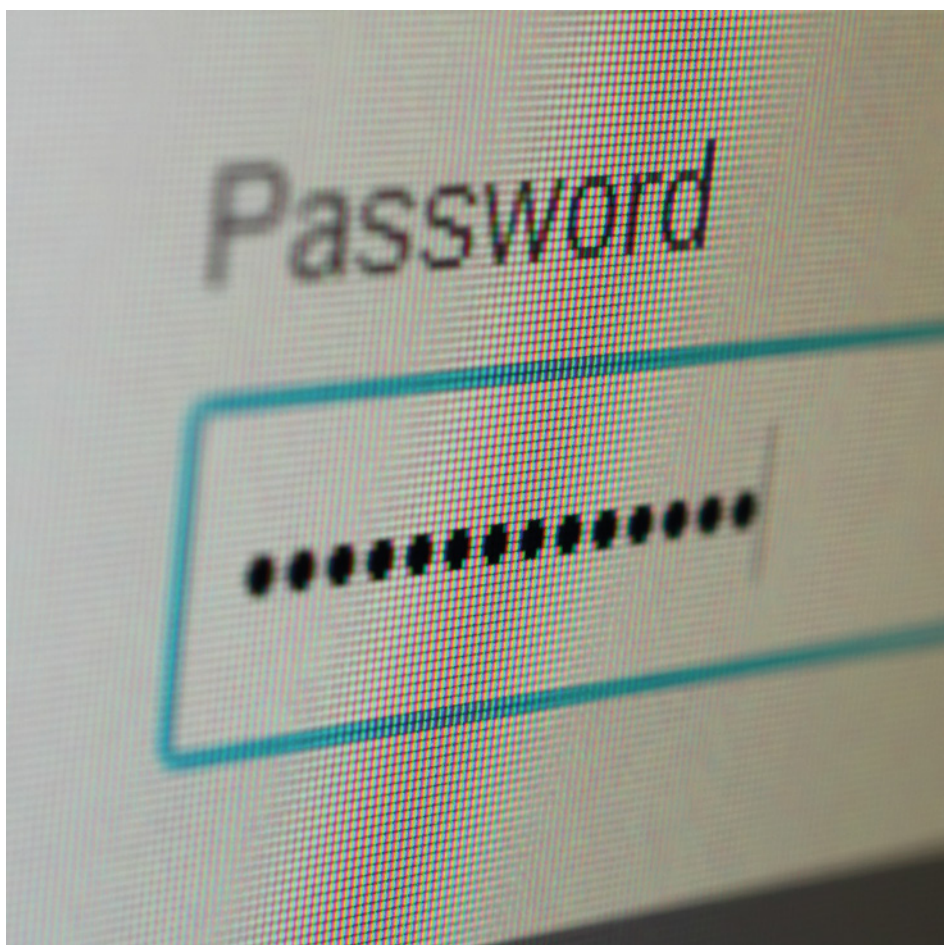
Log In Failed!

Maybe Brownian Motion is getting on a bit and that is the reason for the memory challenges, but the bane of my life is passwords. Every website seems to require one and all too often I visit a site only to find I am locked out. I have been there before but forgotten my login credentials. I am assuming everyone has experienced the same minor annoyance.

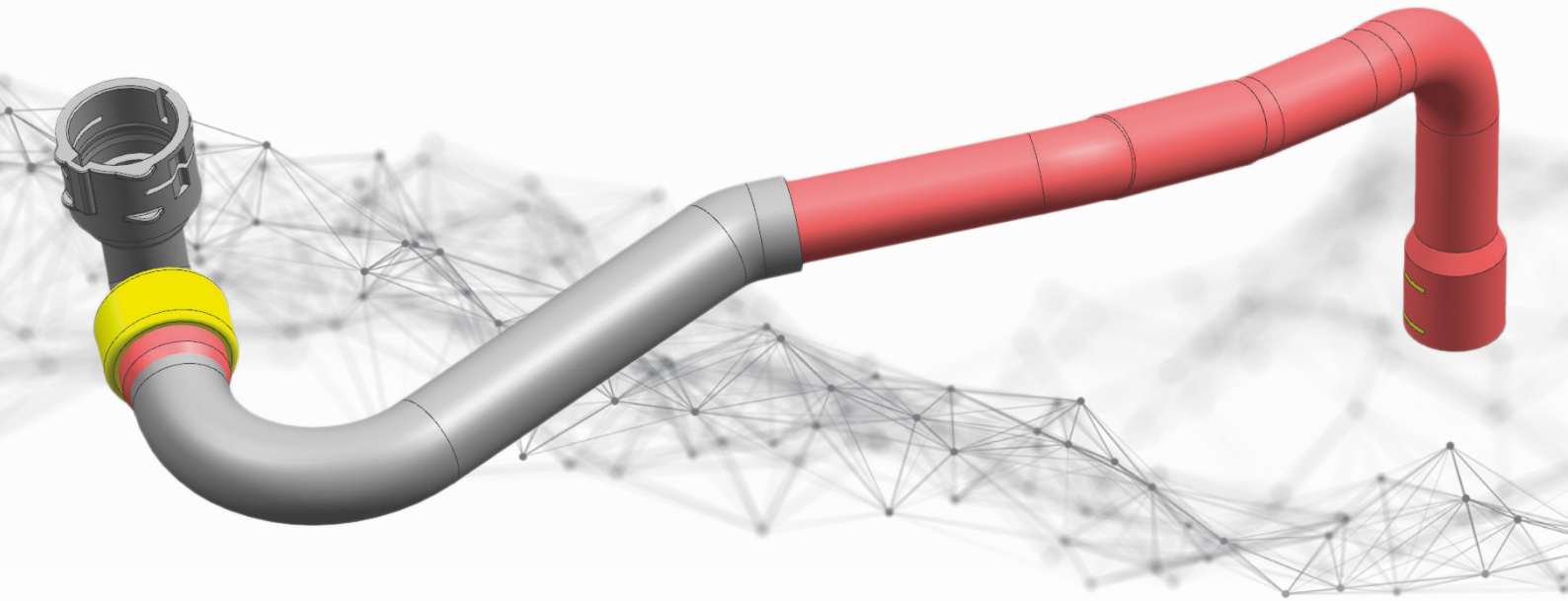
Not that this matters that much for most sites, but when it comes to on-line banking it is rather more important you remember all those characters. Currently the thumb print seems to suffice but not sure what happens when I change phones...which reminds me of a funny story I read recently.

Bitcoins are hot property, or is it Blockchain? But I digress, Bitcoins, state of the art cryptocurrency. Now no-one 'owns' the Bitcoin transaction network so if you forget your password / PIN, who do you call? The Ghostbusters aren't going to help much here. It's decentralized, that is the whole point. Peer-to-peer network with transactions not moving through an intermediary.

So back to the story, it seems some early adopters got in on Bitcoin pretty early (the clue is in the name there!) and have now watched its meteoric rise. One journalist



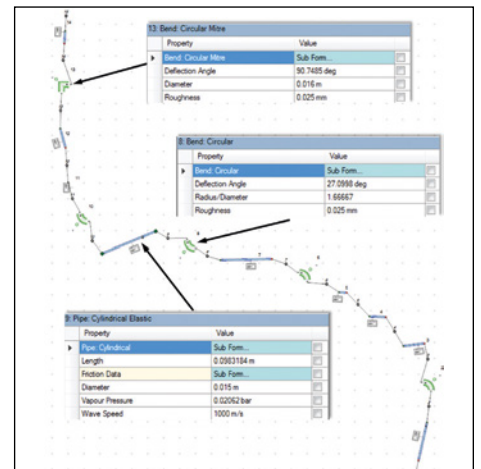
purchased 7.4 BTC for \$3,000 back in January 2016 which is now worth just under \$50k. He wrote some passwords on a piece of paper that subsequently got thrown out. Ouch...bit like losing a lottery ticket, and certainly more than a minor annoyance.



New from **FloMASTER 9.0**

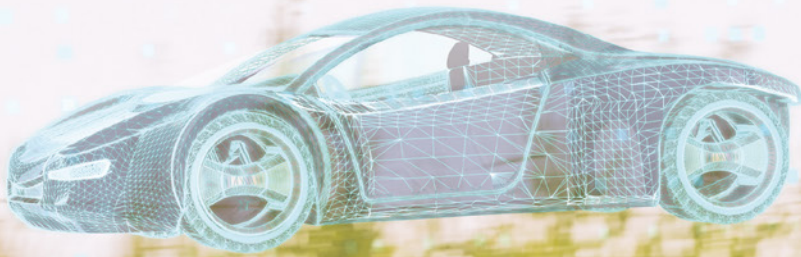
Convert CAD Geometry into a
FloMASTER Sub-System

Systems simulation using FloMASTER enables rapid simulation, sizing and optimization of components in a piping network. New with FloMASTER V9 is a fully automated function to convert MCAD piping geometry into an equivalent FloMASTER sub-system, bypassing data re-entry errors and compressing the time required for such a conversion from hours to minutes.



SIEMENS

Ingenuity for life



Today's dreams need tomorrow's engineering.

Simcenter: Predictive engineering analytics for the new era of smart innovation.

Getting a dream rolling has never been more challenging. Products are smarter. Manufacturing processes are more complex. And design cycles are shorter than ever. Simcenter software can help. With its unique combination of multi-disciplinary simulation, advanced testing and data analytics, Simcenter gives you the power to explore alternatives faster, predict performance more accurately... and deliver innovation with greater confidence.

[siemens.com/simcenter](https://www.siemens.com/simcenter)